Bobynko, Joanna (2018) *Characterisation and absolute quantification of nanosized V and Nb precipitates in high manganese steel using DualEELS.* PhD thesis.

https://theses.gla.ac.uk/30670/

Copyright and moral rights for this work are retained by the author

A copy can be downloaded for personal non-commercial research or study, without prior permission or charge

This work cannot be reproduced or quoted extensively from without first obtaining permission in writing from the author

The content must not be changed in any way or sold commercially in any format or medium without the formal permission of the author

When referring to this work, full bibliographic details including the author, title, awarding institution and date of the thesis must be given

Enlighten: Theses
https://theses.gla.ac.uk/
research-enlighten@glasgow.ac.uk

Characterisation and absolute quantification of nanosized V and Nb precipitates in high manganese steel using DualEELS

Joanna Bobynko

School of Physics and Astronomy

College of Science and Engineering

University of Glasgow

Presented as a thesis for the degree of Ph.D.

Supervised by Dr Ian Maclaren and Dr Damien McGrouther

October 2017

List of acronyms

3DAPT - 3D Atom Probe Tomography

ADF - Annular Dark Field

APT - Atom Probe Tomography

ARM - Atomic Resolution Microscope

BCC - Body Centred Cubic

BF - Bright Field

CBED - Convergent Beam Electron Diffraction

CCD - Charge-Coupled Device

CCS - Cleaning Cross-Section

CL - Core Loss

DC - Dark Current

DF - Dark Field

DM - DigitalMicrograph

DOS - Density of States

DP - Diffraction Pattern

EDX - Energy Dispersive X-ray Analysis

EEL - Electron Energy Loss

EELS - Electron Energy Loss Spectroscopy

EELS -SI - Electron Energy Loss Spectroscopy - Spectrum Imaging

EFTEM - Energy Filtered Transmission Electron Microscopy

ELNES - Electron Loss Near-Edge Structures

EMPA - Electron Micro Probe Analyzer

EU - European Union

EXELFS - Extended Energy Loss Fine Structure

FCC - Face Centred Cubic

(c)FEG - (cold) Field Emission Gun

FIB - Focused Ion Beam

FIM - Field Ion Microscopy

GIF - Gatan Image Filter

GIS - Gas Injection Source

GMS - Gatan Microscopy Suite

HAADF - High Angle Annular Dark Field

HCP - Hexagonal Close Packed Structure

HSLA - High Strength Low Alloy steels

HR - High Resolution

HRSTEM - High Resolution Scanning Transmission Electron Microscopy

HRTEM - High Resolution Transmission Electron Microscopy

LL - Low Loss

MAADF - Middle Angle Annular Dark Field

MCMP - Materials and Condensed Matter Physics Group

MLLS - Multiple Linear Least Squares

MSA - Multi Statistical Analysis

PCA - Principal Component Analysis

PEELS - Parallel Electron Energy Loss Spectroscopy

PIPS - Precision Ion Polishing System

SNR - Signal to Noise Ratio

SBR - Signal to Background Ratio

SAD - Selected Area Diffraction

SAED - Selected Area Electron Diffraction

SEM - Scanning Electron Microscope

STEM - Scanning Transmission Electron Microscope

SRIM - Stopping and Range of Ions in Matter

TEM - Transmission Electron Microscope

TM - Transition Metal

TRIP - transformation induced plasticity

TWIP - twinning induced plasticity

TU Wien -Technische Universitat Wien

UK -United Kingdom

UV - Ultraviolet

UTS - Ultimate Tensile Strength

WDX - Wavelength Dispersive X-Ray Analysis

ZLP - Zero Loss Peak

Declaration

This thesis is a record of work carried out by myself within the Materials and Condensed Matter Physics group under the supervision of Dr Ian MacLaren and Prof. Alan Craven in the school of Physics and Astronomy at the University of Glasgow from 2011 - 2017. The work described is my own with exception of:

- Bulk specimens, which were manufactured by ThyssenKrupp Stahl company in Duisburg
- scripts, which were written by Prof. Alan Craven
- creation the 3D movie of precipitate using Amira software, which was also prepared by Prof. Alan Craven.

This thesis has not previously been submitted for a higher degree.

Some parts of the work have been published in the following papers:

Bobynko J., Craven A.J., McGrouther D., MacLaren I., and Paul G., *Nanocharacterisation of precipitates in austenite high manganese steels with advanced techniques: HRSTEM and DualEELS mapping.* Electron Microscopy and Analysis Group Conference 2013 (Emag2013), 2014. **522**.

Bobynko J., MacLaren I., and Craven A.J., *Spectrum imaging of complex nanostructures using DualEELS: I. digital extraction replicas.* Ultramicroscopy, 2015. **149**: p. 9-20.

Craven A.J., Bobynko J., Sala B., and MacLaren I., *Accurate measurement of absolute experimental inelastic mean free paths and EELS differential cross-sections.* Ultramicroscopy, 2016. **170**: p. 113-127.

MacLaren, I., Sala B., Bobynko J., and Craven A.J., *Absolute quantification of nano-scale precipitates in steel using DualEELS*, in *European Microscopy Congress 2016: Proceedings*. 2016, Wiley-VCH Verlag GmbH & Co. KGaA.

Craven, A.J., Sala B., Bobynko J., and MacLaren I., *Spectrum imaging of complex nanostructures using DualEELS: II. Absolute quantification using standards.* Ultramicroscopy, 2018. **186**: p. 66-81.

Bobynko J., Craven A.J., MacLaren I., and Paul G., *Understanding of V and Nb Nanoprecipitation in High Manganese steels using DualEELS Mapping,* HMnS High Manganese Steel 2014, The 2nd International Conference, 31 August - 4 September 2014, Aachen,

Paul G., Friedel F., (ThyssenKrupp Steel Europe AG, Duisburg, Germany), Pereda B., López B. (Centro de Estudios e Investigaciones Tecnicas de Gipuzkoa, "CEIT", San Sebastian, Spain), Cholewa J., MacLaren I., Craven A.J., (University of Glasgow, Glasgow, United Kingdom), *Erste Erkenntnisse zum Ausscheidungsverhalten von Mikrolegierungselementen in Hoch-Mangan Stählen,* 2012

Alaa Al-Afeef, W. P. Cockshott, P. Barges, I. Zuazo, J. Bobynko, A. J. Craven, I. Maclaren, *Linear chemically sensitive electron tomography using DualEELS and compressed sensing*, Microscopy and Microanalysis MM2015 21 (Suppl 3), August 2015

AlAfeef, A., Bobynko J., Cockshott W.P., Craven A.J., Zuazo I., Barges P., and MacLaren I., *Linear chemically sensitive electron tomography using DualEELS and dictionary-based compressed sensing.* Ultramicroscopy, 2016. **170**: p. 96-106.

Table of Contents

List of acronyms — *iii*

Declaration — *v*

Table of Contents — *vii*

Acknowledgements — *xi*

Abstract — *xii*

1. Thesis motivation and aims — *1*

2. Introduction — *5*

2.1. General introduction to steel — **5**

2.2. Precipitation from alloying and microalloying elements — **11**

2.2.1. The Relationship between microstructure and properties - strengthening mechanisms — 13

2.2.2. Manganese steels — 16

2.3. Transition Metal Carbide Precipitation in steels — **20**

2.3.1. Introduction to transition metal carbides — 21

2.3.2. Analytical microscopy of transition metal carbides — 23

3. Instrumentation and experimental techniques — *28*

3.1. Steel casting and thermomechanical processing at our partners — **28**

3.2. Sample preparation for transmission electron microscopy — **30**

3.2.1. Introduction — 30

3.2.2. Ion milling – Conventional method — 32

3.2.2.1. Procedure of sample preparation by ion milling — 33

3.2.3. Cross section specimens using Focused Ion Beam liftout — 33

3.2.3.1. Physical principles of FIB — 34

3.2.3.2. Procedure of specimen preparation by the FIB lift-out technique — 35

3.3. Transmission electron microscopy – conventional and scanning — **41**

3.3.1. The Transmission Electron Microscope — 42

3.3.1.1. Vacuum system — 43

3.3.1.2. Electron Sources — 44

3.3.1.3. Electron Lenses — 47

3.3.1.4. Condenser system — 49

3.3.1.5. The imaging system - the objective lens and post-specimen lenses 49
3.3.1.6. The apertures 49
3.3.2. The Scanning Transmission Electron Microscope 50
3.3.2.1. STEM images 52
3.3.2.2. STEM Aberrations 52
3.4. Electron scattering in solids and its uses in TEM/STEM 57
3.4.1. Structural characterisation – Electron Diffraction 59
3.4.1.1. Diffraction Pattern indexing 62
3.4.2. TEM Diffraction contrast imaging - Bright Field and Dark Field 63
3.4.3. Quasi-elastic scattering – HAADF imaging 64
3.4.4. Inelastic scattering 65
3.4.4.1. Electron Energy Loss Spectroscopy - EELS 67
3.4.4.2. Electron Energy Loss Spectroscopy - DualEELS mode 72
3.4.4.3. Energy Filtered imaging - EFTEM 75
3.4.5. X-ray Energy Dispersive Spectroscopy 77
3.5. Instrumentation and conditions 78
3.5.1. Conventional transmission electron microscope – FEI Tecnai T20 78
3.5.2. JEOL ARM200F 79
3.5.3. Plasma Cleaner 80
4. Optimisation of the sample preparation process 83
4.1. Motivation 83
4.2. How to optimise – modelling SRIM modelling 84
4.3. How to optimise 87
4.4. Needle-shaped samples 89
4.5. Gold Sputtering 90
4.6. Results 91
5. Microstructure Studies 93
5.1. Microstructure characterisation of base Fe-Mn-C steel 93
5.2. Microstructure characterisation of steel specimen 94
5.3. Crystallographic study of precipitates 101
5.4. Analytical characterisation using EFTEM 105

5.5. Analytical characterisation using EELS – preliminary results ____________________ 109

5.6. Atomic resolution imaging of precipitates ________________________________ 113

5.7. Final conclusions ____ 115

6. Development of a post processing routine for extraction of precipitate spectrum images from the matrix ____ 117

6.1. Background and issues of post-processing __________________________________ 117

6.2. Post-Processing steps ____ 120

Cleaning the spectra with PCA ____ 121

Preparation of the CL and LL for splicing and the splice procedure ______________ 126

Estimation and removal of the matrix contributions ___________________________ 128

Background fitting and edge intensities in the V Steel _________________________ 131

Background fitting and edge intensities in the Nb Steel ________________________ 136

Removal of the amorphous C and the O ____________________________________ 141

Linearisation and final corrections of the data ____________________________ 143

7. The absolute quantification - determination of mean free paths and differential cross-sections in EELS ____ 145

7.1. Basic principles of determining a cross section from a standard ________________ 147

7.2. Geometrical estimation of thickness by needle-shaped specimen and mean free path 149

7.3. Choice of the edge and background subtraction ____________________________ 157

7.4. Determination of the differential cross-sections ____________________________ 158

8. Towards absolute quantification of precipitates using experimental cross sections_170

8.1. Analytical characterisation of V steel ______________________________________ 171

8.2. Analytical characterisation of Nb steel _____________________________________ 179

8.3. Summary ____ 185

9. Conclusions and future work ____ 186

9.1. Future plans, works, research ____ 188

10. Bibliography ____ 191

APPENDIX 1 ____ 204

APPENDIX 2 ____________ *206*

APPENDIX 3 ____________ *208*

APPENDIX 4 ____________ *209*

APPENDIX 5 ____________ *218*

APPENDIX 6 ____________ *228*

Table of figures ____________ *235*

Acknowledgements

I would like to sincerely thank my supervisor Ian MacLaren for his support, patience and understanding. Despite many adversities, he managed to cheer me up and motivate me and share his knowledge during whole project, so it could become a Ph.D. thesis.

Secondly, I would like to thank Ian MacLaren and Alan Craven for their guidance, review, analysis and support when discussing research results. I am grateful for their vast scientific experience they were willing to share with me during my academic experience.

Next, I wanted to thank Sam McFadzean for being a huge support during learning ARM and all his invaluable guidance during acquisition of the experimental data. Also, for solving various problems that came up practically every time I came to the ARM room. It was a great experience to watch Sam cope with them with calm and patience. Every meeting with Sam was positive, pleasant and full of scientific answers.

One cannot fail to mention Colin How and William Smith, who accompanied me with the very first steps in electron microscopy and sample preparation optimization. Colin patiently helped me set up EFTEM, and Billy stubbornly explained how not to damage the Omniprobe at FIB.

I also wanted to thank Donald MacLaren and Damien McGrouther for numerous insightful questions that helped me resolve some of the doubts. I especially want to thank Donald for explaining the intricacies of solid state physics with respect to EELS during our morning talks. Damian, thank you for advice and assistance in producing samples using FIB with unusual shapes (needles). Also sincere thanks to Lucy for her advice in organizing trips, thanks to her some of them were much more welcome.

Keith, for the friendship that lasts, together with his optimism and faith in me.

Next, I want to thank the rest of the MCMP group for the kindness, understanding and many fruitful discussions.

Finally, I wish to thank my dear husband, for the support in the hardest moments. For the faith that I am capable of finishing my plans. I wish to thank my son for helping me realize that priorities in life can change. Thanks to my parents, for education and support throughout my scientific career. I wish to thank to my sister, who had no hesitation in looking after my son, so I could finish writing. I am also grateful to my parents' in-laws and siblings, who showed support and unlimited faith in me.

Thank you very much, without you this work would not have been brought to life.

Abstract

The dispersion strengthening is a process that strengthens the material's matrix with use of the smallest precipitates. The most power comes from the character of the nanostructures, their chemical compositions, crystallographic structures, sizes, shapes and interfaces between matrix and precipitates. Through analytical methods it is possible to study and achieve the optimal mechanical properties of elements produced from high-manganese steels with dispersive nanoparticles such as carbides or carbo-nitrides. So far the most effective research methods are transmission electron microscopy and spectroscopy with use of multiple detectors such as Dual Electron Energy Loss Spectrometer (DualEELS), Energy Dispersion X-ray detector, (EDX) or Gatan Imaging Filter (GIF). The DualEELS, which is mostly developed during this thesis, is a technique which results in spectrum imaging of all elements presented in the analyzed area.

The material studied during this Ph.D. is a high-manganese steel with vanadium and niobium carbides or carbo-nitrides with various sizes from few to dozen of nanometers, but the average is less than 20nm.

The main goal of this Ph.D. is to advance the current available methods of nano-analysis using DualEELS of the smallest precipitates embedded in the matrix supported by improved and optimized sample preparation method with Focused ion Beam (FIB) lamella. The advancement is made in several fields including development of acquisition conditions, development of sample preparation technique using low voltages at FIB, and development and adaptation of the novel post-processing routines of the acquired data using Gatan DualEELS QuantumER post-column detector. The post-processing routine involved quantitative and qualitative analysis of precipitates, which required new values of partial cross-sections and mean free paths of inelastic scattering events estimated and calculated based on experimental (standards) approach. The results consist of fully quantified precipitates (V,Ti)(N,C) and ((Nb,Ti)C) supported by chemical profiles, comparison discussion between specimen, with a pseudo-3D reconstruction of spectrum imaging of these precipitates, which means that all elements have individually calculated thicknesses. The results gave a glimpse into the nucleation of the smallest precipitates, unexpectedly different than in most literature, showing that in this case there is no core-shell structure in mixed transition metal carbides. The Ti, which is not an intentional part of the alloy, acts as a nucleation sites, but is not built over core for the V or Nb mixed precipitates. These results are shown by four examples of V-steel and three of Nb-steel. They are presented as spectrum imaging signals, separated from matrix,

with pseudo 3D representation and quantified in absolute manner with the accuracy down to a few atoms.

1. Thesis motivation and aims

The aim of my PhD work was to investigate and develop a physical understanding of the structure, chemistry and formation of transition metal (especially vanadium and niobium) carbide precipitates in high manganese austenitic steels. This is highly important to the development of high strength, high ductility steels, and support the thermodynamic modellers by providing key information, who are partners in the same project, allowing them to generate realistic and evidence-backed models of phase equilibria in such systems. The created thermodynamic database can be used in the computer-aided design of thermomechanical treatments for use in real-world production processes, including generating precipitate dispersions to tailor the mechanical properties. Specifically, the work reported in this thesis was concerned with characterising precipitates formed after micro-alloying steels with Nb and V and then performing a standard range of thermomechanical treatments.

The key goals of the microstructural/nanostructural characterisation work package of the EU project, of which this work forms a part, are to:

- Identify the crystal structure and lattice parameter of precipitates;
- Specify the orientation relationship of precipitates to the matrix;
- Investigate the shape and size and of precipitates; and
- Quantify the absolute values of stoichiometry and chemical composition of fully embedded precipitates.

In the work described in this thesis, I concentrated on the last point, which is proposal of the post-processing technique for absolute quantification of the stoichiometry and chemical composition of the precipitates. Other points were investigated either briefly by myself, or more exhaustively by our project partners. The identification of crystal structure and lattice parameters were only on minimal scale.

In order to fulfil the key goal of this thesis, a variety of techniques needed to be further developed, which are aims of the thesis:

- Optimisation of focused ion beam (FIB) preparation of steel samples to allow optimal preparation of representative, artefact-free sections in a realistic time-frame;
- Analytical techniques for acquisition of the spectrum imaging maps using the new DualEELS approach with high spatial and energy resolution;
- Post-processing routines for extraction of quantitative nano-resolved and atomic-resolved chemical information from few nanometers, fully embedded precipitates; and

- Experimental determination of inelastic scattering cross-sections and mean free paths from well-understood standards, in order to enable absolute quantification of precipitates.

Recently microscopy techniques like FIB-serial sectioning (including imaging, X-ray mapping or electron backscatter diffraction) or tilt electron tomography using imaging or X-rays have been developed for 3D reconstructions. Inspired by ongoing research this PhD is about to show that DualEELS can also be used for 3D reconstruction. The methodology developed gives the elemental absolute quantification, together with profiles of chemical composition. As a result the shape and size of each element distribution within the precipitate can be reconstructed. The development required the combination of a number of key advances – an optimised sample preparation method, improvement of the acquisition conditions of DualEELS and a carefully constructed data post-processing methodology. Whilst the immediate impact of this research is clearly designed for application to dispersion-hardened steels, this new approach will be of widespread applicability for the characterisation of a range of nanostructured materials with DualEELS, which could also include other alloys containing precipitates and supported catalyst nanoparticles, among others.

Chapter 1 is an overview of materials and their characteristics used in this thesis. The scope of history of steel is presented, followed by the idea of novel, high strength steels in an industry. There is presented a relationship between mechanical properties of steel and their microstructure. The main focus is on strengthening mechanisms and high manganese steels, to emphasise the link between precipitates in the high manganese steel. The chapter contains also the summary of precipitation of transition carbides in the steel, together with the analytical techniques used for their analysis. The literature overview shows the drawbacks and strong sides of available techniques, and possible space for development new technique, as presented in further chapters.

Chapter 3 contains detailed description of analytical techniques used during studies. At the beginning it gives a brief description of thermodynamical treatment of the specimen, which were provided by industrial partners. It is followed by description of general ideas for specimen preparation at University of Glasgow - which contains mainly Focused Ion Beam cross-section lift-out technique, supported by brief description of physical principles of FIB. Subchapter 3.3 contains very detailed description of transmission electron microscopes used during the research - conventional and scanning. It contains information about vacuum system, electron sources, electron lenses, condenser system, imaging system with additional description of objective lens and post-specimen lens, and apertures. Further part of this subchapter contains description of scanning version of transmission electron microscope, which includes aberration description and method of acquiring images in scanning transmission electron microscope. Following subchapter describes electron

scattering in solids and its uses in transmission electron microscopy. It describes methods of structural and microstructural characterisation with use of different imaging method, such as diffraction patterning, high angle annular dark field, inelastic scattering and its uses such as energy filtered TEM imaging, or electron energy loss spectroscopy together with dualEELS mode, which is the main focus during this thesis. There is also another subchapter which summarises all instrumental conditions of acquiring data during the thesis.

Chapter 4 describes the motivation for focused ion beam as a main method of sample preparation with proposed optimisation protocol. Description of steps available so far were insufficient for preparation of such tough steel as high manganese steels, so it was necessary to adapt known protocols. This chapter also contains the description of preparation of needle-shaped specimen, which were used for some additional experiments during thesis.

Chapter 5 shows first microstructure results for base steel (Fe-Mn-C) and for steels containing V and Nb precipitates. The results contain dark field imaging, diffraction patterns, analytical characterisation with EFTEM, preliminary results from EELS and few results of atomic resolution imaging of vanadium and niobium precipitates. The microstructure analysis reveals typical steel structure after the hot deformation, with a lot of defects within. However it also showed that the dark field imaging is successful if the niobium precipitates are observed, but it was insufficient enough for vanadium. Independently the type of observed steel, always dark field images were accompanied by second type contrast, which is a lightened up areas. As it was proven in rearmost part of the research it was caused by uniform thin surface oxide layer. Also the diffraction pattering despite many patterns proved to be insufficient for these precipitates analysis, because their volume fraction is too low, in comparison of matrix or surface contributions. Despite this, the EELS and EFTEM techniques are extremely successful in small precipitates analysis. They revealed nature of precipitates down to 5nm.

Chapter 6 contains detailed description of developed post-processing routine for extraction of the precipitate signal for EELS data analysis. Its main goal is to remove the matrix contribution, so the analysed result is precipitate only signal, which is called digital extraction replica. The development of the technique revealed a lot of discrepancies between ideal specimen and real specimen, so some alterations of the processing had to be applied during development process. The post-processing starts from cleaning the acquired spectra and application of cleaning PCA procedure. Then there is a preparation of core loss and low loss for splicing and splice procedure. After splice, the matrix contribution is removed from the specimen data. Such prepared data is supported by the description of background fitting in front of the V and Nb edge, as each of them have different

characteristics. Final part of this chapter contains the information about removal of unnecessary signal such as amorphous carbon or oxide surface , or linearisation of the data.

Chapter 7 presents the steps necessary for absolute quantification of the chemical composition of individual precipitates. It involved basic principles of determination of the cross-section from standard specimen, together with short description about standards specimen itself. The cross-section is supported by mean free path determination and needle-shaped experiment, which main goal was an experimental determination of thickness and comparison it with geometrically estimated thickness. The mean free path was estimated based on phenomenological biases, so the experiment supposed to compare its accuracy. Such compared thicknesses showed 20% agreement, so simple modification to the equation was applied. Also in this chapter the choice and way of background subtraction of individual edges was proposed with final determination of differential cross-sections. At the end of the chapter the comparison of many cross-sections is done, and final estimation of each single value is set and discussed.

In chapter 8 the determined cross-sections are used for absolute quantification of precipitates. It summarises the analytical characterisation of vanadium and niobium precipitate only signal in separate subchapters. For vanadium there were four fully quantified precipitates, and for niobium there were three fully, but still imperfectly, quantified precipitates. In summary there is an comparative analysis between all of them.

Chapter 9 contains some future plans, and research based on this thesis, or collaborative projects, which this method has been involved.

2. Introduction

Iron alloys have been known and used for more than 3000 years. The XVIII and XIX centuries were a key period in scientific and technological progress in iron metallurgy (just as in many other areas relating to industrial production) with major contributions being made by Berthollet, Monge, Vandermonde, Bessemer and Thomas [1-4]. Such early work formed the foundation for development of modern alloy steels and later for stainless and microalloyed steels. Around the year 1800, Louis Nicolas Vauquelin isolated metallic chromium by heating oxides in a furnace [5]. Chromium is indispensable to the creation of steels with good corrosion resistance. Progress was so significant by 1910 in the field of chromium and chromium-nickel steels that such steels came into bulk industrial production as the first stainless steels. This is just one example of a major technical development in the story of steel. Nevertheless, even today, although steel has such a long history, there remain many open questions in steel metallurgy, especially in view of the huge range of possible alloying elements, the number of possible combinations of multiple alloying elements, and the huge range of possibilities for thermomechanical treatments during processing from initial casting to the final product. There is also a large range of applications for steels, such as in construction, infrastructure, transportation, tools, machines, household appliances, cutlery and culinary uses, and military applications. Each application will have its own specific requirements such as mechanical properties, corrosion resistance, surface finish, formability required from the manufacturing process, and cost-weight ratio, and these criteria will inform the selection of the precise steel grade and production process.

2.1. General introduction to steel

At its simplest, steel is an alloy of iron and carbon from 0.2% up to 2.1%. On cooling from the melt, there are three commonly observed solid crystalline phases found in steels: ferrite (α), which is a body-centred cubic structure, austenite (γ), which is a face-centred cubic structure, and cementite (Fe_3C). Ferrite is a solid solution of carbon within α-iron, although carbon has a very low solid solubility in ferrite (0.005%wt at room temp). Austenite allows a significant solid solution of carbon within iron, and has solubility up to 2.1% at higher temperatures. However, austenite does not exist at room temperature in plain, carbon steel as a thermodynamically stable phase (although it has been found in nanostructured steels [6-8]). This is shown in the phase diagram for plain carbon steels in **Figure 2**. This is a useful start in understanding many of the basic features in more complex steels, since the effect of many common additions, including manganese, silicon, sulphur, phosphorus, aluminium, silicon, chromium, molybdenum, and nickel, is to change the equilibrium

between ferrite and austenite, and thus the temperature and composition ranges over which they appear.

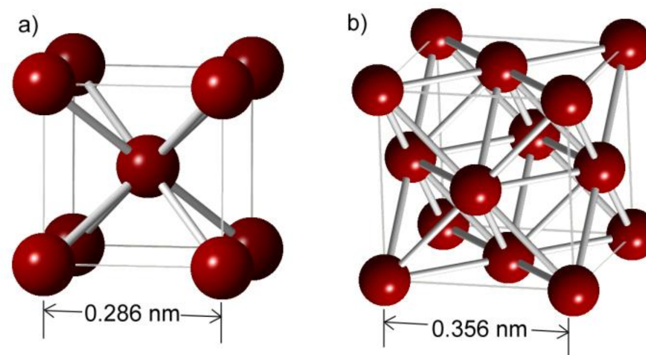

Figure 1. Crystal structures of iron. (*a*) Body-centred cubic (BCC) α-iron. (*b*) Face-centred cubic (FCC) γ-iron.

Phase diagrams are commonly used in materials science and metallurgy to show phase equilibria in an alloy system and how these depend on composition and temperature. Lines dividing areas are called phase boundaries, which refer to the thermodynamic equilibrium between different phases. The areas under and above lines are areas where one or more phases coexist. A phase transformation will occur when a line is crossed by e.g. changing the temperature. As such, they are invaluable in alloy design. It must, however, be pointed out that phase diagrams only apply to thermodynamic equilibrium states, or quasi-stable metastable states – fast changes may result in the formation of metastable states, for instance if temperatures are changed faster than the kinetics of the formation of the thermodynamic equilibrium state. For example, the trace marked A in **Figure 2** shows the transformations during slow heating and cooling of typical carbon steel with 0.4 atomic % carbon. At room temperature there is a mixture of ferrite and cementite. On heating to point A1 at 723°C the cementite is dissolved and austenite is formed, thus above this temperature the structure consists of austenite and ferrite. At point A3 at 800°C there is an allotropic transformation which converts the remaining ferrite to austenite. Melting of the steel begins at 1492°C. On slow cooling from the melt and down to room temperature, the sequence is reversed and there is plenty of time for diffusion, therefore the low temperature structure with a mixture of ferrite and cementite is formed, although the precise micro- or nano-structure of this mixture depends on cooling rate. As mentioned above, if the cooling is very fast, the equilibrium state is not reached. This can have a variety of effects depending on the exact cooling rate but, at higher cooling rates, no significant diffusion takes place which means that the allotropic transformation from the FCC austenite structure (which has a higher carbon solubility) into the BCC ferrite structure (which has a smaller carbon solubility) leads to formation of a carbon supersaturated metastable α-Fe structure. The excess carbon distorts the structure into a body centred tetragonal unit cell and this phase is

referred to as martensite – it has a very fine-grained structure and is exceptionally hard but is brittle and not damage-tolerant.

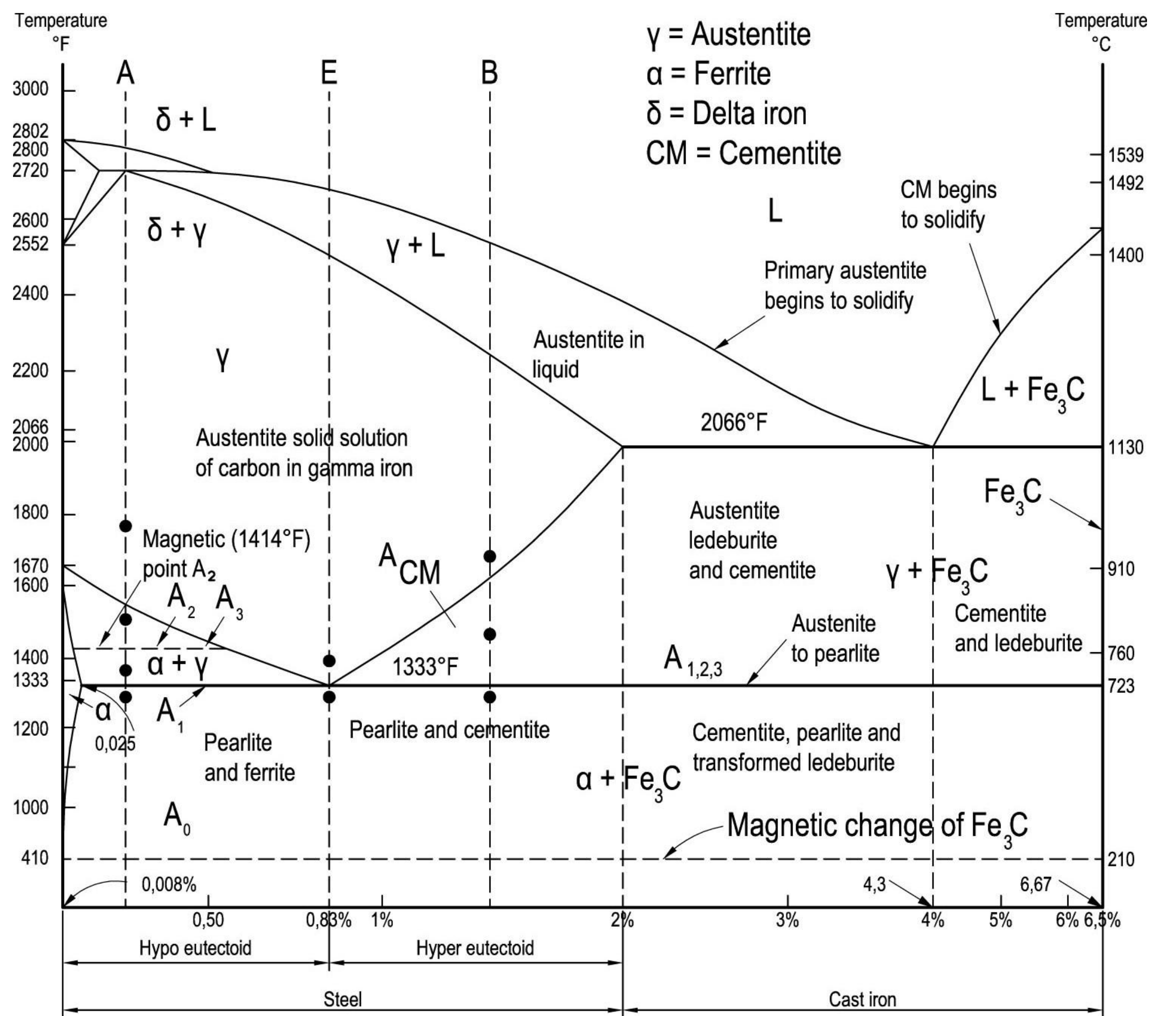

Figure 2. Fe-Fe$_3$C phase diagram with areas of existence each of system phases.

As a result of this complex range of phases and microstructures which can be formed depending on both composition and processing, iron based alloys are one of the most complex group of alloys known, whilst at the same time being the relatively economical to manufacture and produce. This wide range of different possibilities for the design of iron all classic carbon steels is in the range of 200-250MPa, but certain steels can reach strengths up to 2000MPa[9, 10]. Currently, the construction industry and especially the automotive industry require materials with extreme properties, combining both high tensile strength and high ductility and toughness. This allows weight reduction through requiring less material for a specific component strength, whilst preserving damage tolerance and resistance to catastrophic failure. For this purpose High Strength Low Alloy (HSLA) steels are being extensively used [11-16], and this continues to be a vibrant research area. These properties are derived by adding certain microalloying elements to form few nanometre carbo-nitride precipitates resulting in dispersion hardening effects (see below in section 2.2.1), which

results in increases of the yield strength up to 600MPa. Whilst such steels can achieve very high strengths with relatively low production costs, this can be at the expense of ductility, which can cause problems with brittleness for this group of steels [17-19]. This is a reason for the usage of a low amount of alloying elements to produce such steels characterised by the same body-centre cubic (ferrite) structure as pure α–Fe (and are consequently called ferritic steels). This BCC structure has fewer possible deformation mechanisms than the high temperature FCC γ–Fe form (austenite) resulting in a ductility that is intrinsically lower than austenite (more details are described in chapter 2.2.2). Consequently, there are limits on how strong ferritic steel can be made without making it dangerously brittle and at risk of catastrophic failure. Thus ferritic steels are useful for moderate strength, they also exhibit low to moderate cost for structural steels but, which results in reduction of weight components, which is one of major importance to automotive manufacturers, a higher strength is needed without sacrificing ductility, and this will require the use of steels based on the austenite phase which has intrinsically higher ductility.

In last few decades economics is a major factor which limits and defines steel design. One of the main branches of industry which is directly connected to the economy is automotive and transport. Road transport is one of the most important divisions of transport. For example, in Europe it accounts for more than 45% of entire transport performance [20]. Thus any weight reduction will result in cheaper transport and reduced CO_2 and NO_x emission. If improvements in safety can be made as well, this is even better. So, if structural components can be made with higher strength materials, the total mass of the car body can be reduced. Moreover increasing ductility allows design of more complex elements. Thus, it is important is a strong emphasis on research on materials which can reduce the mass but simultaneously maintain good mechanical properties, like strong capacity for work hardening.

The automotive industry specifically requires materials that combine high strength and high ductility for applications as key structural components of car bodies. Their aim would be to absorb energy during impacts, i.e. accidents, and high strength steel which remains ductile would absorb extremely high amounts of energy in an impact, thus saving the vehicle occupants from serious injury during such events. One possible way of achieving such a combination of high strength and high ductility is to use austenitic high manganese steels, as their ultimate tensile strength can reach levels of 2000MPa whilst simultaneously having a ductility allowing up to 95% elongation. As summarised by Bouaziz [21], austenitic high Mn steels are unique in providing such an excellent combination of properties. By the high manganese content the phase diagram of iron-carbon is significantly changed, and the high-temperature austenite phase of iron is stable at room temperature, which is one of the main reasons for such outstanding properties of these steels.

However, the main disadvantage of standard high manganese steels is their relatively low yield strength – i.e. they start to deform at low stress, even if the ultimate stress required to break the component is large. For that reason the interest of project is to enhance yield strength by microalloying the steel with Nb and V to form nanosized precipitates – carbides and carbonitrides. By pinning the dislocations during deformation the precipitates raise the external stress necessary for deformation, thus the yield strength is increased. Control of the amount of the precipitates as well as their volume and size distribution has a direct impact on order of these changes, resulting in dispersion hardening, in addition to standard work hardening and the TWIP/TRIP effects, which also enhance the mechanical properties. This idea was adapted from HSLA steels, which have used microalloying for almost 50 years now, to produce their excellent properties. The dispersion hardening effect was previously observed in HSLA steels and their history and properties are discussed in section 2.2. Unfortunately, the high Mn steels with transition metal microalloying have not been investigated in great detail before this project, and little reliable thermodynamic information was available, which makes alloy steel design very difficult for manufacturers.

Consequently, a project "Precipitation in high-Mn Steels" was started by a consortium of European partners, including ThyssenKrupp and ArcelorMittal, of which this PhD work forms a part. The project covers on one hand the wide range of thermodynamical treatments of high manganese steel with microalloying elements like Al, Nb and V, with general microstructure characterisation supported by detailed qualitative and quantitative analysis of nanostructures. On the other hand, it also has focused on the development of accurate experimentally-backed thermodynamic databases for modeling of such steel under different thermomechanical treatments. This will act as the basis for the further development of specific steel grades for use in automotive applications.

The project partners were focused on various tasks. A first group was mainly focused on casting of many types of alloys, starting with the base one containing Fe, Mn and C, and subsequent additions of microalloying elements such as Al, Nb and V. They tend to use different conditions of isothermal holding for desired type of precipitation such as size distribution, volume fraction, or distribution. A second group was involved in general microstructure characterisation with samples prepared mostly by carbon extraction replicas, and some prepared by electropolishing for comparison experiments. Extraction replica is a technique, which involved coating specimen with carbon layer, and then dissolving the matrix in a solvent, resulting in thin carbon film attached to precipitates. Main disadvantage of this technique is a change to dissolve the smallest precipitates, and any other alterations in chemical composition of the precipitate as a result of exposure to chemical agents. A third group was focused on the creation of new thermodynamic databases for Fe-Mn with the different alloying elements. The fourth group was focused mainly on

characterisation of nano-sized precipitates with electron microscopy and spectroscopy. This also served also to validate the thermodynamic models. There are still a lot of doubts about what type of interactions there are between slip dislocations and twins, twins themselves and their influence on strain hardening behaviour. The latest results obtained by Ebrahimi *et al.*[22] show that, at the beginning, there is one twin system in the material but, if the strain is steadily increased, the second one will be activated. Because of the numerous possibilities the process of plastic deformation where the twinning mechanism occurs is still full of uncertainties, particularly in FCC materials with low stacking fault energy. The reason for that is the twinning mechanism can be described as a sum of two processes – shear in one crystallographic planes and slip on other directions.

The project investigation is focused on maximising the impact of the precipitates on the final mechanical properties by increase the yield strength due to the nanosized particles blocking the movement of dislocations during deformation. This tendency is presented in the **Figure 3**, showing the difference between classic, commonly available materials and ongoing work on the new high Mn austenitic steels. More details about high manganese steels and their properties are described in section 2.2.2.

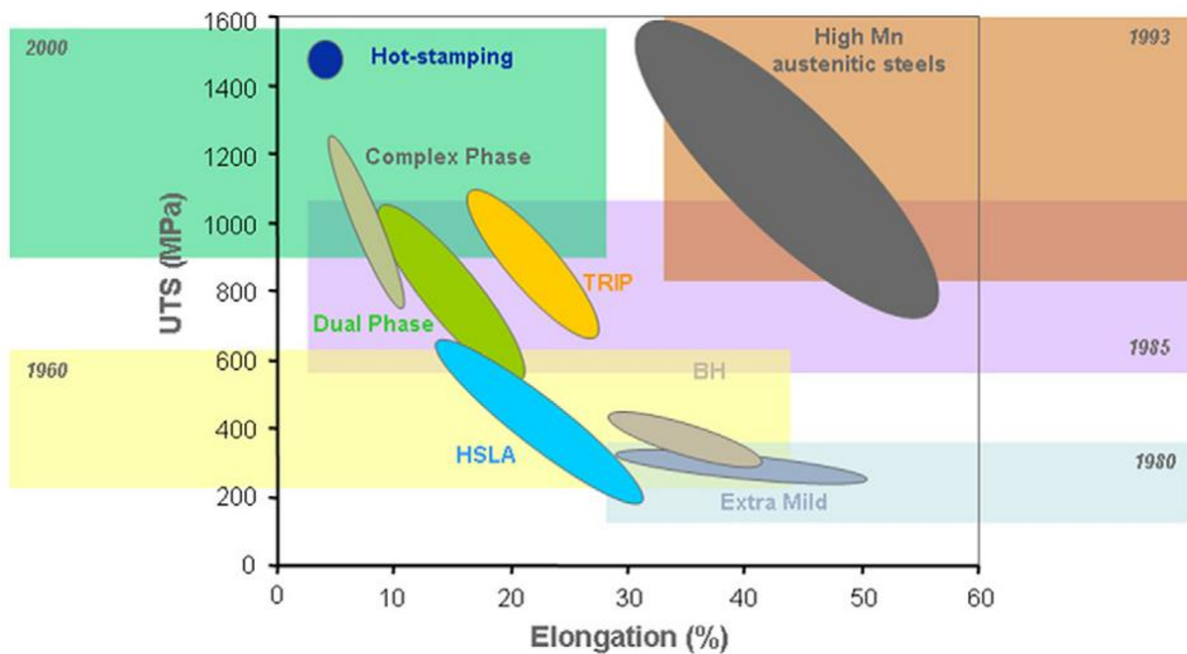

Figure 3. A graph showing the Ultimate Tensile Strength in the function of elongation, together with the years, when the studies of each materials have started [21]. In the left bottom corner the steel properties are the lowest, and knowledge about them is the oldest. IN the right top corner the properties of the steel are the highest (both elongation and UTS). In the top left corner the newest steels are summarised, which are characterised by the highest UTS but short elongation. Republished with permission of O. Bouaziz, S. Allain, C. P. Scott, P. Cugy, and D. Barbier, from *High manganese austenitic twinning induced plasticity*

steels: A review of the microstructure properties relationships. **Current Opinion in Solid State and Materials Science, 2011. 15(4): p. 141-168, permission conveyed through Copyright Clearance Center, Inc.**

2.2. Precipitation from alloying and microalloying elements

Steels which contains additional elements like vanadium, niobium, titanium, chromium of around 0.1% are called microalloyed steels. The addition of those elements has a significant influence on the distribution of second phases, and strengthening process. It is important to mention that their character is different from standard alloying elements, usually presented in a few percentage range. For example, the manganese is an alloying element in the steel used in this research.

The microalloying elements play a dual role in material. If the elements form finely dispersed precipitate particles, their main goal is to strengthen the material by pinning of dislocations during deformation. The uniform and wide-spread distributed particles, leads to the most efficient pinning, thus the most effective strengthening. This dispersion hardening is described in more detail in section 2.2.1. But the alloying elements can also form bigger precipitates, such as AlN particles in the alloys used in this research. The presence of the bigger precipitates lead to the control of grain size of austenite, by raising the coarsening temperature, changing the diffusion coefficient, and causing instabilities in austenite and grains therefore suppresses the growth rate efficiently. The grain boundary contribution is also a important one in overall strengthening processes ongoing in the steels, described in more details in section 2.2.1. This is the idea which stands behind the overall project – the combination of different strengthening processes, their behaviour and understanding for the best final product.

The carbide precipitation process is due to the reaction between substitutional micro alloying elements *X* with interstitial elements *Y* like carbon and nitrogen being dissolved into the austenite. During some deliberate treatment such as isothermal holding, the orderly rearrangement of atoms occurs resulting in formation of second phase. This will precipitate as as mixture of X element and Y interstitial element in the XYn structure (for example vanadium carbide VC, where C is 0.8, which means, that for 1 atom of vanadium there is only 0.8 atom of carbon), and this type of structure is formed because carbides and nitrides are mostly substoichiometric. To estimate the dependence of solubility product which will lead to precipitation during tempering is given by

$$\mathbf{Log([X][Y]^{n}) = -\frac{A}{T} + B} \qquad \mathbf{1)}$$

Where *A* and *B* are constants, *T* temperature in Kelvin and *[X]* and *[Y]* are the concentrations of element X and Y dissolved in austenite given in wt%. This equation is dependent on temperature for many reactions involving precipitation from austenite. The higher the solubility product *[X][Y]n*, the

higher the solubility of the compounds in austenite. For comparison – vanadium and niobium have much higher solubility in austenite than aluminium. Therefore the precipitation will be dominated by vanadium and niobium carbides, nitrides or carbonitrides. The suppression of austenite grain growth is dependent on stability of precipitates, because the stability effectively raises the temperature at which the growth of austenite grain starts [23].

The composition of samples that have been used during this Ph.D. is the base alloy of 20 wt. % of Mn, 1.5%wt of Al, 0.6%wt of C with Fe as bulk. To the base alloy the microalloying elements are added such as 0.1%wt of Nb and 0.3%wt of V to form wide spread nano-sized, precipitates. There might be some unintentional elements like Ti or N resulting from the production process, contamination in the pilot casting facility, and that the steel has been produced from recycled steel. Each element added to the composition has a specific function. The main role of manganese is to stabilise the austenite structure of iron at room temperature (as stated above). The direct consequence is the TWIP effect, which main role is to raise the mechanical properties by mechanical twinning. TWIP happens while external stress is applied to the material, and due to that, the mechanical twinning occurs [24].

The aluminium has a triple role to play. First it is intended to react with all N impurities present in the steel, one of the effects of which is to prevent the formation of transition metal carbonitrides. During this project, the research is focused on the chemical composition of the pure carbides, but it is hard to estimate how much of the N had reacted with the Al. One consequence of the reaction between Al and N is formation of AlN, which is responsible for austenite grain refinement during processing of the steel. These precipitates where never seen during the investigation performed during this Ph.D. because their size is much bigger than small carbides. Also, there have been performed a checks during spectrum image acquisitions if any of Al is present in the small carbides, and it was never the case. Also supported by results from the modellers, the Al should be absent in the smallest precipitates, and this assumption was made in the research performed in this thesis. What the grain refinement is and its process is described in chapter 2.2.1, as it is one of the strengthening mechanisms in material science. The third, major role is change in stacking fault energy, which in direct consequence will decide if the TRIP or TWIP effect is dominant in the material. TRIP is another effect which takes place in material while external stress is applied. Both effects are described in section 2.2.2.

Vanadium and niobium are intentionally added to react with carbon dissolved in austenite and form a nano-sized precipitates whose main role is to provide a dispersion hardening. Even the small amounts, like 0.1%wt or 0.3%wt are sufficient to form plenty of precipitates to increase the strength of steel [25-28].

2.2.1. The Relationship between microstructure and properties - strengthening mechanisms

The details of the chemical bonding are one of the main factors affecting the mechanical properties of a material. Each of the main groups of materials, such as metals and alloys, ceramics, polymers, and composites are characterised by different types of atomic bonding. Pure metals and many alloys have metallic bonding, which is not very directional, promoting fairly close-packed structures, resulting in very good plasticity but quite low strength. Some good examples are copper, aluminium, iron or gold. In general, to enhance the strength the relatively easy movement of dislocations should be suppressed. There are different obstacles that can pin and slow down the dislocation motion, meaning that more energy is required to deform the steels. To understand the strengthening process a short explanation about the main deformation in materials should be presented.

There are two types of deformation in materials, elastic and plastic. Elastic deformation is the deformation proportional to the external stress, which disappears after the load is removed. Hence there are no changes in structure, only the internal energy of deformed material is raised. Plastic deformation is where a material starts to deform irreversibly, and where at least some atoms are displaced by distances larger than the interatomic distances [29].

The most common mechanism of the plastic deformation of metals and other ductile materials is the slip of dislocations, which are crystallographic line defects in the structure. It consists of the mutual movement of one part of the crystal relative to the other along specific crystallographic planes (slip planes) as a result of the dislocation motion. The crystal structure of both parts of the crystal remains unchanged [30, 31]. Therefore, in order to strengthen a metal, various mechanisms can be used, all based on impeding the motion of dislocations.

There are several mechanisms to strengthen the iron alloys by microstructural changes. It is possible to combine several of them simultaneously, resulting in better mechanical properties. Some mechanical properties that are dependent on microstructure include: yield strength, ultimate tensile strength, hardness, elongation, impact toughness and resistance to cracking. All forming processes like cold-rolling, hot-rolling or heat treatment change the microstructure and consequently a wide range of mechanical properties. Accordingly, the choice of strengthening mechanism has direct impact on the application of the material. The most common strengthening mechanisms include:

- Work hardening – dislocation strengthening;
- Solid solution strengthening by interstitial atoms;
- Solid solution strengthening by substitutional atoms;

- Refinement of grain size; and
- Dispersion strengthening [25, 28, 29].

Solid solution hardening from the interstitial dissolved atoms of carbon and nitrogen is a very most important mechanism for conventional steels. However it requires detailed work to quantify the contribution of individual mechanisms to overall properties, because elements such as carbon and nitrogen can also interact with dislocations, or form carbides and carbonitrides, which cause further dispersive strengthening.

Work hardening – dislocation hardening

One of the mechanisms in obtaining high strength steels is work hardening. It is the process where the dislocations are created in the material by deformation. Piling up the dislocations triggers higher order slip systems (which requires higher energy to activate), with slip planes different to the most favourable one in crystallographic structure. The higher order slip planes intersect with other pre-existing slip planes, resulting in dislocation tangling. Due to this process, it is possible to enhance the strength levels even above 1500 MNm^{-2} just by applying work hardening. This hardening process is directly associated with crystallographic slip planes in deformed phase. Basically, the slip traces are the combination of planes and directions in crystallographic structure, which are the closed-packed planes in closed-packed directions [32].

The main goal of work hardening in conventional steels has to form as many defects in material as possible. But it is necessary to remember there is a balance between defect creation and annihilation which means material reached the saturation level of hardening process. Moreover the work hardening has a significant influence on ductility resulting in a major loss of ductility along with the increase in hardening. Defects which were formed during deformation are areas which cause stress concentrations, which can initiate necking (where the material gets thin and the stress is concentrated) [28].

Solid solution strengthening by interstitial atoms

The interaction between misfitting interstitially dissolved elements such as carbon and nitrogen with dislocations is called solid solution strengthening. Carbon and nitrogen have a minor effect on austenite solid solution strengthening, but placed as an interstitial atom can play a significant role in raising the material's strength. The interstitial atoms located into octahedral interstices can be irregularly or regularly placed, but either placement cause similar distortions in the matrix, which prevents dislocation movement. Each such obstacle makes dislocation movement more difficult, and therefore the deformation of the material requires more energy [28].

Solid solution strengthening by substitution atoms

There are a lot of elements that can form solid solutions with both allotropic phases of iron. Both α-iron and γ-iron have wide range of strengths depend on atomic concentration of alloying elements. If the element has different diameter that the main alloy element, it distorts the lattice around. In general, the bigger the difference in atomic size of solute atom and iron atom, the higher the strengthening effect. This happens because this increases the stress necessary for dislocation movement, due to the strain created around the substitution atoms. The strain from the diameter differences is called as a Hume-Rothery size effect [33].

Refinement of the grain size – Hall – Petch effect

Hall and Petch performed the first scientific analysis of the impact of grain size on strength using ARMCO iron [34]. Their research showed a simple relationship between the yield stress and grain diameter. To transfer the deformation from one grain to neighbouring grain activation energy is required, so the more often grain boundaries are met, the more energy is needed to propagate deformation. These relationships are in almost all steels, as well as non-ferrous alloys, and are given by:

$$\boldsymbol{\sigma_y = \sigma_0 + k_y d - \frac{1}{2}} \quad \textbf{2)}$$

σ_0 represents the stress that is required to activate the movement of dislocations in the slip planes in BCC crystals.

Dispersion strengthening

Typically there are several different phases within an industrial material. In the case of iron alloys the matrix is usually ferritic or austenitic, followed by dispersion strengthening. The dispersion strengthening is a process, which allow to control the ultimate tensile strength by dispersion one phase in another. The most familiar and frequent method in steels is a carbide and carbonitride formation resulting from microalloying elements. These particles interact with the dislocations during deformation stopping them. The particles force the dislocations to go round them, or to shear through them, therefore, the deformation requires more energy to take place. In principle, the more the particles, the more the strengthening effect. The yield stress of an alloy containing a dispersion of fine, hard particles is described by the Orowan equation:

$$\boldsymbol{\tau_0 = \tau_s + \frac{T_d}{\frac{b\Lambda}{2}},} \quad \textbf{3)}$$

where τ_0 is yield stress, Λ is the interparticle spacing, τ_s is the Yield strength of the matrix, T_d is the line tension of dislocation and b is the Burgers vector [25, 28]. The key parameter is the number of particles in a short distance, so the smaller and more numerous the precipitates, the stronger the hardening effect. This can have a big effect on strength, for example, by controlling the

size distribution and volume fraction the overall strength of HSLA steels can be increased even by as much as 70%.

Such a well-defined relationship between dispersive particles and yield stress or initial flow stress works best for fine, spherical particles. The interaction of dislocations with small particles is related to yield stress as the inverse of the distance between the particles, as described in **Equation 3**. So if the particles are bigger but fewer, the strength of the whole alloy is attenuated.

Summary

In summary, there are a lot of mechanisms to enhance the yield strength of materials. The most popular methods to improve mechanical properties are heat treatment and dispersion hardening. Usually several phenomena contribute for final strengthening effect. Steel is an alloy with many complex transformations, the main one being from austenite to ferrite, which lead to a wide variety of balanced mechanical properties. The properties might be controlled and changed by metallic additions primarily by changing the temperature of transformations, which leads to better control of microstructures and benefits from it. The choice of strengthening mechanism should depend on the application and work conditions of the component. For example, if steel is supposed to be dispersion strengthened the temperature of working should not extend the dissolution temperature of the dispersion particles. Otherwise they can coarsen or dissolve, causing the softening of the alloy. The same situation happens when the material is strengthened by work hardening. Raising the temperature can lead to recovery and recrystallisation, thus reducing the strength of the material [28].

The choice of strengthening mechanism is usually due to type of material. For example it is common that for HSLA steels grain refinement is the primary mechanism, and this is the only mechanism than can increase the strength and toughness at the same time. If the steel will be strengthened by precipitation the reduction in toughness must be offset by other mechanisms, for example grain refinement. For that reason there is usually a combination of strengthening mechanisms to give the best result as a final product.

2.2.2. Manganese steels

The key element added to steels characterised in this thesis is manganese. It stabilises the austenite phase which then has significant positive effects on the ductility. That feature makes manganese one of the most common elements in design of the advanced high strength steels. Moreover manganese is characterised by very low diffusion rates within austenite, and low segregation or tendency to partition on interfaces [35]. Steel containing 12-13% of Mn is called Hadfield steel, after its British inventor, Sir Robert Hadfield, who created the first ingot from carbon iron and higher amounts of manganese[36]. He was trying to discover a new alloy that would be a

good casting alloy preserving a good hardness and toughness, because classic steels do not have good casting capabilities. He was able to reach fully austenitic structure of ingot after thermal treatment above 500°C followed by quenching. Although this steel seemed to be promising, it was forgotten for almost 60 years. First transmission electron microscopy (TEM) analysis showed lack of understanding of process of nature of work-hardening in this steel, and researchers did not know what was the reason for such mechanical properties [37]. Later investigations confirmed the presence of twinning to be the reason for such strong work-hardening behaviour [38, 39]. Even with such outstanding results the steel was not investigated further, and in 1975 Remy presented a PhD thesis explaining the contribution of twins as obstacles for dislocation glide [40]. More recently after a 15 year break, the first patents were proposed by Kobe steel [10, 21], Sumitomo and Nippon Steel, a Japan steelmakers in early 1990s, and by the Korean Posco company[41]. In 1995 the next set of Posco patents were accepted, which was followed by two Europe leading steelmakers – ThyssenKrupp and ArcelorMittal. Since that time, the steel manufacturers and researchers started to produce a lot of new patents and results regarding high manganese steels, the work-hardening mechanisms followed by new methods of production (different casting procedures etc.). These technical developments were followed carefully by a number of leading car makers, including Fiat, Honda, Hyundai, and Daimler. Even so, there have been few cases of commercial use and mass production of high-Mn steels, especially due to the low yield strength without microalloying.

High manganese steel after casting is a relatively low yield-strength and high-ductility material. However a precisely controlled forming process leads to interstitial strengthening from C and substitutional strengthening from Mn together with significantly improved work-hardening properties. In general, the manganese steel possesses extraordinary properties when external stress is applied.

Figure 3 is a comparison of all structural steel classes, on a plot of ultimate tensile strength against elongation to failure, together with the year of development. As shown on this figure, the high ultimate tensile strength and the high ductility (presented as elongation in %) are almost never found simultaneously, therefore it is almost impossible to have both of them high enough to satisfy the ideal specifications of constructors at the same time.

In 1960s the researchers started to microalloy classic carbon steels with vanadium and niobium, and less frequently with titanium, and they observed that the values of UTS and ductility simultaneously stay moderately high [12-14]. Later research by Vaccai *et al.* [16] confirmed these preliminary results, and showed that such steels (High Strength Low Alloy, HSLA steels) can be effectively used as a structural material with much better formability than other commonly available materials, such as plain carbon steels.

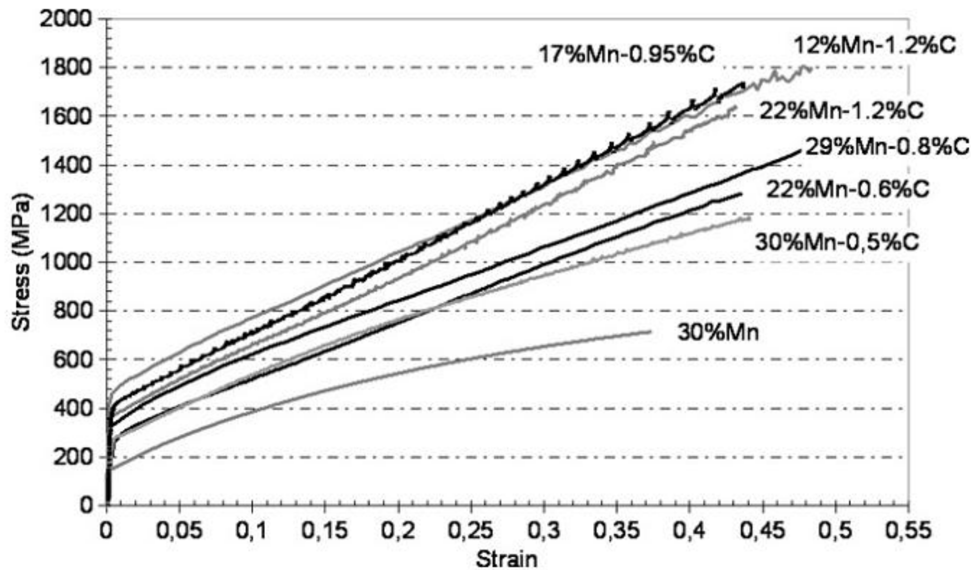

Figure 4. The graph of tensile test of high manganese steels with different Mn and C content. The graphs of 12%wt Mn and 17%wt Mn show the oscillations of the lines resulting from TRIP effect occurring in these steels. Republished with permission of O. Bouaziz, S. Allain, C. P. Scott, P. Cugy, and D. Barbier, from *High manganese austenitic twinning induced plasticity steels: A review of the microstructure properties relationships.* Current Opinion in Solid State and Materials Science, 2011. 15(4): p. 141-168, permission conveyed through Copyright Clearance Center, Inc.

Figure 4 presents stress-strain curves of tensile tests to failure of a range of Mn/C steels showing the differences in the ultimate tensile strength (UTS) and the elongation to failure in relation to the content of the Mn and C in the steel. Compared to classic carbon steels, all of presented alloys have a superb UTS and elongation to failure during the deformation. At the same time the yield strength is relatively low for all of the examples, but it is lower for higher contents of Mn and higher C. The maximum values for the UTS are achieved for alloys with lower amounts of Mn.

In fact, these properties can be improved due to the work hardening that occurs in the steel with higher C content and lower Mn content. The sawtooth shape of the graphs is characteristic of TRIP effect, and is seen most strikingly in the materials with the highest UTS. According to this the strongest work hardening is presented in the steel with 12%wt Mn and 1.2%wt C or 17%wt Mn and 0.95%wt C.

There is a clear reason for this extraordinary ductility. In contrast to regular carbon steel containing body-centred cubic (BCC) ferrite, which has only 8 different slip systems, the face centre cubic (FCC) austenite stabilised by Mn alloying has 12 different slip systems (i.e. 12 different directions in which a crystal can deform) in FCC structure and is intrinsically more ductile as a result [42-44].

Next to the standard hardening effect, the addition of Mn results in two other effects which can enhance the ductility and strength. The twinning induced plasticity (TWIP) and transformation induced plasticity (TRIP) effects are both related to the high Mn content, and can significantly raise worked hardening rates.

The TWIP (twinning induced plasticity) effect is related to the formation of twins while applying the stress during cold-rolling (deformation twinning). The extant of twins is related to the stacking fault energy in the material, and they form much more easily when the stacking fault energy is low. For high Mn steels, this effect depends on the manganese content in the austenitic but also on the presence of aluminium and silicon in the steel. This is because both aluminium and silicon change the stacking fault energy. If the steel contains around 25% wt. of manganese, more than 3% wt. of aluminium and 2-3%wt. of silicon the TWIP effect occurs [24]. This increases the tensile strength of the material whilst promoting ductility (high elongation to failure).

The TRIP (transformation induced plasticity) effect occurs when under the stress the austenitic structure starts to undergo the phase transformation to martensite. In the case of high-Mn steels, the transformation is from FCC austenite to hexagonal close packed HCP ε-martensite. In contrast to the TWIP effect, no twins occur while applying the stress, but a large amount of energy is absorbed in this phase transformation. This happens for steels of composition range above 20-25% wt. of manganese. Both effects occur under plastic deformation. [45] The TRIP effect is considered to be one of three mechanisms of strengthening the austenite steels [46]. It was observed not only in austenite steels but also in very expensive high Cr, Ni-Cr alloys as an effect which gives outstanding combination of mechanical properties [47].

Cold-rolling followed by annealing is a typical treatment to obtain a TWIP steel with fully austenititic microstructure. However this method consumes a lot of energy to roll the material until the necessary level of internal stress is reached, so other techniques, especially hot-rolling, which is less energy-consuming and requires lower forces, have been more favoured recently. Because of the multiple processes occurring simultaneously it is hard to control the final microstructure, which has an impact on the mechanical properties [22, 48-50].

Although there are an increasing number of studies about TWIP and TRIP effects, there is still a lot of uncertainty regarding the understanding of the behaviour and mechanisms in the Fe-Mn-C alloys, and unfortunately the mechanisms responsible for high strain hardening rate are still not very well established.

One mechanism which can increase the strain hardening rate depending on the stacking fault energy is the mechanical twinning process. As the strain increases the more twins occur. As a result the mean path of dislocation movement is reduced. This effect can be described as a dynamic

Hall-Petch effect because of the appearance of twin boundaries as a consequence of deformation, resulting in continuous refinement of the effective grain size and consequent hardening [51-54].

There are relatively few studies on the evolution of the microstructure in these types of steels [25, 46, 55, 56], so it is hard to be sure which effect is in reality principally responsible for the excellent properties of these steels. Data available in literature are not sufficient for statistical deduction, but there are some indications. For example, the steel with 22% wt. of manganese and 0.6%wt. of carbon has an ultimate tensile strength around 1800MPa and an elongation before rupture of over 90% [21, 53, 57-59]. These properties are described as outstanding and it would be very useful to understand better their features and the reasons for their occurrence [21, 46, 52, 54, 55, 58-60].

2.3.Transition Metal Carbide Precipitation in steels

The most common precipitate in carbon steels is cementite, which is the iron carbide of composition M_3C. This is a good example to emphasise how the conditions of thermal and mechanical treatment can change the size, shape and, at the end, the impact on the mechanical properties. Depending on the thermomechanical treatment the cementite can have shape of plates, small rods, or spherical particles. However, cementite is usually formed as precipitates that are too large to produce the dispersion hardening effect.

The precipitation of nanoscale carbides or carbonitrides is more easily accomplished when the alloy is microalloyed with transition metals (TM) like V, Mo, Cr, Ti, W, Co, Ni, or Fe in combination with the presence of non-metallic elements, such as C and N. This then allows hardening by interactions between newly formed particles and dislocations within material as described in section 2.2.1 above.

One application for the TM carbides discussed above is the HSLA steels. These steels have a range of chemical compositions, but a common feature is the use of relatively small amounts of alloying elements to create nanosized carbides for dispersion hardening. For example, dispersion hardening can result from a Nb addition to the alloy, which was extensively studied by Patel *et al.* [11]. Their research was based on examination of all roles Nb can play in the alloy, both in austenite and ferrite phase. As a conclusion they stated that the main roles are grain refinement, precipitate hardening, and dislocation hardening, or change in the grain shape due to recrystallisation. Despite the complexity of the many roles Nb can play in different alloys, the main point is very clear – it causes the increment of strength as a dual consequence of grain refinement and precipitation hardening. It was also pointed out that the steel production type (cold rolling, hot rolling) is dependent on the type of the steel. Classic, ferritic HSLA steels are produced by cold forming, whereas the dual-phase steels or even tri-phase steels are produced in many other ways including

combination of mechanical and thermomechanical treatments. Because of these undeniable advantages of steel microalloying many other research laboratories have studied the impact of Nb, Ti or V, showing that HSLA steels have advantageous properties for automotive applications [11-16, 61-63]. For example J. Patel *et al.* [11] showed that some of the profiles used for automotive construction can be reduced from 10mm down to 2mm, which would provide a huge reduction in the weight of these elements.

In past years there were several studies performed on these materials and their precipitation behaviour. HSLA steels are characterised not by uniform chemical composition, but very precise design of mechanical properties. Thus there are plenty of different types of HSLA steels: dual phase steels, acicular ferrite steels, microalloyed steels, etc. The presence of big precipitates (more than 100nm) results in grain refinement, and small ones in dispersion hardening. Both of these strengthening mechanisms are described in section 2.2.1.

2.3.1. Introduction to transition metal carbides

Transition metal carbides are commonly formed during precipitation treatments of steel alloys. They consist of transition metal atoms and carbon atoms, usually nominally in a 1:1 ratio, for example TiC, ZrC, HfC, VC or NbC. They are characterised by the high melting point, extraordinary hardness, semimetal electrical conductivity, and low chemical reactivity [64]. All monocarbides crystallize in the NaCl (rock salt) structure [65] or slight variants thereof [66, 67]. Many basic studies were carried out on bulk samples of such carbides to identify the compositional stability range carbides [68], the crystal lattice parameters, and to study their mechanical, thermal, and electrical properties [69].

The chemical composition of transition metal carbides can be described as MC_x. It suggests that the stoichiometry of compound might be different. The x represents the carbon to metal ratio, and it may vary from 0.5 to 0.97 without changes in crystal structure. This variety is assigned to high density of vacancies in FCC carbon sublattice in the rock salt structure[28]. The high density of vacancies also affects in other features like atomic diffusion, or scattering points for electrons and phonons. Consequently properties related to defects like transport, or related to chemical bonding have been studied some time ago [64, 70], and are also well described from the theoretical point of view by [23, 71, 72].

Nevertheless, the main property of the rock salt carbides required for use in dispersion hardening is their high hardness and low ductility. So far the majority of work on dispersion hardening in steels has been performed on HSLA steels, where the precipitates have small sizes (less than 100nm). The main impact is on the mechanical properties comes from the smallest ones, as it is believed they are responsible for the strongest hardening effect [73]. Investigations to date were

done with several different techniques involving electron microscopy, x-ray spectroscopy, and in last decade the atom probe tomography [74-78]. Each of the available technique has advantages and disadvantages[79].

One of the first microstructural studies of precipitates was done in 1957 by Wilson [80]. Using an early scanning electron microscope (SEM) he studied all stages of tempering and size and distribution of the carbides and nitrides within the specimen. At that moment it was almost impossible to perform a TEM study, because this technique was very rare, and the specimen preparation techniques were not well understood. Just two years later, the development of the TEM technique allowed, Leslie *et al.* to observe cementite (Fe_3C) precipitates in ferrite [81] in two low carbon steels and one steel alloy with 3.25% of silicon using a combination of diffraction contrast imaging and electron diffraction.

Some years later Ray *et al.* [82] used TEM to study cementite and ε-carbide precipitation in low carbon steels with additions of phosphorus. They proved that the elements can have a significant impact on the precipitation rate, nucleation sites, types of carbide and rate of growth. They have used the thin foils prepared by jet polishing in solution. Despite well-prepared specimens, they were not able to record a diffraction pattern from the precipitates alone and the SAD images were dominated by the signal from the ferrite.

Of more direct relevance to the present study, studies were performed on precipitation in HSLA steels by Hirsch and Parker in 1980 using extraction replicas [83]. By TEM and simultaneous x-ray chemical analysis they showed that the reheating specimens for maximum of 2 hours cause a secondary precipitation, which leads to a secondary hardening effects, and the maximum size of the precipitates was 100nm. Whilst a detailed chemical analysis was not possible at that time with an early Energy Dispersive X-ray system, they were able to show that the Nb:Fe ratio in the precipitates appeared to increase with increasing size of the precipitates. With the benefit of hindsight, it seems unlikely that there would have been significant Fe content in such rock salt carbides, and there is a chance that there was some incomplete dissolution of the ferrite matrix in the replica extraction which led to this conclusion.

L'Ecuyer *et al.* [84] made a very detailed investigation of impact of the microalloying elements such as Mo, Al and traces of Ti on precipitation in HSLA steels. As for the earlier studies of cementite and ε-carbide, this mainly used conventional diffraction contrast imaging and selected area electron diffraction, although in this case the metal content of precipitates down to 30-40nm in size was also studied with X-ray point analysis, whereas some down to just a few nm in size were imaged [84]. They observed the dynamic precipitation of M_xC_y rich in Mo and proposed a precipitation sequence. Firstly, the Mo-rich M_xC_y or a mixed type of carbide Mo-Ti is formed,

presumably during the deformation. Later, during annealing, the AlN is build over the pre-existing precipitates. They also suggested that if it is desired to form AlN precipitates, there should be very limited or no Ti in the alloy, because during the deformation it will trap any N in the alloy forming TiN. Unfortunately, the development of the technique was still insufficient for precisely determination the chemical composition of the carbides.

Just two years later, Güth *et al.* published a very detailed study about Nb precipitation in HSLA steels used for bar reinforcements [85]. The microstructure studies were done using TEM, and chemical composition was tested using SEM. They determined the Nb, Ti and V content of several cuboidal precipitates using EDX analysis, but only larger particles were investigated greater than 30 nm in diameter and carbon contents were not measured. The smallest precipitates which have a stronger influence in dispersion hardening were not studied in detail.

Ubhi *et al.* [86] studied the importance of microalloying elements for precipitation of vanadium carbide. They studied four different HSLA steels with Mn and Si, and found that Si increases the precipitation rate by about a factor of 4. In contrast to this, the Mn only affects the rate of the ferrite-austenite transformation. However this study mainly concentrated on the analysis of precipitate size distributions using bright field TEM imaging and did not examine precipitate chemistry.

2.3.2. Analytical microscopy of transition metal carbides

More technical details on Electron Energy Loss Spectroscopy (EELS) are given in the following chapter, but a few words should be said about the history EELS and its sister technique, Energy-Filtered TEM (EFTEM), prior to reviewing more recent studies in which EELS and EFTEM played an important role in the understanding of precipitation in steels. The development of the EELS technique started in the 1940s with Hillier and Baker [87]. Whilst it started in the 1940s, it was not really applied to transmission electron microscopes to any significant degree until almost 30 years later. Experimental references to EELS on STEM instruments start in the late 1970s and early 1980s. Some of the pioneers were Jeanguillaume and Colliex in France [88-91], Howie [92, 93], Egerton [94-96] and Craven [97-99] in UK, prior to the commercialisation of the post-column spectrometer by the Gatan company. A further key development without which this thesis would not have been written was the idea of spectrum imaging and what could be done with it by Jeanguillaume *et al.* [88], even if it was not practical with the instrumentation available at the time of writing that article. EFTEM is a technique, where images are formed with electrons of just a small energy range, and by recording three images, two before and one after an elemental edge, the background is removed creating an image of a specific elemental distribution[100, 101].

Allison *et al.* [102] seems to be the first, who tried to attempt to predict interaction cross-sections for transitions in atoms. In these early cases, these were based on a hydrogenic approach, which uses a simplistic model that all atoms have the same orbital structure as hydrogen. Allison *et al.* [102] tried to make first quantification and present stoichiometry of the VC_x carbide. However, it was found that the known values of *x* from chemical analysis were 10-25% higher than those determined using EELS with calculated cross sections. For K shells the accuracy is acceptable and the hydrogenic model is quite good, but for outer shells the accuracy becomes less good. An advance was made in the quantitative analysis of EEL spectra by Egerton [94, 95], where he made the first attempt at the evaluation of inner-shell ionisation cross-sections using the Hartree-Slater approach [103]. At the same time Thomas *et al.* [104] compared available techniques to investigate the light elements, and their results showed that EELS is a good method for such type of analysis, but was still in need of further development at that point. Ultimately, the most satisfactory method is to use experimental standards appropriate to the samples under analysis and not to trust simplistic calculations like the Hydrogenic or Hartree-Slater approaches [105-107]. Indeed, Egerton noted some significant discrepancies between measured and calculated cross sections, especially for M-edges[108].

The extensive work of Baker *et al.* [86, 109] investigated the formation of vanadium precipitates in more details. Prior to this, it was believed the Fe,V carbide is formed [109], but they proved that instead of iron taking part in this precipitation, the other transition metals in steels are forming the rock-salt carbides. It was confirmed in later research by Baker *et al.* [110] in 2009, so this work used newer techniques for analysis including EELS, Energy-Dispersion X-ray (EDX) and EFTEM imaging, which had previously been little used for the study of steels. One of the benefits of this was unambiguous proof that the precipitates contain carbon and/or nitrogen. A bit earlier, another group conducted similar research by Hofer *et al.* [107, 111], which used EFTEM with both the three window and two window jump ratio methods for the formation of elemental maps using the inner ionisation edges. They detected precipitates down to 2nm, but they used EDX on larger ones (10nm) to chemically quantify them. Unfortunately, they were not able to determine whether the precipitate contains C and N using this technique. Further studies from Hofer's group developed the jump ratio technique to achieve improved contrast for small precipitates [112] and [113]. Whilst EFTEM is good for imaging, it is not easily quantified, and in such studies was always supported by EELS and EDX for chemical analysis.

An important step forward in analytical quantification of precipitates with EELS was performed on HSLA steels by Epicier et al. [114]. They proved the presence of N in the precipitates with EELS, whilst mapping them effectively with EFTEM, and were able to distinguish between larger

nitride precipitates and smaller carbonitrides, the two classes of precipitates originating from different points in the thermomechanical processing of the steel. Similar research was performed by Scott *et al. [115] which* confirmed the importance of N in the very early stages of precipitation due to the innovative alumina extraction replicas.

A recently developed alternative to TEM/STEM for precipitation analysis is atom probe tomography (APT). The idea of atom probe tomography was derived from field ion microscopy, which allows the imaging of the atomic structure of a fine needle in 3D by evaporation of the atoms one by one from the surface of the specimen in a strong electric field. This was first done in the late 1950s by Müller [116-118]. In 1956 [116] the first observations of individual atoms were recorded with the atomic resolution and called field ion microscopy (FIM). The first modelling of surface evaporation fields was presented by Brandon [119], and used in experiments at the beginning of 1970s [120]. Classical FIM gives no information about chemical composition, but the idea of APT was to perform chemical analysis on the field-evaporated ions to make a 3D chemically sensitive map of the different atoms. The basic principle of APT is to do mass spectrometry by time of flight on the evaporated atoms allowing the chemical reconstruction of the needle-shaped specimen [121]. The needle is put under the high voltage into the cryo chamber and by applying a small impulses to the high voltage already in use, the individual crystallographic planes are ejected, and the atoms detected at the end of the chamber (usually around 1 meter away), giving at the end the reconstruction of the 60% of the atoms in the specimen. Since a high fraction of atoms are detected, APT is very good for small precipitates and quantitative measurements. But the material volume surveyed is orders of magnitude smaller than that surveyed in a TEM/STEM specimen, with no visibility of microstructural features like grain boundaries or dislocations unless these contain chemical segregation, so linking precipitation to microstructure is difficult. Also, a high collection efficiency comes at the expensive of spatial resolution, so atomic resolution is lost. Moreover, not all atoms are equally likely to evaporate, so quantification can be complex.

There have been studies of small precipitates in steels with APT ongoing since 1978 by [122] [123] although more work has been carried on since the 1990s. For example, in Rouen, Danoix and co-workers have published extensively on APT studies of precipitation in steels [76, 78, 121, 124-126]. They, like others, such as Menand *et al.* [127], Thuvander *et al.* [128], and Craven in Glasgow [129] were able to chemically investigate and analyse many types of steel, with precipitates even in early stages of precipitation, but usually, the earlier studies only used 1D APT, which means that the reconstruction was done only in one direction.

Recently, Nohrer *et al.* [130] performed a very detailed research of HSLA steels using cutting-edge technique - atom probe tomography 3DAPT. They investigated a specimen containing

vanadium carbide precipitates with the diameter size maximum of 20nm. They showed plenty of small precipitates, with chemical analysis supported by TEM studies, showing the orientation with the matrix. The APT studies revealed two types of precipitates, with different shapes, sizes and chemical compositions. They also proved that the type of precipitate (V-rich, or Mn-rich) is dependent on the nucleation site, and that using the APT allows nanosized precipitate studies. However, the specimen preparation for this study can be problematic for hard materials, therefore it is important to develop a technique, which can give similar results with, for example, classic TEM specimens.

3DAPT is used in evaluation of differences in solubility alloy elements in each of phases – steel matrix, carbides and to calculate the chemical compositions profiles across the interfaces. However, despite being an excellent technique it is relatively difficult to prepare a needle shaped sample, with a radius on a tip less than 80nm [131]. Also due to the pulsing high voltage applied to the sample during analysis, it is somewhat difficult to avoid breaking the sample, especially close to bigger precipitates [76, 125, 132]. Moreover it is possible that the light elements like carbon or nitrogen will move on the surface before being ejected, inhibiting the estimation of element concentration within the nanosized structures. The APT also does not give any information about the crystallography, or orientation relationship between nano structures and matrix, because its result is only a reconstruction of atoms presented in the specimen with detection close to 80%. For that reason it is a very good technique as a complementary technique combined with electron microscopy. Both of the techniques used simultaneously are very powerful combination, which is irreplaceable for total picture of the microstructure and the chemistry. The advantages of this combination was used with a great success by Craven *et al.* [129], as they were able to investigate precipitates less than 4nm in diameter. Due to the APT they showed the cloud of precipitates segregated in one region, but the microscopy results supported the low C content in particles theory by presence of big Fe_3C formed in their vicinity. Their complementary results eliminates the blindspots of each of the technique. The microscopy can eliminate the lack of microstructure information in APT results, whereas the APT eliminates the lack of the third dimension in TEM/STEM images, giving also direct information about the chemistry instead of the contrast.

To summarise, it has been shown that nanoanalysis using conventional and scanning transmission electron microscopy has played a key role in understanding nanoscale precipitation in steels over the last 40 years. Initially, this was limited to imaging and some point analysis using X-rays. In last two decades developments in techniques (e.g. spectrum imaging, EFTEM) and instrumentation (clean vacuums, better electron sources, improved spectrometers, better cameras etc.) has allowed major steps forward to made in understanding the chemistry of even few nm

precipitates. Nevertheless whilst qualitative chemical mapping is relatively straightforward, high accuracy quantitative analysis remains difficult, especially for the very smallest precipitates, and especially for carbon and nitrogen content. Until such an analysis can be reliably performed, the exact effects of microalloying and of carbon and nitrogen contents in steelmaking are hard to assess fully. The remainder of this thesis describes progress towards this goal of reliable quantitative analysis of nanoscale precipitates in steels, starting with a more detailed consideration of the preparation and microscopy techniques used in this work. The new technique of analysis, together with the data processing, which was also developed during this PhD, is critically dependent on use of the DualEELS technology first developed in Glasgow by Scott, Craven and co-workers [133]. The simultaneously recorded low loss and core loss gives a chance to fully quantify every single phase in spectra, because of the easy removal of multiple scattering and the possibility to separate signals from the precipitate from other signals such as from the matrix or the surfaces. In the following chapters, the techniques used in this thesis are presented, such as microscopy and spectroscopy methods supported by development of the specimen preparation method. The results of proposed solutions are presented in following chapters.

3. Instrumentation and experimental techniques

In this chapter I will explain the specimen preparation methods and microscopy techniques used for analysis of the materials examined in this thesis. The description will cover the principles of these experimental techniques, as well as the precise experimental conditions used in the work reported in this thesis. Firstly, the processing of the steels by our partners is summarised briefly. This is followed by a section detailing the preparation of thin V and Nb steel specimens for microscopy. Finally, the details of the techniques in transmission electron microscopy (TEM) and scanning transmission electron microscopy (STEM) used in this work are described in detail.

3.1.Steel casting and thermomechanical processing at our partners

The ThyssenKrupp Company (SE-AG) provided material divided into two groups of high manganese steels with a base composition of Fe-20Mn-1.5Al-0.6C. The first group, which is the principal one studied in this thesis, is micro-alloyed with 0.1% niobium or 0.2% vanadium. A second group of alloys was also prepared for the project with differing contents of manganese, aluminium, carbon and micro-alloying elements, mainly for thermodynamic and thermomechanical simulation studies. The V and Nb were chosen to perform dispersion hardening by carbide formation to enhance the yield strength. In addition, these micro-alloying elements, in comparison to a reference material free from micro-alloying elements, influenced the mechanical properties and the kinetics and thermodynamics of the nucleation of precipitates such as carbides or carbo-nitrides. The Al in the alloys in Table 1 was present to serve as a trap for any residual N by the formation of AlN precipitates at the beginning of processing. In addition to reducing the N content, which results in the formation of pure secondary carbides and prevents formation of the TiN, AlN precipitates also play an important role in controlling the austenite grain size.

From the large range of alloys produced in the project, a limited number were supplied to the University of Glasgow for detailed microstructure and analytical characterisation. These were nominally 0.1 % niobium microalloyed steel and 0.2 % vanadium microalloyed steel, and the base steel without microalloying for comparison studies; the exact compositions are listed in **Table 1**. The choice of these chemical contribution is supported by modelling results from Aachen University group, which showed that the secondary precipitation is the strongest at these chemical compositions.

Name	Target Composition (wt. %) with base Fe-20Mn-1.5Al	Actual Content (wt. %)					
		C	Mn	Al	V	Nb	N
Base composition	Base	0.61	20.6	1.5	<0.01	<0.01	
Nb steel	base-0.1Nb	0.62	20.5	1.22	0.002	0.11	0.0031
V steel	base-0.2V	0.58	19.7	1.5	0.19	<0.01	

Table 1. The chemical compositions of alloys used in thesis during first two years. (Ti, less than 0.005%)

The production process used by SE-AG consists of several steps. Firstly, the material is cast and then reheated and hot rolled to a thickness of 45mm. This procedure can unfortunately lead to cracks and holes on the surface of the material. Therefore special electron probe microanalysis (EMPA) is used to select areas with no segregation and good surface quality for micro- and nano-characterisation. A consistent procedure was agreed upon for thermomechanical treatment in the dilatometer, where simultaneously the deformation of a cylinder under compression and the heating or cooling was performed, with very rapid heating or cooling possible. The procedure involves the following:

- Reheating at 10°C/s to 1250°C, dissolution treatment at 1250°C for 10 minutes time. These conditions are chosen to dissolve all microalloying elements. In case of the Nb and V this composition suppose to be the optimal conditions [134-137].
- Cooling at 10°C/s to 1150°C, with simultaneous grain refinement by deformation by compression with strain value of $\varepsilon = 0.30$ [%], and strain rate $\varphi = 1\ s^{-1}$. The conditions of thermomechanical treatment allow reduction of the final grain size to about 5µm.
- Cooling at 10°C/s to the test temperature (usually 800, 850, 900, 950, or 1000°C), deformation by compression to $\varepsilon = 0.36$ at strain rate $\varphi = 1\ s^{-1}$. This thermomechanical treatment is a multi-hit deformation and stress-relaxation process and it is performed to investigate the strain-induced precipitation and its impact on the mechanical properties, mainly for yield strength.
- Isothermal holding at the test temperature between 1s and 3600s, to give enough time for diffusion of elements and precipitation. Specimen from this group were sent to University of Glasgow for detailed analytical research performed during this Ph.D.
- An optional second deformation at the test temperature for the double hit technique, which is a part of the studies during annealing. The specimens prepared with additional deformation were used by other partners to investigate the kinetics, progress and impact of chemical elements on the softening behaviour occurring during annealing.
- Quench to below 200°C prior to metallographic investigation.

The scheme of total process of casting, grain refinement, hits and cooling is presented on **Figure 5**.

Then small samples were cut off from regions classified by EMPA analysis as free from microsegregation and cracks and sent to other partners, including the University of Glasgow, for micro- and nano-structure characterisation with transmission electron microscopy (TEM) and scanning transmission electron microscopy (STEM).

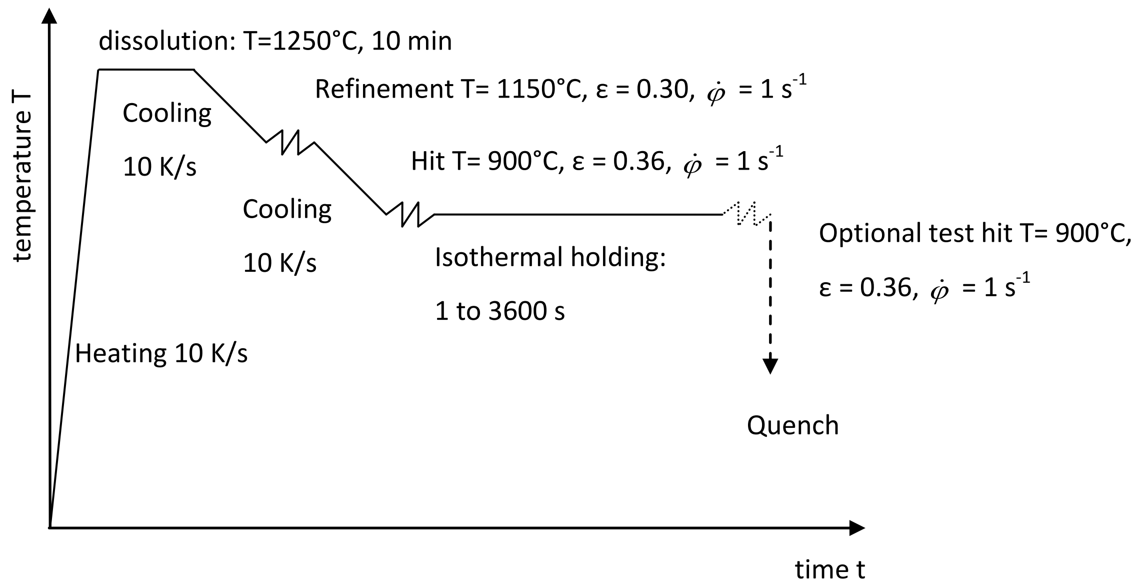

Figure 5. Technological scheme of precipitation treatment during production of steels used in the project [138], the temperature of the two hits and the isothermal holding was varied for different samples and was either 850°C, 900°C or 950°C.

3.2. Sample preparation for transmission electron microscopy

3.2.1. Introduction

Each analysis technique requires different and well-standardised shapes and dimensions of specimens. All mechanical and thermal analysis techniques require bulk samples with dimensions and shapes as defined by testing standards. For optical studies on a scanning electron microscopy, the best metallographic sample is a polished and etched surface. In case of transmission electron microscopy the sample demands are much more sophisticated, because the specimen has to be transparent for electrons and contain a representative sample of the material under investigation, with no or minimal alteration of the structure by the preparation technique. Thus, the thickness of the sample should be in the range 10-80nm and the diameter of sample or its supporting mount less than 3mm. Ideally, the sample should be stable under electron irradiation, have parallel sides, and be non-magnetic; or if composed of ferrous materials, the sample should be very thin and small in volume to minimise any effect of the magnetic induction in the sample on the electron beam.

There are two main types of specimen used in TEM. The first is a self-supporting sample, and the second one is a grid-supported sample, where the grid is usually made of Cu. The main rule of sample preparation is to prepare specimen as thin as possible, without altering the structure. In case of the samples used for this research the uniform thickness and surface free from any preparation artefacts was achieved as a result of using the optimised techniques explained in Chapter 4. Top quality specimens are essential for producing reliable data with analytical techniques such as DualEELS. In order to achieve the best possible results, the sample preparation process should be finished with a surface cleaning procedure eliminate any surface contributions such as oxides, or organic carbon-containing contamination.

There are many methods of sample preparation for TEM studies of precipitates in an alloy, such as electropolishing [139-142], carbon replica extraction [143-146], ion milling [147], [148-150], or Focused Ion Beam (FIB) cross-sections fabrication [151-155], all of which could potentially deliver a suitable specimen. Each technique has advantages and disadvantages. For example, the replica extraction method can give unrealistic results about the number density and size of precipitates. In the case of FIB there are plenty of technical parameters controlling the conditions of beam, which can damage, transform or add artefacts to the specimen. On the other hand, the FIB gives great freedom in choosing the orientation of the specimen or the area from which the specimen should to be prepared. Other conventional methods like ion milling are very dependent on human factors, because more than half of the procedure involves manual operation with the specimen such as polishing, dimpling and punching. Therefore the choice of method is made by the user according to the material, the strengths and weaknesses of the different techniques for preparation, and the available equipment. Also the choice of sample preparation technique is governed by the details of the information and the size of investigated structures, for example nanoscale precipitates in the present case. In the case of steel it was essential to take extra care of the surface of the prepared specimen. It was not acceptable to damage the surface with ions or by any other mechanical polishing method, because this would affect the structures under analysis. Ion milling or focused ion beam methods can also lead to oxidation of the damaged surface, and redeposition of products of ion milling onto other parts of the sample, but it may be possible to remove this in later stages of preparation using low energy ion milling [156, 157].

In the case of the specimens prepared in Glasgow, ion milling with a Gatan PIPS 1 was used as a conventional method, but most of the specimens were prepared by the focused ion beam (FIB) method. The FIB method allowed to choose the desired area with higher precision, together with optimisation of time required to prepare single specimen from a bulk. These methods are described in more detail in the next sections.

3.2.2. Ion milling – Conventional method

The principle of ion milling is to sputter away the surface of the sample using ions (such as argon), which applies momentum exchange between the incoming ions and the surface atoms of the solid. This must, of course, take place under high vacuum. The process starts when the bombarding particles have higher kinetic energy than the binding energy, which is typically a few tens of eV. Upon prolonged exposure to the cascade of Ar^+ ions, or other inert gas particles, the erosion of the solid starts and this is called ion milling. This is depicted in **Figure 6** showing the incident beam and its interaction with the solid, in this case showing a specimen being prepared for TEM. The inert gas ions can be stopped in the solid, but because the average energy is between 2-6kV, the ions are inert (noble gases), and the angles of incidence are low (7-10°), few ions are implanted into the sample surface. The bombarding ions can also excite the atoms within the solid by ejection of the electrons from the shells, changing the ionisation states of the surface atoms. If the Ar^+ ions have enough momentum, the target atom is removed (sputtered) into the vacuum, which then leads to the erosion of the solid surface. It is most likely that surface atoms are removed as they are more weakly bonded than atoms within the solid.

The chamber of the ion milling machine, where the specimen is placed in a special holder, is all the time under vacuum. The holder used in Glasgow is designed to hold the specimen in two places, separated by 180°, to allow the maximum milling angles range. The holder is rotated during the experiment, and the specimen is milled from the bottom and top at the same time by two separate beams.

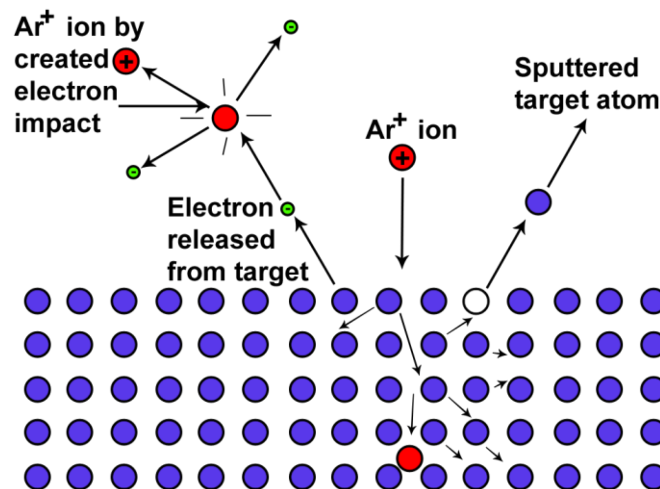

Figure 6. Interactions and possible effects during sputtering of a solid surface by an Ar^+ ion. The surface of specimen (blue dots) is bombarded by argon ions (red plus dot) and cause displacement of atoms randomized and showed by arrows with the final effect (red dot); sputtering with sputtered atom (white dot); and electron release due to the excitation process (green dot with minus), which then can interact with argon ions.

3.2.2.1. Procedure of sample preparation by ion milling

A sample was cut from the bulk material using a low speed circular saw with a cubic-BN blade. To avoid microstructural changes due to local heating, the blade was lubricated with a suitable proprietary cutting medium and the cutting was performed at a rotation speed of about 2-3 rpm.

A slice of approximately 1mm thick and 5x5mm in size was cut out and attached to a glass slide using acetone-soluble wax for further polishing. This was carried out with SiC wet and dry paper with grit sizes of 320 up to 1200 (which is related to the median diameter of the SiC particles; at 320 it is 40.5µm, and at 1200 it is 2.5 µm), lubricated by flowing colloid prepared to avoid corrosion of the steel and carry away removed material. After each change of paper the sample was cleaned with flowing water to carry away the removed material and to ensure that loose abrasive particles were removed before grinding with a finer grade paper, so that damaging and scratching of the specimen was avoided. The polishing process was done for both sides of the sample. Care was taken to keep the sample parallel-sided. The grinding was performed until the sample had the thickness lower than 250µm. 3mm discs were then punched out using a special tool. These discs were then dimpled from both sides with a changing load from 10 to 40g and diamond polishing paste from 3 µm, 1 µm and ¼ µm median diameter size. After dimpling around 80µm from each side the thickness was reduced to about 40 µm in the centre. Finally, the sample was cleaned and placed into the PIPS for final polishing with use of Ar^+ ions at 4kV at the angle about 4-6° for about 5 hours, with the finishing stage at 500 eV for about 30 minutes.

With this procedure, only two specimen were prepared, and the process was performed by Brian Miller. The individual steps were also performed by me, but the prepared specimen were never used in the analysis.

3.2.3. Cross section specimens using Focused Ion Beam liftout

An alternative to preparation via argon ion milling is the focused ion beam (FIB) lift out technique. Focused ion beam instruments are now frequently used in material science and biological science for site-specific analysis, deposition, nanofabrication and sputtering of material. Most FIB manufacturers in the last 10 years have combined the device with a Scanning Electron Microscope (SEM), with both beams focussed at the same point, although using separate columns at an angle to each other (52° in our instrument). Typically, the electron beam is used for imaging the surface of the specimen, while the ion beam is principally used for deposition or ablation.

FIB technique was also relatively quick in comparison to other, conventional methods, preserving the good quality together with control of parallelism of the sides of specimen, which

allows the analysis of a range of areas. Moreover, for ferritic steels or other magnetic materials (not studied in this work) the FIB method allows the preparation from a very small volume of material, since the large amount of material in a conventionally prepared specimen can cause significant magnetic deflections of electrons; small FIB specimens do not have the same problematic effect on the beam. However this technique has the same disadvantage as any other technique – it can result in damage of the sample and formation of artefacts. In this case, there can be ion damage of the top surface and sidewalls, together with ion implantation. The level of implemented artefacts and depth of the damage depends on the ion species, the incident energy, the angle of incidence and the density and structure/bonding of material of the specimen. The elimination of these artefacts is key to preparing suitable specimens for high-resolution microscopy.

3.2.3.1.Physical principles of FIB

The principle of the FIB technique is very similar to that of SEM with the difference that the beam is formed of ions, and that why ion beam is focused with electrostatic lenses instead of the magnetic lenses used in SEM. The electrostatic lens are used almost exclusively because the forces of the charged particles by electrostatic field is independent of the particle's velocity. In contrary the velocity in the magnetic lens is directly connected with the focusing force, and effectively the focusing power is less than in case of the electrostatic lens. The most common source of ions to date in commercial instruments is a liquid gallium source with a tungsten needle. By applying the fixed potential to reservoir the liquid gallium is drawn into the conical shape channels to tip of the tungsten, and by a combination of surface tension and a strong electrostatic field, a liquid needle is created with a tip diameter around 2nm, which is called a Taylor cone. The strong electrostatic field formed around the tip of the tungsten needle causes the ionisation and field emission of ions. The range of acceleration ions is from 1keV to as much as 50keV, with a variety of beam currents, and a very low energy spread [158].

The focused ion beam can be operated at a wide range of currents, from low currents for imaging, to high currents for rapid ablation of the sample material. **Figure 7** shows how the focused ion beam interacts with the surface of a material. The key factor governing this process, as for ion milling above, is the transfer of momentum from gallium ions to the surface atoms. If the kinetic energy of the bombarding Ga^+ ions is higher than the bonding energy of the surface atoms, then sputtering will occur. The difference between the Ga^+ ion energy and the bonding energy determines the sputtering yield. The consequence is the destruction of the chemical bonding of the material at the surface, either by knock-on damage or radiolysis, which causes the formation of free negative or positive ions, or neutral atoms. These are often freed (ablated) from the surface, but can

also be displaced across the surface as secondary ions. The ion beam also forms copious quantities of secondary electrons, which can be used for imaging, much as for SEM imaging [158-160].

The idea of interactions of ions with the surface in focused ion beam is very similar to the argon ions interaction during ion milling (for example in PIPS), with the difference that the argon is neutral, noble gas, which do not interact with the material. Whereas in case of the FIB there are ions used for sputtering (removal of the material from the surface due to the knock-on damage) of gallium, which can chemically interact with the specimen material. The nature of interactions between ions and matter is different than those for an electron beam. First of all, the ions are much larger and heavier than electrons, and their charge is positive. Because they are larger and heavier they have very significant momentum, and knock-on damage or sputtering is highly likely. However the range of penetration, which is defined as the interaction of a single ion with the solid of the surface, is shorter than in case of the electrons' penetration range. Therefore the interaction stays only in the surface or the first few nm below the surface, which is very important in the case of TEM sample preparation [158].

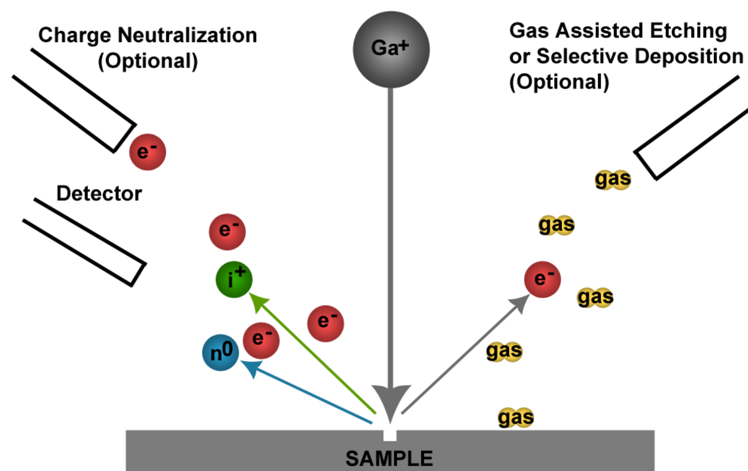

Figure 7.The scheme of Focused Ion Beam process [161]. The grey ball of Ga^+ bombards the surface causing emission of electrons, ions and neutral particles, as a result of knock-on damage. The gas assisted injector (for example Pt deposition) is inserted on the right, the ion detector is on the left.

3.2.3.2.Procedure of specimen preparation by the FIB lift-out technique

The FEI Nova 200 DualBeam FIB system used in this work combines Scanning Electron Microscopy and Focused Ion Beam columns in one instrument, as described above. **Figure 9** presents a schematic diagram of this instrument. The essential FIB components are the Sidewinder FIB column (which allows the formation of small ion probes down to 2 or 1 keV energy), the SEM column at 52° to the ion column, the Omniprobe 100 micromanipulator which can be inserted into the main chamber on the opposite side to ion column for lifting out small specimens, and the main chamber with a sample holder which can be tilted up to 52° and moved in *x*, *y* and z directions. There is also a

gas injection source (GIS) needle, which is situated between the ion column and electron column. This GIS needle is used for deposition of the protection layer of metal, usually Pt, to protect the material surface from damage by the ion beam during thinning down to a (S)TEM cross-section specimen. Later, during the lifting-out in FIB, the GIS is used for attaching the specimen to the holder. The GIS is set next to the specimen(approx. 150µm above the specimen) and by heating the GIS nozzle the material is liberated and can be deposited on the surface. Usually the gas is the Pt-carbonyl gas in the crucible, which is connected with the needle. The GIS is inserted so that the tip is 50µm to the side of the ion column and 150µm to the side of the electron column for Pt deposition. The scheme is shown in **Figure 8.** The Ga^+ interaction with the gas causing the platinum-carbonyl chemical bonds to break, resulting in the deposition of the Pt on the surface. The residue carbonyl gas is removed by the vacuum system. This is extremely useful feature, because it allows to protect the surface from further milling by the gallium ions during further steps during lift-out technique.

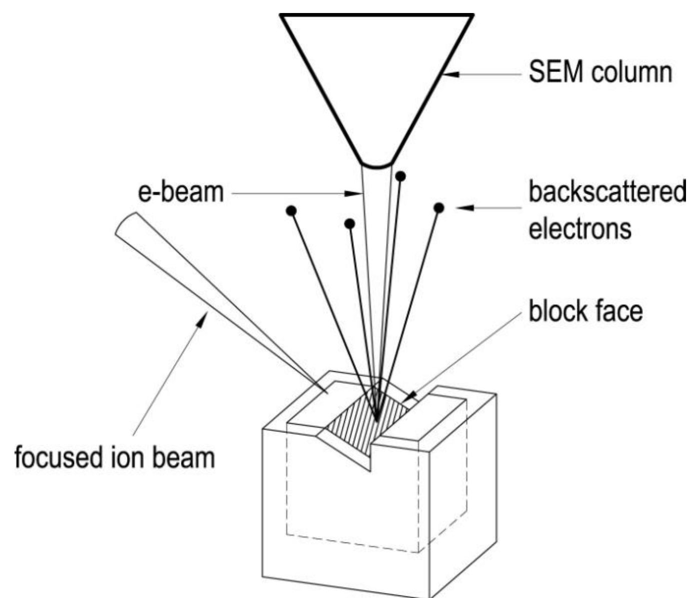

Figure 8. Scheme of columns in DualBeam. The SEM column is in the zone axis, the focused ion beam source is on the 52° off axis. The backscattered electrons are shown, as they occur as an effect of the surface interactions. The block face is the place, where the lift-out take place.

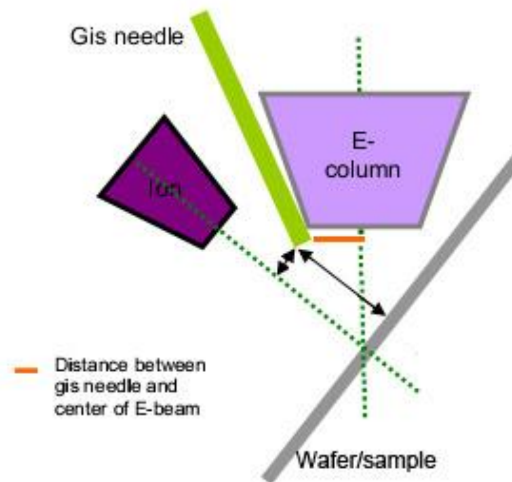

Figure 9. The scheme of the position of GIS needle in the column in relation with the electron and ion beams and the specimen surface.

Steel specimen requires extra care while preparations, because during the preparation material can react chemically with the material, which is very undesired while analysing the precipitation in steel. Prior to inserting the specimen into FIB, the samples are prepared as described in **section 4**. The polished half cylinders with the mirror-like surface , was put into the FIB to lift out the lamellae. First step is platinum deposition, as described in previous paragraph. The whole surface has to be covered prior to lifting out with a protective layer, usually Pt, C or Au. This can be performed using separate deposition machines, for example, by thermal evaporation for C or sputter deposition for Au and Pt. The conditions of the process (time and current) were chosen to provide a layer of approximately 80nm thickness. Then, the bulk material was placed mounted on the FIB holder and a suitable area was chosen for FIB lift out preparation. The procedure for preparing the cross-section prior to lifting out is summarised in **Figure 10**. The procedures used in this work were based on some developed for the preparation of silicon [156], but it was clear that the details would not be optimal for high strength steels for a number of reasons. Steel is much harder to mill as it has a much lower sputter yield, so with the same beam conditions the time necessary to mill whole specimen is much longer. This also means that the whole area can be badly affected by redeposition on the sides of the lamella. Firstly, the largest current is used for milling two trenches to either side of the area that will become the lamella; usually the beam conditions used for that purpose are the combination of 30kV voltage and current 0.92nA. In the case of the steel specimens used here the size of the lamella was 2µm in depth with a thickness around 1µm cut with use of the AutoTEM option, which is an automated milling script. This allows unattended and fully automated sample milling of cross-sections prior to lifting out. The nanomanipulator needle is then brought to one corner of the lamella and a square of Pt is deposited on the junction between

specimen and manipulator to attach the two. **Figure 10a** shows an image taken with an ion beam with a top view of the specimen. In the left corner, the Omniprobe nanomanipulator is seen, as it is attached to the specimen. The sides and bottom of the lamella are then cut away with the ion beam and **Figure 11b** shows an image by the electron beam with the needle attached to the specimen, which has now been cut away from the bulk.

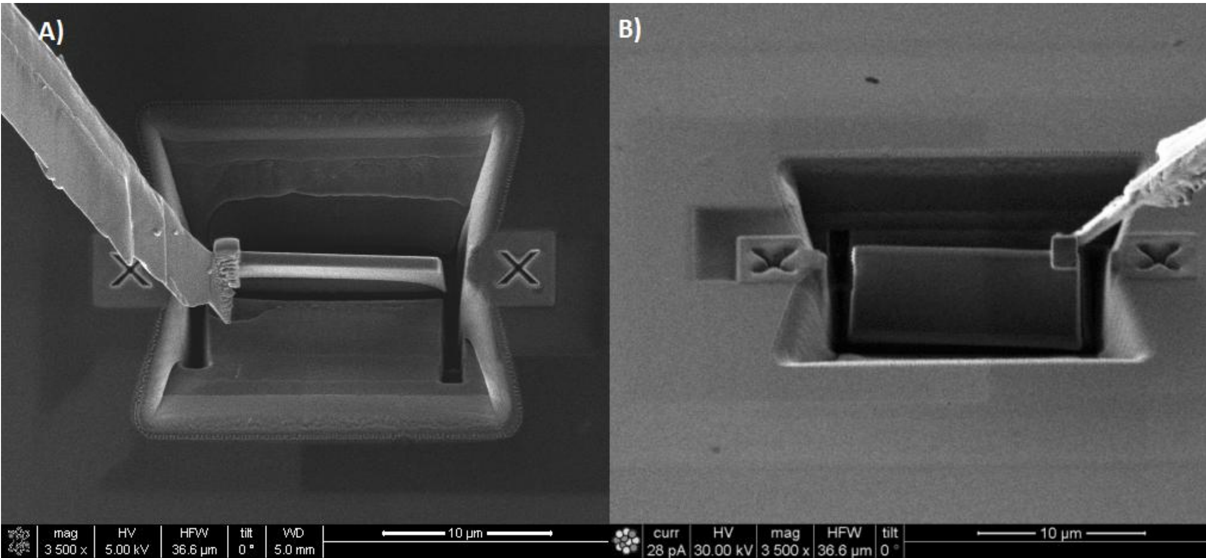

Figure 10. The cross-section cut out from the bulk material, a) with the ion beam from the top, b) at 52° with the electron beam. The figure shows the same moment of the operation - the lamella attached (GIS Pt deposited rectangle visible on the contact between Omniprobe and specimen)to the Omniprobe, just after the specimen was cut away of the bulk.

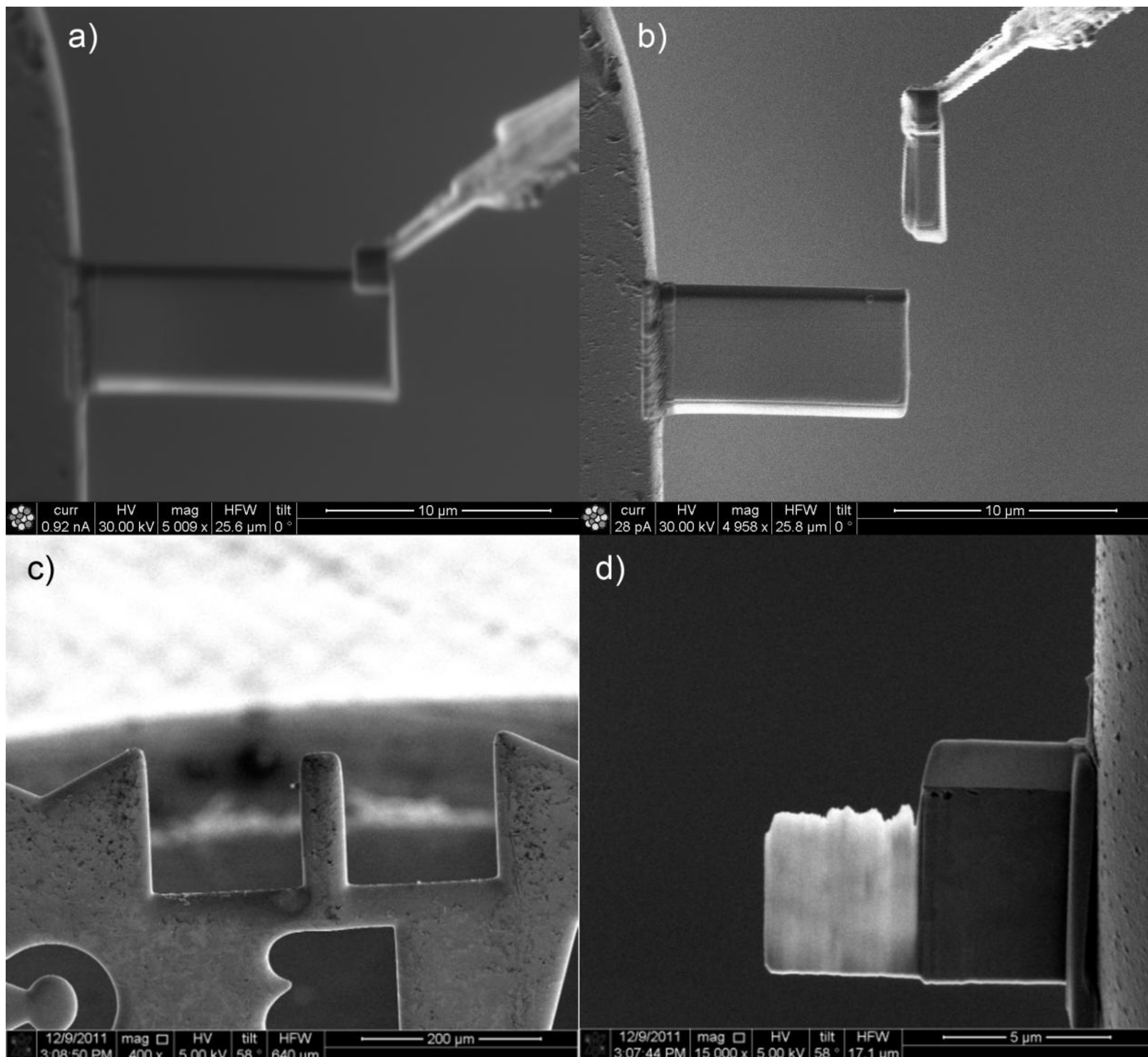

Figure 11. Specimen attached to the Omniprobe grid a) before b) after separation of the micro manipulator, c) the Omniprobe holder with specimen on the left B holder seen with 400x magnification with electron source, d) specimen after thinning from both sides, with the visible platinum and other sample contrast. Photos were acquired during standard specimen preparation session.

The next step is to lift the prepared cross-section away from the substrate and attach the cut sample to the Omniprobe copper support (often called a grid, shown in **Figure 11c**). With the sample attached to the Omniprobe needle it is attached to the copper support using more Pt deposition, as shown in **Figure 11a**. The end of the lamella is then cut of to separate the nanomanipulator needle, as shown in **Figure 11b**. Then, the thinning process can be started, which is the critical part of FIB specimen preparation.

The incident angles used for final thinning of steel samples were between 0.5° and 2.2° to the surface normal. The thinning process starts using 30keV at 1.2°. To prevent gallium implantation and artefact creation during thinning the optimal procedure was applied, and its origin was taken from the stepping downwards the acceleration voltage process as was done previously by Schaffer *et*

al. [156]. For the steel used here the combinations of tilts, time and acceleration voltage has to be modified and optimised, because the conditions described in the paper are for Si-based materials, which have much lower sputtering yield. These are presented and described in details **chapter 4.5**.

The final specimen is presented in **Figure 11d**. During thinning, some microstructure features start to appear, which means that the specimen is becoming electron transparent. The largest difference is between the platinum and steel. Also the whole Pt layer (and the Au layer below) is removed in the thinned region, so the top surface of the specimen is a little damaged: this is not a perfect specimen. Milling just half of the cross-section shortens the preparation time and gives the user a further chance for improvement if, for some reason the prepared specimen is bad. In such a case, the second half of the specimen can be thinned and used for microscopy instead.

Part of this work was a development and implementation of a new procedure of FIB preparation of samples for STEM to minimise preparation artifacts known as curtaining, which are stripes of unevenly milling, running parallel to the beam direction. Their presence hinders quantitative microscopy, especially with EELS, which requires a near-uniform thickness in the investigation area. They also hinder imaging because of the additional contrast that they cause. The whole procedure aims to provide a sample with the highest quality, suitable for high resolution study, in the shortest possible time. In case of the high manganese steels, which are characterised by high strength, the preparation of a good quality sample from scratch may take up to eight hours, so there was a particular desire for a reduction of the time required for full sample preparation. Hence, by combination of different voltages and currents, it was intended that the time might be shortened to 4h without diminishing the sample quality to increase throughput and make the best use of costly equipment time. The whole optimisation procedure and its motivation is described in **chapter** 4.

Using focused ion beam technique, the V steel specimen were prepared for samples deformed and then held for 100s and 10s at 850°C, 900°C and 950°C for comparative investigations. Samples were also prepared from Nb steel deformed for 1s, 10s and 100s at 900°. At the same time the specimen were used with different conditions (time and accelerating currents) in order to optimise the whole preparation procedure for steel specimen. To provide a baseline for comparison, the basic steel sample without any microalloying elements was also prepared, using the optimised FIB procedure.

The absolute quantification of the chemical compositions of the precipitates using spectrum imaging required the acquisition of steel spectra from standard specimens of known chemical composition and stoichiometry. These were also prepared with FIB using the same lift-out procedures. Additionally, one specimen was lifted out and prepared with a cylindrical needle-like shape, in the same manner as is sometimes performed for atom probe tomography needles [154].

The needle-shaped specimen was used for the experiment of evaluation of the mean free path, which is necessary for absolute quantification of the precipitates. The details of this procedure are described in **chapter 4.4.**

3.3. Transmission electron microscopy – conventional and scanning

Conventional light microscopes have resolutions down to 0.2µm, limited by the wavelength of light. To be able to resolve smaller structures, the simplest way is to use shorter wavelengths. It was realised with the de Broglie postulate of 1924 that electrons and other particles have a dual nature – simultaneously behaving as waves and particles. With electrons, wavelengths shorter than 1Å are easily achieved at even modest accelerating voltages, so there was an idea to use electrons for microscopy, so that smaller structures can be resolved. The first step towards manufacturing the electron microscopes was the invention of electromagnetic lenses to focus electrons by Hans Busch in 1926 [162]. This was then the starting point for the invention by Ernst Ruska and Max Knoll of the transmission electron microscope in 1931 [163].

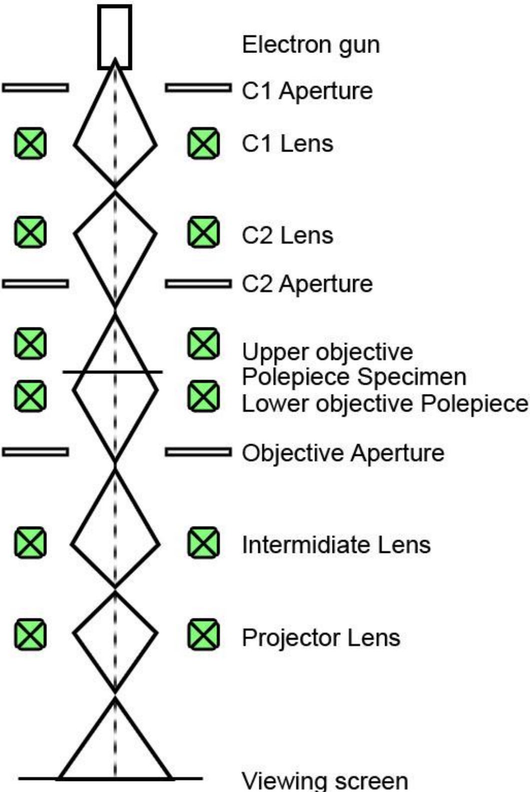

Figure 12. The schematic microscope rays. The source is in the top named electron gun. Then the rays are passing through C1 and C2 lens, forming a beam which illuminates the specimen, which is at the same height as the objective lens. The objective aperture is just below the specimen, and below are magnifying lens - intermediate and projector. The end of the electron rays path is a viewing screen.

A simple schematic diagram of a transmission electron microscope is presented in **Figure 12.** Its principles are similar to those of light microscope. It requires a source of waves, the lenses which

focus the beam on the specimen (C1 and C2) and a recording device such as an electron-sensitive camera or photographic film. Since the time of Ruska and Knoll, there has been constant development with work on various aspects of the microscope that restrict the resolution such as the quality of the electron source (gun), the aberrations of the magnetic lenses and the quality of the specimen.

The electron beam passing through the sample can undergo several interactions including transmission, elastic scattering, backscattering, inelastic scattering, excitation of secondary electrons, x-ray stimulation and more. Each interaction can be used to reveal different information about the sample. This is the reason why the transmission electron microscope is so useful, gives so much information about the structure and chemistry of a specimen, with high spatial resolution.

Nowadays there are two types of transmission electron microscopes in commercial use, which were extensively used for purposes of this thesis:

- The Transmission Electron Microscope, known as the TEM, where the sample is illuminated with a broad, parallel fixed beam, resulting in an image or diffraction pattern from a whole area of the specimen.
- The Scanning Transmission Electron Microscope, referred to here as STEM, where the sample is scanned with an electron beam focused to a sub-nanometre diameter spot, resulting in local image or analytical information collected serially to form an image or spectrum image.

The combination of transmission electron microscope and scanning transmission microscope gives an extraordinary opportunity for extensive characterization of nanostructures like the nanosized precipitates examined in this thesis, using a combination of imaging and spectroscopic techniques. Recent developments in transmission electron microscopy and scanning transmission electron microscopy, including electron guns, aberration correctors, improved detectors and cameras, and analytical attachments such as spectrometers allow not only an atomic scale analysis of the structure but also of the chemical composition and bonding. In the following sections, the main principles of these microscopes are outlined.

3.3.1. The Transmission Electron Microscope

Transmission Electron Microscopy is the technique of choice for investigation of microstructure with high spatial resolution by imaging or electron diffraction methods. This technique is based on the transmission of electrons though an ultrathin sample (typically 5 to 100 nm thin), prepared using one of the techniques described above.

Whilst a commercial Transmission Electron Microscope is a very complex device, it consists in principle of some simple components. The TEM can be split into two main systems for illumination and imaging. The illumination system is contained in the upper part of the microscope column. It contains the electron source (or gun) which produces the electrons, the accelerating system which accelerates the electron beam to some energy:

$$\boldsymbol{E = eU} \tag{4}$$

where e is electron charge, and U is the total accelerating voltage. The condenser lenses control the illumination of the specimen. By changing the voltage to higher values, the momentum of electrons is increased, and as a consequence according to de Broglie formula the electron wavelength will decrease,

$$\boldsymbol{\lambda_B = \frac{h}{p}} \tag{5}$$

where λ_B is the de Broglie wavelength of electrons emitted from electron gun, h is the constant of Planck and p – momentum of electrons emitted from electron gun:

$$\lambda_e = \frac{h}{\sqrt{2m_0eV}} \tag{6}$$

where m_0 is rest mass. For traditional transmission electron microscope the accelerating voltage is in the range of 100-300kV [164], thus the relativistic approximation needs to be applied. As a result the wavelength equation is given by:

$$\boldsymbol{\lambda_e = \frac{h}{\sqrt{2m_0eV(1+\frac{eV}{2m_0c^2})}}}, \tag{7}$$

where c is the speed of light in vacuum. Under such circumstances the wavelength of electrons is of the order of a few picometres. For the atomic resolution microscope (ARM) used in analysis during this work the electron wavelengths can be less than 3 picometers for 200kV accelerating voltage.

The imaging system consists of specimen in the holder, objective lens (both at the same height), projector system with intermediate and projector lenses and finally screens in TEM or detectors in STEM. The example ray paths through illuminating and imaging systems is shown in the **Figure 12**. The source is in the top part of the image and it is named electron gun. Then the rays are passing through C1 and C2 lens, forming a beam which illuminates the specimen placed in the middle of the objective lens pole pieces. The objective aperture is just below the specimen, and below are magnifying lens - intermediate and projector. The end of the electron rays path is a viewing screen.

These different components will now be examined in more detail in the following sections.

3.3.1.1.Vacuum system

The electrons are scattered not only by atoms in solids, but also in gases. Therefore to control the coherency of the electron, beam the whole column, together with the specimen and

specimen holder is held in the high vacuum. Another reason for using high or very high vacuum is the electron gun, which produces high electric fields. With gas molecules around instead of producing electron beam it will cause discharges or cause molecules to stick to the gun tip, and as a result, stop it working, or even damage the source. Guns, especially the newest ones, need the best vacuum, like for example, in the case of ARM used during this thesis, the required vacuum is higher than 10^{-11} mbar.

To achieve high vacuum, a diffusion or turbo pump is usually used. Both need to be supported with low vacuum pump, coming a rotary or diaphragm pump. In the case of the newest microscopes, the sterile work conditions of the whole assembly is very important, therefore the pumps for them are oil free, such as turbo and diaphragm pumps (the choices made for ARM) However if any molecules are in the vacuum they are trapped by anticontaminators such as nitrogen cooled, or other pumps such as ion getter pump, installed usually in critical areas. The Ion getter pump also is oil free.

To keep the constant vacuum the sample has to be controlled remotely. Therefore, the specimen is put into the special holder, which goes into the TEM via an airlock, that is pumped separately. Extra care has to be taken to clean the specimen holder and specimen itself, because any organic hydrocarbons or water during the analysis, while hit by the beam will evaporate and significantly decrease the quality of the vacuum, making the quality of image worse. Too low a vacuum can also damage some parts of the TEM (such as gun). The high vacuum is held in whole microscope column at that time.

3.3.1.2.Electron Sources

The first component in the optical system is the electron source. The properties of the final image will be dependent on the source. The quality of electron beam may be characterised by its temporal and spatial coherence, which depend on the source and how it is operated. The spatial coherence depends on how small the emitting area is on the electron source – the smaller it is, the higher the spatial coherence. Spatial coherence (the concept of the wave disturbance in the periodic two points of wavelength) has a strong effect on how small a probe may be in STEM. The temporal coherence related to the spread of electron wavelengths in the beam, which is clearly related to the energy spread coming from the gun. Temporal coherence restricts resolution in both TEM and STEM due to the loss of contrast at high spatial frequencies as a result of chromatic aberration in the lenses. The energy spread also affects performance in electron energy loss spectroscopy.

Three other parameters of importance are brightness, total beam current, and the stability of emission over time. The brightness is defined as the current density per unit solid angle. A higher brightness is important in getting high quality image and spectroscopy data in a short time. Since

the acquisition time is usually between 2 and 20 seconds for a full image and several minutes for a spectrum image, stability of emission over such timescales is important to the evaluation of the data afterwards. High total beam current is useful for scanned analytical or diffraction work where the spatial resolution required is not so high, but speed of analysis is paramount.

The electron gun produces electrons by two main methods – field emission and thermionic emission. A thermionic gun is heated up till it emits the electrons with sufficient energy to escape the material, which are then accelerated away using an electric field. On the contrary, a field emission gun (FEG) only requires a high electric field, which will provide sufficient amount of energy for electrons to escape.

Thermo-emission guns

Thermionic guns are made usually from tungsten wire or ceramic materials like LaB_6, because only materials with high melting point (usually higher than 2900K) can withstand the temperature necessary for to provide enough thermal energy that conduction band electrons can overcome the relatively low work function for these materials. In modern TEMs only the LaB_6 is used. The fabrication process is limited by the smallest emitting area, so the LaB_6 tip is a [110] grown crystal with a sharp tip from which electrons are emitted. The crystal is attached to a metal wire (for example rhenium) which is heater through resistivity, and as a consequence the thermionic emission occurs. The vacuum required to use this source is close to 10^{-6} mbar. A comparison of properties of each type of source is shown in **Table 2.**

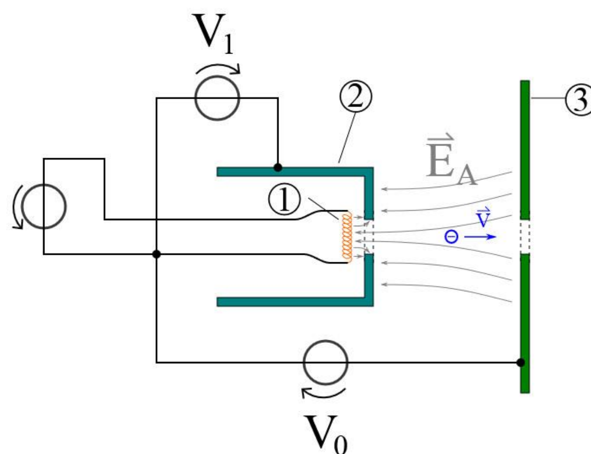

Figure 13. A schematic diagram of a thermionic gun source with 1) cathode, 2) Wehnelt cup, 3) anode.

Figure 13 shows the scheme of electron thermionic source. It presents how the electrons are accelerated by use of the electric potential between anode and cathode and how the Wehnelt cylinder forms the beam after they are emitted from the source.

Wehnelt cylinder (cap), also called grid cap made from platinum or titanium foil, which is an electrode just below the electron gun, forming the gun assembly, which was invented by Arthur

Rudolph Wehnelt in early 1900s. It has a structure of a hollow cylinder with a aperture with diameter between 200-1200µm in the centre. The cap, charged to a high negative voltage, serves as a electrostatic lens, which focuses the electron beam, which goes through Wehnelt aperture. The anode, charged positively and numbered 3 in **Figure 13**, just below the cap, accelerates the electrons passing through.

Field Emission Guns

A cold field emission gun (CFEG) consists of a cathode and two anodes as shown in **Figure 14**. The electrons are extracted directly from the cathode due to a very high electric field at its sharp tip due to an extraction voltage on the first anode (often 2-4 kV), there is then a second anode at a higher voltage. The combination of both anodes plays an equivalent role to the Wehnelt cup, which creates the cross-over below both anodes with electrostatic focussing.

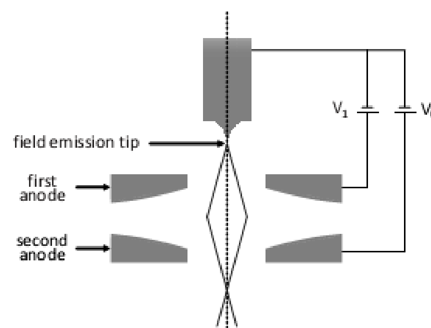

Figure 14. Schematic diagram of a field emission gun [164]. The electrons are emitted due to the high electric potential V_{1}, which provides extraction voltage to pull the electrons out of the tip. The fine cross-over is formed by two anodes reacting as electrostatic lens. The second anode accelerates the electrons to 100, 200 or more KV. Republished with permission of D. B. Williams and C. B. Carter , from *Transmission Electron Microscopy*. 2009, New York: Springer; permission conveyed through Copyright Clearance Center, Inc.

A cold field emission gun (CFEG) consists of a cathode and two anodes as shown in **Figure 14**. The electrons are extracted directly from the cathode due to a very high electric field at its sharp tip due to an extraction voltage on the first anode (often 2-4 kV), there is then a second anode at a higher voltage. The combination of both anodes plays an equivalent role to the Wehnelt cup, which creates the cross-over below both anodes with electrostatic focussing.

In contrast to thermionic guns, a cold FEG is operated at room temperature, but it requires a much better vacuum of about 6.6×10^{-9}mBar. This is because molecules are ionised by the high field around the tip and stick to it, reducing the ability of electrons to tunnel out under high field and reducing the current. Even with such a high vacuum, the current drops with time due to

contamination. Thus, the tip does need to be switched off periodically and heated to high temperature or “flashed” briefly to remove the contamination and restore the ability to produce the full beam current. There are also short period (μs – ms) stochastic variations in beam current on such a gun, which are characteristic. The typical parameters for such a gun are listed in **Table 2.**

A hybrid type of electron source, the Schottky FEG also exists, which is a FEG that is heated. This allows more stable emission, is not so sensitive to contamination (and does not need flashing), but has worse source size and temporal coherence than the CFEG. Such a gun was not used in the work in this thesis. Details for guns used in this thesis are also listed in **Table 2**.

Type	Brightness $A/cm^2/sr$ @100kV	Source size	Total current	Energy spread	Stability/Lifetime	Vacuum mBar
Thermionic LaB_6	~10^6	~1μm	High	≥1eV	Excellent Months	10^{-6}
Cold field emitted	>10^9	~1nm	Low	≥0.3eV	Decays/Flickers Can be regenerated ~1 year or longer	10^{-11}

Table 2. Key parameters of different types of electron sources used during thesis.

In **Table 2** the most important features of sources such as brightness, source size, total current or necessary vaccum. In the second row there are characteristics for the thermionic LaB_6 source presented. In third row the same characteristic are collated for the cold FEG source. The cold FEG source required much higher vacuum than thermionic LaB_6, and it is 10^{-11} mBar, and it's the highest required vacuum in the transmission electron microscopes. The brightness is also higher, and it is above $10^{9,}$ which is three times higher than the thermionic LaB_6.

3.3.1.3.Electron Lenses

In transmission electron microscope the lenses are cylindrically symmetric electromagnets with the magnetic field parallel to the optic axis. Since they are electromagnetics the magnetic field and thus the focussing power (or alternatively the focal length) can be changed smoothly by altering the current in the lens. These can be used much like convex lenses in classic light optics, and the relationship of the object and image distances is given (at least to a first approximation) by the classic equation:

$$\frac{1}{u}+\frac{1}{v}=\frac{1}{f} \qquad 8)$$

where *u* is the object distance, *v* is the image distance, and *f* is the focal length. The second equation for calculation the final magnification of image is given by:

$$\mathbf{M} = \frac{\mathbf{v}}{\mathbf{u}} \qquad 9)$$

Combinations of such lenses are used in the microscope as outlined below, using well-established principles that can be found in any standard optics textbook.

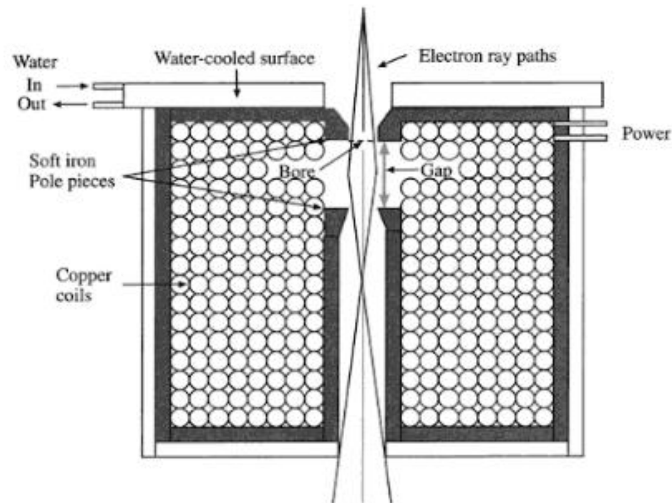

Figure 15. Scheme of the cross-section of magnetic lens. Two separated pole pieces are visible, with bore and gap. The polepieces are cooled with water, and filled with copper coils. The magnetic field deflect the electrons with the strength directly proportionally to the off-axis position of the electrons [164]. Republished with permission of D. B. Williams and C. B. Carter , from *Transmission Electron Microscopy*. 2009, New York: Springer; permission conveyed through Copyright Clearance Center, Inc.

First success in focusing electrons was achieved by Bush in 1927, who used electrostatic lens to focus electrons. But the magnetic lens are much better, mostly because they are not receptive to the changes in the high voltage breakdowns. The focusing power is based on the magnetic interaction between field perpendicular to the electron beam, and the negative particles - electrons. The magnetic field is formed by current passing through the copper coils. This field is inhomogeneous through the total length of the lens, but it has preserved axial symmetry. The trajectory of the electrons is related to the force of magnetic field created by the copper coils, i.e. the current passing through them. It can be said, that due to the changing magnetic field, the magnetic lens have variable focal length. There are different types of magnetic lens in the microscope, which magnify or demagnify the electron beam. The objective lens are the strongest lens in the microscope. The idea of focusing electron beam is schematically presented in **Figure 15.** It presents the magnetic lens. The soft iron, water-cooled polepieces surround the electron beam in the space called bore. The gap between the polepieces is also visible. The polepieces are full of copper coils, which are connected to the power. The magnetic field, which focus the electrons is the

weakest on the axis, and increases tits strength towards the sides of the lens, so the more the electrons travel off axis, the more strongly they are deflected.

3.3.1.4. Condenser system

The first part of microscope column is the condenser lenses that control the illumination of the specimen. A schematic diagram of a TEM column is presented in **Figure 12**. A typical scheme has two condenser lenses, C1 and C2. First of all the C1 lens forms a demagnified image of the gun crossover. The gun crossover is the point just under the gun where the electrons leaving the tip cross as a result of the crude focussing from the Wehnelt cap or extraction anode, and this forms an object (object plane) for the C1 lens. The focus point (image) plane of the C1 lens is then the object for the C2 lens. Depending on the excitation of C2, the electron beam can arrive at the specimen as a parallel beam or be focussed to a spot.

The excitation of the C1 lenses controls the probe size, which illuminates the sample. If the lens is strongly excited the spot size is very small, but with a larger range of angles, and more intensity will be cut out by any apertures in the condenser system. So, C1 can be set for either large spot size and high current, or small spot size and low current. For example, during EELS investigation, a weak excitation is chosen to increase beam current, and thus signal-to-noise ratio at the expense of a larger spot size and worse spatial coherence. However for HRTEM a strong excitation is more desirable to improve coherence as much as possible (whilst still retaining enough current to record good data in a short time).

3.3.1.5. The imaging system - the objective lens and post-specimen lenses

The most critical lens to the performance of a transmission electron microscope is the objective lens [164]. This focuses the rays leaving the specimen forming a diffraction pattern in the back focal plane of the lens, together with a first image of the specimen further down the column. The first post-specimen or projector lens is then adjusted to focus on either the back focal plane of the specimen or the first image, depending on whether a diffraction pattern or image is desired. Then using a combination of several further lenses, that image or diffraction pattern is magnified onto a screen or detector,

The resolution of a transmission electron microscope is dependent on the design and manufacturing quality of the objective lens. It is also designed to work at a specific (and very small) focal length, which means the specimen must be adjusted to a set height above the objective lens - the eucentric height. It is usually also set as the height at which the line through the centre of the specimen does not move while tilting about the principal axis of the specimen holder.

3.3.1.6. The apertures

Apertures are used at various points in the electron microscope and can have a range of effects including controlling resolution, the depth of focus, image contrast, or the collection angle for electron energy loss spectroscopy. Practically, most aperture mechanisms in an electron microscope allow the interchange of a number of apertures of different sizes. Ernst Abbe was the first to defined the term numerical aperture, as the sine of the half angle multiplied by the refractive index of the medium of the lens. He is also credited for discovering the resolution limit **r** of the microscope. His formula was published in 1873 and is given by

$$r = \frac{\lambda_i}{2NA} \qquad \textbf{10)}$$

where λ_i is the imaging wavelength, NA is the general term for the microscope numerical aperture. In case of the T20 instrument the point resolution is 2.4nm, whereas in the ARM the spatial resolution is below 0.8nm. The rest of the information is given in chapter 3.5 in subchapters for each microscope used in this thesis.

In 1874 Abbe wrote a paper titled "A Contribution to the Theory of the Microscope and the nature of Microscopic Vision", where he defined the resolution of a microscope. He describe it is inversely dependent on its aperture size, but the full formula describing the resolution limit of a microscope has not been posted yet. This paper was very useful, as its completion was enough to construct an electron microscope based on it.

There are three main apertures in the electron microscope – the condenser, the objective and the selected area aperture. Starting from the top of the microscope (the gun) the first aperture is the condenser aperture. It is located in the condenser lens assembly and is used to control the convergence angle of the electron beam and thereby controls spatial coherence and beam current. In STEM mode, this controls the probe size falling on the sample by the Abbe criterion given above, which says that to maximise the resolution, the largest possible convergence angle is required (although the convergence angle is limited by aberrations, as described in the next section).

The second aperture, the objective aperture, is located below the sample just below the objective lens andin its back focal plane. This can therefore select or exclude different diffraction spots to contribute to the image. The objective aperture is used primarily in TEM to control image contrast and resolution. As before, from Abbe's criterion, a large aperture will give a higher resolution. It will also give less contrast and a short depth of focus. The use of apertures to define contrast is described below in section **3.3.2**.

The third aperture is the selected area diffraction (SAD) aperture, which is placed in the plane of the first image formed by the objective lens. This selects a region of the image, such as one

rich in precipitates, in order that only this region contributes to diffraction patterns that are projected onto the viewing screen or camera.

3.3.2. The Scanning Transmission Electron Microscope

The principles of Scanning Transmission Electron Microscopy (STEM) are similar to TEM, which means that both of them form the image from transmitted electron beam. However, in a STEM microscope the beam is focused on the surface, and scanned across it by scanning coils to induce signal only from local areas. As a consequence, it is useful for quantitative nanometre resolution chemical analysis of specimen using EDX or EELS.

The first STEM was developed by Manfred von Ardenne in 1937, but suffered from terrible sample contamination under the focused beam in a poor vacuum. After this the STEM was not developed further until the late 1960s. In 1971 Crewe and co-workers reported the development of a STEM with a field emission gun and an objective lens that allowed them to focused enough current in a small probe to record one of the first good quality point by point acquisition image in STEM [165, 166]. The instrument was able to record simultaneously bright field and dark field images. Bright field image is formed by selecting the direct beam, and the dark field image is formed by selecting diffracted beams either by tilting the beam, or by moving the objective aperture to the selected diffracted beam. The first effective EELS microanalysis was done on 1976 by Leapman and Cosslett at Cambridge [167], but important contributions to its development were made by Isaacson *et al.* [168]. Crewe introduced the use of annular detectors instead of classic photographic film (as was then used in TEMs). The annular dark field detector, called ADF, produced an image with a high contrast, which results mostly from Rutherford-like scattering electrons from atomic nuclei if the inner angle of the annulus is high enough. Thus, he showed with his experiments, that brightness of the image depends on the atomic number and the thickness of specimen (i.e. the number of nuclei taking part into the scattering). Crewe named this type of imaging 'Z-contrast imaging' [169]. Later, Howie showed that an HAADF detector gives contrast almost proportional to Z^2 [170]. More recently, Pennycook and Jesson [171] showed a more detailed justification for this simplistic interpretation of HAADF images. Detectors placed with a lower inner angle are called medium angle annular dark field (MAADF) detectors. These show more diffraction contrast as well as the Z-contrast, whereas the high angle annular dark field (HAADF) detector gives contrast mostly free from diffraction contrast due to the high scattering angles.

Of course, a further advantage of annular detectors for imaging is that the low-angle scattered electrons can be collected simultaneously using an EEL spectrometer to allow elemental analysis. In principle, it is not necessary to have any post specimen lenses for HAADF imaging, but it may be useful to have them for a variety of reasons. For one thing, the magnification of the

diffraction pattern in the HAADF detector plane can be varied to allow different inner angles at the detector. Furthermore, if the EELS investigation has to be performed, the acceptance angle for the EEL spectrometer can be tuned to match the convergence angle of the probe to ensure the highest possible signal to background ratio [97].

3.3.2.1.STEM images

In the STEM microscope the scan coils are shifting the beam and scanning the specimen. Any imaging detector placed at the bottom of column transmits the signal to the computer controlling the scan to build up an image. Unfortunately the image is built up slower than in TEM as it is done serially (pixel by pixel). This can cause more problems with drift and distortion in the image, which may need correction if quantitative measurements are needed on an image.

3.3.2.2.STEM Aberrations

Over 300 years have passed since the first light microscope was invented, so there has been plenty of time to perfect lenses for light, for example, by using array of lens prepared with different materials: flint glass or crown glass. However, round electromagnetic lenses, which were invented almost 90 years ago, are still very imperfect. Moreover, Scherzer showed back in the 1930s that it is impossible to produce a cylindrical symmetric magnetic lens free from spherical and chromatic aberrations [172, 173]. In order to produce high quality images, the Abbe criterion has to be understood. A key requirement for this is that the focal length has to be constant over the angular range of rays passing through the lens to produce a diffraction limited spot. If this focal length is not constant due to some lens imperfection (or aberration), then the condition breaks down.

Normally, the optics of thin lenses is described by Gaussian or first order optics, which is an approximation for a very small angles θ between the optic axis and rays, such that sin θ = θ and cos θ = 1. Although the angles between rays and the axis in electron microscope are tiny in comparison to light microscopes, a first order approximation is not enough. There are then a number of geometrical lens aberrations that can distort the wavefront, and they all depend on both angle from the optic axis, θ, and can also depend on angle about the axis, φ. The total aberration can then be described as a sum of each aberration and its coefficient (describing how strong this aberration is), in a polynomial function described by Krivaneke *et al. [174]* where α is the convergence angle, φ is the azimuthal angle with $\theta x=\alpha\cos(\varphi)$ and $\theta y=\alpha\sin(\varphi)$ and $2\pi/\lambda$ is the incident electron wave vector:

$$\chi(\theta_x,\theta_y)=\frac{2\pi}{\lambda}[C_{1,0}(\theta_x^2+\theta_y^2)/2+C_{1,2a}(\theta_x^2-\theta_y^2)/2+C_{1,2b}\theta_x\theta_y+C_{2,1a}\theta_x(\theta_x^2+\theta_y^2)/3$$
$$+C_{2,1b}\theta_y(\theta_x^2+\theta_y^2)/3+C_{2,3a}\theta_x(\theta_x^2-3\theta_y^2)/3+C_{2,3b}\theta_y(3\theta_x^2-\theta_y^2)/3$$
$$+C_{3,0}(\theta_x^2+\theta_y^2)^2/4+C_{3,2a}(\theta_x^4-\theta_y^4)/4+C_{3,2b}\theta_x\theta_y(\theta_x^2+\theta_y^2)/2$$
$$+C_{3,4a}(\theta_x^4-6\theta_x^2\theta_y^2+\theta_y^2)/4+C_{3,4b}(\theta_x^3\theta_y-\theta_x\theta_y^3)+\ldots]$$

11)

All aberration coefficients are noted as $C_{n,m}$ where C denotes an axial aberration, n is the order of the aberrations and 2π/m denotes the smallest angle that results in the same phase shift (for m ≥ 1; m=0 is used for cylindrically symmetric aberrations). The suffixes a and b refer to 2 mutually orthogonal contributions to the same aberration that arise for all non-cylindrically symmetric aberrations. The *ϑx2 + ϑy2* term is equal to α2 and highlights the rotationally symmetric nature of the C1, C3 and C5 aberrations.

The higher order aberration coefficients are insignificant at small angle, but become increasingly important at larger angles. This means that aberrations are not a limiting factor for small angles, but at high angles (i.e. large apertures in the image-forming lens) aberrations will have a strong impact on the image quality. The most important low order aberrations are spherical aberration, astigmatism and coma.

There is also additional chromatic aberration arising from the fact that there is a range of electron wavelengths in the beam, and the focussing power of the lenses depends on wavelength. Chromatic aberration is not described here in detail, because it is not the limiting factor in this work. Each of the aberrations causes the electron to focus at a disc of least confusion, not a sharp point. The diameter of this disc describes the level of each type of distortion.

Astigmatism is an aberration where the focussing in one direction perpendicular to the optic axis is a different strength to that for the perpendicular direction to this (also perpendicular to the optic axis). It may appear due to the lenses not being totally cylindrical, which may arise from imperfections in manufacturing. Also, apertures tend to charge up if they have dirt on them, which can also lead to distortions which appears (at least to a first approximation) as astigmatism.

For the case of STEM, astigmatism results a spot that has an elliptical shape, except at focus, where it is circular but larger than that for zero astigmatism (the disc of least confusion). For TEM, features are streaked in the image, in perpendicular directions either side of focus, and the resolution is limited at perfect focus. However, this aberration is straightforward to correct with simple optical elements named stigmators, which are usually quadrupoles or octupoles (non-cylindrical lens) and can provide an opposite distortion of the wavefront to the astigmatism in order to cancel it out.

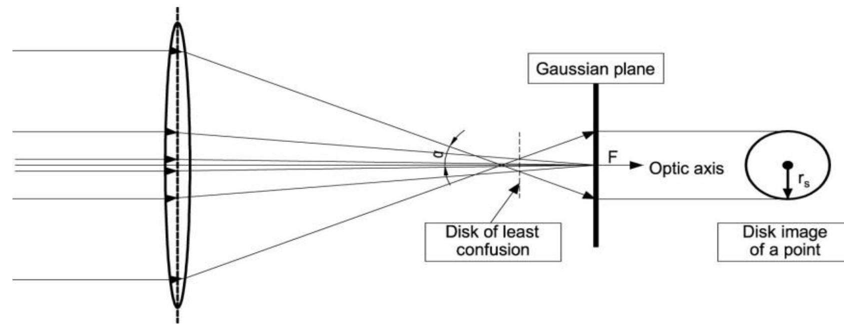

Figure 16. Scheme of the rays in microscope suffering from spherical aberration. a point object is imaged as a disk with radius $r_s \approx C_s\alpha^3$ due to spherical aberration that causes the off-axis rays are not focused at the same point F.

Spherical aberration is a geometrical lens aberration due to the geometry of lens' electromagnetic field [172][172][165][167] and is unavoidable for cylindrically symmetric lenses, as originally noted by Scherzer [172, 173]. The problem with it is that the off-axis rays are not focused at the same point as paraxial rays. The greater the distance from the optical axis, the stronger the Lorentz force deflecting the electrons. These high angle electrons are focused more strongly than the low angle electrons. As a consequence, the final focus point has the shape of a disc at the plane of least confusion, instead of a point at Gaussian plane (see **Figure 16**). The effect of spherical aberration (r_s) is directly proportional to the cube of the collection semi-angle of the electrons, α, which is described by radius r_s:

$$r_s = C_s\alpha^3 \qquad 12)$$

where C_s is the spherical aberration coefficient, which is a constant for a particular lens. The classic mechanism for correcting this using glass lenses is to use lenses of negative focal length and negative spherical aberration in the optical system. There are no such cylindrical lenses for electrons, and thus spherical aberration is the lowest order aberration that cannot be corrected simply for electron microscopes. It can be minimised by careful design, but can only be corrected by complex schemes, such as those described below.

Spherical aberration is responsible for limiting the resolution in TEM, because it limits the angle that can be collected from the objective lens. In case of STEM imaging it limits the angle of the probe that can be formed, and thus the probe size via the Abbe criterion.

Coma is an aberration that arises from off-axis illumination in a lens. As for other aberrations, this means that rays at different azimuthal angles are focused differently. This time the focus discs are in different points on a line perpendicular to the optic axis resulting in an elongated spot, resulting in a comet-shaped spot at Gaussian plane. Similarly to astigmatism, coma can be corrected in a straightforward manner. In this case, it can be corrected by user to use the coils to tilt

the beam and align the incident electrons along the optic axis. A schematic diagram of rays suffering from coma is shown in **Figure 17.**

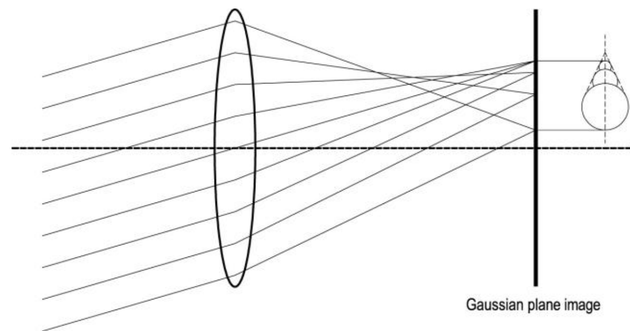

Figure 17. Scheme of the rays in microscope suffering from coma, which means that electrons travelling through outer parts of the lens are focused in different point that the ones travelling closer to the axis. The result is off-axis object point image in the form of a comet-shape disc.

In this thesis, aberration-correction is only used for STEM, so the discussion will henceforth only concentrate on aberration-correction of the probe formed by the condenser system. In STEM, it is possible to visualise either the image of the probe or the diffraction pattern of the probe, and schemes exist to use both for the diagnosis and correction of aberrations. For the user, it is easier to use the diffraction pattern of the probe, which is called the Ronchigram, and is basically an image of the sample at infinite magnification. By changing the focus, the different aberrations – astigmatism, coma and spherical aberration can be seen, therefore it might be used for tuning the STEM. The best case is to set it up on some amorphous material, because the diffraction contrast from crystallographic structures is not disrupting the image (the more artefacts from contrast imaging, the more difficult is to separate the aberrations and real features). Ronchigram image is an area that appears like a bright field image of the sample, but outside there are very distorted areas and rings where aberrations dominated, as shown in **Figure 18**. In the **Figure 18** the uncorrected simulated amorphous specimen Ronchigram is shown. In the middle part is the shadow of real specimen features at high magnification. The diameter of this circle is used for optimal choice of aperture size, because the region which will stay inside the aperture will be almost aberration free. All the rays, which are related to higher order aberrations (higher angles) are excluded by the aperture, but at the same time allow to chose the higher possible angles. Outside the potentially chosen aperture the two region of ronchigram stay - the region of radial infinite magnification, and the outer circles known as infinite azimuthal magnification, which is formed with the highest angles. If the microscope is equipped with a probe corrector as described below, this Ronchigram can be used in tuning. Tuning of the STEM ends up with placing of the aperture in the middle of Ronchigram, where the image is the flattest, which means the astigmatism, coma can be manually corrected.

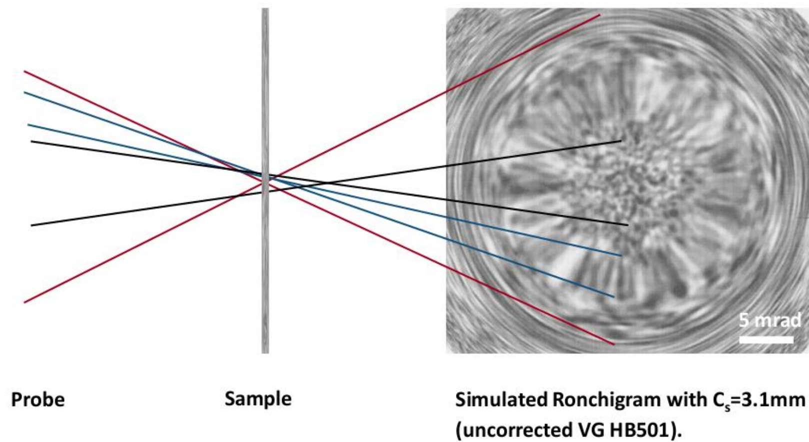

Figure 18. Simulation of Ronchigram with aberrations and uncorrected Cs [175]. In the figure the beam rays are scattered through the amorphous sample, and presented in the position on Ronchigram. The outer rings presents the infinite magnification, the inner 'flat' circle represents the shadow image of specimen. The ronchigram was simulated with a defocus of 500nm and for a spherical aberration of 3.1mm. Quentin Ramasse, unpublished work.

To improve the quality of the image, aberration correction is necessary. In 1947 Scherzer described schematically some different methods for the correction of C_s by using lenses without cylindrical axial symmetry, such as quadrupoles and octupoles [176], which was unachievable in practice at that time. What was possible then was also described by Scherzer [176], in that there is always a positive C_S in lenses, but it can be compensated at least to a certain angle (maybe 10 mrad) by a little negative defocus. More advanced schemes involving multipole lenses (such as the hexapole presented in **Figure 19**) were investigated for many years, because in some symmetry directions they have the negative C_s and by using a combination of several of these, the C_S of the imaging lens could be corrected, at the expense of some higher order aberrations that cause restrictions at higher angles. Finally in the mid 1990s Zach and Haider succeeded in producing a working hexapole-based corrector for low-voltage SEM [177, 178] which was successfully demonstrated in 1995 [179]. Three years later Haider and co workers implemented a similar corrector into the TEM and recorded the first corrected image [180]. At a similar time a first C_s corrector for STEM was constructed by Krivanek and Dellby [181] using a quadropole-octopole scheme. Their corrector compensated not only C_s but also other low order aberrations, which allowed the formation of probes with a convergence semiangle up to ~ 30mrad at 200kV. The ARM microscope used for the work described in this thesis was performed has a CEOS corrector based on the Haider hexapole scheme mentioned above and this allows correction to >30 mrad at 200 kV with the probe size down to 0.78Å [182].

The example of a multipole lens is shown in **Figure 19.** This is a 6th order symmetry sextupole, which squeezed the electron beam into the triangular-like shape. This graph shows field

lines corresponding to the magnetic field present into the sextupoles. The main point, which makes them important in correction of the aberrations is the fact, that the field in multipoles is perpendicular to the beam, not almost parallel like in the round ones. Therefore instead of rotating the electrons, the main effect in the sextupole is the deflection.

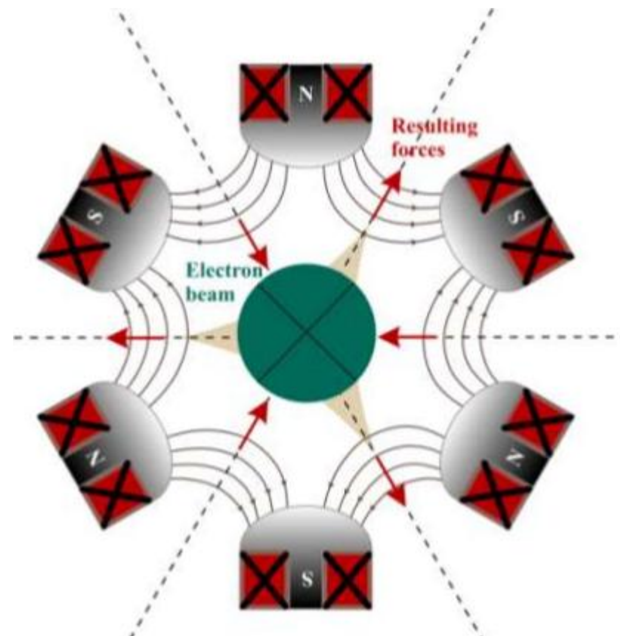

Figure 19. The scheme of sextupole correcting the Cs in the electron beam travelling through the electron column [175]. The multipole of 6th order with an impression of the correspodning field line. The resulting forces on an electron beam travelling down the optic axis have effect as impart a triangular distortion to the beam. Quentin Ramasse, unpublished work.

3.4.Electron scattering in solids and its uses in TEM/STEM

One simple reason for using electrons instead of other radiation like visible light or infrared is because electrons have a much shorter wavelength which is suitable for investigating the microstructure and nanostructure of materials. The shorter the wavelength, the smaller the resolution of the microscope. Another reason for using such a kind of 'radiation' is because electrons can interact with matter in many ways producing a huge range of primary and secondary signals. The information carried by those signals can be used for analytical and structural analysis of solid specimens. The quality of the results is dependent on both the details of the microscope and the quality of the sample preparation. For analytical work, the best solution is to obtain the smallest probe possible (certainly less than 1nm, and better than 1Å in modern aberration-corrected instruments), which allows an interaction with a smaller volume of material.

Figure 20 shows the incident beam and some of the possible primary and secondary effects that occur as a result of electron beam-specimen interaction. The primary signals are usually produced by interaction between the electron beam and the electron or nucleus of an atom.

Included in primary or direct processes are diffraction to obtain diffraction patterns or images with diffraction contrast, as well as inelastic interactions like phonon excitation, plasmon excitation, single electron excitation and Bremsstrahlung losses.

Secondary signals occur as a result of primary scattering and can be described as the production of electrons or electromagnetic radiation such as secondary electrons, backscattered electrons, and relaxation of excited atoms by three different processes – Auger emission, X-ray emission and cathodoluminescence.

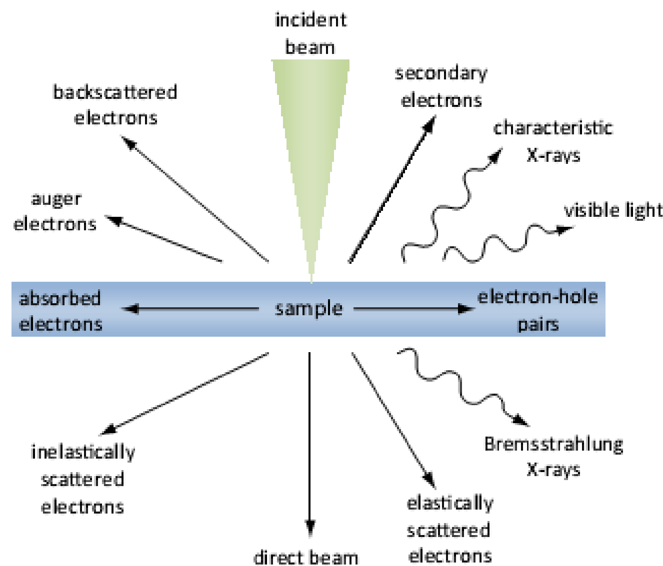

Figure 20. The different types of electron interactions with specimen in TEM [164]. Republished with permission of D. B. Williams and C. B. Carter , from *Transmission Electron Microscopy*. 2009, New York: Springer; permission conveyed through Copyright Clearance Center, Inc.

The scattering of the beam of electrons can be divided into two types: elastic and inelastic. Elastic is where the electrons lose no energy (except tiny amounts from momentum transfer), whereas inelastic scattering is where significant energy transfer to the sample occurs [183, 184]. Elastic scattering takes place when the electrons undergo Coulomb interactions with atomic nuclei and are deflected to different angles with the only energy transfer being that due to momentum transfer (tiny fractions of an eV, except for isolated low mass atoms). At low angles of scattering (~ 3° at 200 kV) in crystals, this is usually also coherent scattering and so Bragg's law applies, resulting in specific diffraction angles of diffraction. At higher angles, the scattering become more incoherent as explained below, and Bragg diffraction becomes less dominant. On the other hand, inelastic scattering of electrons is always incoherent for all scattering angles. The angles of scattering are distributed right up to 180°, although the angular distribution depends on the scattering mechanism. There is a simple correlation between sample thickness and the mean angle of scattering – the thicker the sample, the more interactions are likely to happen in the passage of the electron beam

through the sample, therefore the larger the total scattering angle. It is easier to interpret results if the sample is thin enough that only one scattering event happens in the sample, but this is difficult, because it requires very thin specimens – approximately 10-20nm. Moreover the likelihood of interaction between the electron and matter is described by an interaction cross-section σ, which is dependent on the energy of the electron. These are quoted in units of area, usually Barns ($10^{-28}m^2$). This cross section interaction does not describe a real physical area, but divided by physical area gives the probability of an incident [164, 184].

There is a strong connection between elastic scattering and diffraction. Elastic scattering is a deflection of electrons by Coulomb interaction with atoms or electrons in specimen, resulting in some exchange of the momentum. However, because of the large differences in the mass of the electron and the atom, together with the bonding between atoms in crystal meaning that the electron is basically interacting with the mass of the whole crystal, the electron momentum change is significant, whereas for the change in crystal momentum is undetectable. With such a large mismatch, the kinematics means that the energy transfer for elastic scattering is miniscule in this case. In this case of small angle scattering of less than few degrees (around 10-100 mrad) the energy transfer is so small that there is no detectable wavelength change for the electrons, the scattering is therefore coherent, and thus the results are strong diffraction peaks in some directions, and absences in other directions where the wave interference is destructive.

However, elastic scattering can occur to higher angles (> 100 mrad) and at these higher angles, the energy transfer is still small, and still beyond the ability to detect in a conventional EEL spectrometer, but it now results in a shift in the electron wavelength that is enough to destroy coherence [164, 175, 184, 185]. For this reason, diffraction becomes much weaker at these higher angles due to the loss of coherence. For this reason HAADF images are mostly incoherent.

3.4.1. Structural characterisation – Electron Diffraction

There are three ways of recording the diffraction pattern in transmission electron microscope. Usually diffraction patterns are taken using the selected area technique, and it is called SAED – Selected Area Electron Diffraction. The optics of this technique is presented in the **Figure 21**, where the left part represents the SAED technique, and right part represents the classic imaging technique. As it can be seen, the SAED requires inserting SAED aperture, which is few cm below the specimen, and limiting the focused image of objective lens. It is then magnified by the intermediate lens and projector lens, resulting in a diffraction pattern from selected area. It gives local information such as crystallographic lattice parameters of the unit cells of the phase currently investigated. The minimal diameter of area investigated during diffraction in that case is around 1µm. There is also a second way of obtaining diffraction pattern, so called nanodiffraction – CBED

Convergent Beam Electron Diffraction. The diameter area which is diffracted in that case depends on the minimal size of the spot (i.e. the type of the electron source), and it is less than 80nm [164] (in case of the ARM it can be close to 1 nm). Phenomenon of diffraction SAED is used to characterize the crystallographic structure of materials, whereas the CBED technique was not part of this research, so any further reading is recommended in any classic microscopy literature.

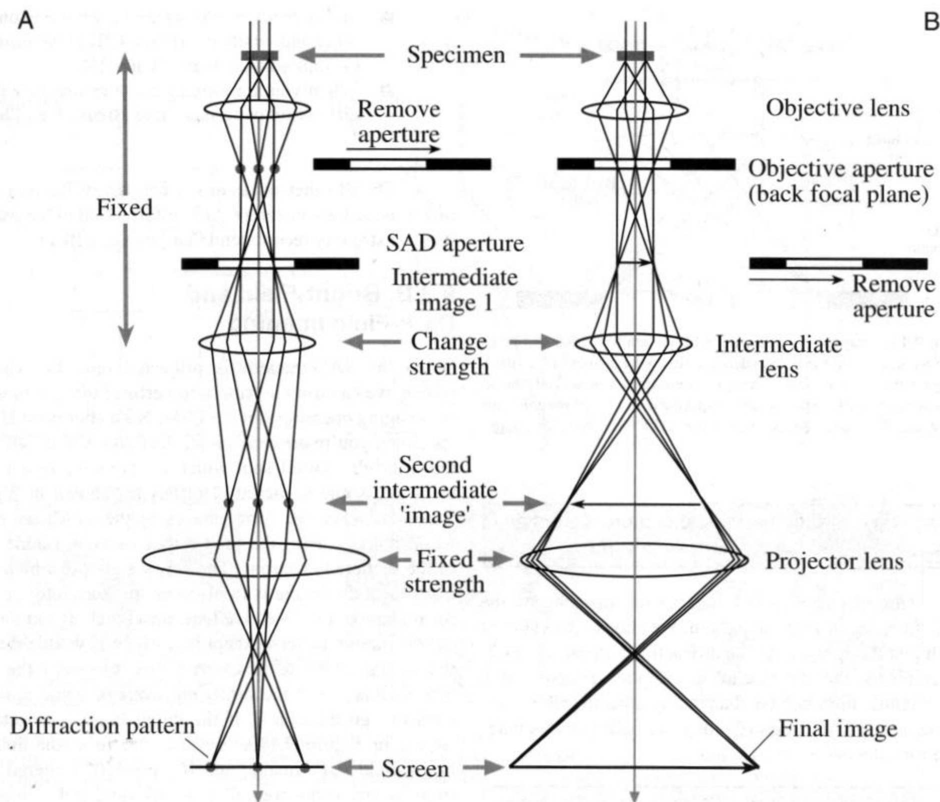

Figure 21.The two basic operations of TEM imaging system showing a)diffraction pattern on the viewing screen, b)classic imaging . In each case the intermediate lens selects either the back focal plane or the image plane of the objective lens as its object. Republished with permission of D. B. Williams and C. B. Carter , from *Transmission Electron Microscopy*. 2009, New York: Springer; permission conveyed through Copyright Clearance Center, Inc. [164]

The specimen is an ordered array of atoms forming planes, which are separated by interplannar distance d_{hkl}. Each wave of electron *K* creates after interaction with matter (the array of atoms) at least two rays. The incoming plane electron wave interacts with the atoms, and secondary waves are generated which interfere with each other. This occurs either constructively (reinforcement at certain scattering angles generating diffracted beams) or destructively (extinguishing of beams) . One is transmitted vector *k*, and next ones are scattered *k'* vector. The *k'* wave vector scattered under specific Bragg angle equals to *2*θ as shown in the **Figure 22**. Then electrons transmitted through specimen in TEM forms two types of beams – direct beam, which is so called 'central spot' (k wave vector) and several diffracted beams (*k'* wave vector), which together

forms diffraction pattern. The transmitted beam is used to create bright field image, and every scattered spot forms dark field image. The formation of diffraction patterns is based on Bragg law, and reciprocal lattice idea, which is a geometrical description of diffraction.

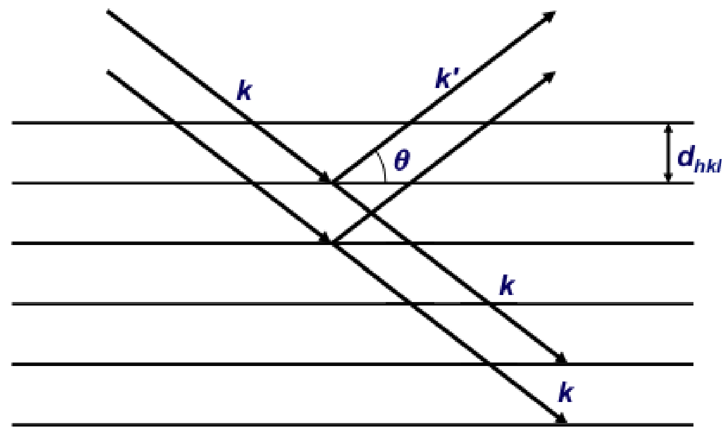

Figure 22. The scattering of the rays on the crystallographic planes together with the Bragg angle.

The Bragg angle θ needs to be specified because scattered electrons have the same wave phase. This compatibility will take place when the difference between two ray paths – transmitted and diffracted – is equal to an integer multiple of wavelengths λ. Hence there is a formed Bragg's law:

$$\mathbf{n}\boldsymbol{\lambda} = \mathbf{2d}_{\boldsymbol{hkl}}\mathbf{sin\theta} \tag{13}$$

This equation determines how many scattered beams will be visible after transmission of incident beam, because every crystallographic plane with *hkl* indices which fulfil the Bragg equation will produce one diffracted spot on diffraction pattern. The *hkl* are Miller indices, that form family of orthogonal planes, which are connected by lattice vectors (vectors that indicates the smallest unit cell of the analysed phase) by equation $hr_1+kr_2+lr_3=g_{hkl}$. G_{hkl} is the reciprocal lattice vector, which represents the interplanar distance d_{hkl} as reversed length of this vector. This shows how the real lattice is connected with the reciprocal lattice formed by electron and observed by user, therefore it gives formulas allow to analyse the crystallography of the phases.

In general, recorded diffraction patterns show spots from transmitted and diffracted beams. The arrangement of spots is closely related to the orientation of diffracted planes. The vectors $\boldsymbol{r_1}$, $\boldsymbol{r_2}$ and $\boldsymbol{r_3}$ which depict the distance between central spot and any other diffracted spot, are perpendicular to those planes. The real distance between these planes, so called interplannar distance d_{hkl} is inversely proportional to the measured distance on diffraction pattern.

The example of diffraction patterns are presented in the **Figure 23.** The left diffraction pattern is from vanadium steel observed under (111) axis and the right one is observed on (110) axis. Both of them have been indexed using method described above. The main spot (direct beam) is in

the middle of each pattern, which started from defining which distance is r_1, r_2, and r_3 (the example of the vectors are draw in left diffraction pattern, and they match non-stoichiometric VC phase). It is a simple measurement of the distance between the middle spot and all surrounding spots, and comparison of the values with the vector length with the library of values for each phase. Therefore it is necessary to estimate what phase is analysed at that particular time. In case of this specimen the distances were chosen to match non-stoichiometric VC, Fe_3O_4, and austenite. The preliminary results gives hope for evaluation of the lattice parameters of each type of precipitate, however there have been too many differences between literature values of the each lattice vectors, that the results were not obvious. Later research proved that actually the amount of precipitates is so small in comparison to the matrix and surface oxide that what was taken to be precipitate is actually surface oxide. Therefore diffraction pattern was not a technique which was used in this research. More diffraction results are described in **section 5.3** with all other microstructural analysis of the steel specimens.

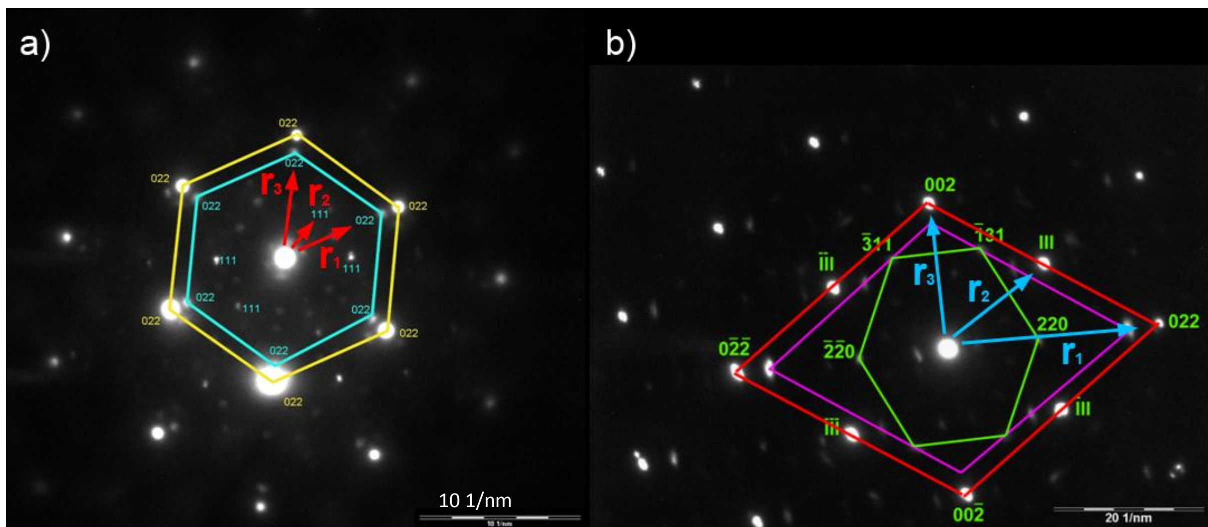

Figure 23. Two diffraction patterns obtained from V-steel. a) shows the DP taken on 111 zone axis, with the indexing of austenite (yellow) and probably precipitates (green) b) shows the DP taken on 110 zone axis with indexing of austenite (red), and green and violet being the patterns from Fe_3O_4 which is an oxide formed on the surface, dominating the whole signal from precipitates. The distances r_1, r_2, and r_3 which are used for indexing are presented on both; red arrows for precipitate, blue arrows for austenite.

3.4.1.1. Diffraction Pattern indexing

The indexing of diffraction patterns is an important step in gathering information about phases present in an analyzed area. To index the pattern the 2θ angle of diffraction of electrons has to be known, also the distance of indexed spot from the centre spot, and camera length which is the effective distance between a specimen and a detector recording the diffraction pattern, L. The distance is described by the equation

$$\mathbf{r = Ltan2\theta} \,. \qquad 14)$$

Because the diffraction angles are very small in transmission electron microscope studies, the following approximation can be used (from trigonometry)

$$\mathbf{tan2\theta = 2sin\theta} \qquad 15)$$

and by implementing above equations to Bragg's law and the *r* distance is obtained (n=1 for the first plane) in form of:

$$\mathbf{r = L2sin\theta = L\frac{n\lambda}{d_{\mathit{hkl}}} = \frac{L\lambda}{d_{\mathit{hkl}}}} \qquad 16)$$

The product $L\lambda = C$ is constant for microscope, for the same conditions during acquisition (accelerating voltage for example), and it can be easily determined by reference sample of well known crystallographic structure. When *C* and *r* are known, there is an easy way to calculate *d*, the real interplannar spacing. This gives the answer which plane diffracts the electron beam.

3.4.2. TEM Diffraction contrast imaging - Bright Field and Dark Field

The general condition for the formation of images in transmission electron microscopy is to have the specimen thin enough for the electron to be transmitted through with one or just a few scattering events. The transmitted electrons create a magnified image of transmitted area, which is called bright field image (BF) by arrangement of lenses in TEM, or by special main detectors in STEM.

The electron beam travelling along the microscopy axis is transmitting through the specimen, where some small fraction of it is diffracted on crystallographic features (precipitates, grain boundaries, etc.) and the image is formed only by the direct beam. The objective aperture is placed in the back focal plane which allow only the direct beam to pass, and the electrons, that are scattered above a small angle are blocked by the objective aperture. The electrons, which are allowed to pass through the aperture are forming the beam by the post-specimen lenses and form an image of specimen on the imaging device (screen or camera).

A dark field image is formed by one of the diffracted electron beams passing through the objective aperture instead of the direct beam. In reality, there are two methods to form a DF image, either displacing the aperture, or tilting the sample illumination, and only the latter does not introduce additional aberrations. The beam is tilted using coils before the objective lens by an angle 2θ, where θ is the Bragg angle, so that the desired diffracted beam leaves the specimen along the optic axis of the microscope.

In crystalline materials, like the one used in this thesis, the contrast in BF and DF mainly is caused by diffraction, hence it is called diffraction contrast. In BF, the areas that diffract strongly appear dark in the image, and the rest appears as bright (including any holes in the specimen). In DF, the areas diffracting strongly into the chosen diffraction spot are bright, and all other areas (including holes) are dark. To make the contrast stronger it is necessary to use a smaller aperture,

hence more scattered electrons will be cut off. But it is worth mentioning that changing the aperture for smaller diameter reduces the total intensity of image, and also reduces the image's spatial resolution. Diffraction contrast reveals such elements of structure like dislocations, grain boundaries, stacking faults, strain field or precipitates.

3.4.3. Quasi-elastic scattering – HAADF imaging

Generally speaking, the formation of bright-field and dark-field TEM/STEM images normally obeys the principle of the monotonic increase of cross sections $\sigma(Z)$ for thermal diffuse, elastic, and inelastic scatterings. For instance, the high-angle scattered electrons in HAADF measurements are predominantly those electrons which have undergone thermal scattering. Therefore, if there are no diffraction effects, darker (lighter) contrasts in bright-field (dark-field) images [186], respectively, are associated with heavier elements. So it can be said that the high-angle annular-dark-field (HAADF) signal is mainly generated by quasi-elastic scattering. The HAADF images are formed by electrons scattered at high angles and are collected by annular detector. The collected signal intensity depends on the atomic number of the scattering atoms[187], its amplitude of vibration and the total number of atoms encountered by the probe. This imaging mode can reveal high-Z sensitivity and eliminate most of the diffraction contrast present in low-angle ADF images. In a STEM instrument, secondary electron images with a resolution approaching the probe size (~0.5nm in diameter) can be obtained simultaneously with HAADF images. During this research the HAADF image was used for choosing the area of interest for simultaneous EELS signal acquisition.

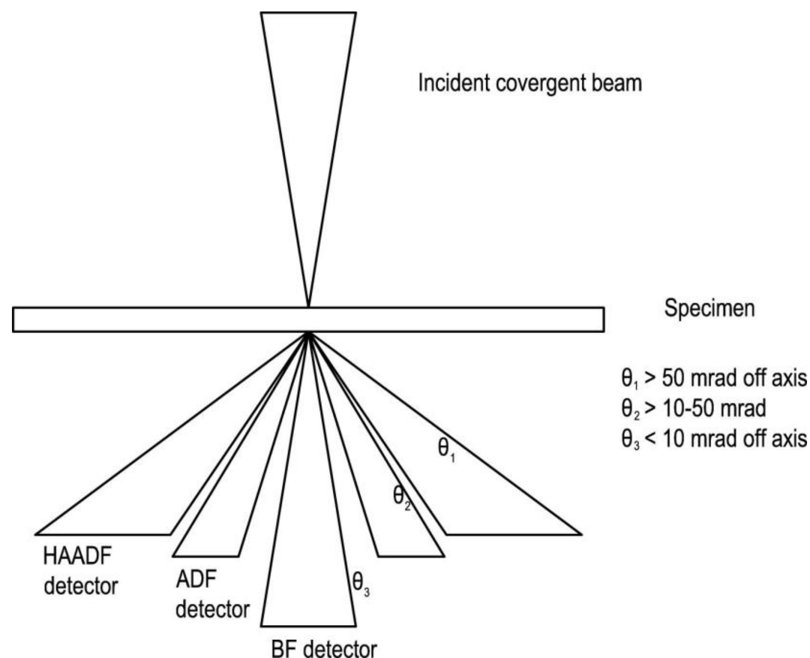

Figure 24. STEM BF, ADF and HAADF detectors and their annular ranges. The conventional ADF and BF detectors are shown as well as the HAADF detector set-up for Z- contrast imaging, together with the range of electron scattering angles for each detector.

Figure 24 shows the scheme of position of detectors in STEM regarding the scattering angle. In the middle, where the mostly forward scattered electrons are transmitted, the BF detector is placed, or any other post column detector such as GIF or EEL spectrometer. The electrons which forms these images are scattered at θ_3 less than 10mrad. The ADF detector is placed between BF detectors and HAADF detector, and the electrons that forms these images are scattered at the angles θ_2 which is in between 10 and 50mrad. All electrons, which are scattered at the angles higher than 50mrad are taking part in forming images in HAADF detectors, which are placed farthest off-axis.

In general, HAADF is one of the most often imaging techniques used in STEM nowadays. Images acquired with this method are easier to analyse than classic high resolution TEM images, because of the Z-contrast, which generally indicates the atoms columns free from diffraction contrast.

3.4.4. Inelastic scattering

Inelastic scattering as opposed to elastic scattering results in the loss of some significant amount of electron energy during transmission of the specimen, and there are a number of processes for this. Inelastic scattering is always incoherent. In reality, inelastic scattering gives a lot of chemical information about the sample, because of the atom-specific nature of interactions between the electron and specimen.

There are different electrons in the solid that can interact with the electron beam. For example, there are electrons which are strongly bound (close to the core of atom) and those which are lightly bound, for example valence electrons. If the electron interacts with lightly bound electrons, or with the phonons, the energy transfer is small. Together with the electrons which traverse through the specimen without any interactions, they create a low loss region in the EEL spectrum. The electrons which did not lose any energy form the zero loss peak (ZLP), which is the most intense part of the EEL spectrum.

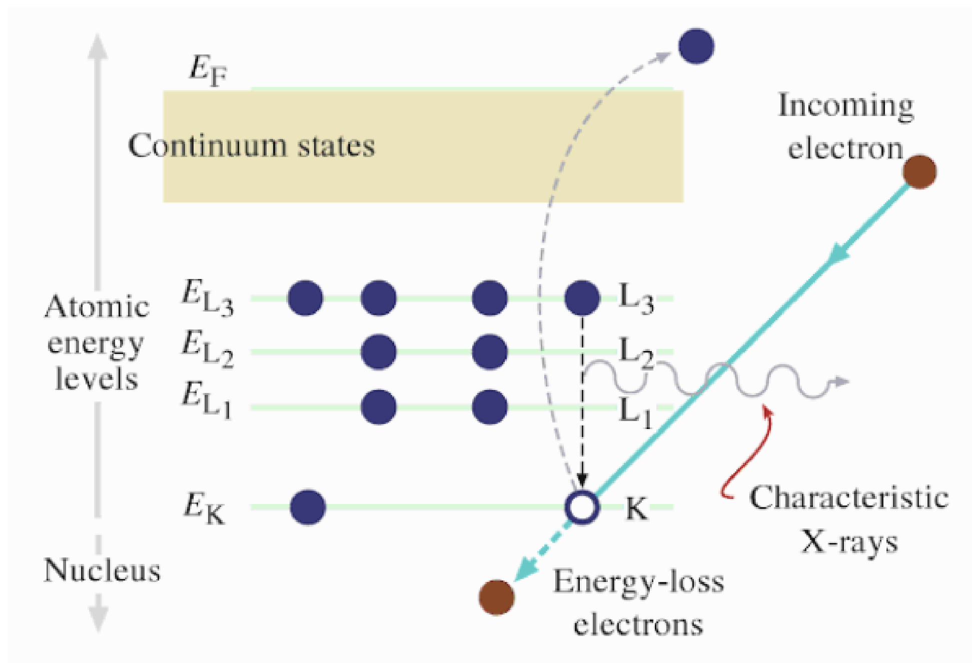

Figure 25. The ionization process. An inner (K) shell electron is ejected from the atom by a high energy electron. When the hole in the K shell is filled by an electron from the L shell, characteristic X-ray emission occurs. The beam electron loses energy but continues on through the specimen. [164] Republished with permission of D. B. Williams and C. B. Carter , from *Transmission Electron Microscopy*. 2009, New York: Springer; permission conveyed through Copyright Clearance Center, Inc.

If the incoming electron interacts with and promotes one of the strongly bound electrons, they lose larger amounts of their energy. The detection of electrons which loses energy is highly important in EEL spectroscopy. The most important signal is generated by interactions with inner-shell electrons, whose energies are specific to each element, they carry chemical information, and hence their detection gives the answers about chemical composition of the excited atoms. Unfortunately because of the smaller cross-section of these interactions their intensity above the continuum scattering background is much smaller, but they are still easily recognised and used in analysis, especially in thinner specimens.

The excited atom tends to relax back to the ground state as soon as possible. The excitation occurs when the electronic structure of an atom is changed by ejecting an electron from an inner shell by an inelastic interaction with an incident high-energy electron. The relaxation is a process during which an electron in a higher energy state will fill the gap in the inner shell. The effect which usually accompanies the relaxation process is emission of radiation. This could be an X-ray, or it could be a cascade of electrons from various closely spaced energy levels leading to emissions in the UV or visible, which is often called cathodoluminescence. In some cases, the energy can be transferred to another electron in the atom which leaves with a specific energy as an Auger electron.

X-rays are commonly also used in elemental analysis in the TEM or STEM, usually using Energy Dispersive analysis – EDX, but sometimes also Wavelength Dispersive analysis – WDX [185].

The EDX and EELS are signals from the same phenomenon but the signal which is recorded is different. The whole ionization process is depicted in the **Figure 25**. The ionization starts when the electron is ejected from a inner shell (in case of this figure it is K shell). It is directly followed by relaxation process, which is the movement of the outer shell electron to a K shell. The filled hole is accompanied by the emission of specific radiation, which is linked to the type of atom, from which the electron was ejected. During the beam electron interaction with inner atom electrons the beam loses some portion of the energy, and magnitude of this loss is related to the type of the electron shell and atom. This phenomenon is recorded as a small peak of the intensity above the continuous background. Meanwhile, some of the electrons knocked out of the energy levels in the primary inelastic interaction leave the sample with small amounts of energy (typically a few 10s of eV) as secondary electrons, which are commonly used for imaging in scanning electron microscopes [185].

3.4.4.1.Electron Energy Loss Spectroscopy - EELS

The Electron Energy Loss spectrum is formed by inelastic scattering. The inelastic scattering means there is a loss in energy of electrons, and change in momentum after interaction. Therefore the design of the spectrometer needs to consider different angles of scattering of electrons coming through the specimen, although for lower losses the scattering angles are relatively small (just a few mrad). The number of scattering events is very important, because it can change the information carried by electrons, hence the preparation of samples is very important. The main goal is to obtain a flat, very thin specimen without curtaining effects (differences in thickness in stripes from the ion-beam preparation). The inelastic scattering can occur repeatedly, which can blur the final results, due to: phonons and plasmon excitation, inter-intra- band transitions, and inner-shell ionization.

The spectrum image, or electron energy loss spectrum, which is recorded by specially designed spectrometer (during analysis the Gatan QuantumER spectrometer was used) carry information like the elemental composition and chemical bonding of the specimen, as well as other features including the electronic structure of the specimen. The **Figure 26** presents the Gatan QuantumER spectrometer with electronic fast shutter, which allows acquisition of DualEELS, which is simultaneous record of low loss and core loss regions with separation up to 2keV. It is a new generation post-column spectrometer which is equipped with gradient magnetic prism, which usually is excited by two electric coils of a polepiece shape. The drift tube, which is placed inside the magnet is connected to a microscope vacuum system. This drift tube is used for offsetting the spectrum by a certain amount of voltages, by applying the desired shift to a current coils polepieces,

so the kinetic of the electrons is altered. As a consequence the electron energy loss spectrum is shifted on the detector (Usually CCD camera).

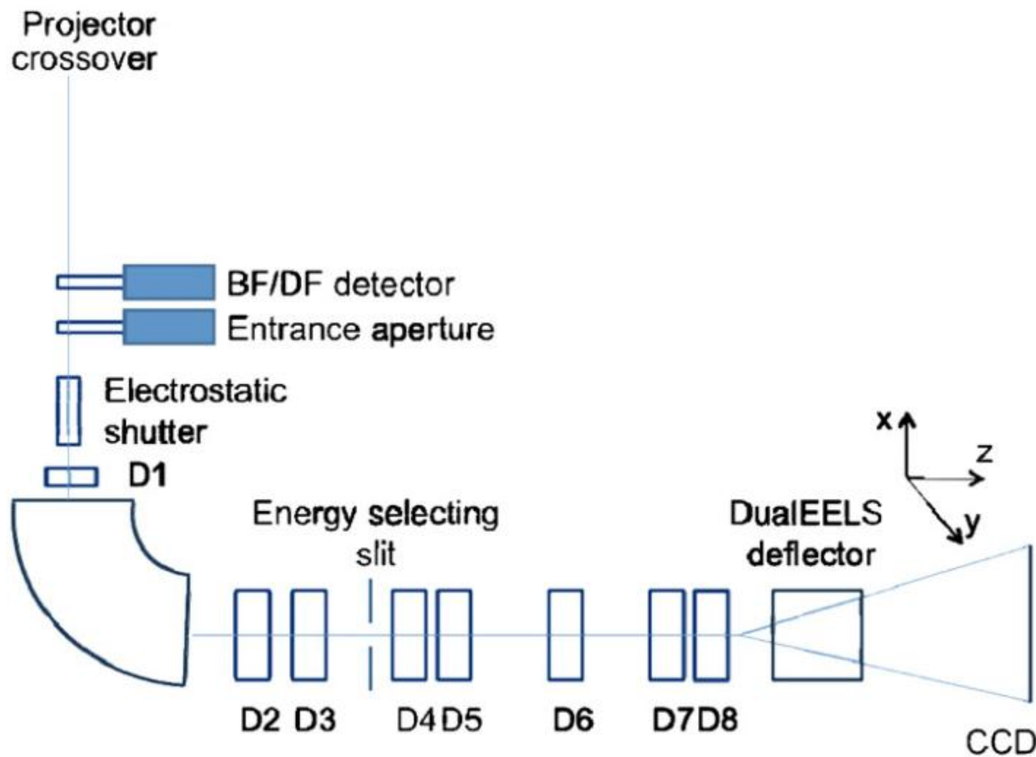

Figure 26. Schematic layout of GIF Quantum showing the location of key components [188]. Republished with permission of A Gubbens, from *The GIF Quantum, a next generation post-column imaging energy filter.* Ultramicroscopy, 2010. 110(8): p. 962-970; permission conveyed through Copyright Clearance Center, Inc.

The principle rule of spectrometer is to bend the electrons through a 90° angle with the 75 mm radius, which allow the dispersion to be reduced in comparison to other spectrometers and by the Lorentz force bend the electrons of different energy (velocity) to emerge from the spectrometer at different angles. After the electrons pass the drift tube, they undergo focusing and aberration corrections by eight dodecapoles assembly and finally are recorded using multi-element detector to record the whole spectrum at the same time. In case of the ARM microscope it is equipped with high resolution CCD camera (UltraScan). Additionally the QuantumER is equipped in fast electronic shutter prior the magnetic prism which deflect the beam into the trap. The resulting spectrum is a separately recorded spectrum of low loss and core loss in separated opposite halves of CCD camera with the independent time ratios.

The main limiting resolution factors of this spectrum are the energy spread of the electron source, energy resolution of the spectrometer and the camera. However, there are other factors which characterise the quality of the spectrum, such as spectrometer dispersion which is the vertical displacement of the electron beam per unit change in electron energy and it is typically a few

micrometres per eV at the exit of the magnet. Because the ARM is a Cs-corrected microscope, the to the acceptance angle of the spectrometer, is much smaller than the collection angle of the microscope. Therefore, using the aperture 5mm is enough to collect whole necessary signal for good quality spectrum with high signal to noise and signal to background signal. The collecting aperture limits the collection angle for the spectrometer.

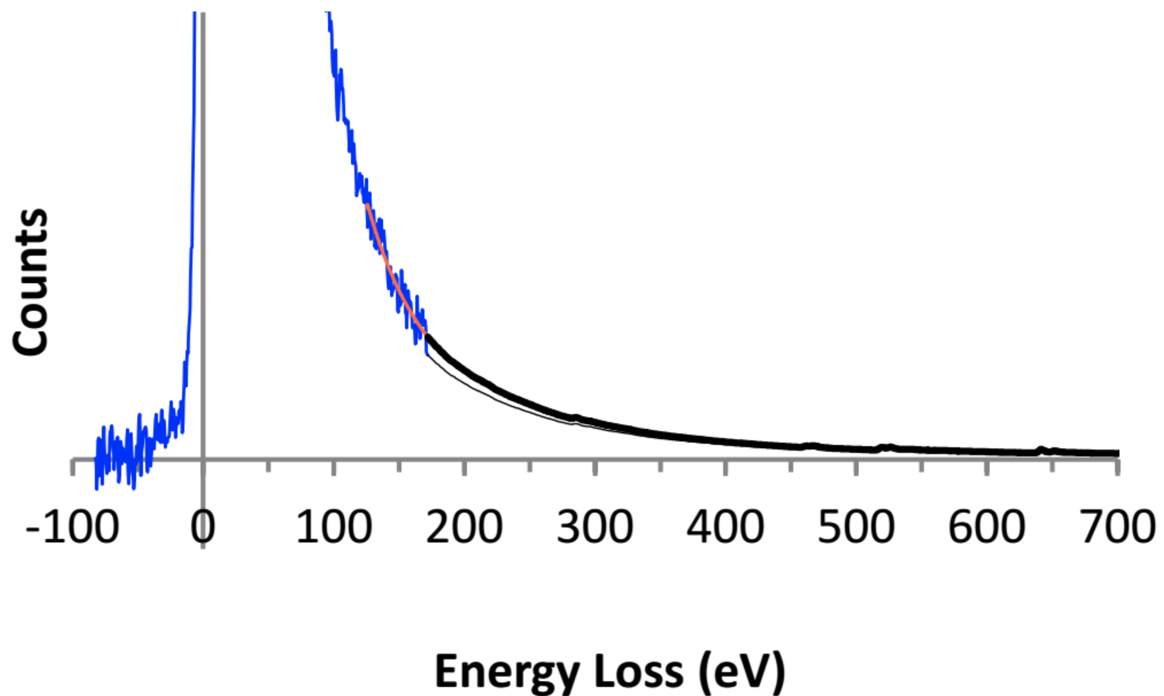

Figure 27. Schematic spectrum of the electron energy loss. Contains the ZLP, two plasmon peaks, and spliced core loss. The splice point is around 170eV loss (visible step change at that region in blue graph). This spectrum is from the vanadium precipitate, where C-K edge is visible at 280eV, Ti L-edge is visible at 450eV, Vanadium L-edge visible at 513eV followed by oxygen K-edge is slightly visible (525eV loss),and manganese edge (640eV loss). The spectrum shows the splice problem, which is described in chapter 7.

Figure 27 represents the schematic example of the energy loss spectrum of one of the specimen used in this thesis. It can be divided into two groups – up to 50eV loss energy, called the low-loss spectrum including the zero loss peak, plasmons peaks, and the high-loss spectrum, which is above 50eV loss energy. The low loss region means that the energy portion which is lost during the interactions is close to zero, or very little. The zero loss peak is the transmitted electron beam with no energy loss, or so small that it is impossible to detect. Usually the energy loss from phonon excitations is so small, that it is inseparable from zero loss peak in most microscopes without monochromators. Those electrons which are forward scattered usually do not have wide range of angles, they are found around the optic axis, i.e. the central spot on the diffraction pattern. It is important to mention, that the diffracted peaks usually do not go into spectrometer, because the angles are too high.

The low loss energy spectrum is generated by plasmon excitations, inter or intra-band transitions. Plasmons are collective oscillations of weakly bound electrons. The electrons responsible for these oscillations are free electrons, therefore in metals a peak corresponding to plasmon excitations is obvious, but similar peaks appear in almost all materials, even these who do not have free electrons, like polymers. The peak generated by plasmons is usually second strongest peak in EELS spectrum, and it is located just after the zero loss peak (often 10-25 eV). The intensity of this peak is affected by the thickness of sample, therefore the number of free electrons, and the probability of the scattering event taking place. Moreover if the sample is thicker there is usually more than just one peak of plasmon interaction (i.e. a weaker two-plasmon peak, and maybe higher orders in thick specimens).

If the electron within an outer energy band in a solid is promoted into a higher vacant band it can be said that it is inter- or/and intra band transition, otherwise called "single electron interaction". This is common in semiconductors or insulators with band gaps. The energies involved are typical hundreds of meV or a few eV.

The interactions with orbitals closer to atom core require more energy, because the bonding is much stronger. Therefore the energy loss of the electron which has excited the electron on inner-shells of atom to unoccupied states above the Fermi level is higher. Hence the electron transmitted through the sample loses more energy, and creates an absorption edge in the high loss spectrum starting at the binding energy of that inner shell electron. This feature of the spectrum is related directly to the identity of the atoms in the specimen, therefore to the chemical composition. The ionisation edge intensity in spectrum is much smaller than the plasmon peaks mentioned above [64, 185]. Energy loss in high loss region starts from about 50eV to several thousand eV. The character of this excitation reflects the chemical character of the specimen, therefore the core loss is used for quantitative and qualitative studies. The consequence of this excitation is sharp increase in intensity in the spectrum at the energy, which corresponds to the energy necessary to perform this excitation, and is determined by binding energy, and it is called ionization edge. This ionizatin edge is a characteristic value for each chemical element and it is different for every electron-shell from which the electron excite in the atom. While choosing a window 50eV wide, which includes the ionization edge and few eV range former to the edge, the elemental map is created, that represents the distribution of the element of which the electron got excited.

The edge appears as a result of electrons promoted from a specific core state into the lowest empty states in the solid. So details of the absolute energy of the edge, and its shape depends on the details of the unoccupied energy bands above the Fermi level. This is called the unoccupied density of states (DOS). This may depend on oxidation state, on the crystal structure, on the atoms

surrounding the atom being probed. by the technique Electron Loss Near-Edge Structures (ELNES) the electronic structure can be revealed, by investigation of unoccupied local density of states, and the nearest neighbours of each atom. Each of the array of atoms has different density of states, thus energy loss near edge structure is a sensitive probe of bonding and chemical details. ELNES can give a direct insight of the associated electronic structure and atomic bonding in the solid, like determination of local coordination, or valence states of atomic species. This is because, in solids, the unoccupied electronic states just above the Fermi level can be significantly modified by the chemical bonding between neighbouring atoms leading to a complex but specific density of states (DOS) which will be reflected by the ELNES as spectral fingerprint. The ejected electrons at each specific energy, which do not occupy the empty state becomes a electron characterised by a wavelength that will interfere with reflections from surrounding atoms. In some cases, the wavelength will be constructive and peaks will arise. At other energies, the interference will be destructive and emission at such energies will be weakened. So the EEL intensity 50eV above an edge will be modulated to some degree due to these interference effects [164].

The near-edge region is followed by a region of these extended weaker modulations. Together with the decreasing background signal, this core loss feature is known as extended energy loss fine structure (EXELFS). The details of the oscillations may be used to probe the coordination of a particular atom, and for the investigation of the specific bond lengths, for the first few nearest neighbours. On the other hand, the low loss spectrum can, in principle, be used to determine local structure. Because the energy of these electrons is higher than those for multiple ELNSES, the EXELFS are considered to be single scattering event. Unfortunately, the more salient point is that it makes the background problematic for the next edge.

The different interactions can be detected by EXELFS technique, so is the specific bond lengths to be investigated, for the first few nearest neighbours.

In STEM microscope apart from elemental maps, the EELS can be used to produce so called spectrum imaging (SI). It is a technique which acquire an energy loss spectrum at each pixel as the STEM probe is scanning over the chosen area of the specimen. While spectrum imaging is acquired a three-dimensional data array is created which corresponds to electron intensity within a three-dimensional volume of (x,y,E) space [189], **Figure 28** shows a schematic diagram of the three-dimensional data array. Because spectrum image is formed by inelastically scattered electrons some other detectors might be incorporated into the microscope, for example it is possible to record a wide range of data at each pixel simultaneously, like electron dispersive x-ray and HAADF. Such combination of techniques was used all the time during this Ph.D., where all spectra were supported by HAADF imaging. Such combination allowed better understanding of impact of drift or

contamination overbuild in further analysis of the data. The drift which occurs quite often during acquisition is a distortion of the image resulting from movement of the stage, or specimen within the holder. It is minimised by drift correction, which is a short exposure time acquisition area, which is reacquired every 10 line (in case of this research. If necessary it might be more or less lines) of the spectrum. The comparison of former image and reacquired image the level and direction of movement is estimated and correction of the drift is applied to the original image. This may extend the acquisition time, so it is very important to minimise the movement of the stage prior to study, for example, by letting the specimen to steady the holder after moving to desired area. Also using the innovative equipment is helpful, for example Gatan Quantum spectrometer is very useful, because it allows fast parallel recording, which can record even a 1000 spectra per second. With such efficiency the decent size spectrum image can be recorded in just a few minutes even with the drift correction.

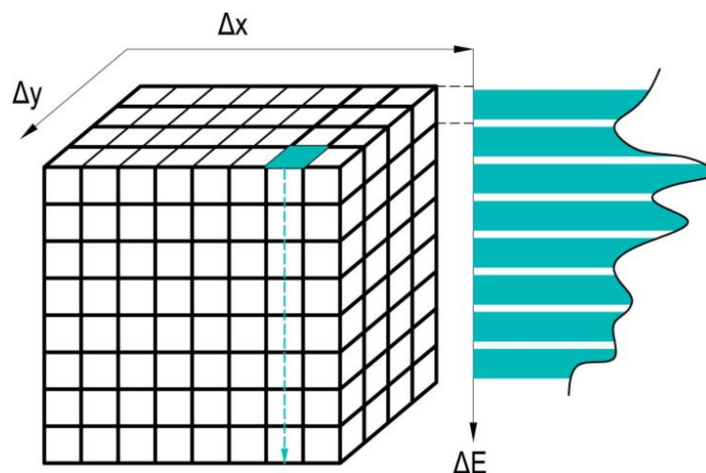

Figure 28. *A* schematic diagram of spectrum imaging technique, which can be used for quantitative analysis.

3.4.4.2.Electron Energy Loss Spectroscopy - DualEELS mode

In the **section 3.4.4.1** a single EELS technique is described. In recent years a modification in mode acquisition was made called DualEELS. DualEELS is a system for EELS which allows the low loss and core loss region of the spectrum to be recorded at each pixel of a spectrum image (SI) separately [133, 190]. The DualEELS recording is only possible because the fast beam switch, called recently fast shutter, was incorporated into spectrometer builds [133, 191] allowing overcome the limited dynamic range of the CCD detectors, and record the low loss and core loss separately, with individual time ratios. The fast shutter with a microsecond response time allows rapid deflection of the beam resulting in wide range of the exposures times necessary for energy range for both core loss and low loss. As a consequence, a core loss spectrum at each pixel can be recorded after a low loss spectrum with the same electron optical conditions, but in different area of the CCD detector. This

pixel correlation provides two spectra which can be spliced at one point, so that the core loss will contain the information about zero loss intensity (ZLP). The ZLP is used for normalisation of the core edge intensities allowing absolute quantification [192]. When the core loss contains the ZLP it is possible to apply Fourier logarithmic deconvolution [193], which gives the single scattering distribution of all core loss edges. Such processing allows the determination of local thickness in terms of the inelastic mean free path (λ) [194] in the chapter 3.4.1 which describes Poisson's Law of inelastic scattering. This is one of the most important advantages over classic EELS, that the data can be processed for absolute quantification preserving the all two-dimensional results such as elemental mapping distribution. Nowadays, the microscopes with aberration correctors allow sub-Angstrom probe size, resulting in atomic resolution in elemental maps supported by HAADF imaging, like in case of ARM microscope used during this thesis. The unquestionable advantage of DualEELS over for example EFTEM is high spatial resolution, wich does not require selection of an energy loss windows. Therefore the DualEELS is one of the most powerful techniques leading to an absolute quantification of elements in the specimen.

The DualEELS acquisition mode is only used in this thesis, as the processing of the data acquired with this mode is extensively studied. In chapters 6 and 7 the whole idea behind this thesis is described based on examples of acquired data from high manganese steel with fully embedded precipitates and processed up to the total quantification. It is considered an extraneous success to quantify precipitates of such small size (down to few nm) with division on all elements metal, and non-metal.

A key requirement in choosing the acquisition conditions for recording the DualEELS SIs is that the two spectra can be spliced accurately. For this, there must be sufficient channels on the energy gain side of the low loss spectrum to verify that the stray scattering is sufficiently low (for more details please see chapter 6). The energy offset of the core loss must be chosen so that the low loss spectrum has sufficient intensity in the overlap region with the core loss spectrum. Ideally, this overlap region should be featureless so that a smooth function can be fitted to the low-loss spectrum prior to splicing, as described in [195]. Finally, criterion determines the exposure times for the two spectra.

The DualEELS technique and post-processing of its data allows improved quantitative characterisation via the separation of the precipitate signal from the matrix signal (details to be published separately). In this thesis, the concentration is on the application of DualEELS to the quantitative analysis of nanoscale carbides in V and Nb microalloyed high Mn steels. The whole post-processing steps and absolute quantification is described in chapters 6,7, and 8.EEL Spectroscopy allows qualitative analysis of chemical content and quantitative analysis of chemical

concentration of elements. To perform the quantification using acquired spectra, the spectra have to be single-scattered, the edges have to be integrated and the partial cross-section has to be known. The edges chosen for that purpose are then extracted from the background by background extrapolation from before the edge threshold. The extrapolated background shape, which is described as AE^{-r} function is then subtracted, resulting in integrated edge signal. The AE^{-r} which is called power law function is used, because it fits the background shape, living the smallest possible error in under subtraction or over subtraction of the real signal. The extrapolated edge intensity has to be integrated, which means that the edge signal has to be limited from the threshold of the edge up to some point after the edge which contains all the information (structures) from particular element. The integrated edge intensity is then linked with the total intensity (ZLP) taken from low loss region and deconvolved with Fourier deconvolution procedure resulting in single-scattering spectra . Single-scattering spectra can be linked with thickness, and mean free path which allows determination of the number density of atoms by equation $\mathrm{I_k = I_0 N \sigma}$ (see description on page 147). The number density of atoms is a normalized signal, which is divided by a partial cross section, but also to determine the number density of atoms the thickness is required. So, to be able to quantify the specimen in absolute manner the partial cross section is necessary.

The partial cross sections can be estimated by using a theoretical approach or by experimental determination based on comparison of spectra with known standards. In case of the experimental approach the determination of the thickness of specimen and the standard has to be known, which is a serious limitation. However, the partial cross section can be precisely calculated if I_0 is known, which is possible thanks to the DualEELS system, because only then the zero loss peak (I_0) can be implemented into the core loss region, resulting in single scattering event spectrum It is possible because the I_0 is necessary for removal of plural scattering in core-loss region, which makes the quantification accurate and reliable, because the determination of the thickness is more or less straightforward. If there is an error during calculations of the partial cross-sections, the differences in the final qualitative values can be close to 20-30%, which in case of few atoms, is unacceptable error. There are other methods of quantitative analysis, which can replace case with lack of the inelastic scattering-cross sections, and they are called relative quantification, because mostly it is based on the ratios between different specimen. If the standard EELS is used, and there is no chance for normalization of the edge signal with the ZLP intensity based on the [164][164][3][164][166] *k*-factor method, which is a sensitivity factor characteristic for any study and standard specimen. All of these is widely explained in chapter 7.1.

EELS is a potentially powerful technique, which gives information about several characteristics in the specimen. Not only the quantitative and qualitative information can be

extracted but also very detailed fine structures related to the electron-atom and electron-electron interactions dependently which technique is used - ELNES or EXELFS, but both of them quite extensively represents the quantum nature within the specimen long after the beam interaction occurs.

3.4.4.3.Energy Filtered imaging - EFTEM

Energy Filtered TEM is a technique used in conventional TEM, which takes its principles from EEL Spectroscopy. With use of the mechanical slit it filters the part of the spectrum formed by the electrons transmitted through the specimen and allows only particular energy range electrons to contribute for images or diffraction patterns. The energy slit can be used according to edges of energy loss, resulting in the information about the specimen elemental composition. EFTEM is very useful technique for microanalysis with relevant special resolution, because it provides quick qualitative and quantitative elemental maps from wide range of areas. The limitation for EFTEM is spatial drift, background noise, elastic scattering, and also the quality of the camera used. These values are mostly in contrary, because if the image suppose to have better spatial resolution, the longer exposure time is required. As a consequence, the drift is more visible which is the reason for limited resolution. In reality it is possible to obtain 1nm resolution by precise choice of apertures and good cameras. Moreover the quality of obtained elemental map is strongly dependent on thickness and quality of the prepared sample. It is due to the fact that thickness variations results in differences in signal in the spectrum, thus in differences in the filtered image. Because the EFTEM imaging is formed by amount of electrons, which lost the same portion of energy, and in case of thickness variations, there is also a amount of electron variations. As a result, the image shows some areas which may be different in chemical composition, whereas in reality it is the same phase, only thicker. Moreover, if the additional diffraction contrast is provided, the real chemical composition is unclear. In more detailed analysis , the choice of energy slit, the exposure time, settings of focus and intensity of incident beam are some of the factors, which can affect the quality of the EFTEM image [164].

The background removal is necessary post processing operation, which provides a material analysis. To estimate the background under the investigated edge usually three images are required. It is called three-window method, and it consists of two pre-edge windows and one post-edge window. The choice of characteristic features of these windows, such as width, beginning of eV, position of window, can affect the quality of the created image as well. If the energy slit will be too big, the signal-to-noise ratio will be better, but the estimation of background fit will be much more difficult. Also the window from pre-edge and post-edge can overlap and give negative counts, resulting in unreal data.

Because there are a lot of pitfalls, it is common to obtain several series of data at the same area, thus the combination of quality and beam condition is also necessary to be taken into account, to avoid specimen damage. However it is very useful technique, because it allows quick elemental map collection with good detection (less than 1% in reasonably thin samples) and resolution approximately 1nm [164].

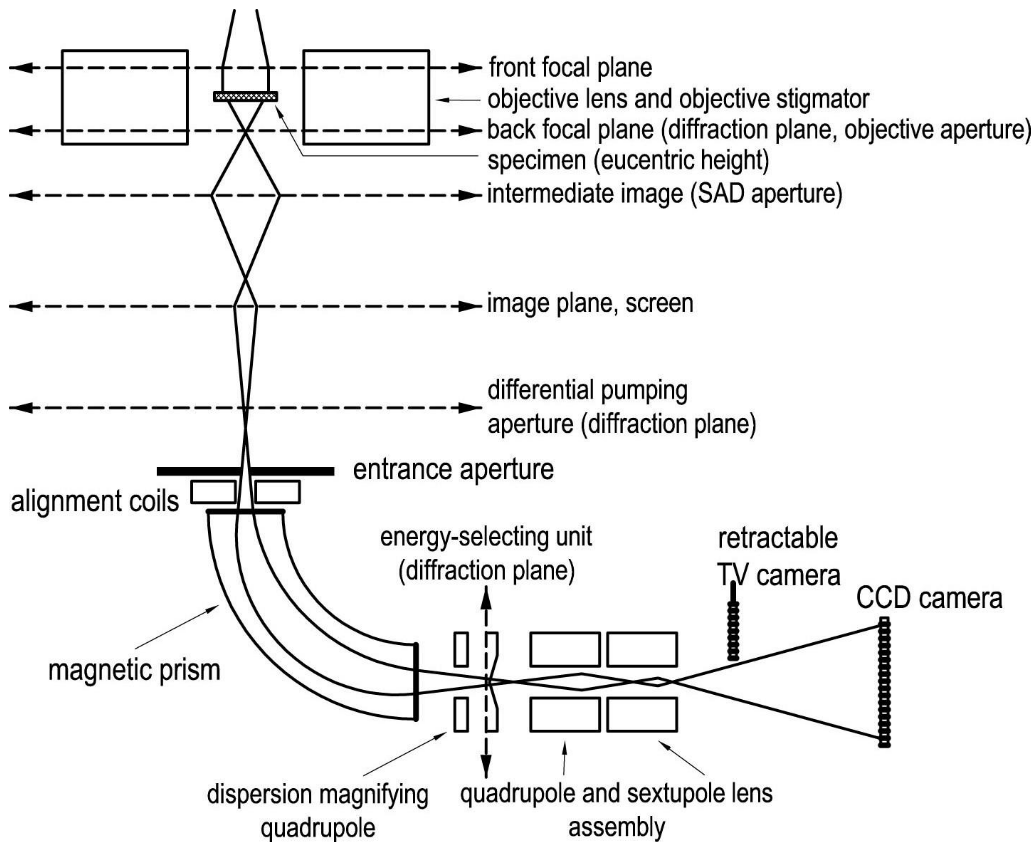

Figure 29. Figure 23: Simplified setup of the electron-optical path for energy-filtered imaging using a post-column energy filter (GIF).

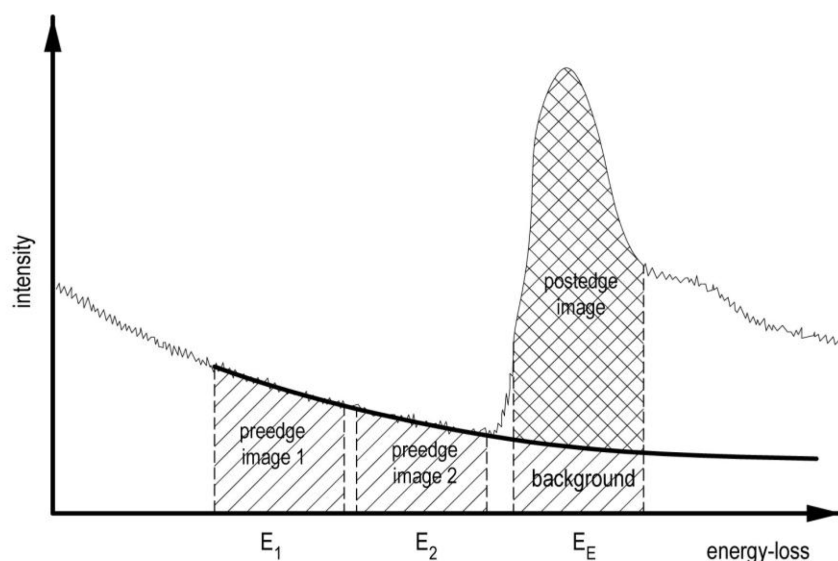

Figure 30. Three window method, shows the part of the spectrum with the edge. Three window method uses two pre-edge windows of chosen energy width, and one post- edge window, which width is chosen to include the edge intensity.

The removal the background in EFTEM can be performed by either the "jump-ratio" or "three-window" methods[113]. In the "jump- ratio" method uses two separately recorded images by selecting an energy window before and after the ionization edge to create an elemental map. This method is suitable for qualitative mapping of small elemental concentration from noisy images. In case of the "three- window" method, background subtraction is achieved by using two images recorded by selecting two energy windows before (pre-edge 1 and 2) the ionization edge and the third image after (post) the ionization edge (See **Figure 30**). Three window method is for more qualitative research than rump-ratio, but is not suitable for noisy data.

3.4.5. X-ray Energy Dispersive Spectroscopy

Among the group of the inelastic event interactions, the electrons from inner-shell are included. The primary electron is scattered inelastically by electron of inner-shell, causing the excitation of atom energy, by ejecting the electron or its transition to a higher band. The excitation of atom is extremely short time (approx. 10^{-15}s), and it is followed by downward transition of valence electron, which is higher-energy state. Therefore some additional energy needs to be released, and it has a form emitted portion of energy *hv* which is equal to the energy difference in binding energy of two shells taking part into the excitation process. This emitted portion of energy is named as characteristic x-ray radiation, and it is used in spectroscopic investigations of chemical structures. X-rays intensity depends on Z number, thus the number of inner-shells and transitions between them. The x-ray spectrum consists of characteristic peaks and Bremsstrahlung radiation, which is continuous background radiation due to Coulomb force deflection of electrons [164, 175, 185, 196].

The spectrum is generated by a dispersive device which will distinguish different photon energies. Usually for Energy Dispersive Spectroscopy a semiconductor diode is used. The energy of any electron that enters the p-, n- junction releases some amount of valence electrons from semiconductor, resulting in momentary active electrical junction. The whole energy of x-ray is used for formation of this electron-hole pair. The time necessary to recording a useful spectrum is dependent on number of channels and their correspondence to phonon energy. If the time will be too short, the spectrum will be too noisy, because the whole process is a statistical number of counts per channel.

The advantage of EDX is its quantitative studies. It gives a good estimation of element ratios and its chemical concentration within the specimen in reasonably short time. EDX and EELS are

complimentary methods, but EDX is much better in detecting high Z elements, whereas EELS is better for light elements. However the drawback of this method is the signal intensity which is detected. Usually the EDX detector is placed above the sample at some angle (for example 40° angle) and maximum signal detected is approximately 20% of total signal. Also EDX does not provide the electronic configuration, but the readout signal is much easier to interpret than EELS.

3.5.Instrumentation and conditions

The FEI Tecnai T20 and ARM JEOL 200F microscopes were used for experimental data collection present in this thesis. The T20 microscope was particularly used for diffraction pattern, dark field imaging and energy filtered imaging. Also the studies were performed on ARM 200F, which has two operated modes – conventional TEM and scanning mode. It is equipped with high standard CCD camera, 9 different detectors from JEOL and GATAN, Bruker EDX detector and EEL Spectrometer Quantum with the electric shutter for performing DualEELS acquisition. Both microscopes were operational at 200kV with different imaging modes. The detailed description of the experimental conditions is given below.

3.5.1. Conventional transmission electron microscope – FEI Tecnai T20

The FEI Tecnai T20 microscope is designed to combine a wide range of standard imaging methods with simple to use software and an easy to use interface. It has a LaB_6 filament with an accelerating voltage of 200kV. Such a combination gives opportunity for fundamental research within variety of materials such as metal, ceramics, or life biological specimens with moderately high resolution and wide range of magnifications.

The T20 was both used in its own right for lower resolution characterisation with diffraction contrast imaging, diffraction and EFTEM, but was also as a key preparatory tool for higher resolution STEM investigations, since small precipitates are difficult to locate in the STEM mode and elemental mapping in STEM is slow and only works for small areas of observation. The diffraction contrast in the T20 microscope in bright field, or dark field is stronger than annular bright field, or annular dark field detectors in STEM. Therefore the T20 was used to find areas of interest containing precipitates, record suitable images, then allowing the precipitates to be located in the STEM.

The second extensively used technique on the Tecnai was acquisition of diffraction patterns. Because the specimens which were used have polycrystalline structure, they contain many randomly oriented grains. A grain which is believed to contain precipitates, was oriented along a major pole like [001], [011], [111] using Kikuchi lines in CBED mode. Kikuchi lines are pairs of diffraction lines, which are from single crystal in thick regions enough to undergo a multiple scattering, and serve as a orientation guidelines. Then by spreading the beam and putting a selected area aperture in, zone

axis diffraction patterns were recorded. Such diffraction patterns were intended to be used for evaluation of lattice parameters of precipitates. However closer analysis revealed that in reality the amount of oxidation on the surface was higher than the volume fraction of precipitates, and the signal was dominated by surface oxide, thus the diffraction patterns were found to give little information about the crystallography of precipitates.

Nevertheless, the diffraction patterns were used to set up dark field imaging conditions where a tilt was set up such that a diffraction spot for the precipitate should go through the aperture, assuming a cube-on-cube orientation relationship between the fcc austenite matrix and the fcc carbide precipitate. The precipitates should have a larger lattice parameter, so the spot should appear inside that for the austenite in every case. This was therefore performed with the smallest objective aperture just inside an austenite matrix spot and in many cases allowed dark field images of precipitates to be recorded. In some cases the precipitates were observed, but they were often accompanied by extensive strong contrast all over the observed area from the surface oxide.

The Nb precipitates were also mapped with the EFTEM technique. Due to the slow rise of the $M_{4,5}$ edge, this does not produce good Nb maps. However, the lower energy $N_{2,3}$ edge is sharper and could be used for mapping as previously shown by Epicier and Deschamps [114, 197]. In case of Nb samples, the EFTEM technique was used not only for finding precipitates, but rather to obtain a quick map of a large area for volume distribution or size distribution measurement.

3.5.2. JEOL ARM200F

The JEOL ARM 200F was delivered in December 2011 and was almost fully operational by June 2012. This is a high specification TEM/STEM equipped with a CFEG gun and is probe corrected to allow STEM imaging with a resolution down to ~0.6Å. It was equipped with JEOL and Gatan imaging detectors, together with a Bruker X-ray detector. The high brightness of the CFEG means that the current per area solid angle was huge, in a very small spot. This made it perfect for spectroscopic investigations, even to the extent of atomic resolution spectroscopy (although that was not performed in this work). The main feature of the microscope used in this work in addition to the standard imaging detectors was the Gatan GIF Quantum ER EEL Spectrometer with fast DualEELS.

In order to make the most of the large convergence angle made possible by the probe corrector (up to 29 mrad), the camera length for EELS has to be extremely small in order for all the signal to pass the entrance aperture. In this work, the JEOL ARM200F was operated at 200kV and usually with a 2.5μm aperture and a camera lengths of 2cm for EELS. The STEM data were recorded using a 40μm condenser aperture to give a convergence semi-angle of 29 mrad, which includes the mostly flat area of the centre of the Ronchigram and excludes the highly aberrated portion of it. With these conditions the ARM should be operational with a probe size ~ 1 Å, even at higher probe

currents, and a probe current of approximately 400pA and a spectrometer acceptance entrance aperture semi-angle of 36 mrad were normally used (for the entrance aperture/camera length combination given above). In case of the spectrum imaging, the dispersion was set at 0.5eV/channel and spectra with 2048 channels were recorded giving an energy range in each spectrum of 1024eV. The zero loss peak (ZLP) was positioned in the low loss spectrum so that there were sufficient channels on its low energy side to allow the correction of the bleed-through artefact, where required. The origin and removal of this artefact is discussed later in the chapter 6.1. The start energy of the core loss spectrum was offset by applying a known voltage to the drift tube of the spectrometer. The integration times were set so that the counts in the most intense channel (the zero-loss peak (ZLP) in the low loss region and the low energy end of the core loss region were just below the saturation level of the CCD. This required times of tens of microseconds for the low-loss spectra and tens of milliseconds for the core-loss spectra, resulting in maps recorded in a few minutes for a rectangular 50-100 pixel wide size. The typical size of a pixel was of the order of 0.3 – 0.5nm. Because of the stability of the whole microscope and especially the stage the drift correction was performed when absolutely necessary. Each acquisition was finished with the dark reference correction using an averaged dark reference, reducing the noise in the spectra. The dark reference is a null signal, which is always present in the camera, as there is always some residue electronic signal on the surface of the camera.

3.5.3. Plasma Cleaner

The Fischione Plasma Cleaner is a machine that was used to which removes any organic carbon contamination on the surface of the specimen with the use of oxygen-argon plasma (10% oxygen in argon is the feed gas). The removal of carbon contaminations enhances the imaging results, and also significantly improves the quality of acquisition of spectrum images, by suppressing the grow of the amorphous carbon during study. This is extremely important, because the studies of chemical composition of carbides and carbonitrides are very vulnerable to amorphous carbon contamination, as it is preventing the study to give and realistic values of carbon within the investigated region. The whole procedure of cleaning with oxygen plasma is fast, because it takes only 5 to 10 minutes. The primary advantage is that the plasma interacts only with organic materials, leaving the structure of the sample unchanged. But there are also two other important parameters which makes the plasma cleaner undoubtedly helpful device in sample preparation – the assembly is oil-free, and the whole procedure is held under the vacuum. Because the good quality of images is key feature in case of nanoscale investigation with high resolution, hence the plasma cleaner is a standard finishing procedure while preparing specimens for ARM studies. All specimens were baked at 100°C either overnight or at least for several hours in a Gatan PIPS system, which also has an oil-

free vacuum system. The high vacuum of the PIPS prevents further oxidation of the specimen surfaces, something that is always a possibility if a plasma cleaner involving an Ar-O gas mixture is used as with the Fischione Plasma Cleaner. However, this was used to clean the specimen holder for at least 3 minutes prior to using them. The surface of the specimen's and holder's cleaning is performed for a few minutes prior to insertion it into the microscope. Otherwise the carbon contamination can grow very quickly and makes the quantitative and qualitative analysis of acquired spectra impossible. Growth of the amorphous carbon is a process activated by electron beam, during the organic contaminations from the specimen, or holder loses its structure and form the amorphous layer on the beam-specimen contact area.

In this chapter, I introduced research methods, that allowed me to conduct complex quantitative and qualitative analysis on nanosized particles in steel. Using TEM, it is possible to analyse specimens using imaging contrast and distinguish individual microstructure elements, such as grain boundaries, precipitations, or dislocations. Another method is diffraction technique which allows to approximate the structure of individual phases - matrix and precipitates. However to successively examine the structures the indexing is required, and for that purpose it has to be known more or less what constitutes the studied structure contains, which is a certain inconvenience. Apart from diffraction patterns, an EFTEM is also used. This is a study that allows wide area analytical study to determine the elements in the test area. Unfortunately, it has some limitations in resolution and in acquisition the signals from light elements such as carbon and oxygen. For that reason the transmission electron microscopy were supported with scanning transmission electron microscopy. Despite microstructure imaging in STEM, the main focus is put in to analytical research with special spectrometer detector. This method, called EELS is more efficient than EFTEM, and allows acquisition of light elements, while keeping at the same time the highest possible resolution.

All results obtained with the TEM and STEM were of the highest resolution, but unfortunately required rigorous limits for sample preparation. This was due to the fact that any contamination or post-preparation artifact was immediately visible in the study. Consequently, for effective usage of proposed methods and techniques an optimized way of sample preparation has been developed to minimize the amount of contaminants in the study and is described in the **chapter 4.**

4. Optimisation of the sample preparation process

Focused Ion Beam is a technique which results in damage of the sample and formation of artefacts such as: Ion damage of the top surface and sidewalls, and ion implantation. The level of implemented artefacts and depth of the damage depends on the ion species, the incident energy, the angle of incidence and the density of material of the specimen[198].

4.1.Motivation

The successful elimination of implemented artefacts and damage due to FIB preparation is crucial for data collection with ARM. The sizes of the analysed precipitates are in order of few nanometers. Such small dimensions of features are easily induced by any defects of artefacts implemented by sample preparation techniques, which makes the characterisation difficult. Therefore the special effort is put into development of an optimised technique of specimen preparation with FIB[159, 199, 200].

The second step, which can be carried out inside FIB – is a proper combination of tilting from front to back and changes in voltage and current of the beam each time the specimen is getting thinner. Because of the shape of ion beam it is necessary to change the angles while milling with different voltages. The lower the voltage, the wider is the tail of the beam, which causes milling of the sample on the top or bottom edges, which leads to a wedge-shaped sample. The procedure described so far by Schaffer *et al. [156]* is optimised for Si-based specimens so for the specimen with relatively weak bonding between atoms, therefore the combinations of angles and voltages are not suitable for harder-to-mill materials, such as steels. The problems, which have to be taken into account, are redeposition of ablated materials, and too high angles likewise rapid ablation of protective platinum [201]. As a consequence, the milling of material at the top or bottom of the section is accelerated resulting in damage to these parts of the specimen. So, the lack of optimisation leads to wedge shape of the specimen, or other things, which may destroy its quality. There are several conditions, which describe well-prepared specimen which can be used for DualEELS or HR imaging. Without fulfilling these rigorous conditions it is challenging to record beneficial data. According to Schaffer *et al. [202]* the crucial parameter of the specimen is thickness less than 30nm with minimum ion beam damage and controlled redeposition. So the most

important requirements, the specimen used for analytical research suppose to fill, are described below:

- Have as parallel sidewalls as possible for better qualitative analysis
- Have reduced artefacts and implemented Ga^{+} ions
- Have reduced the amorphised layer by the Ga^{+} ions
- Have reduced the curtain effect
- Have reduced the layer of oxidation on the surface
- Have reduced amount of nano particles which might be milled out of the specimen
- thickness less than 30nm
- Be prepared in optimised time according to used ion beam energy.

Moreover the sample needs to be as thin as possible to avoid spreading the electron beam, which is usually a range less than 50nm for standard specimens, and thinner for much heavier atoms.

The optimisation of the process, which combines the shortest time of preparation and the best quality of sample, is necessary for specimens used in ARM microscope. Any contamination or artefact, or lack of parallelism will result in unreliable or artificial data. As a consequence, the qualitative analysis of chemical composition and the kinetics of first stage of nucleation of precipitates is impossible to carry out. There have been some modifications in the heavier materials than SI, such as multiferroics, which was demonstrated by Wang *et al. [203],* but despite magnificent results, the procedure proposed in this paper was insufficient for materials as hard as high manganese steels.

The optimisation of the process was a key task, and a first step to the atomic resolution studies. This will also give a good insight into the FIB steel sample preparation in general, because so far different methods like carbon replicas, or electropolishing was the most common ones. Development of a new method might be of a big importance, due to the research performed on the smallest nanosized precipitates, which with high probability are destroyed or removed from the specimens and obscure for example the volume fraction calculations while the specimen are prepared with available methods. The development described and published in this thesis is an original and new material.

4.2.How to optimise – modelling SRIM modelling

Modelling is important, it helps experimental studies by saving time and money on materials. It can be treated as guidance, support, or comparison data. Modelling has few advantages over experimental data, such as lack of requirement of good samples, and the results are usually fast

- It doesn't require good samples

- It can be done automatically
- Usually it is faster method to obtain reasonable data.

The SRIM Pro software were used to plan the new approach of specimen preparation. There is no significant information in the literature about low voltages samples made with steel, or other high strength alloys. Therefore it was important to plan, make an assumptions and predict how the gallium beam interacts with the surface of the specimen to reduce to minimum the artifacts created by FIB.

To perform the optimisation of the specimen preparation technique with FIB the simulations are required, prepared prior to experiments. The basic simulation was used with SRIM software, which was helpful during optimisation sample preparation process, as it simulates the ion interaction with matter.

SRIM PRO is Monte Carlo based simulation software which calculates many features of the transport and interaction of ions within matter. It is primarily concerned with the quantitative evaluation of how ions lose energy into matter and the final distribution of these ions after they stop within the target. Also considered are the first order effects of the atoms on solids, particularly the electronic excitation of the atoms, the displacement of lattice atoms by energetic collisions (lattice damage) and the production of plasmons and phonons within the solid by the passing ions. No evaluation is made of thermal effects in the solid, especially redistribution of lattice atoms or implanted ions by thermal or vacancy induced diffusions.

SRIM software can be applied for simulation of variety of packages, such as ion stopping, ion implantation, sputtering interactions and ion transmission packages. The package that was useful for this research was Ion Stopping and Range in Targets. It can calculate the energy loss of ions in matter as well as calculate the depth of interaction of ions with matter. The software provides quick calculations which produce the tables of parameters like depth of interaction, or stop energy of all possible ions and matters. For more advanced materials it is possible to calculate even interactions with multilayer components.

The motivation to use SRIM PRO is an optimisation of sample preparation process with Focused Ion Beam method. The advanced STEM Microscope requires higher precision in sample preparation, because any contamination, deviation in thickness, or imperfections very easily can disrupt obtained data. Therefore a new, more optimised method need to be developed, which will take into account following points:

- Reduction of used voltages, so called low-voltage method for reduction any damage or implemented Ga^{+} ions during preparation

- Combination of type of thinning process and angle of incidence
- Optimisation of time and voltage used during process
- Reduction of any induced-strain phase transformation.

SRIM PRO software was used to simulate depth of interaction Ga^+ with matter, thus Fe and Mn specimen. According to different voltages, information, and taking an amendment to the all of the simulations are done in 0K the proposition of interaction was done, as presented in **Table 3** and depictured in the **Figure 31**. In the figure it can be seen that for the highest ion energy the penetration depth is the highest, close to the 80nm(modelled at 0K gives 10nm, so the value is approximately doubled at room temperature). It means that if the specimen should be free from ion interaction artifacts this depth has to be milled away with lower energy. At 5kV the depth of penetration is only 20nm, which is quite easy to fix with the final polishing procedures.

The simulated depth of interaction was used to estimate the damage depth that resulting from ions with different voltages. Estimating the depth allowed the determination of the maximum thickness, which should thin sample with certain voltage. This procedure allows choosing optimal shortening time to the best quality of specimen, because it allowed to reduce the time to execute a specimen with the smallest amounts of damage and potential deformation and artifacts formation. Mainly, because it shortens gallium ion bombardment time, which reduces the contamination with ions. However the whole procedure was based on approximation of the depth of interaction, the results were satisfying.

The reduction in voltages and currents is complicated procedure, because each beam needs to be aligned. Moreover the cross-section of each beam is different, thus the angles of incidence must be different as well, and the valuation of the proper angles in this case needed to be done experimentally. This is crucial because the wrong angle will lead to wedge edge of the sample, which need to be eliminated. Unfortunately, the wedge samples cannot be use in STEM microscope and in the analytical research.

First attempt to find optimised angles was based on method produced by FEI company based on simulations and development, with modifications by taking into account the fact that the simulations are for Si standards [156]. The proposed combination of angles is presented in table. The combination of small angles at higher voltages and higher angles on lower voltages we were able to obtain a sample with large parallel area, which can be easily observed in STEM.

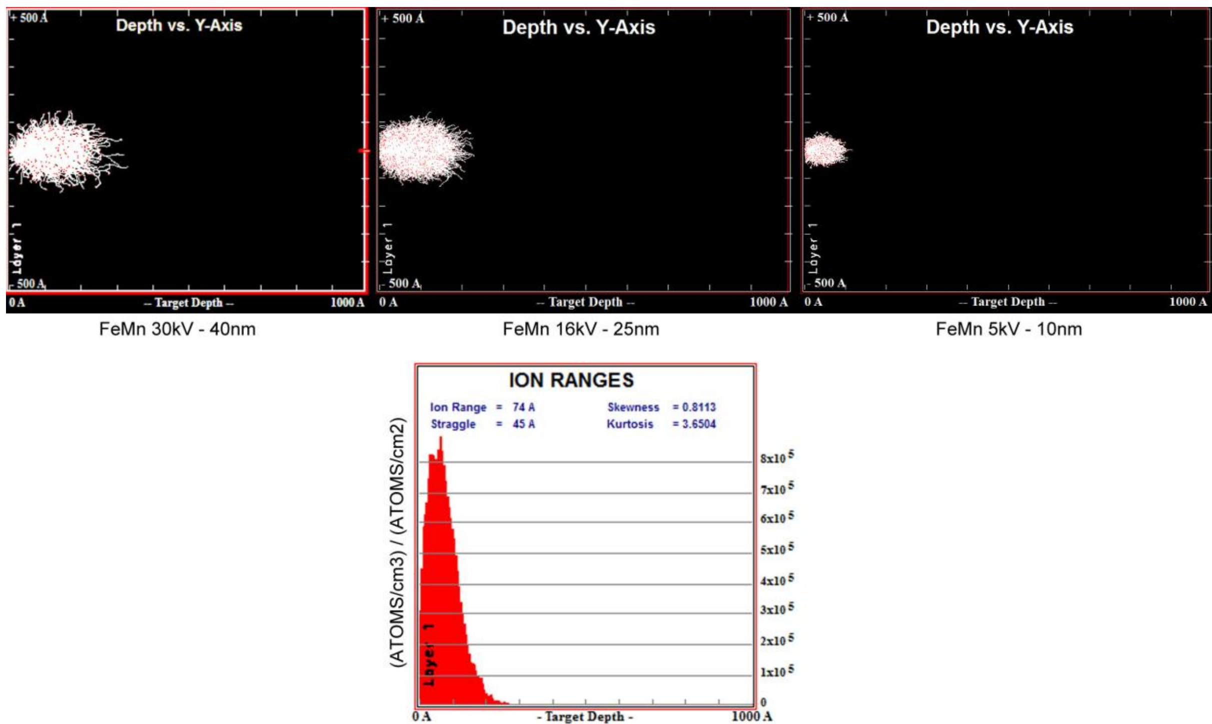

Figure 31. Modeling results in SRIM PRO Ga$^+$ ions interacting with the surface at 90° with different ion energy.

4.3.How to optimise

The optimisation process relies on maximizing the quality parameters of samples while maintaining the shortest time for achievement of these characteristics. In case of Focused Ion Beam there are several parameters which can be consequently controlled to achieve desired quality of specimen. Those parameters include accelerating voltage of gallium ions, its current, angle of incidence, time of thinning, type of thinning, or even conditions less direct like the size of the aperture, or the life being of gallium source. The foundation for the procedure was the SRIM PRO interaction modelling of Ga$^+$ with the surface of the sample for different voltages. This provided a good range of conditions to try out. After several attempts the best conditions seems to be as presented in **Table 3.**

The innovative nano-mills using the Ar source are also a good solution for final polishing [204]. The diffraction patterns taken from sample prepared by FIB only, and prepared by FIB with additional final argon milling revealed that the surface from the latter is much clearer, the amorphised structures are removed, the sample is clean and this allows the investigation of the precipitates to be facile in comparison to the difficulties people occurred with standard FIB samples.

Voltage	Current	Thickness left	Angle	Type of thinning	Modelled penetration
30 kV	**0.28 nA**	**500nm**	**1.2°**	**Rectangle**	**40nm**
16 kV	**0.45 pA**	**200nm**	**2°**	**Rectangle**	**25nm**
8 kV	**0.62pA**	**100nm**	**2.2°**	**Rectangle**	**15nm**
5 kV	**47pA**	**40nm**	**7**	**CCS**	**10nm**
2 kV	**10pA**	**20nm**	**7°**	**Rectangle**	**6nm**
1 kV	**14pA**	**10nm**	**7°**	**Rectangle**	**5nm**

Table 3. Successful conditions for sample preparation with FIB technique developed by SRIM PRO modelling of Ga^+ interactions with the surface of specimen.

In Table 3, there is a collate of all steps, which were applied as a optimised method of sample preparation. These conditions are based on trial's and errors preparation of tens of specimen and checking their parameters (quality, thickness, surface damage) in microscope. All type of thinning were rectangle which assumes the same amount of current in total area (usually rectangle shaped area) apart from 5kV step. This step required CCS thinning type, which is a cleaning cross-section, and it consists of several lines, which mill the specimen deeper with each line. This pattern is used when the ion beam has a broad tale, so using the rectangle shape results in thinning the specimen in unwanted regions, and as a consequence damaging the final specimen.

The first step is the most substantial thinning part, which removes majority of the material, leaving approximately 500nm of the specimen. It is performed at the lowest angle to keep the beam as parallel to the specimen as possible. Limiting the voltage, the beam width changes, so the angle has to be modified. Increasing the angle allow better control of the area which was milled and the parallelism of the specimen is kept. Second step involves the reduction of the voltage and increase of the incident angle. The third step reduces the voltage to 8kV, and increases the incident beam angle to **2.2°,** and specimen at this stage supposed to have approximately 100nm. Following 60 nm is thinned down by using cleaning cross-section at the 7°angle and it is performed at 5kV. The last two steps, are mostly polishing steps, but they also mill down a little bit of the specimen. Their role is mainly to remove any residue curtaining, or any other thickness fluctuations.

The finish procedure involves the PIPS cleaning for time of 2h from bottom and top under 8° angles, with 1keV energy. The sample after additional Ar milling is much cleaner, with sufficiently diminished surface oxide layer. Likewise such time is enough to remove any artifacts which occurred

during FIB preparation, such as curtaining, surface Ga^+ implantation, or anything else which might generate additional contrast fading the real microstructure image.

4.4.Needle-shaped samples

The evaluation of cross sections of interactions of electrons with the Nb and V precipitates requires sample of a known thickness. The easiest thing to estimate a thickness in FIB is to use a needle shaped piece of material, with known diameter. If the sample is cylindrical, it should be simple to estimate the cross-section for each material. The cross-sections are used for estimation of the local thickness of each of the elements consist on precipitates, with use of the needle-shaped samples with standards, such as NbC, VC, TiC, TiN or VN.

The procedure of thinning the sample in a cylindrical shape requires mounting a piece of standard material on top of the omniprobe holder and milling it down with circular pattern with combination of time, currents and diameters like given in the **Table 3**.

The size of the lift-out lamella used for preparation of needle-shaped sample is thicker than the standard TEM sample lamella. The standard thickness for a TEM specimen lamella is 1μm, whereas the needle-shaped specimen requires 2μm thickness with a standard depth, which is usually 7 μm. This is necessary, because the lamella is mounted on top of the Omniprobe holder instead of the sideways, and cut to the 2x3x7μm cuboids, which allows annular milling of the material. The lamella has usually a 2x10x7μm, so from one lamella it is possible to mount 3 cuboids, each one on separated omniprobe grid [153, 205].

The mounting process is important, because annular milling will mill down the omniprobe grid as well. So, if the cuboids will not be stable and safely attached, the needle sample might tilt preventing further milling, or fall off the holder and disappear in the vacuum. Thus, the mounting carries on by situating the lamella 50-80nm above the top of the omniprobe grid and filling the space underneath with Pt. Such mounted material can be milled down perpendicular to the ion beam, without any tilts of the FIB table, like in case of classic TEM lamella.

The annular milling has two diameters, which indicates how much material is milled down at one time. The outer diameter D_0 which at the first milling is set to 4000nm and inner diameter D_1 which is set to 2000nm at starting point with the beam conditions set to 30kV and 0.92nA current. The milling is conducted from the outer diameter to inner diameter. After 15s the first reduction of outer diameter occurs – down to 3500nm, with the same beam conditions. After next 15s, the outer diameter is reduced to 2300nm. This will reduce the amount of material removed from outer regions, to focus just on the inner part, where the needle shaped sample starts to occur. After next 10s, the inner diameter is reduced to 1600nm, with the same outer diameter. It will form the more vertical shape of the specimen. The forming will continue for 30s. After that the inner diameter is

changed for 1300nm and sample is milled down for about 10-15s. During the milling the apex of the needle has to be controlled all the time, if it is in the middle of the annular patter. Otherwise it has to be adjusted to nullify the bending as a consequence of non-perpendicular beam. The next stage requires reduction in outer diameter down to 1800nm and inner diameter down to 1000nm and milling down with constantly unchanged beam conditions for another 20s. At this stage the first change in current is done – from 0.92nm down to 0.28nA and first 10s are without any changes in diameters. After that the D_1 is reduced to 800nm and milled for 20s. If the Pt is milled down to quickly, the reduction in current might be necessary. It is very important to focus the beam, and observe how the apex of the specimen is moving. The next diameter change happens when the current is reduced down to 93pA, and the D_0 is still 1800nm, but the D_1 is set at 600nm. The reduction of inner diameter to 400nm and 300nm are in 15s intervals with constant outer diameter and beam conditions. When the inner diameter is set to 200nm the current is reduced to 48pA. It is important to observe the apex shape. If it loses the cylindrical cross-section it may requires the adjustment the pattern, or that the current is too low.

The final milling is with D_0 = 1600nm, and D_1 = 200nm, with the current 48pA and 30kV voltage. It is also important to avoid imaging with the ion beam if possible. The needle-shaped samples are prepared with a dual-beam instrument, which allows the imaging with the electron beam. This is one of few ways of reduction of Ga^+ implantation. Also the final milling with voltages as 1-2kV is helpful with the reduction of the level of ions implanted.

4.5. Gold Sputtering

The sputtering machine is used for thin layers sputtering such as gold or aluminium. Usually it is used for sample protection prior to FIB sample preparation. In general, it is used for sputtering the protecting nanolayer of Au. It is more uniform than electron platinum thus it is not milled down randomly resulting in better side milling during lift-out sample preparation. The idea of deposition Au instead of Pt was firstly suggested by [206] with a promising results, so the idea was implemented as a part of the optimised standard procedure of specimen preparation.

The instrument is a machine consists of work chamber, safety shield, and rotary pomp system. The Work chamber is made of borosilicate glass with integrated polyethylene cylindrical safety shield. On the lid there are two different targets; A which refers to gold, and B, which refers to aluminium. By choosing the proper electric current there can be sputtered one, or both layers. The combination of current and time gives different thicknesses of surface coating as well as different qualities. In general the quality films are good due to rotating stage with rotation speed 8-20 rpm.

During the gold coating, the 0.25mA electric current is used. It is sufficient for obtaining layer with approximate thickness of 70nm. This coating is then covered with platinum during standard FIB

preparation procedure. According to lower voltages paper, written by [156] used for less invasive method of preparation in FIB, the profile of ion beam is wider, and more difficult to control. The Gaussian-like profile leads to wedge shape of sample, which is undesirable shape for atomic resolution microscope's sample. This difference is thickness gives wrong interpretation of obtained data, because the chemical composition is valued by Z, atomic number, which can vary for different thicknesses.

The results presenting the quality improvement are shown in chapter 6.

4.6.Results

In the end a unified procedure was proposed. First of all, the specimen has to be coated with Au, just for the protection reasons. Then it can be placed into FIB and coated with protection Pt, where the lift-out is performed. The cutting the lamella out is the same as in any other TEM cross-section preparation. The optimisation process is applied to the thinning only. The conditions of each step are presented in **Table 3**. The precise time for each milling voltage and side is still a matter of experience and user judgement, since this requires the understanding that sometimes the material can be milled down a little bit quicker. So there are slight variations from sample to sample, but the overall procedure is in **Table 3**, and can be treated as a good reference at starting point. Final step is to put the specimen into a PIPS for 30 minutes for a low voltage final polishing with argon ions. This will help to reduce any FIB artifacts and contaminations to be removed. Just before the microscope studies a 10 minutes plasma cleaning is applied to remove any organic carbon contaminations that may originate from the storage box or from dirt on the specimen holder or the tools used for handling the specimen.

The new sample, prepared with the optimised technique is better, cleaner, with more uniformed thickness with almost parallel sidewalls, it has enough thin regions to analysis, and the Ga implantation is low.

The Pt, which is usually deposited in the FIB, is actually a nanostructured Pt-carbon composite, and does not have a uniform structure. This may lead to an uneven milling of the Pt, resulting in higher probability of formation of the curtaining, because some of the regions will be milled down quickly, whilst others are still protected by the Pt. To reduce this, the bulk material is placed into a Sputter Coater to deposit a thin layer of gold. The layer is usually around 70nm thick. Moreover the ion beam has the funnel-shape so if the sample is flat and has quite long square area to be thinned down, the Au coating prevents the ion milling of sample, therefore the rounding effect on the top. Instead of that the Au on the surface is milled down. This is very important if the sample will be used for quantitative analysis, because the differences in thickness influence the information of chemical composition of sample.

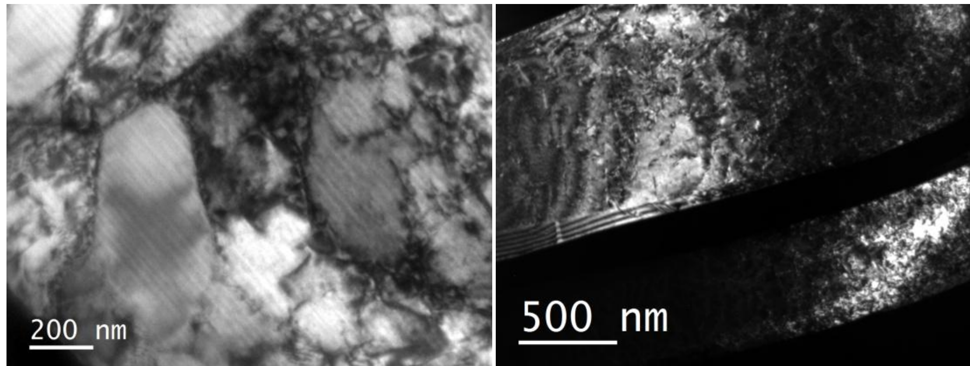

Figure 32. Dark Field TEM Images of V steel a) without deposition of protection layer of Au, b) with protection layer of Au. In first case the artifacts such as curtaining are visible; in second case despite a lot of contrast in different grains no such thing is visible.

This chapter describes the results of optimised method for sample preparation for (S)TEM observations. One type is a classic FIB lamella prepared with lift-out technique, and the other is a needle shaped specimen used specifically for one experiment. In the first case, the quality of the specimen is consequential. Based on experiments done by others the preferential steps for FIB currents and tilts were proposed. Following these steps a thin lamella and free from artefacts is created, with relatively wide area transparent for electrons, and thin enough to conduct successful analytical research with DualEELS technique. The specimens prepared with the proposed method are studied using classic TEM techniques (see chapter 5) and using advanced analytical techniques in STEM such as DualEELS (see chapter 8).

5. Microstructure Studies

The standard microstructure investigation involves TEM DF and DP studies, supported by EFTEM imaging. Both techniques are very useful and can provide different information about precipitates. Especially, Nb- and V-containing precipitates give various responses while interacting with electron beam.

In this chapter I will present most important results from TEM studies for the base steel, and both steel microalloyed with niobium and vanadium. The TEM techniques used for primary investigations are dark field imaging, which helps to identify all characteristic elements for deformed steel. DF is supported by EFTEM imaging, because in case of some of the specimen it is easier to distinguish elements by filtering the electron energy, than actually see the separate structures in DF. DF is unfortunately susceptible for diffraction contrast similarities, which mean, that if two structures will have the same scattering angle, with high probability they cannot be well separated.

The research was also supported with electron diffraction, however as the investigation has proved in case of such small precipitates, and their relatively small volume fraction it is not preferred way of analysis precipitates in this PhD.

5.1.Microstructure characterisation of base Fe-Mn-C steel

The base steel contained 20% of Mn and 0.6% of C with the Fe as a bulk. It was produced for comparison purposes from the point of view of structural investigations and thermomechanical treatments at other partner's facilities. The base steel was produced and thermomechanically treated in the same way as all other specimens, and the scheme of the process is presented on **Figure 5**.

It was found that there are no precipitates in the base material, and the microstructure is a classic hot deformation microstructure without any anomalies. There are visible twins, from both annealing and deformation, many dislocations throughout, sometimes more condensed in some places than others, all of which is to be expected. Also, there is some contrast from the surfaces showing from time to time at certain specimen orientations, which will suggest the whole surface is covered with oxide, just as in the case of Nb and V steel specimens.

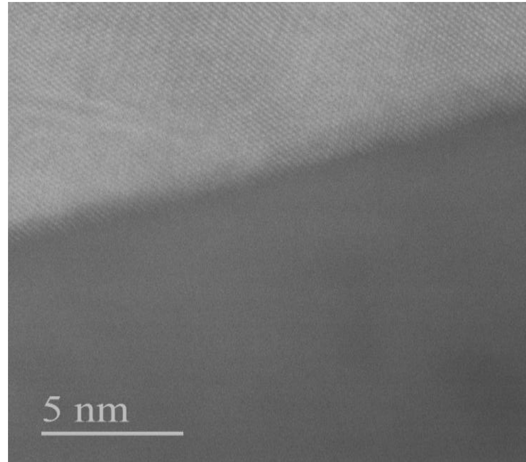

Figure 33. A grain boundary between two grains in the base steel (without microalloying elements), showing no precipitates even in such places.

Figure 33 shows a grain boundary in the base steel. It is well known that grain boundaries can act as a site for the heterogeneous nucleation of precipitates, because of the higher energy of grain boundary structures with respect to the matrix and the higher diffusion coefficient of atoms in grain boundaries. Despite this, no precipitates were found in this region or in any grain boundary in the base steel.

5.2. Microstructure characterisation of steel specimen

The microstructural research was a three year ongoing process, which involved specimen thermomechanically treated in various ways, together with different conditions of observations. The specimens which were prepared and investigated were deformed as shown in **Figure 5** with different temperatures and times of the isothermal holding in the single hit test.

V steels:

- Sample held at 850°C for 100s
- Sample held at 900°C for 100s
- Sample held at 950°C for 10s
- Sample held at 950°C for 100s.

The Nb steels are described later on in this chapter.

The main comparison is done between samples held for 100s at the different temperatures, because the preliminary results showed that most precipitates are well developed after 100s. The TEM sessions were whole day sessions directed to record complex data, for example dark field imagining with diffraction patterns from certain diffraction spots.

DF imaging was found to be effective at highlighting some precipitates in the matrix, but never actually illuminated all precipitates at once. This suggests that there might be more than one orientation relationship to the matrix, but also happened due to sample bending leading to a change in the diffraction condition with position.

All the acquired DPs were indexed, initially on the assumption that the weak spots arose from precipitates. Later investigation proved that this assumption was wrong, because the surface oxide layer is the dominant signal swamping the much weaker signal from precipitates (see **section 5.3.**). However in case of vanadium steels, DPs and DF imaging were not the main techniques used in location and imaging of these precipitates. Instead, it was found that energy filtered imaging was very effective at mapping V in the precipitates, and other elements could also be mapped by energy filtered imaging including iron, manganese, carbon and nitrogen. Such a clear distinction between matrix and precipitate contributions was extremely difficult to achieve with other imaging methods. The example of problem with contrast in Vanadium steel is showed on **Figure 34.**

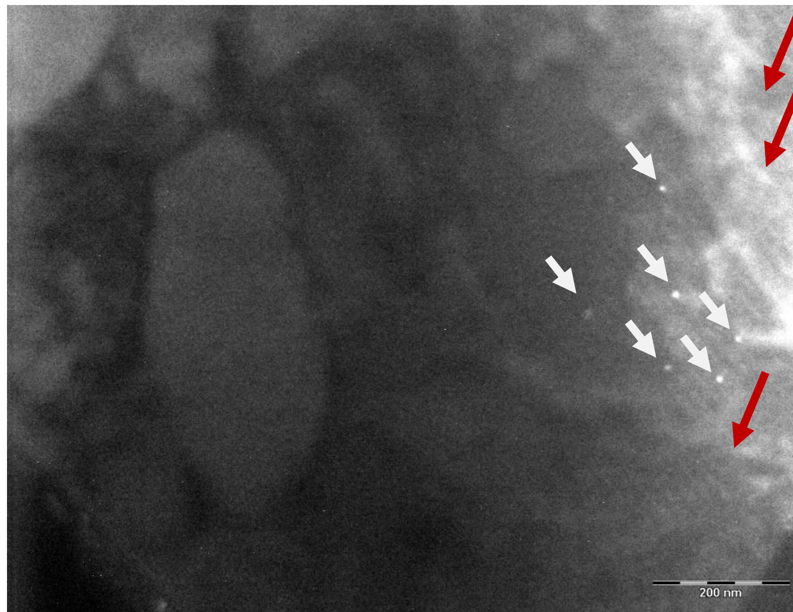

Figure 34. A DF image of vanadium steel with only a few precipitates visible(pointed out by white arrows). The red arrows points out the FIB artifacts like curtaining and second type contrast arising from surface oxidation, which are undesirable features.

This DF image shows the polycrystalline nature of this specimen, which has been strongly deformed during production. The grain boundaries are distinguishable with different contrast suggesting various orientations. In the right part of the figure just a few precipitates are seen as small bright spots. Such inhomogeneity is not very common for these materials[79, 207], which suggests that these are not the only precipitates in this region, just the rest is not visible due to changes in specimen orientation across the field of view. Moreover the sample preparation technique requires further optimisation. Visible linear features are post-preparation artefacts and need to be removed (shown by red arrows in the **Figure 34** and **Figure 35**).

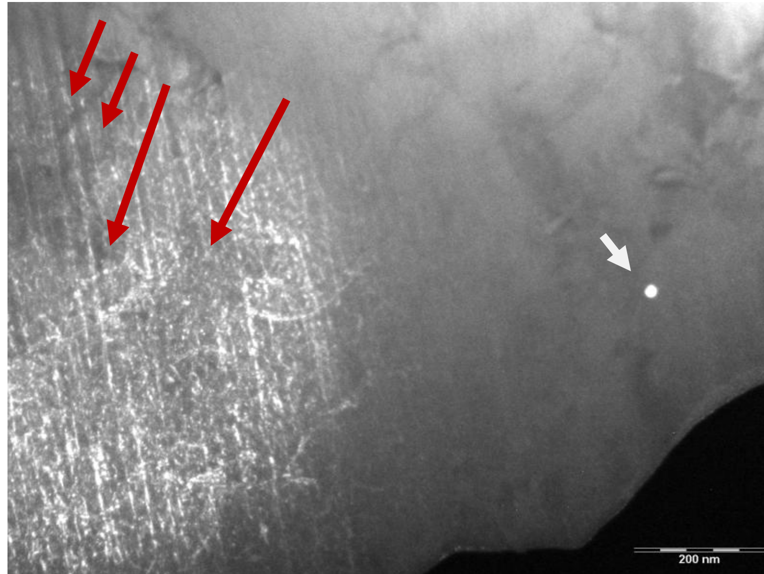

Figure 35. The DF image of a vanadium steel with additional second contrast occurring during tilting the beam. Also the artifacts like curtaining from the FIB are visible (pointed by the red arrows). There is one clear precipitate (pointed by white arrow), but the rest possible ones are hidden beneath the second type contrast. Some of the dislocations are also visible, due to the dislocation contrast.

The second problem with the vanadium steel studies is the second contrast, which is visible in the left part of the figure(red arrows), unexplained at first, but better understood later in the PhD. The strong contrast visible overall on almost all DF images arises from the surface oxidation, which is explained based on the diffraction pattern indexing later on this chapter. It is visible in **Figure 35,** where one precipitate has shown up, but the half of the specimen is highlighted.

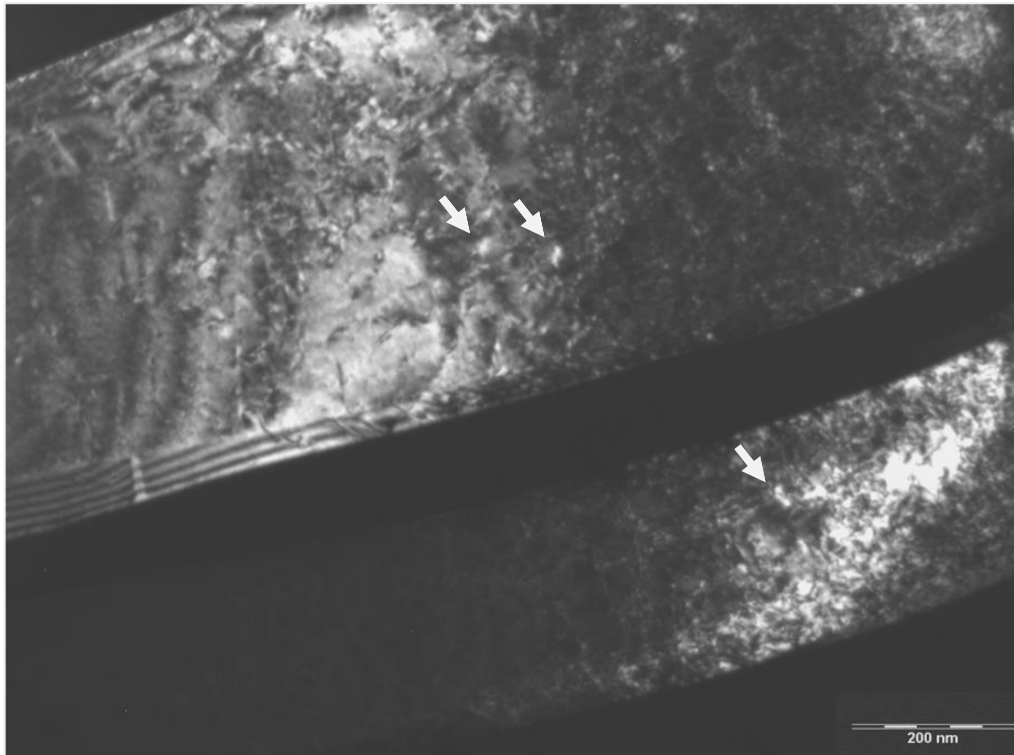

Figure 36. A dark field image of a vanadium steel sample deformed for 100s in 900°C. Despite a lot of contrast, which reveals such things like grain boundaries, dislocations, parallel fringes, and surface oxide just a few precipitates are nearly visible.

Figure 36 is a DF image which is dominated by matrix contrast on the left of the bright grain, and as it gets darker to the right, by surface oxide contrast. Whilst this is a good quality specimen, it is barely possible to distinguish whether bright spots arise from precipitates, from dislocations, or anything else. Also this is a good image showing the high level of deformation of the specimen. In the **Figure 36** in the middle part there is a thick black line, which is a high angle subgrain boundary, which separates two grains of similar orientation. On the lower boundary of the upper bright area there are parallel fringes known as Δ-w fringes, which occur when both grains have correlated lattices and are oriented by similar diffraction plane, so the diffracted beam changes in extinction on the steep grain boundary between them [208].

The Nb steel specimens prepared by FIB were previously thermomechanically treated as follows:

- Sample held at 900°C for 100s
- Sample held at 900°C for 40s
- Sample held at 900°C for 1s

The main emphasis was on interface investigation using HRSTEM, and comparison studies between characteristic of precipitates in 900°C and 100s in V steel and Nb steel. Also the studies involved detailed analytical characterisation of individual precipitates. The figures below show a typical, hot deformed microstructure with plenty of precipitates homogenously distributed

throughout the whole volume. There is no obvious inhomogenous type of distribution, such as the concentration of precipitates on grain boundaries, or annealing or deformed twins. This is shown clearly by **Figure 37** and **Figure 38**. **Figure 37** shows typical a BF TEM micrograph of the general microstructure of this material after hot deformation with significant evidence of the recovery of dislocations into subgrain boundaries. **Figure 38** is a DF image of the same image showing a number of precipitates.

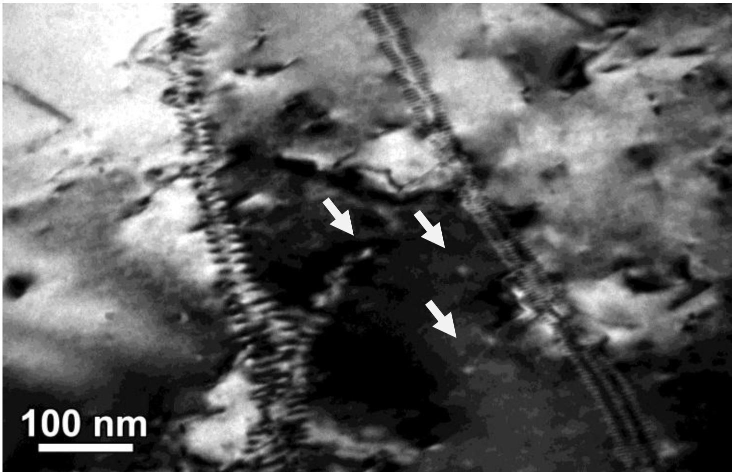

Figure 37. BF TEM image of the microstructure of the Nb microalloyed steel after thermomechanical treatment at 900°C for 100s. A classic thermomechanical structure in the stage of dynamic recovery is visible - the stair like pattern of relaxed dislocations. Most of them are in the oriented line, whereas the grains stay free from dislocations.

Figure 38. DF TEM image of the same area shown in Figure 37. A high density of subgrain boundaries are visible as a result of dynamic recovery during warm deformation, with a precipitates shining brightly (pointed out by white arrows), which are different than the ones highlighted in Figure 37.

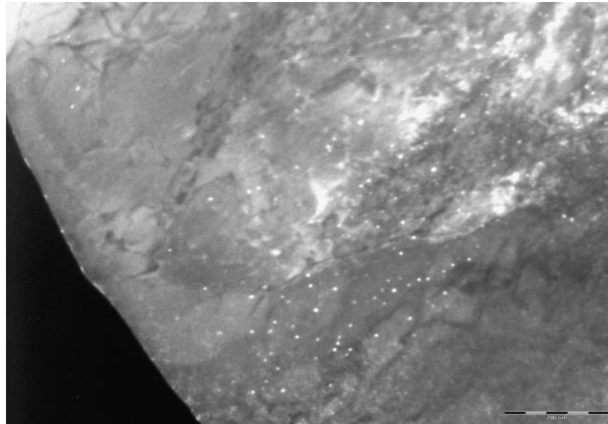

Figure 39. A classic dark field image of Nb steel isothermally treated for 100s at 900°C with plenty of precipitates highlighted at the same time with subtle contrast overall, especially to the top right, probably from surface oxide.

Figure 39 is a classic dark field TEM image, focused on precipitate imaging. The conditions (the angles between the specimen and the incident beam) were set to maximise the signal coming from precipitates, to roughly estimate their volume distribution together with type and level of homogeneity. In comparison to previous **Figure 38** almost no dislocations or grain boundaries are visible here. These studies proved that almost all of the precipitates appear simultaneously on the screen, which suggests only one orientation with the austenite matrix. Unfortunately, similarly to V steel, there is a second type of whole surface contrast just showing up on this figure. All the precipitates have size smaller than 20 nm, with average size below 10nm. Although it was not easy to highlight precipitates in V steel using DF imaging technique, it was much easier to collect good and extensive data for steel containing Nb precipitates. This probably happened because the lattice parameter for NbC is significantly larger than that for VC, this means that the diffraction spots for NbC would be further from those for austenite than for VC, making it easier to find diffraction conditions that only select NbC for the formation of DF images.

The preliminary studies of nucleation kinetics were done using Nb steel specimens. These involved studies of steel processed at 900°C for 1s, 40s and 100s. This type of study can show how the shape, size and distribution of precipitates changes with time.

After 1s at 900°C, very few precipitates are seen and those that are seen are very inhomogeneously distributed. Most areas had no precipitates, but a few had a significant number, as shown in **Figure 40a**. After 40s, precipitates were widespread throughout the sample, as shown in **Figure 40b**. Similarly after 100s, precipitates were widespread. Using Nb $N_{2,3}$ mapping it was confirmed that all small precipitates were Nb-containing, as expected, and samples of such images may be seen in **Figure 47.**

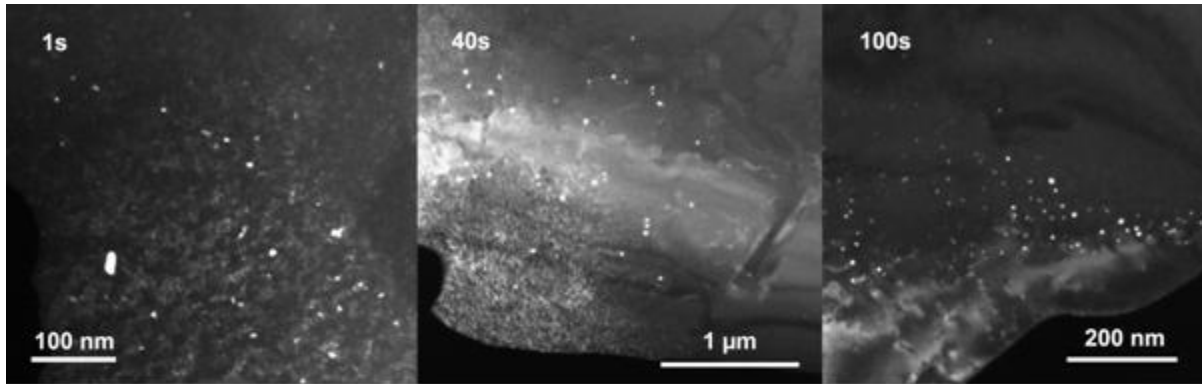

Figure 40. Precipitates in Nb steels heat treated at 900°C: a) Untypical area after 1s, with several small precipitates and one rather large one (most areas were free of precipitates); b) typical area in the 40s sample with numerous precipitates; c) typical area in the 100s sample with many precipitates.

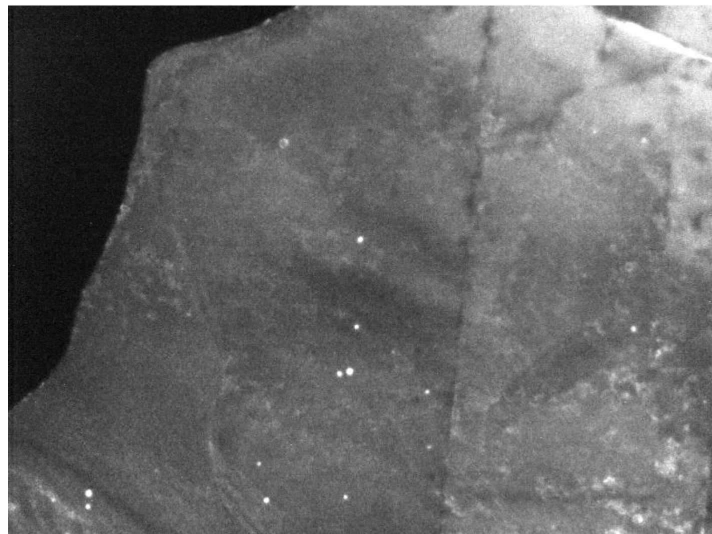

Figure 41. DF image of Nb steel isothermally treated for 40s in 900°. The grain boundary visible in the middle, and precipitates are highlighted in both grains suggesting the grains have the same crystallographic orientation. Some residue second type contrast is showing up in the right top corner.

The dark field imaging revealed plenty of other features like grain boundaries, twins, dislocations, and sometimes some defects resulting from sample preparations. The density of defects is high, which is a direct consequence of production this steel, which was the hot rolling. Similar features are present in all observed samples. However with a tilting the specimen is it possible to reach the conditions where the Bragg's law is fulfilled for precipitates only, and they pop-up as a bright, widespread spots. This trend is depicted on **Figure 38, Figure 39, Figure 40** and **Figure 41**.

5.3.Crystallographic study of precipitates

Dark field imaging is usually combined with the acquisition of diffraction patterns, recorded with the use of the selected area diffraction (SAD) method in order to aid the interpretation of the DF images. With this technique it is usually possible to classify the phases present in the studied area. If there are several phases, as in the case of specimens studied in this work, it is important to assign the spots to a right phase. Because the specimens were polycrystalline, they contain many randomly oriented grains. The chosen grain for precipitate analysis is observed with CBED conditions. If the specimen is thick enough for electrons to undergo multiple scattering (approximately > 80nm) Kikuchi patterns are seen [209]. These were used in this work as guides for sample orientation, aiding the sample tilting to an appropriate direction for diffraction patterns or high resolution imaging. Following the Kikuchi lines it is possible to set the crystal with the beam along a major zone axis like [001], [011], [111], or [112]. Then by spreading the beam and inserting the selected area aperture, the selected area diffraction pattern along one zone axis can be recorded. Such diffraction patterns may be useful for evaluation of lattice parameters of precipitates. However closer analysis revealed that in reality the amount of oxidation on the surface was higher than the amount of precipitates, and the weak spots were dominated by oxides, thus the diffraction patterns give little information about the crystallography of precipitates. It is not clear that the diffraction spots are coming from precipitate, leading to a conclusion as suggested above, that the contribution from oxidation is much higher than from precipitates, and the spots from precipitates are hidden beneath much more intense spots from the oxides.

A series of diffraction patterns was acquired for several samples and dark field images were acquired with the objective aperture placed where one of each where believed precipitate reflection should have been, assuming the known difference in lattice parameter between carbide and austenite and that the two form in a cube-on-cube orientation relationships. These DF images were acquired with the smallest objective aperture. In some cases the precipitates were observed, but they were usually accompanied by extensive strong contrast all over the observed area. Thus, it confirms the idea presented above that the oxide dominates the weak spots in the diffraction. For example, in the **Figure 42** the spots, which were chosen for DF imaging, were all major spots on the pink outline. The ones that are the corner, which is 002, 022, and middle 111 sometimes gave a glimpse of precipitates in DF. But the ones, which are connected to the pale green outline in the middle, gave nothing else than white, flat, wide-area contrast all over the specimen (it can be seen on some of the DF images for example **Figure 35** or **Figure 36**). So the crystallographic information determined separately from High Resolution STEM imaging is described in the next chapter.

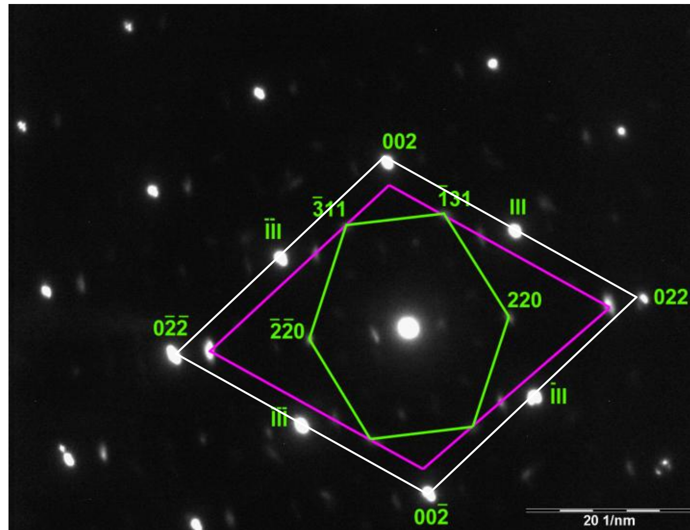

Figure 42. a) A [110] selected area diffraction pattern from a vanadium steel sample. Three groups of spots are indicated with coloured outlines: austenite in white, and two others in pink and green. Green is purely from Fe_3O_4, whereas pink may be a combination of Fe_3O_4 and vanadium carbide.

Figure 42 is a [110] diffraction pattern from the vanadium steel deformed for 100s at 900°C, apparently with three patterns superimposed. These are marked with white lines for the austenite structure, pink for the VC precipitate structure, and green lines for other spots that match neither. The white and pink are always present in a cube-on-cube orientation, which is very much as expected for a cubic rock-salt carbide growing in austenite. However with more detailed analysis, it was found using DF imaging that the spots lying on both pink and green outlines come from the same crystal – the surface oxide. All of this is consistent with cube-on-cube growth of spinel Fe_3O_4 (magnetite) on the surface. Whilst spots on the pink outline may include intensity from the vanadium carbide, these are lost under the intensity from the magnetite.

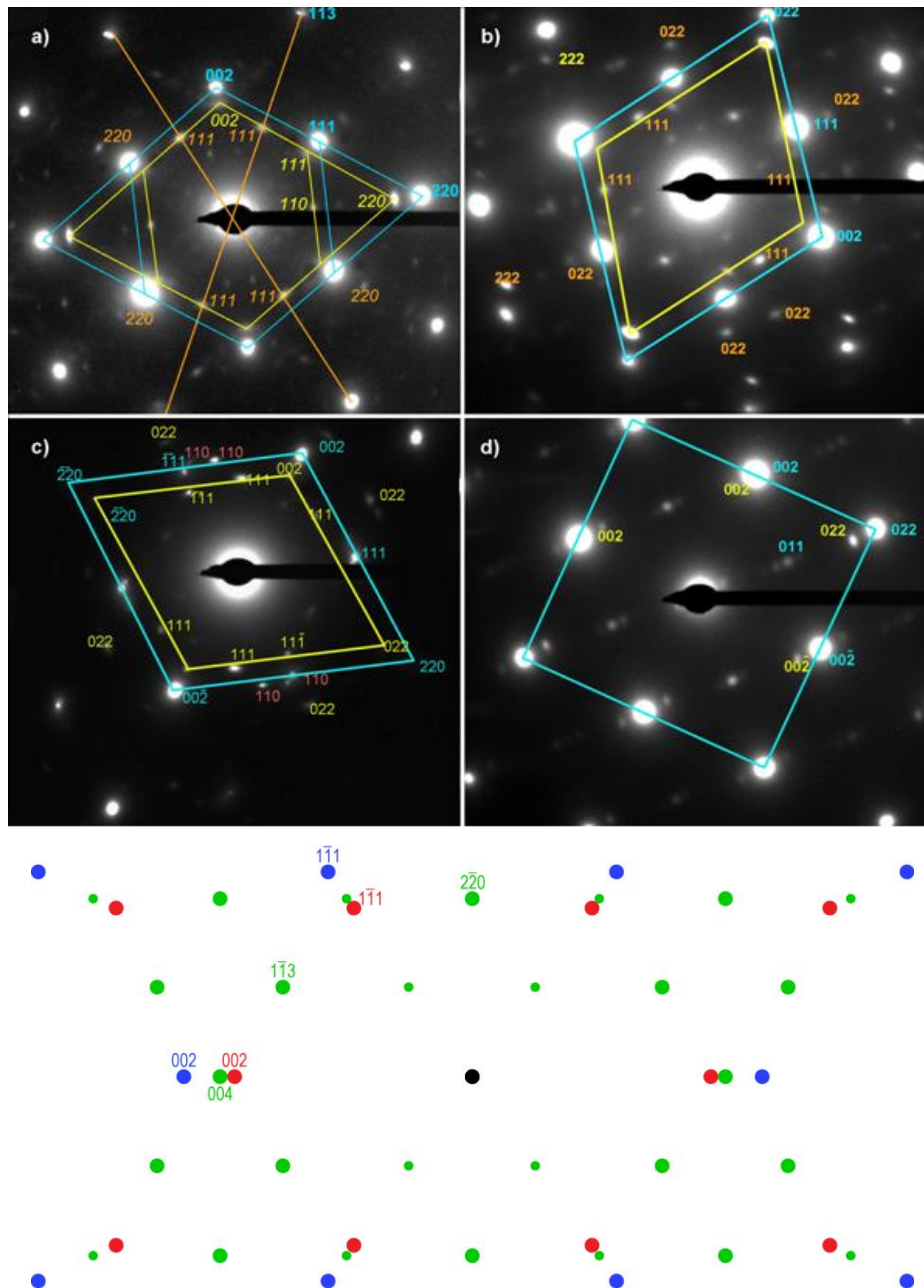

Figure 43. Zone axis diffraction patterns from Nb steels heat-treated for different times at 900°C showing weak spots originating from different sources. Pale blue refers to the austenite matrix; yellow refers to spots which could relate to NbC in cube-on-cube orientation relationship; red and orange refers to spots that relate to Fe_3O_4, but not in the cube-on-cube orientation relationship. e) Schematic diagram of the indexing a [110] diffraction pattern from cube-on-cube Fe-Mn, Fe_3O_4 and NbC, where green is Fe_3O_4, blue is austenite and red is NbC (for Fe_3O_4 large circles represent strong spots, and small circles represent weak spots).

Examples of diffraction patterns with beam directions along [100] and [110] are presented in **Figure 43**. **Figure 43a** presents a diffraction pattern recorded along the [110] direction from the 900°C/40s sample (deliberately overexposed to bring out the weak spots). As well as the expected

austenite spots marked in pale blue, there are a range of weaker spots. Whilst some of these can be attributed to double diffraction involving both a precipitate and the matrix, and thus need no further consideration, at least three clear patterns of weak spots were found. In this pattern, the austenite matrix spots sit on the cyan rhombus. The NbC reflections should sit on the yellow rhombus. These sit inside the austenite reflections since NbC has a lattice parameter about 23% larger than that of austenite, and thus we would expect that these NbC particles are mostly relaxed and either semicoherent or incoherent with the austenite matrix. Moreover, other spots are found with spacing matching those for NbC but not in a cube-on-cube orientation, these are highlighted in orange and include 111 and 220 spots. The spots with 111 spacing appear to point in the same direction as the 113 spots for austenite (as indicated by the orange lines), suggesting that these planes are parallel to 113 in the matrix. The angle between the spots with 111 spacing does not match expectations for a cubic system. The 111 spacing for NbC has a spacing that seems to match 111 for the FCC structure of NbC, but in reality they match semi-length of [113] when related to the FCC austenite As mentioned above these spots correspond to Fe_3O_4. The problem with the spots is for both VC and NbC structures, as presented in the **Figure 43e)**. It shows a [110] diffraction pattern including a few indices with austenite in blue, NbC in red and Fe_3O_4 in green. Strong Fe_3O_4 spots are large, weak spots are smaller.

The reasons standing behind difficulties with imaging precipitates are twofold. Firstly, because the VC spots are weaker and their distance between central spot and the actual spot(r_1, r_2, or r_3) is almost the same as the distance for Fe_3O_4. This is also a reason why the VC were barely visible by DF imaging, because the secondary contrast, coming from the Fe_3O_4 surface layer was diminishing the signal from all of the precipitates. Secondly, for NbC, the lattice parameter is larger, so the spots sit further inside the Fe_3O_4 spots (closer to central spot), and even if they are hard to see in the diffraction patterns, they do generate enough contrast in DF with a correct DF tilt (below the value to catch the austenite spot) to make good images, which is confirmed in **Figure 41**.

Figure 43b shows a diffraction pattern from close to the <110> plane for the sample isothermally held for 100s and many of the same features are seen. Again, the spots appear close to the expected orientations for cube-on cube precipitates (marked yellow). Again, spots appear in the other positions that fit NbC spacings but do not fit the cube-on-cube orientation relationship. **Figure 43c** shows similar features to the previous two diffraction patterns, but extra spots appear which do not correspond to austenite or to NbC. These could possibly fit α'-martensite and are indexed as such. Alternatively, these could also fit ε-martensite. It is uncertain why these are present, and future work will investigate whether these are a general feature of such materials, or whether these are a specimen preparation artefact. Later research proved that there is no

possibility, that martensitic transformation could take place in this material [134, 210], thus other contributions are mainly from surface Fe_3O_4. **Figure 43d** shows additional spots at 110 positions for the austenite, in addition to some spots for the NbC. **Figure 43e** shows that the spots marked in yellow and orange can all be attributed to epitaxial cube-on-cube oriented Fe_3O_4 on the surface, and any weak NbC spots would appear so close to the Fe_3O_4 spots that they would be impossible to separate. This therefore demonstrates that reliably separating precipitates by diffraction or diffraction contrast will be very hard, and therefore spectroscopic mapping will be a more effective approach.

5.4. Analytical characterisation using EFTEM

As shown above, DF imaging is not convenient for V-steel analysis, because it is extremely difficult to find and investigate precipitates containing this element. Energy Filtered TEM is a technique which gives complementary results to DF. Mapping regions full of precipitates with sizes down to a few nanometres is possible using EFTEM. One example of using this technique with V-steel is presented in **Figure 44** where five small precipitates are visible in the Ti and V maps. This did not only happen on this figure, but during all investigations the strong V signal is always accompanied by Ti signal, which indicates that the precipitation always occurs in the presence of Ti impurities. In several previous studies it was be found that TiN are favoured nucleation points for V carbonitride precipitation [81, 83, 211]. Whether this is the mode of precipitation here will be examined later in this thesis. Usually V-precipitates tend to occur in groups, and are less widespread than Nb carbides, which were more homogeneously distributed. Unfortunately it is impossible to precisely estimate the precipitates' chemical composition using EFTEM, both because this technique is difficult to make very quantitative, and because light elements like C, O and N were found to be hard to map in such small precipitates with the equipment used in this work.

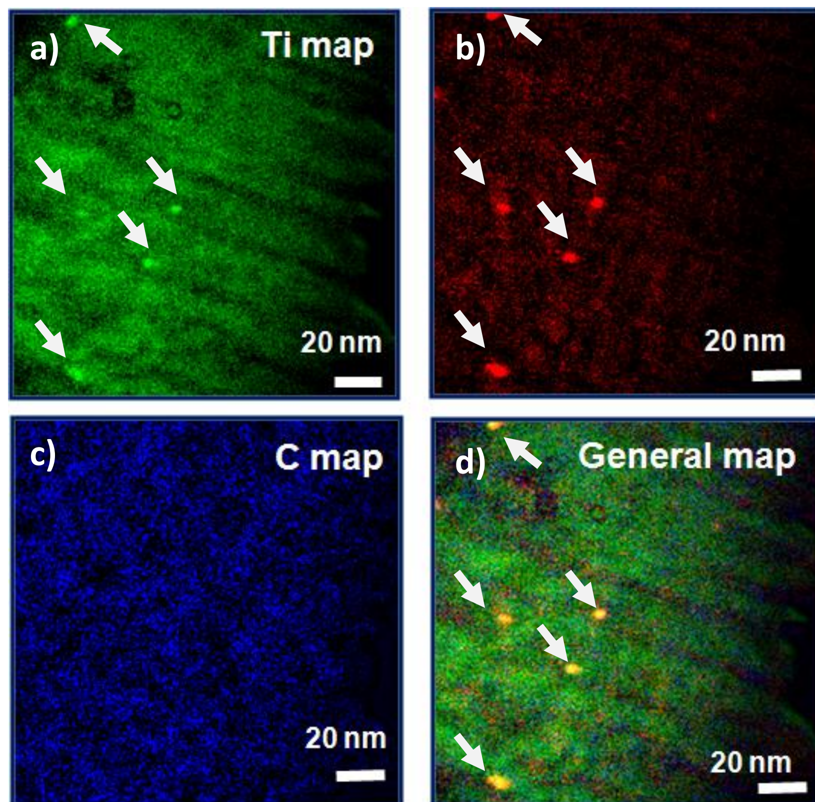

Figure 44. EFTEM imaging of a V steel held at 900°C for 100s: a) the chemical map of Ti, b) the chemical map of V, c) the chemical map of C, and d) a combined three colour map of the three chosen elements. The precipitates are highlighted by the white arrows on the Ti, V elemental maps, and general map. They are not visible in the C map.

Since EFTEM is not very quantitative for analysis, and because the field of view in STEM-EELS is much smaller than in EFTEM, this was mainly used to find areas which contain precipitates for more detailed analysis later in STEM-EELS. Later, when the specimen is put into the ARM, it is possible to magnify the area which is of high interest, avoiding wasting time for looking for anything useful for investigation. One such example is presented in **Figure 45**, which is an EFTEM image of a V precipitate. This is an image taken using the V-$L_{2,3}$ edge, which is at 513eV loss, with a slit width of 20eV. This gives enough contrast to image precipitates for further EELS studies using ARM microscope.

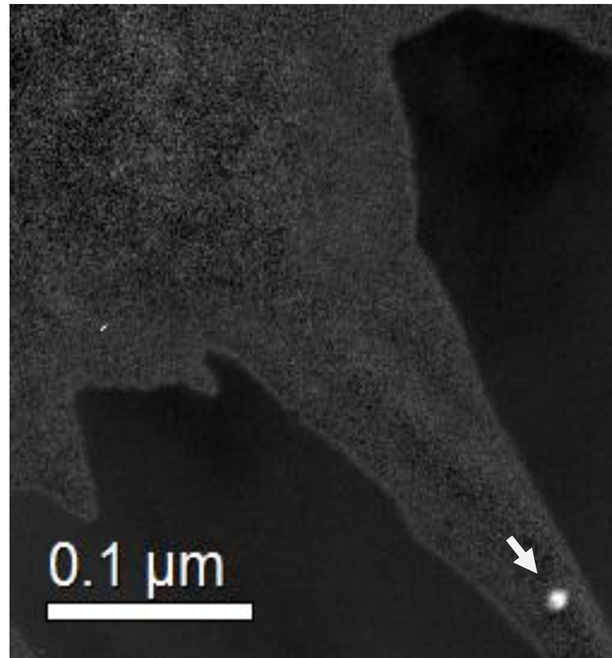

Figure 45. EFTEM image taken before ARM session prior investigation is to find desirable area for spectrum imaging. This is a V steel isothermally treated for 100s in 900°C, which in a very thin region has clear precipitate of a size of 20nm (see white arrow)

It was also possible to map Nb precipitates with the EFTEM technique. Due to the wide and slow onset of the $M_{4,5}$ edge starting at 205eV loss, the $N_{2,3}$ edge at 34eV was used for mapping instead. This peak in the low-loss region is easier to use and has a sharper onset, and it forms better maps, as previously noted by Courtois *et al.* [114]. The Nb $N_{2,3}$ map in the **Figure 46** is created with high contrast proving that this edge is good for Nb mapping using EFTEM technique.

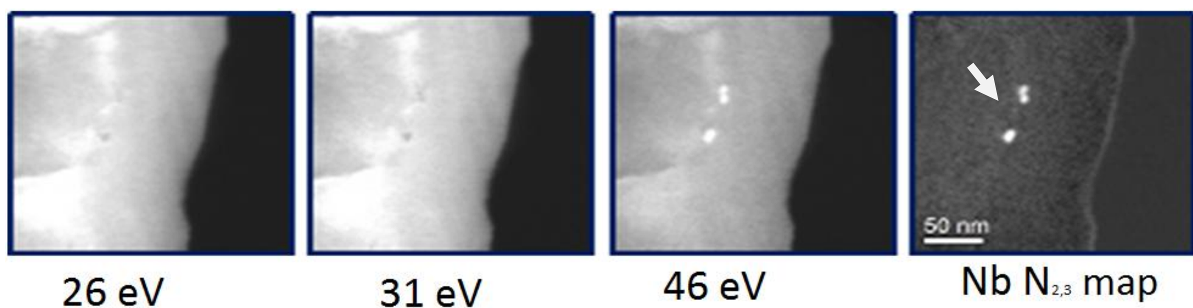

Figure 46. EFTEM three window method of Nb $N_{2,3}$ edge imaging of three precipitates. The specimen was isothermally held for 40s at 900°C. Two pre- edge windows starts at 26eV and 31 eV loss, and the post-edge window starts at 46eV. The last image presents the subtracted edge signal. The images presents three precipitates which nucleated on dislocation (see white arrow), which have approx. 15nm.

As was described in previous paragraphs, both DF and EFTEM give good results for imaging precipitates in Nb-steels, in contrast to the V-steels where DF was ineffective. Therefore there are several datasets combining both techniques, some of which are presented below. In **Figure 47** there

are two DF images taken with different conditions together with an EFTEM image, all of the same precipitates. DF1 shows mainly contrast from grains and crystal defects although a possible hint of precipitates can be seen. DF2, in contrast, is a dark field condition that just reveals three precipitates. The EFTEM image created using the Nb $N_{2,3}$ edge reveals the same three precipitates. Therefore, in this case, all three images confirm the presence of three particles in the same position, and the last confirms that they contain Nb.

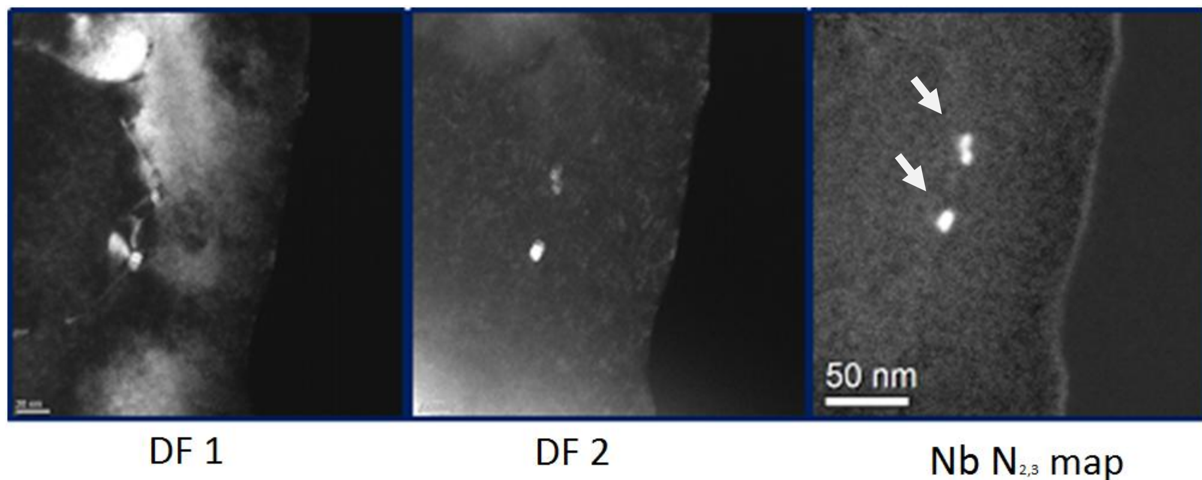

Figure 47. Nb-steel specimen imagined with DF and EFTEM isothermally held for 40s at 900°C. a) Precipitates nucleated on dislocations or grain boundary recorded with the DF imaging technique; b) precipitates observed by DF with different imaging conditions than a); c) EFTEM imaging using energy loss $N_{2,3}$-edge at 34eV, matching the Nb edge. The images presents three precipitates which nucleated on a dislocation or grain boundary (see white arrow), which have approx. 15nm.

The EFTEM technique is very convenient for Nb-steel observations. It works better than DF, and is sufficient enough to map precipitates down to 4nm. EFTEM has the advantage over DF in that it leaves no doubt as to whether something is a diffraction contrast of something other than a precipitate. **Figure 47a** shows an example where there might be some doubts if observed bright spots are really particles, or not. The second two images confirm this, but if the conclusions were made based only on image a) they would be less certain. EFTEM is also very sensitive in detection of small precipitates, as shown on **Figure 48**, where the particles as small as 4-5nm were observed and successfully mapped.

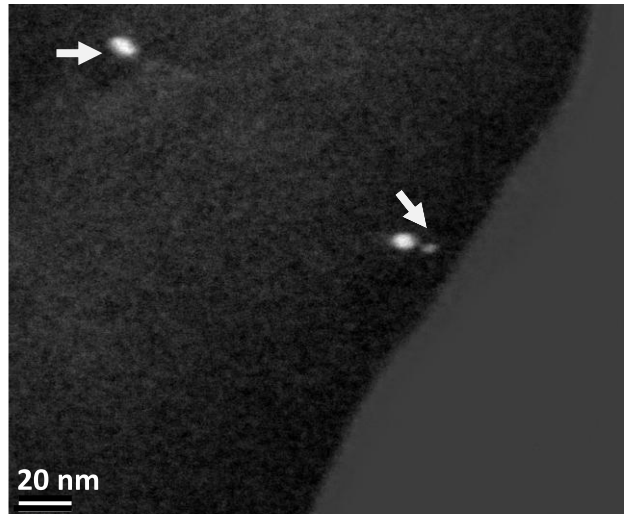

Figure 48. EFTEM mapping with the Nb $N_{2,3}$ edge down to 4nm sized precipitates in a steel isothermally held for 40s at 900°C. Three precipitates are recorded (see white arrrows). Two of them have the size of about 8nm and one is half that size. The top one has elongated shape, whereas the two below seem to be round.

In the **Figure 46, Figure 47, Figure 48** and **Figure 49**, it has been shown that precipitates can be mapped using EFTEM with C-K, Nb-$M_{4,5}$ and Nb-$N_{2,3}$ edges, and can be imaged using conventional dark field methods. **Figure 49** shows a comparison of C-K jump ratio and Nb-$M_{4,5}$ jump ratio maps for a group of precipitates in a Nb-steel. As it was described above, the $M_{4,5}$ edge, in particular, leads to weak contrast in EFTEM and it is difficult to image the precipitates using this. In EFTEM, it is much easier to use the lower energy $N_{2,3}$ edge at which there is both more intensity and higher contrast and this is shown in **Figure 49c**.

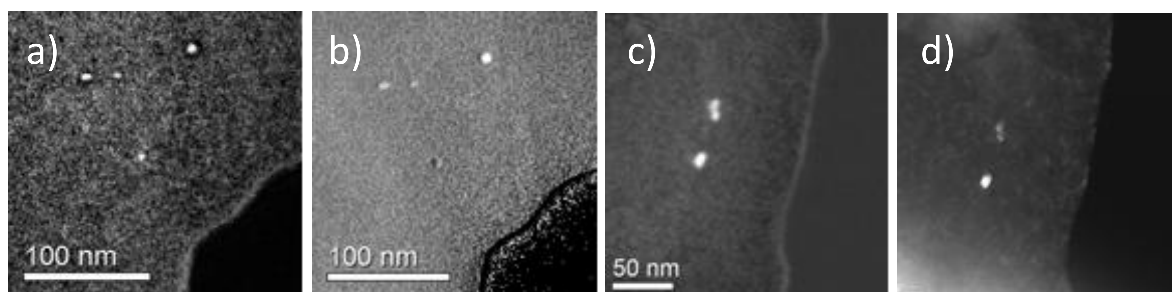

Figure 49. Mapping and imaging of C and Nb in precipitates using EFTEM in sample isothermally held for 40s at 900°C: a) jump ratio image at the C-K edge; b) jump ratio image at the Nb-$M_{4,5}$ edge; c) elemental map at the Nb $N_{2,3}$ edge (a slightly different area); d) dark field imaging of a the precipitates seen in c).

5.5.Analytical characterisation using EELS – preliminary results

EELS mapping starts with HAADF imaging using the Gatan HAADF detector at a 2cm camera length with the CFEG noise cancellation on. Using this detector allows precise area selection, because there is enough contrast to record the image, and sufficient signal for EELS later on. Then

two areas need to be chosen: an area of interest for spectrum imaging containing a precipitate, and a second area free from precipitates, but with some clearly distinguishable features useable for alignment. The first one is used to record a spectrum image and the second is used for spatial drift correction. One problem with such EELS studies is that they can be slow to record maps with larger numbers of pixels, and this can result in carbon contamination on the surface if the specimen or holder is not totally clean. Fortunately, the microscope and spectrometer allowed good quality spectra to be acquired rapidly, enabling the measurement of volume fraction and volume distribution. Also, another consequence of these capabilities is the post-processing technique described in chapter 6, which reveals a lot of useful information which was not possible to obtain before, i.e. chemical profiles, absolute thickness, or pseudo-3D representation of individual precipitates.

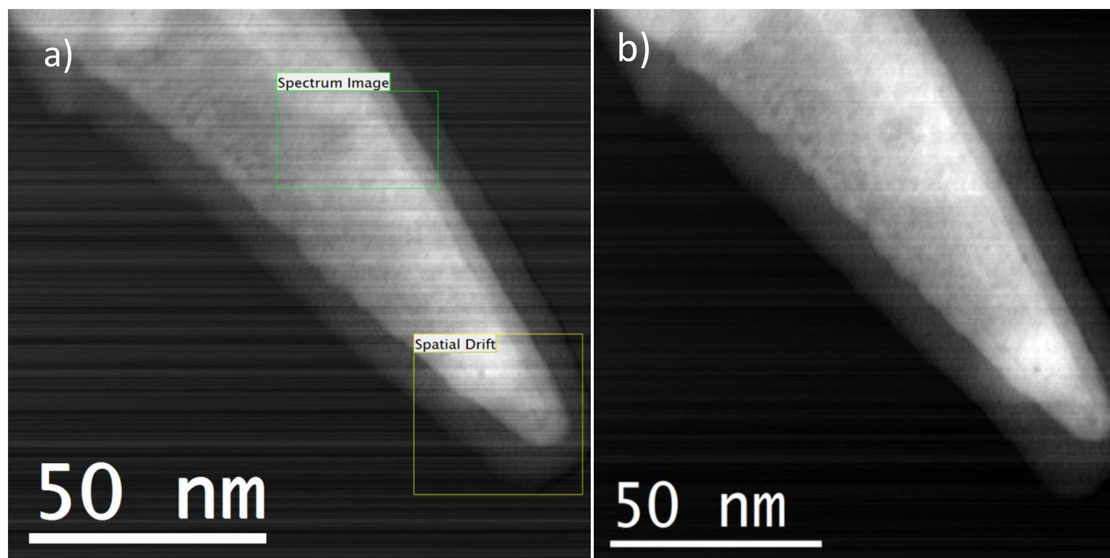

Figure 50. LEFT: The survey image for spectrum imaging from V steel isothermally treated for 100s in 900°C. Two areas highlighted – area of spectrum imaging data, and of spatial drift. a) The HAADF image without noise correction image taken with Gatan detector on ARM before the spectrum image is taken, b) The HAADF image without noise correction image taken with Gatan detector on ARM after the spectrum image is acquired. There is a significant improvement in the quality of the image with the noise cancellation on. Unfortunately in the region of spectrum image and spatial drift there is a huge amorphous carbon contamination due to the thigh current in ARM (brighter circles).

The precipitate shown in **Figure 45** was studied using DualEELS mapping. The survey image is shown in **Figure 50a**. In these figures there are two regions highlighted used for mapping. The green area called spectrum image and yellow called spatial drift used for correction of drift. There is a precipitate in the green box, however the contrast is weak and the precipitate is barely visible. Therefore the results from EFTEM shown in **Figure 44** were essential in finding the correct area for analysis. **Figure 50b** shows a HAADF image which was taken with noise cancellation after acquiring

the spectrum image. The figure shows a common problem during spectrum imaging in ARM, which is the carbon overbuild on top of the studied area. The current on the sample is very high, and as a consequence any residual organic contamination causes the growth of carbon in the area of interest – which is particularly noticeable in the area of the map (which is the green box named "spectrum image"). This shows how important is specimen preparation, cleaning prior inserting into the microscope, and clean storage in vacuum desiccators. **Figure 51** shows an early mapping of elements from a precipitate in a V-steel covering the region of interest in **Figure 50**. The spatial resolution is much better than EFTEM images, however this experiment was still rather preliminary and major technical optimisation was required to make such maps fully quantitative. The analysis revealed a co-formation of Ti and V of the precipitate, similarly to EFTEM images. Unfortunately due to growing carbon contamination it was impossible to quantify the amount of this element present in the precipitate.

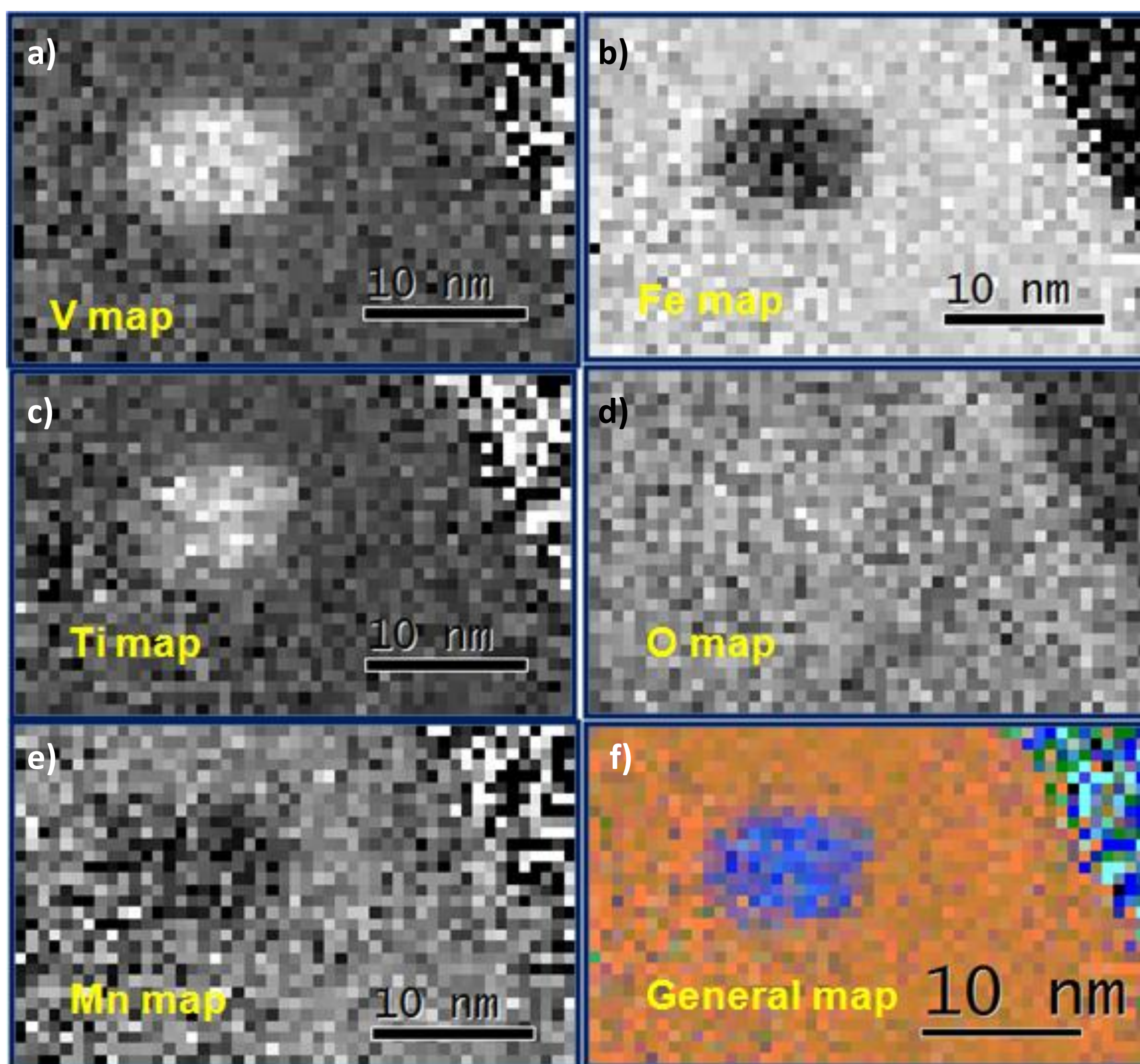

Figure 51. Elemental maps obtained by post-processing of a spectrum image from the V-steel held at 900°C for 100s using standard procedures within Digital Micrograph: a) vanadium; b) iron; c) titanium; d) oxygen; e) manganese; f) multicoloured map with iron in orange, vanadium in green and titanium in blue.

Profiles of the chemical composition were taken across the particle of **Figure 51** in vertical and horizontal directions, and these are shown in **Figure 51**. In the horizontal direction (**Figure 52a**) the particle was about 15nm long, whereas in the horizontal direction (**Figure 52b**) it was approximately 8nm. Moreover the chemical profiles reveal that there is no core-shell structure of V-Ti within, since there is no sharp switch in Ti and V between the inside and outside. The meaning of this observation will be discussed later after improved mapping techniques are developed in the forthcoming chapters. One thing that may be noted is that the maps and profiles are very noisy, and that it would therefore be difficult to measure small compositional changes in the precipitate with the technique as it is – further developments of the acquisition and post-processing procedures to overcome these limitations are described later in this thesis in chapter 6.

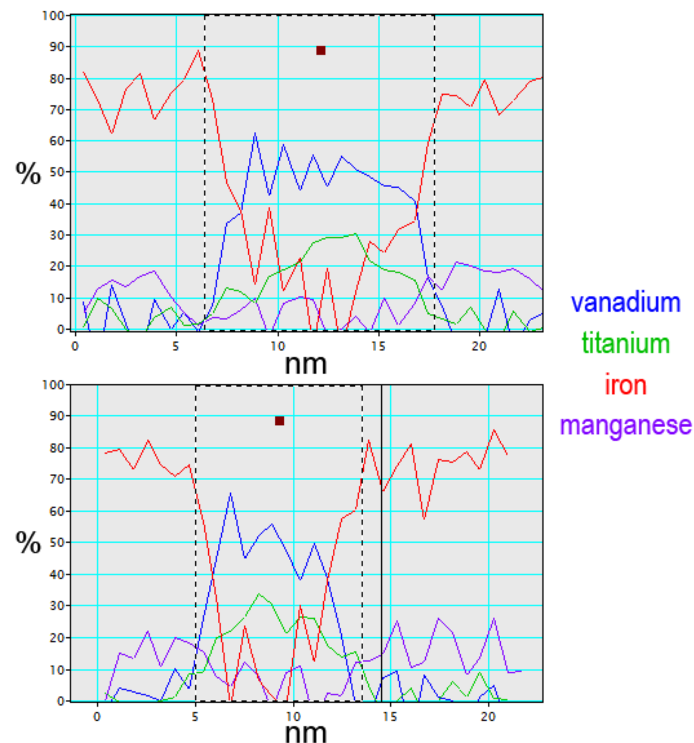

Figure 52. Chemical composition profiles across the precipitate of Figure 51. A) horizontal profile, b) vertical profile. Blue indicates vanadium, green – titanium, red - iron, and violet - manganese.

5.6. Atomic resolution imaging of precipitates

Whilst performing atomic resolution imaging with HAADF imaging in the STEM was not the main focus of this thesis, some imaging was performed in both V and Nb steel samples. In **Figure 53** the dark shadow is a V-precipitate, which shows the difficulties with the contrast (the vanadium is darker than the matrix, which makes it harder to separate from matrix). In HAADF imaging the contrast depends on the atomic number, Z (usually believed to be proportional to Z^n where $n < 2$, ignoring any channelling effects). In this case, there is only a small difference between $Z_{Fe}=26$ and $Z_V=23$. Additionally, about half the atoms in VC are C atoms with Z=6. So VC precipitates will show as less bright than the Fe-Mn matrix, which is the reason they show such poor visibility. For this reason, little of value was done with atomic resolution HAADF imaging for V steels. This image, for example shows Moiré fringes over the whole area, which probably come from semicoherent oxide on the surface.

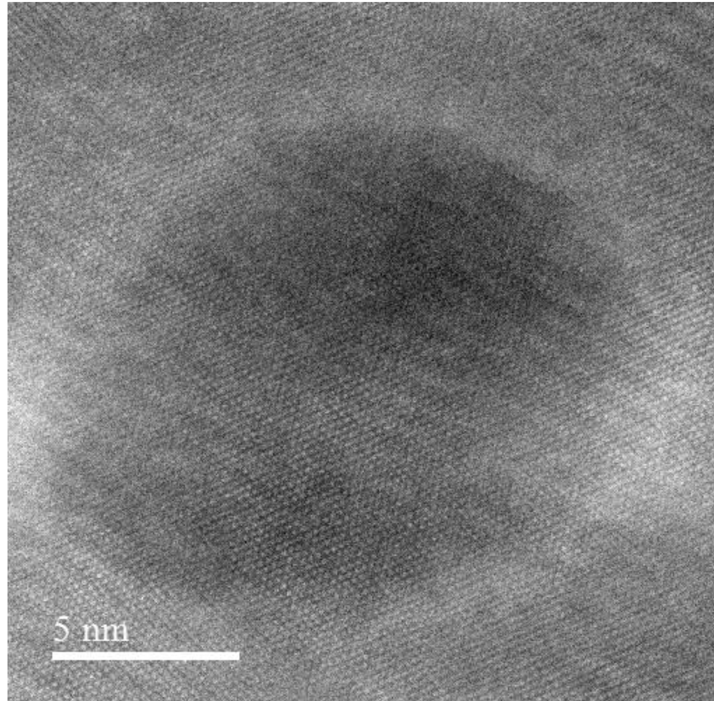

Figure 53. Atomic resolution HAADF image of a precipitate in a V steel held at 900°C for 100s. The light grey region represents the matrix, the darker shade of circle represents the vanadium precipitate of size about 14nm.

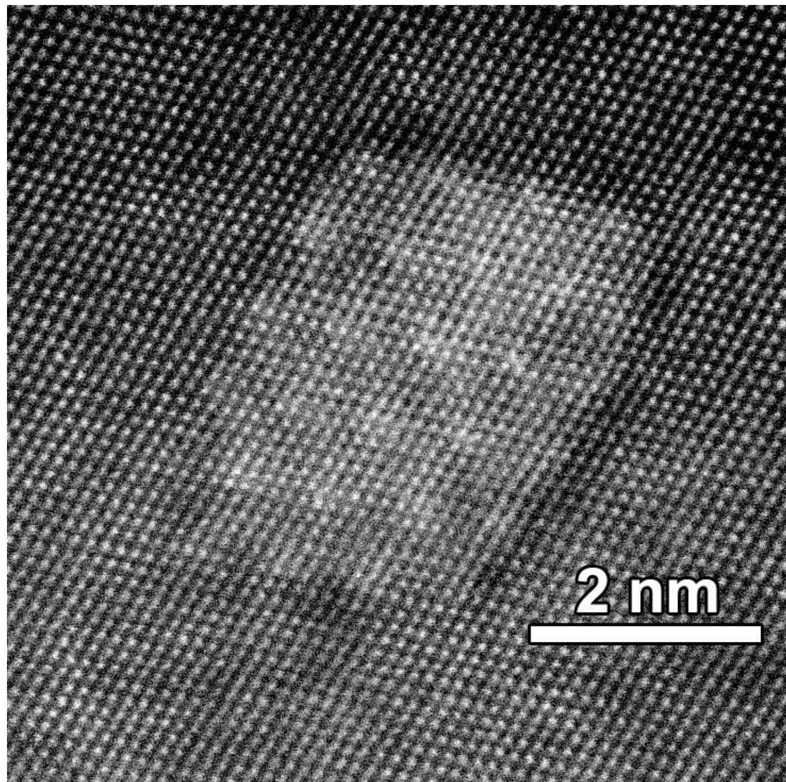

Figure 54. HAADF STEM image of a carbide in the Nb steel viewed along [011]. The darker spots represents the matrix, whereas the lighter spots represents the Nb precipitate of size approx. 8nm. The precipitate is on cube-on-cube orientation with the matrix. Also the Moiré fringes can be seen across the precipitate suggesting the lattice parameter mismatch between matrix and precipitate.

An atomic resolution HAADF image of one precipitate in a Nb steel is shown in **Figure 54** recorded along the [011] zone axis. This shows much better contrast along this direction as Nb has a much higher atomic number than Fe, so the Nb columns will show up bright, as observed. The image shows a precipitate with a cube-on-cube orientation relationship to the matrix and with a clearly faceted shape dominated by (111) planes, but with shorter facets on (200) and (220) planes. This suggests that these may be favoured low-energy interface planes between the carbide and the austenite matrix. A regularly spaced array of Moiré fringes is seen across the carbide, because of the lattice parameter mismatch to the austenite. This allows an estimation of the lattice parameter as 4.41Å. With such mismatch it can be said that the particle is semi-coherent, with lattice parameter close to the bulk lattice parameter of NbC.

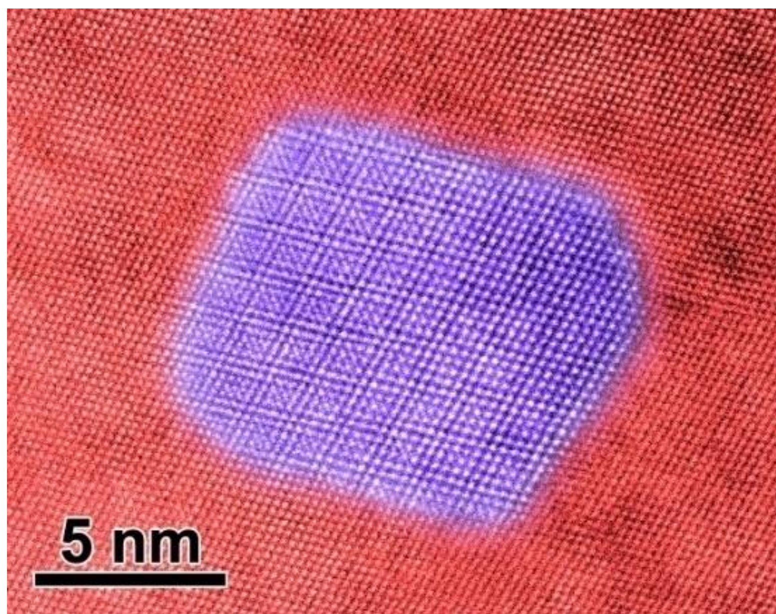

Figure 55. The HAADF image of NbC particle surrounded by the matrix. The image was acquired with a Jeol ADF detector at 8cm camera length. The red spots represents the matrix, whereas the violet spots represents the Nb precipitate of size approx. 11nm. The precipitate is on cube-on-cube orientation with the matrix. Also the Moiré fringes can be seen across the precipitate suggesting the lattice parameter mismatch between matrix and precipitate.

Figure 55 presents another HAADF STEM image of a Nb-carbide precipitate. In this case, Photoshop was used to highlight the matrix in red, whereas the precipitate was given a purple. The analysis of the image reveals that the lattice parameter of this particle is approximately 4.41Å, and it has a width of 8.5nm and a length of 10nm. The lattice parameter differs slightly from the known literature value of 4.4702Å for NbC [212]. The reason for this will be discussed later once chemical analysis of such precipitates has been performed. The mismatch between the matrix, which has a lattice parameter of 3.668Å, and the precipitate is 16%. The interface appears to be semi-coherent.

As for **Figure 54**, the favoured interface planes are (111) and (200). There are also two short (220) planes.

5.7.Final conclusions

In this chapter the main focus was on microstructure analysis of specimen containing precipitates. It was proven that the precipitates can be found for detailed analysis using EFTEM along (V steels) or a combination of EFTEM and DF imaging (Nb steels). For vanadium steels DF imaging is somewhat impeded, due to the surface oxide. This oxide is also present in the Nb steels, however the contrast for Nb-carbides is much higher, so they can stand out. The oxide present on all surfaces may affect chemical mapping. It was also shown that STEM-EELS mapping is possible for both V and Nb precipitates, but using standard, well known techniques results in noisy maps, which were unable to separate amorphous carbon or any other surface contaminations. In all spectrum images formed with EELS and on filtered images created with EFTEM technique the Ti is routinely present in all V and Nb carbides.

The HAADF imaging showed that all the precipitates have a cube-on-cube orientation relationship with the austenite matrix, as expected. Some of the larger ones show strong faceting onto mainly {111} close-packed planes.

Unfortunately, these techniques are not sufficient enough to examine such small precipitates with a fully quantitative manner. To get more quantitative data in the chemical analysis of the precipitates there is a need for more careful methodological development, to fully exploit the possibilities of DualEELS – this is the subject of the following chapter.

6. Development of a post processing routine for extraction of precipitate spectrum images from the matrix

6.1.Background and issues of post-processing

Spectrum images are datasets that contain plenty of information about a specimen is chemical composition. However, the extraction of the information requires detailed, multistep processing, with the use of special software such as Gatan's Digital Micrograph. Although Digital Micrograph is well known and well developed, its capabilities are often unrecognised, especially with the capacity for scripting complex functions. In this work, it was a useful and irreplaceable tool in development of a combination of steps based on EELS Analysis tools and the Spectrum Imaging package to reconstruct all necessary knowledge about the chemistry of nanosized particles . This development required detailed understanding of the impacts of certain factors affecting the quality of the data, such as the quality of the specimen, the characteristics of the electron beam, the conditions of microscope and the quality of spectrum image itself (and how this was set up). The quality of specimen and optimisation of its preparation was already discussed in chapter 4.

The chemical composition or the thickness evaluation of the nanoprecipitates is a key point in their characterisation, as it can lead to the evaluation of the carbon to metal ratio, kinetics trends, or 3D localisation of elements within the precipitate. Conventional (non-quantified due to the lack of ZLP in core-loss region) elemental maps are a very useful tool, but they only give limited information, principally an estimated chemical relative composition. Absolute analysis of elemental contents should be possible with DualEELS [133]. It should also be possible to reduce the noise in the analysis by appropriate use of both acquisition conditions and statistical techniques. The processes developed for the purpose of this project allow the user to make useful conclusions from most collected data, even noisy datasets, and to reveal and quantify more detailed features, such as small (few atoms) N contents in carbides.

The fundamental post-processing idea was to remove the matrix signal, so the final result will be a precipitate-only spectrum image, which when quantified can give absolute atomic contents, and in some cases a 3D pseudo-reconstruction. However, as the preliminary results show, the spectrum image did not contain only signal from matrix and precipitate as was initially (and naively) believed. There are number of issues that had to be overcome to reach this fundamental goal. So, to overcome these issues, arising from different origins, the post-processing procedure set out in this chapter was developed. This requires a specific order of actions, to prevent the reproduction of

errors and creation of artefacts, and to minimise any systematic errors. This allowed the extraction of reliable precipitate signals from the specimen with a high enough intensity to use them for absolute quantification.

The issues that had to be dealt with arise from three sources, which were (i) instrumentation, (ii) the specimen and (iii) the inevitable shot noise in the data. These were the principal sources identified here, although further sources of noise or problems may need consideration in future research, beyond the scope of this PhD. These sources of problems could cause more than one type of issue, some of which were challenging to overcome. For example, from instrumentation there were problems with instabilities and drift in the accelerating voltage and spectrometer magnet current, which result in shifts of the position of the spectrum on the CCD detector. Also, in addition to a spectrum of energy loss electrons, a high energy x-ray or cosmic ray can from time to time hit the scintillator, resulting in a ZLP-like intensity peak in one, or a few neighbouring CCD pixels: these are usually called 'x-ray spikes'. The extreme right and left hand side of the end parts of spectrum usually suffer from a tiny loss of collection efficiency and may thus have reduced intensity. The most important problem, that prevented ongoing work from progress was the so called 'bleed-through' of some fraction of the core loss signal to the low loss spectrum, probably as a result of multiple electrons backscattering (at many angles) inside the detector chamber. Some of the earlier spectra also suffered from non-linearity in dispersion, which due to the relatively low dispersion used in the research was a significant problem for quantification of the edges.

The sample issues arose from the differences between the ideal sample, where only matrix and precipitate would be present, and the real sample, where the matrix was covered in a uniform, thin layer of epitaxial Fe_3O_4 on its surface, often superimposed by a layer of amorphous carbon of variable thickness from stray hydrocarbon contamination. it has a variable thickness, because it grows under the beam, not by the epitaxial growth like in case of the oxygen. These ideal and real cases are shown schematically in **Figure 56a** and **Figure 56b** respectively. For simplicity, the surface layers are shown on one side only. The presence of them is confirmed: the Fe_3O_4 is visible in DP as additional spots inside the spots related to matrix and as a thin, mostly even layer in HAADF images; the C is also visible in HAADF images as growing contamination during DualEELS acquisition as a bright spot before the acquisition, and brighter, less transparent white spot, or even as a area, which was of chosen spectrum image region.

Correction for these residual surface contributions is made at the end of the processing procedure. More details about issues with the specimens are described in the subsection on matrix subtraction below.

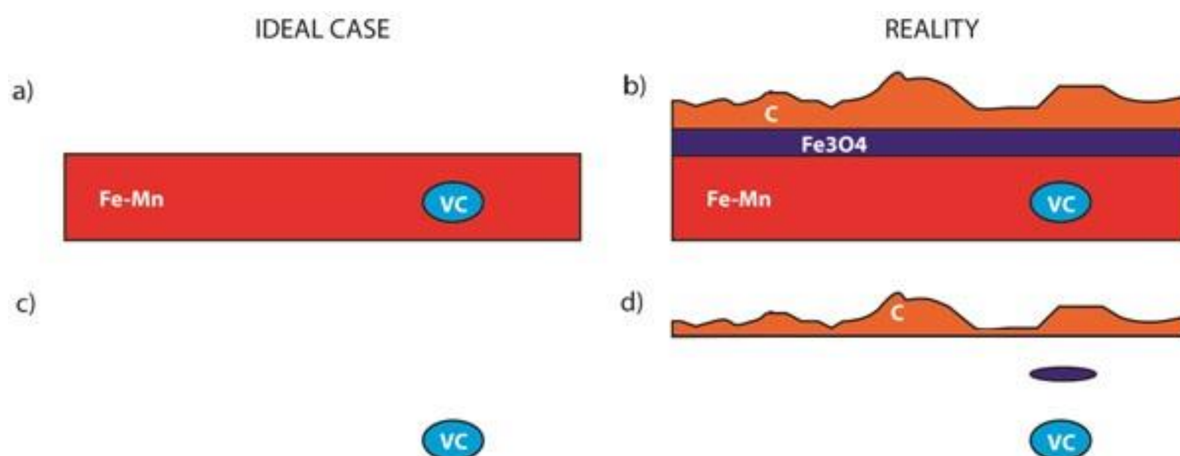

Figure 56. Schematic diagrams of the ideal (a) and real (b) samples with the contributing material left after removal of the matrix in the ideal (c) and real (d) cases. All the Fe_3O_4 and amorphous carbon are shown on one surface for clarity.

The optimal quality of spectrum is dependent on the energy resolution, signal-to-noise ratio (SNR) and signal-to-background ratio (SBR), however it is impossible that all of them will be optimised concurrently, as they are have contradictory requirements. The energy resolution is strongly connected to the type of electron source and the filament emission current, but also to the focusing parameters (or dispersion) of the spectrometer and the details of the CCD detector. By screening out any effects of external conditions (e.g. magnetic fields, vibration), and reducing the energy spread of the electron source, the spectral resolution can be improved. The SNR is determined by the number of electrons reaching the detector, which is controlled by both the electron source and its emission current, but also by the size of condenser aperture and by the effective collection angle at the spectrometer (which could be controlled by an objective aperture, the spectrometer collection aperture, the camera length of the microscope, or by distortions and aberrations in the projector lens system). For the core-loss region the SNR increases with increasing current in the probe or with increasing exposure time. The detection sensitivity or visibility of edges in EELS is also limited by the SBR, which is limited by the thickness of the sample, the concentration of the element of interest within the sample, and the spectrometer collection angle. Higher acceptance angles tend to include more electrons from plural scattering by valence electrons, which mainly form the background signal, thus limiting the collection angle increases the SBR. Since the SNR and SBR both depend on collection angles in opposite senses, a balance is required. This is usually best when the collection angle is just larger than the probe convergence angle. These considerations demonstrate some of the compromises that must be met to collect good quality data, which is as easy as possible to interpret and quantify. These experimental optimisations make it easier to use the post-processing sequence set out below in the most effective way[113, 213].

6.2.Post-Processing steps

The whole idea of post-processing is driven by the DualEELS spectrum image datasets to allow the extraction of the precipitate signal from the matrix and all other extraneous signals in the dataset to allow subsequent quantitative analysis. This proceeds by the following recipe:

1. Energy alignment of all spectra and preparation of the data for Principal Component Analysis (PCA), including removal of X-ray spikes and trimming of the edges of the spectrum images
2. PCA to remove random noise from both the low-loss and high-loss spectra
3. Splicing of the datasets, after the removal of any background stray signal in the datasets and smoothing the low loss
4. Deconvolution of the plural scattering from the spliced spectrum image using the Fourier-log method
5. Estimation of the matrix spectrum and the creation of a matrix-only spectrum image, on the assumption that the precipitate contains no Fe, followed by subtraction of this from the deconvolved spectrum image
6. Separation of the precipitate spectrum image from any amorphous carbon on the specimen surface using MLLS fitting
7. Quantification of all elements in precipitates by determination of the mean free paths and partial cross-sections of each present phase in the precipitate

This procedure should then yield a spectrum image containing just signals from the precipitate and a low level of noise outside, which would then be suitable for detailed quantitative and qualitative analysis. The present chapter describes this processing procedure in detail, together with some of the problems that can arise and how they may be overcome. Also the quantitative analysis of the extracted precipitate datasets is discussed in **chapter 7.** For better understanding the scheme of each individual steps and alternatives is presented in the **Figure 57**. Each of the boxes (steps) were described in next paragraphs.

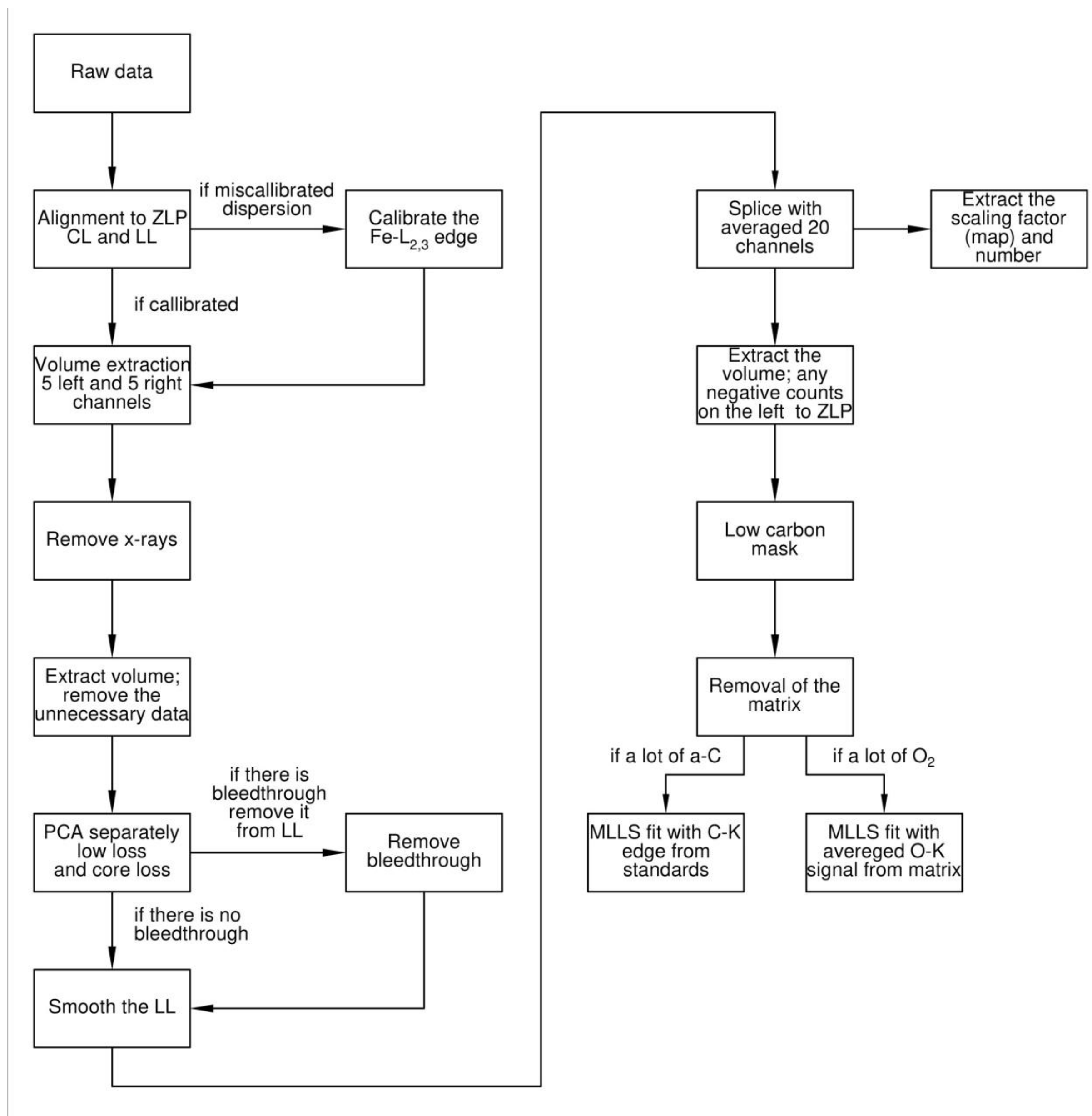

Figure 57. Schematic graph of individual post-processing steps for removal of the matrix, and unwanted signals resulting in precipitate only signal.

Cleaning the spectra with PCA

The multistep post-processing procedure starts with cleaning the spectrum prior to splicing, to avoid discontinuities at the splice point, which will perturb the future background subtraction in front of the Nb-M edge and C-K edge. The procedure consists of few steps from which the first one is aligning the zero loss peak. This allows correcting zero-loss drifts related to at least three sources: random small shifts, larger abrupt shifts or scanning effects. The first ones are related to instabilities in high tension, or other stray or high frequency electromagnetic signals. The larger shifts are related to pseudo-DC fields shifting on a timescale of seconds, for instance due to the subway 600m away. The scanning affects the optical projection of electron beam through the column in the way

that the diffraction pattern is static at the EELS entrance aperture and then, the energy position of the spectrum on the CCD is moved with the scan position. This routine first determines the energy drift of the zero-loss peak from zero eV for spatial pixel of the spectrum image as a drift map, and then shifts the energy scale of each spectrum to centre the zero loss peak in each pixel's spectrum, followed by applying the same energy shifts. After this re-alignment, the peak of the ZLP is calibrated to be zero and, in the ideal case, the equivalent channel in the core loss spectrum is calibrated to a value equal to the offset voltage applied to the spectrometer drift tube. However, because of the non-linear dispersion in the spectrometer in some earlier datasets, prior to a complete realignment, edges are slightly miscalibrated in position in such datasets, and the strength of the effect depends on energy loss. Thus, a standard procedure in such older datasets was to set the onset of the Fe L_3 white line to 708eV. Below this energy (between ZLP and Fe L_3 white line), this results in edges appearing at energies slightly different to their tabulated values, for example shifted by 3eV to the right or left.

Energy alignment was followed by the volume extraction routine, which, when considering the spectrum imaging as a 3D volume with axes of *x*, *y* and *E*, extracts a smaller volume without the 5 leftmost and rightmost E channels to avoid shifts and artefacts in these last few channels at the edges of the CCD. Usually, there is a slight roll-off of intensity at the left edge of the CCD.

The outcome of PCA noise reduction is found to be more successful if the x-ray spikes caused by spurious internal scattering and external radiation and are first removed. In the case of the x-ray spikes, the inbuilt routine in Digital Micrograph 2.3 "*Volume → Remove X-rays*" was used. The routine compares the numbers of counts in each channel in each pixel with the number in its neighbours and if any channel count deviates by more than 10 standard deviations, its value is set as the local median. If this is not performed prior to Principal Component Analysis (PCA), these appear as extra components in the PCA decomposition and make the separation of real signals from noise more difficult.

Noise in the data is always an issue in spectrum imaging because of the limited dynamic range of the EELS detector and the limited dwell time imposed on spectrum image acquisition by system stability and/or operator patience. Principal component analysis (PCA) is a statistical method that separates out the information present into a number of components. A limited number of components carry most of the information while the rest contain only noise. Unfortunately, the information contained in the individual components is not easily interpretable in physical terms. However, the data can be reconstructed using only the information-containing components, thus ruling out the noise [214]. Care has to be taken not to introduce additional artefacts by excluding components which actually contain significant information. In principle, PCA should be applied to

the as-recorded data. In practice, the artefacts in the data appear as information spread over a wide range of components. Thus, a pragmatic approach is taken and PCA is applied at the most effective point in the processing procedure.

The realignment of the spectra causes a small range of channels at each end of the spectra to contain unreliable data. In addition, two other effects can be dealt with at this point: one is the loss of detection efficiency at the ends of the spectrum due to shadowing, and the other is there can be areas of the spectrum image where the acquisition was corrupt for one reason or another. If not removed, these effects can cause problems in subsequent processing. The "*Volume* → *Extract* → *Extract Volume*" function in GMS 2.3 is used to select the central region of the dataset where these effects are not present and thereby cut of the outside edges containing the alignment and other artefacts.

The experience of post-processing in this work reveals that it is better to perform the PCA on heavily truncated datasets (on the energy scale). As described in previous paragraphs, the artefacts during applying PCA can generate fake pixels, which then generate errors during Fourier deconvolution. Thus, the best way to perform PCA is to truncate the dataset in energy as much as possible, leaving only the important range of the energy loss in the low loss and core loss spectra. In the case of the low loss it is a range from the negative energy tail of the ZLP up to a little beyond the splice point, which is usually chosen to be ~ 50eV beyond the predicted splice point (in most cases it is around 250eV for steel specimens used in this research, but it might be different for other materials). For the core loss it is from the beginning of the dataset up to the extended features of Fe-$L_{2,3}$ edge (e.g. to 800 eV). Such prepared data should not generate any fake pixels, or steps on splice point after further processing.

PCA is then applied to both low loss and high loss datasets to separate the clear, real spectroscopic signals from random noise in the datasets [214] using the Multivariate Statistical Analysis plug-in of Lucas *et al.* [215]. According to Lichtert and Verbeeck [216] it has to be taken into account that PCA may add some artefacts to the spectrum image, such as fake pixels. PCA allows the evaluation of the number of components with little significant noise based on the scree plot, to determine which should be used for further reconstruction of a noise-reduced spectrum. The scree plot is a logarithmic scale showing eigenvalues versus number of components. The eigenvalues containing the information about the random noise decrease exponentially, thus the experimental noise should be in the region of the graph, where the line is straight, and those components should be excluded from reconstruction. It may happen, however, that the different with numbers of components in order to determine how many are needed to include all features originating from the

sample in the spectra in the spectrum image whilst minimising noise. In this thesis the number of components was usually below 20.

While this approach works well for the V steel data, PCA does not significantly reduce the noise in the low loss data from the Nb steel. Here, a big improvement in noise reduction by PCA is found if the region prior to the zero loss peak and that above 250eV (well above the splice point energy) are removed from the low loss dataset prior to using PCA. **Figure 58** shows that these regions contain no important information but very significant noise – this noise can appear as many significant components in the PCA decomposition, unless these regions are removed prior to running PCA. However, in order to do this, the correction for the core loss bleed-through described in the next section must be applied first, if required.

The aforementioned bleed-through is an artefact which has a major impact on the splicing, and consequently on everything that follows including the absolute quantification and elemental map extraction. This is a continuous background underlying the whole low-loss spectrum, which has the form of a logarithmic graph, very close to the core loss spectrum. It appears at certain time ratios and seems to arise, at least partially, from internal scattering within the spectrometer onto the low-loss side of the CCD during the acquisition of the core-loss data. It occurs more strongly at high time ratios and in thick specimens. It is real scattering of the high loss electrons across the whole CCD (including the low-loss half) during acquisition of the high loss spectrum. If this time is long, with respect to the low loss acquisition time, there will be a lot of scattering from the high loss into the low loss spectrum.

Whilst this extraneous signal would ideally be eliminated by modification of the spectrometer, it is possible to remove it using a combination of software processing and a slight modification of the acquisition conditions. An additional thing that can be done to help minimize this effect is to shift the low loss spectrum by -300eV using the drift tube, whilst keeping the high loss spectrum in the normal place (usually energy shift +150-200 eV). This has two benefits. Firstly, the zero loss peak is 300 V further right than before and the stray scattering under the peak is reduced. Secondly, this also gives sufficient background in front of the zero loss peak for background fitting. This background shape is extracted by extrapolating a power law ($A[E-E_0]^{-r}$) from a window set before the zero loss peak on a spectrum integrated from all pixels in the spectrum image. This background shape is then normalised to the appropriate size per pixel in a new spectrum image using a custom script (see Appendix 1), and then subtracted from the original low loss spectrum using a second script to leave a new version of the low loss without any bleedthrough. A typical corrected spectrum is shown in black in **Figure 58**.

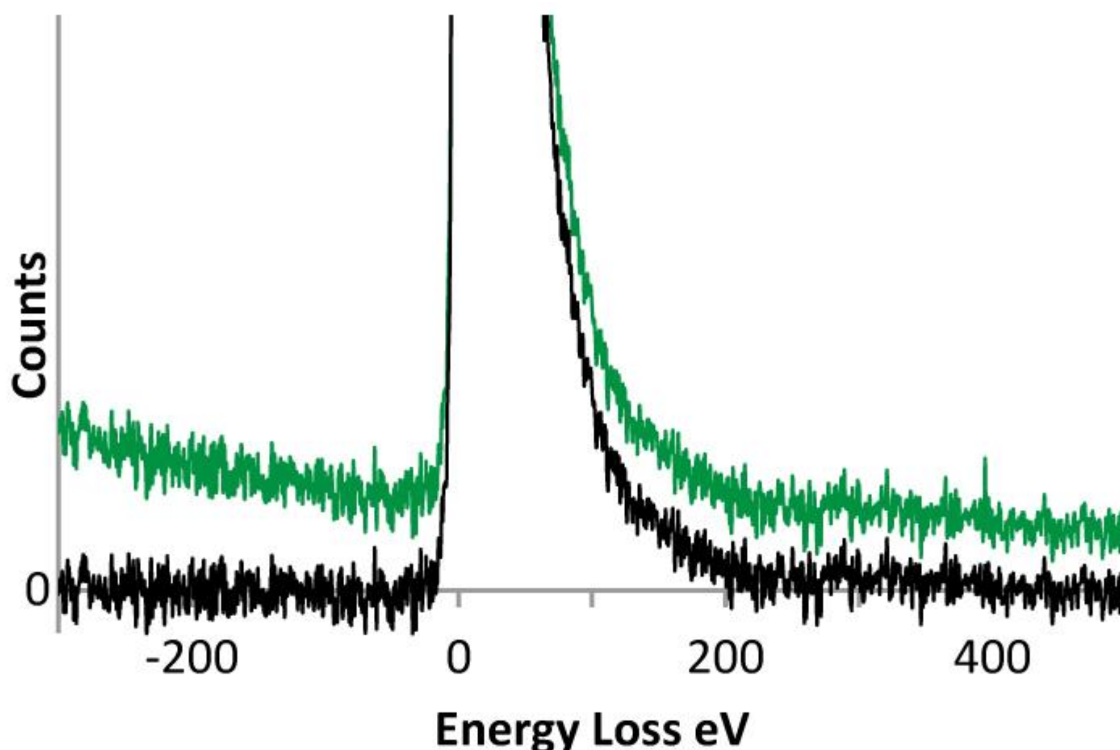

Figure 58. The effect on the low loss spectrum of the bleed-through between the core-loss and low-loss regions (green), together with the corrected low-loss spectrum (black).

In **Figure 58**, the spectrum in green shows the effect of the bleed-through of the core loss region into the low region. Significant bleed-through has two significant effects on subsequent processing. The first is that it gives a major error in the determination of t/λ from the low loss spectrum, since the DM2.3 function for this assumes that the spectrum has a true zero value. The second is that it perturbs the slope of the low loss spectrum in the region of the splice point and or that reason it has to be removed. As it is presented in **Figure 58** the slope changes rapidly in the region between 70 and 120eV, and the splice point is usually around 120-150eV. Splicing so close to the ZLP is derived from the first edges which are interesting in the core loss region, which is Nb at 205eV. Without sufficient background in front of it, the fitting is impossible, and any analysis with this element is not possible. However later research with Nb particles showed, that the splice point should be limited down to 80-100eV due to the high background variations resulted from Fe and Mn EXELFS (extended energy loss fine structures).

Preparation of the CL and LL for splicing and the splice procedure

While PCA significantly reduces the noise in the data, the low loss still has significant noise at high energy end arising from the limited dynamic range of the detector (the ratio between the highest and the lowest intensity on the detector) and the need to keep the exposure short enough to

not oversaturate the high intensity ZLP. Thus the splicing procedure introduces “noise” into the scaling factor, even when the splice ratio is calculated using the average of 20 channels around the splice point. It means, that the scaling factor was calculated based on the average value of 20 left-handed core-loss end channels. This is shown in **Figure 60**. Additionally, noise at the splice point can result in a sharp step, which results in Fourier artefacts on deconvolution, so should be avoided where possible. In many situations, there is no chemical information in the part of the low loss region adjacent to the splice point, just a monotonic decline. Thus the noise can be averaged (smoothed) by fitting a power law function to the data in this region and then replacing the data by the fitted function. In this way, the “noise” in the scaling factor is significantly reduced if this low loss with smoothed tail is used. The smoothing procedure takes the LL spectrum, extracts the fitted power law for the energy window used to tail up to the splice point using a script (see appendix 2) and then replaces this part of the spectrum with the power law values from the averaged background shape. This is shown schematically in **Figure 60**.

The next step is splicing the processed low loss and high loss datasets. Using the DigitalMicrograph *Spectrum* → *Splice* routine with 20 channels ignored at the left edge of the high loss dataset (in case there are artefacts on the edge of the CCD) and just using 1 channel to estimate the scaling factor a new, full-range spectrum image is created. The overlapping channels allow the scaling of the lower energy part to the higher energy, and if all were correct, the scaling factor (the splice ratio) should equal the time ratio between high loss and low loss acquisition times. So this is the reason for using only one channel, to minimise the chance of averaging the intensity by wrong scaling factor. The scaling factor is calculated on a single channel only, since that results in a continuous fit between the low-loss and core-loss datasets and avoids any introduction of steps. The splice ratio is extracted from the data by applying a script (see appendix 3).

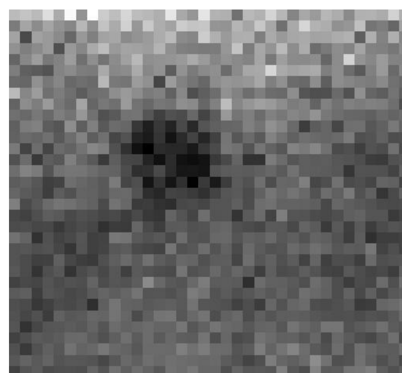

Figure 59. Example of splice factors map for vanadium steel specimen obtained from post-processed data up to the splice. Extraction of the splice factor was with use of script (see appendix 3).

Figure 59 shows the map of scaling factors from vanadium specimen. It proves the pixel-by-pixel scaling method, and also shows that there is quite a variation between the scaling factors from

region to region. First of all, in the precipitate area the scaling factor is the lowest (minimum is a 445 value), and at the top rows the value is the highest (maximum is 593). The average is 505, which suggest that if the averaged splice factor have been used, the scaling factor for precipitate area would be wrong, resulting in errors in later quantification. The errors will occur as a consequence of higher or lower values in the spectrum as it is depictured in **Figure 60** as a thin black line.

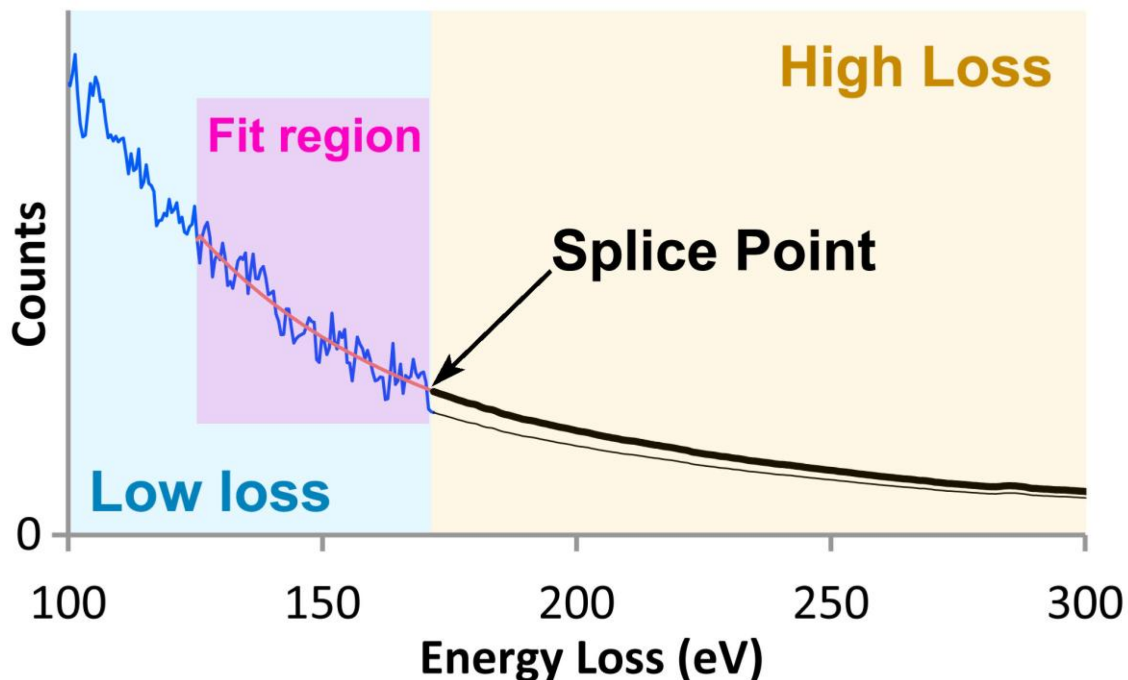

Figure 60. Comparison of splicing the low loss and core loss regions of the spectra without and with prior smoothing of the end of the low loss spectrum using a power law fit. Details can be found in the text. The raw low loss data is shown in blue, the smoothed low-loss in red, the spliced high-loss to the raw low loss in thin black, and the spliced high loss to the smoothed low-loss in thick black.

Figure 60 shows the result of splicing the core loss region and the low loss region after correction for the bleed-through, including the effect of smoothing the low loss spectrum. The noise in the low loss region in the vicinity of the splice point gives considerable uncertainty in the scaling factor and leads to steps in the spectrum which size varies from spatial pixel to spatial pixel depending on the precise details of the splicing procedure. The thin black line in the high loss region shows this in an exaggerated fashion by splicing at a minimum in the noise. Thus the effect of the noise can be minimised by fitting a power law in this region and replacing the actual low loss data by this fit as shown by the red line in **Figure 60**. The low loss and core loss regions can then be spliced at a single point and will fit without any discontinuity, as shown by the thick black line in **Figure 60**.

The result is called the *spliced spectrum image*. This approach to naming datasets is used below to indicate the point in the processing associated with a particular spectrum image.

The next step in the procedure is the removal of plural scattering using Fourier logarithmic deconvolution, using the function in Digital Micrograph, the theory for which is described by Egerton [194]. This is particularly important for removing the effects of any thickness variations from the spectra across the area scanned in the spectrum image. However this function gives artifacts if there are negative or zero counts in the data, and this problem would occur if the black dataset in **Figure 58** were used in a Fourier deconvolution, where there are negative counts present on the left hand side of the ZLP after correction for the bleed-through. Thus, prior to the deconvolution, the "*Volume → Extract → Extract Volume*" function of Digital Micrograph 2.3 is used to extract just the region of the spectrum image that contains positive counts and exclude the area to the left of the left tail of the ZLP, where there is no real information, just noise.

Estimation and removal of the matrix contributions

As described above, the removal of plural scattering was provided using Fourier logarithmic deconvolution [194]. This provides several important advantages for later process steps. The low loss shape can change due to variations in the specimen thickness (including the effect of carbon contamination) or changes of composition (e.g. the presence of the precipitate in the matrix). This changes both the shape of the edges and the shape of the background in the spectra. Thus, removing the plural scattering helps in scaling and subtracting the matrix contribution since the shape of the contribution to the overall spectrum from the matrix should now be now the same at all pixels (even if its magnitude varies). It also allows the use of standard spectra taken under similar conditions but at different times from suitable well-understood standards, provided they have also had the plural scattering removed. Finally, it improves power law background fitting, particularly if the sample is not ultra-thin.

Such prepared data should now allow the correct separation of the matrix contribution from the precipitate contribution, as well as allowing better background fitting before edges. The latter is especially important in front of lower energy edges such as C-K at about 284 eV or Nb-$M_{4,5}$ at about 205 eV

In the present case, the key assumption for separating the matrix spectral contributions from that of the precipitates is that the precipitates do not contain iron or manganese (thermodynamic modelling suggests levels of the order of < 1 at % for both Fe and Mn, which would be undetectable at present) [134]. The specimens in this investigation should ideally consist of sparsely distributed nanosized precipitates of VC or NbC, maybe also containing Ti and N, in a matrix of Fe-20%Mn austenite. Additionally, the surfaces of the FIB-prepared slices can be a little damaged and oxidised

(typically with a thin layer of epitaxial Fe_3O_4) and can sometimes also have a little surface contamination of amorphous carbon forming under the beam in the microscope (despite efforts to minimise contamination with careful handling and plasma cleaning of the specimen in the specimen holder prior to microscopy). The form of the specimen is illustrated schematically in **Figure 56a**.

The key aim of this post-processing technique is to remove the contribution of the matrix to the spectrum image. To do this, an average spectrum of the matrix only has to be generated. In order to subtract the correct amount of matrix signal at each pixel, this spectrum must be scaled so that the iron edge intensity matches that at the pixel. To calculate the scaling factor, a map is made of the iron signal at each point using a defined range window on the Fe $L_{2,3}$ edge divided by the total intensity in the same window on the average matrix spectrum. Typically a 50 eV wide integration window starting at the $L_{2,3}$ threshold is used. A spectrum image is then calculated by multiplying the average matrix spectrum by the scaling factor at each pixel. This average matrix spectrum image is then subtracted from the original spectrum image, ideally leaving only the contribution from the precipitate. All this is done in a form of scrip written by Alan Craven for the purpose of this Ph.D. (see appendix 1).

The main part of **Figure 61** shows the summed spectra from 5 x 6 pixels in the centre of a V(C,N) precipitate in the precipitate spectrum image. The spectrum shown in red is that after splicing and deconvolution. The C K-edge, the Ti $L_{2,3}$-edges, the V $L_{2,3}$-edges, the O K-edge, the Mn $L_{2,3}$-edges and the Fe $L_{2,3}$-edges can be clearly seen. The black spectrum is from the same region after subtraction of the matrix contribution. At the positions of the Fe and Mn $L_{2,3}$-edges, there is only a small perturbation due to errors in the subtraction in the neighbourhood of the sharp white lines. Also the background in front of the C K-edge, the Ti $L_{2,3}$-edges, and the V $L_{2,3}$-edges is flatter, which also helps in future signal extraction and analysis. The intensity of the O K-edge immediately after the V $L_{2,3}$ white lines has diminished significantly. The ELNES on the C K-edge is much clearer and the background under all the remaining edges is much reduced.

The inset in **Figure 61** shows the comparison of the precipitate low-loss deconvolved and non- deconvolved spectra. It may be noted that the intensity has dropped dramatically, showing that the most of the sample thickness was matrix. Also, the bulk plasmon has shifted slightly, and the Mn and Fe-$M_{2,3}$ edges at just above 50 eV have disappeared leaving the Ti and V $M_{2,3}$-edges much more visible. One interesting feature of this matrix subtraction procedure is that the t/l calculation can be performed on the precipitate-only spectrum image to then determine the absolute thickness profile of a precipitate.

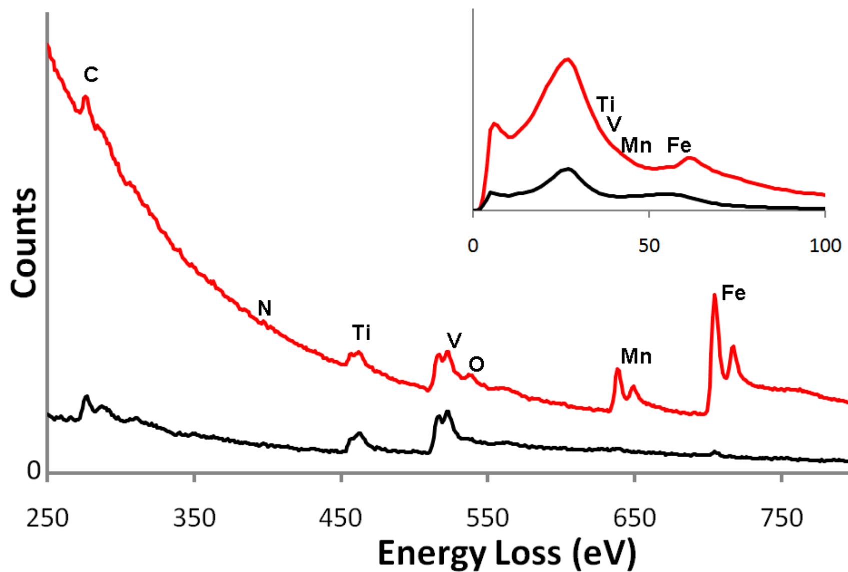

Figure 61. The effects of matrix subtraction on the summed spectrum from 5 x 6 pixels in the centre of a (V,Ti)C precipitate. The deconvolved spectrum without removal of the signal from steel matrix is shown in red. The spectrum after removal of the matrix contribution, i.e. the (V,Ti) precipitate only, is shown in black. The low loss region is shown inset.

However, the scaling prior to matrix subtraction also scales the amount of oxide or amorphous carbide removed, which may leave a residual in the pixels containing the precipitate data. The problem is even worse with the carbon, as the thickness of the carbon is non-uniform in most cases as shown schematically in **Figure 56a**. In the ideal case, when the matrix spectrum is scaled and subtracted, the only material from which information comes is the precipitate itself, as shown schematically in **Figure 56c**. In the real case, when the matrix spectrum is scaled and subtracted from a pixel with only signal from the matrix, essentially the entire oxide signal is removed. However, since the thickness of the amorphous carbon may be non-uniform, the residual signal from it will vary from pixel to pixel. In the case where the matrix signal is scaled and subtracted from a pixel where there is also signal from the precipitate, only a fraction of the oxide signal is removed (since there is less matrix here) and so the spectrum in that pixel will contain precipitate data, some residual oxide signal and possibly some amorphous carbon signal. **Figure 56d** shows schematically the material from which information comes after removal of the matrix contribution in a real sample. If the average spectrum of the matrix is taken from everywhere except the area of the precipitate, then the average carbon level will be higher than the lowest carbon level in the spectrum, which will result in negative counts in the spectrum image after subtraction. Hence, only regions where the amorphous carbon is thinnest are used to form the average matrix spectrum. These regions are chosen based on the carbon intensity map, and the mask, which allows only the region with low (subjectively assessed) carbon content. After subtraction, this results in residual oxygen in the region of the precipitate and residual amorphous carbon both in the matrix and

precipitate regions as shown schematically in **Figure 56b**. The detailed procedure for removing these contributions is described in a separate subsection after considering the effects of the matrix subtraction for a precipitate in a "good" thin specimen.

Background fitting and edge intensities in the V Steel

The standard procedure for removing the background under an EELS edge is to a fit a power law background to a region before the edge and extrapolate the fit function under the edge [194]. For this to be successful, the background shape in the fitting region must have this power law dependence (i.e. $I = A\ E^{-r}$, where I is EELS intensity, A is scaling constant and r is slope exponent usually between 2 and 6.). The wider the energy over which a good fit can be made, the more reliable the estimated background (especially in the presence of noise). When the background fit is correct only random noise around zero should be in the fitting region. Also, if there is any shape visible in the fitting region it means something is wrong with the fit. The presence of any structure is a problem, because moving the fitting window or modifying its width will change the extrapolated background, which shouldn't happen, and which would change the quantification results.

A number of factors can prevent such a good fit being obtained. If there is a lower lying edge sufficiently close to the edge of interest, the overall shape of this edge, either its ELNES or its extended energy loss fine structure (EXELFS) can perturb the background shape in front of the edge of interest. If the specimen is relatively thick, plural scattering can also modify the background shape, causing deviations from the power law. This is more of a problem for moderate energy losses (up to a few hundred eV), where the background slope changes on the scale of the plasmon energy, whereas, at higher losses, the background slope changes more slowly and is little affected by plural scattering.

Figure 62 shows examples of background-subtracted spectra from a few pixels in the centre of the precipitate. The elemental maps are presented in the **Figure 63**. This precipitate had a t/λ of 0.07 in a specimen with an overall t/λ of ~0.4, and t/λ is referred as relative thickness. It is calculated as a negative logarithm of ratio between the ZLP and total spectrum intensity. It is a straightforward computational plug-in in the DM, and it can be used on all low loss data, or spliced full energy range spectra after multiple scattering was removed. Each edge is shown at three stage of the processing: after splicing (light green); deconvolved (red); and after removal of the matrix contribution (black). **Figure 62a** is the C K-edge**, Figure 62b** the N K-edge, **Figure 62c** the Ti $L_{2,3}$-edge, **Figure 62d** the V $L_{2,3}$-edge, **Figure 62e** the V L_1-edge and the Mn $L_{2,3}$- edge, and **Figure 62f** the Fe $L_{2,3}$- edge. The

background-fitting window is shown in **Figure 62** in all the parts as a pale red box. The signal integration widow used for the maps in **Figure 63** is shown above the edges in green.

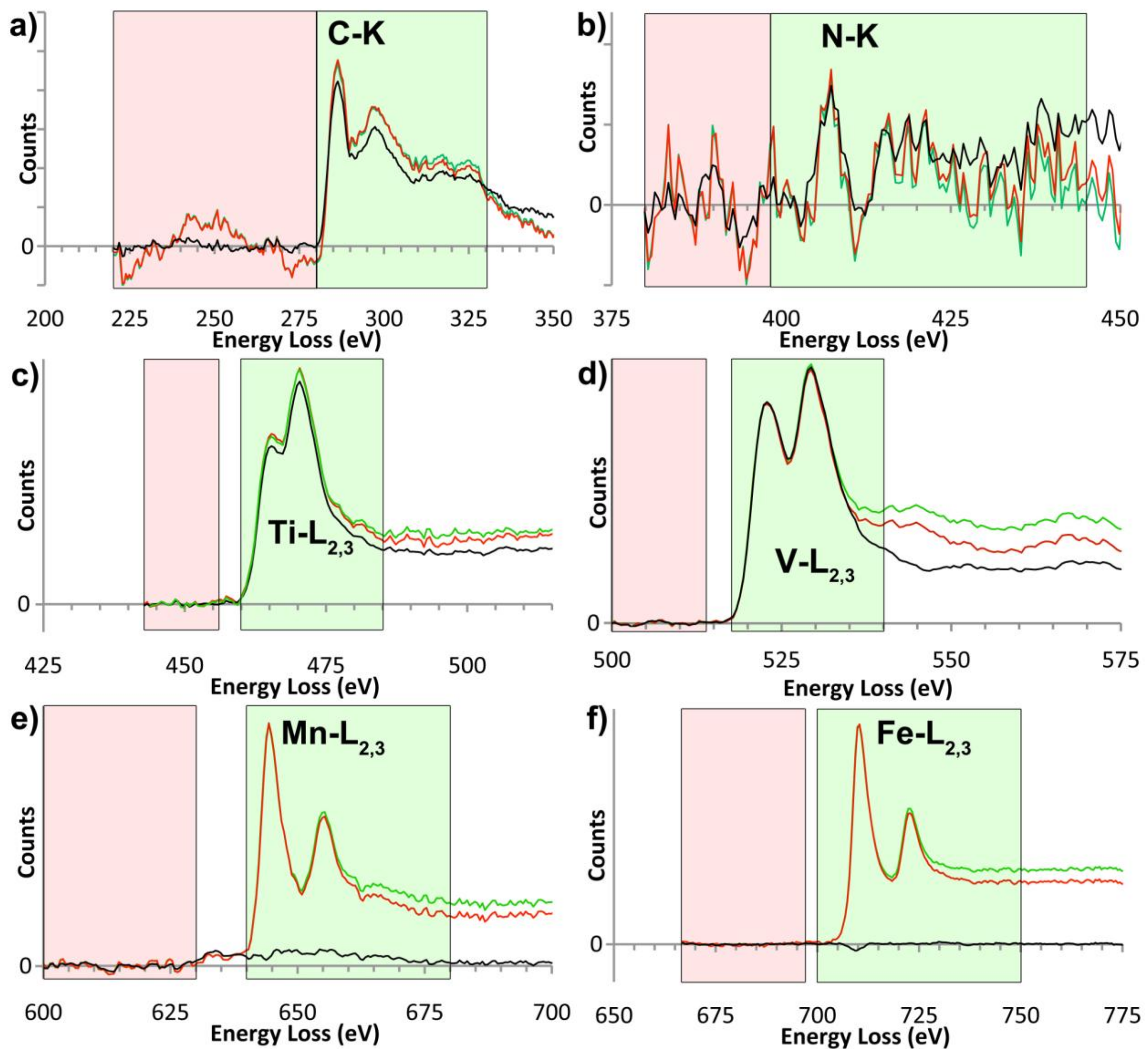

Figure 62. Edge intensities extracted at three points in the processing: after splicing (green); after deconvolution (red); and after removal of the matrix contribution (black). a) the C K-edge; b) the N K-edge ; c) the Ti $L_{2,3}$-edge; d) V $L_{2,3}$-edge ; e) the V L_1-edge and the Mn $L_{2,3}$-edge; f) the Fe $L_{2,3}$- edge. The background-fitting window is shown as a pink box on each plot. The signal integration windows used for the maps in figure 9 are shown as boxes above the edges in pale green.

Figure 62e and **Figure 62f** show that the Fe and Mn signals are very effectively removed by the matrix subtraction, as expected. The Mn $L_{2,3}$-edge sits on top of the V L_1-edge at 628 eV and the signal from the latter edge remains after the matrix subtraction. The interesting phenomenon is the small dip in the signal in the **Figure 62f,** after the subtraction of the matrix. The while lines of the Fe $L_{2,3}$- edge should have the same ratio, so after the removal of the matrix there should be no negative

peak, as it occurred in this figure. This may suggest that there is some difference in oxidation states between the iron in the matrix and iron in the surface oxide, as the assumption is made, based on the thermodynamical modelling, that there is no iron in the precipitate. If there are negative counts it means that there has been oversubtraction in the precipitate area. The region with the precipitate has a lower ratio of matrix to the oxide surface, therefore after the subtraction, the oxide state from the oxide can be dominant. So, if there is significant over subtraction it would be consistent with the expectation that the oxidation state of the iron in the oxide is higher than that in the matrix, since white lines are typically stronger for iron oxides than for metallic iron [217].

In samples with a t/λ approaching 1, deconvolution often improves background fitting before EELS edges. However, in the sample used for **Figure 62**, there is little apparent improvement in the quality of the background fit after deconvolution as the total amount of multiple scattering is low. Nevertheless, deconvolution does have a more subtle effect. Comparing the fractional changes in edge intensity before and after deconvolution, that for the Ti edge is small, that for the V edge is large and those for the Mn and Fe edges are medium and similar. The fractional change in the edge intensity caused by the deconvolution would be expected to be very similar if caused solely by multiple scattering of the edge signal. The explanation for the differences is that the deconvolution process also modifies the background shape in front of the edge. The Fe and Mn edges are well separated and at higher energies and so the changes in background shape would have least effect. However, since the V edge sits on the tail of the Ti edge, the background shape before the V edge will be the most changed leading to the largest fractional change in the edge intensity. On the other hand, the fractional change in the Ti edge is small because the background in front of the edge is made less steep by the multiple scattering. Thus, in the non-deconvolved spliced data, the signal extracted from the Ti edge is reduced as the energy loss increases, leading to a smaller difference between this edge and that extracted from the deconvolved data.

The situation for the C and N edges is more complicated. **Figure 62a** shows the background shape before the C-K edge is still far from the ideal power law shape after deconvolution. The perturbation to the background shape is caused by strong extended energy loss fine structure (EXELFS) from the Mn and Fe M edges causing oscillations in intensity about the power law shape. Subtraction of the matrix contributions removes these oscillations and the background before the C-K edge now behaves according to a monotonic power law, giving a good background fit. The C K-edge no longer goes negative after background subtraction, giving a much more reliable extraction of the C-K edge for detailed analysis or quantification. The results are presented in **Figure 63**, where on the left is the graph after preliminary matrix subtraction with a lot of noise and negative counts

on the C profile in **Figure 63b**. With a better fit in front of the C-K edge as a result of matrix subtraction the negative counts disappeared and the C profile looks much better (on the right graph **Figure 63c**).

This subtraction of the matrix contribution also has major benefits around the weak N edge. Prior to subtraction of the matrix contribution, the intensity of the extracted N edge becomes negative before the Ti edge. After removal of the matrix contribution, it remains positive right up to the Ti edge and allows the improved mapping of the N edge intensity demonstrated below.

The V $L_{2,3}$ edge also benefits significantly from the subtraction of matrix contributions, since some of the signal from the O present as surface oxide is subtracted when the matrix contribution is removed. **Figure 62d** shows a very significant decrease in the O K-edge intensity after the V L_3 and L_2 white lines.

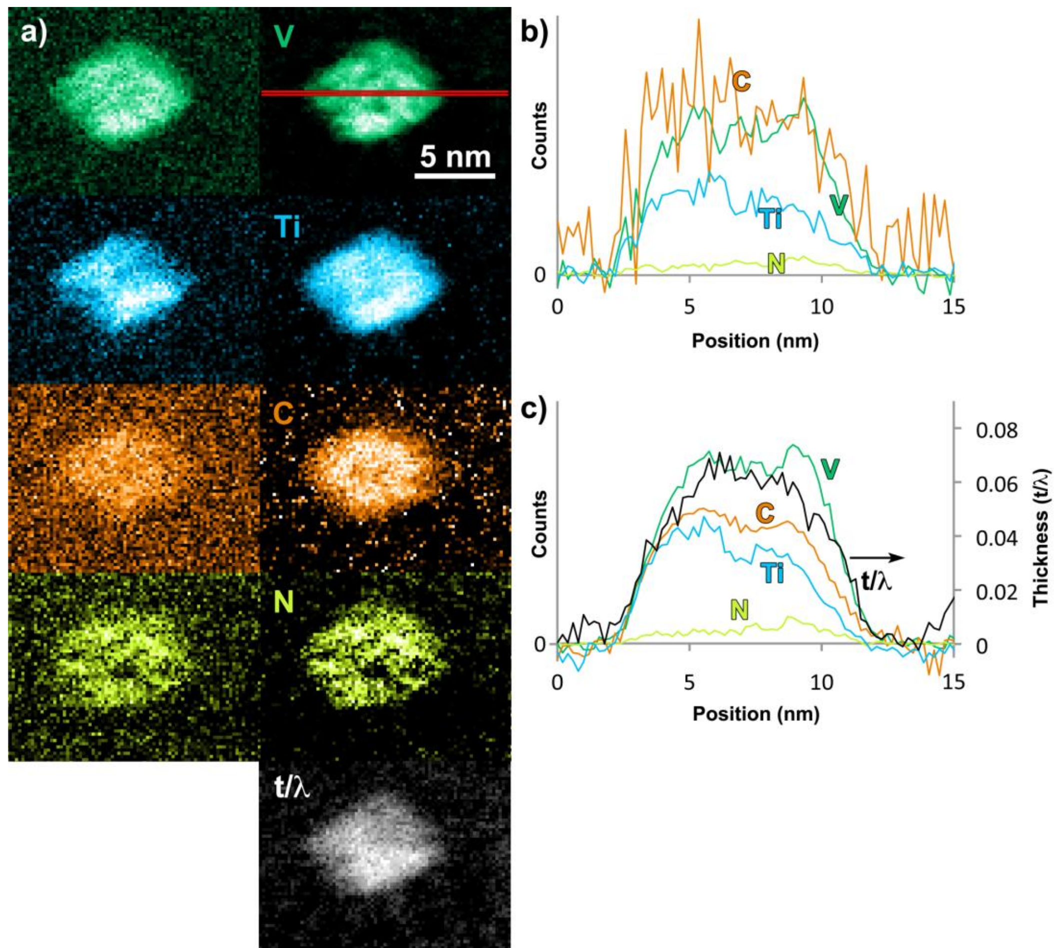

Figure 63. a) Maps of the edge intensities for a precipitate in the V steel: left column from the as-recorded data; right column from the fully processed data. Black in the maps corresponds to zero counts. b) Line profiles across the maps from the unprocessed data (colours as for the maps in a), the position of the line for the profile is shown in the upper right V map). c) Line profiles across the maps from the fully processed data; the elemental signals are plotted against the left hand *y* axis and the thickness plot (black) is plotted against the right hand *y* axis.

The effect of the digital extraction replica technique on the resulting maps in a vanadium steel is shown in **Figure 63**. The dataset is the same as that used to give the edge shapes in **Figure 62**, where the signal integration windows are shown. In all the maps, black corresponds to a signal of zero. The left hand column shows V, Ti, C and N maps calculated from the original raw EELS-SI dataset. The right hand column shows the same maps extracted from the digitally extracted precipitate spectrum image plus the t/λ map for the precipitate. The t/λ map can only be obtained by applying the processing route proposed in this thesis, because of the multiple scattering removal in the core loss region of the spectrum.

The V map is already clear in the raw data but is exceptionally clear and with low noise after the extraction processing. The Ti, which is present at a lower level, gives a noisier map in the raw spectrum image but is much clearer with similarly low noise to the V map when the fully processed data is used. Extracting the C signal from the as recorded data is problematical. The poor background subtraction, combined with any surface carbon present, appear to give a C signal everywhere. A much clearer C map, with similarly low noise to the V and Ti maps, results from the fully processed precipitate spectrum image. A N signal can be mapped in the raw dataset, although it is only just emerging from the noise. After digital extraction, it is possible to map N much better, and with much reduced background noise due to the more reliable background fitting. Considering that the N signal in each pixel of the map comes from a very few N atoms, the power of the processing procedure is successful.

The improvement in the quality of the maps is emphasised by the comparison of the profiles through the maps shown in the graphs in **Figure 63b** and **c**. All the profiles are taken from the position of the line shown in the V map to the top right. **Figure 63b** shows the much noisier profiles through the maps from the raw datasets and **Figure 63c** shows the significant improvements achieved using the fully processed precipitate spectrum image. The profile of t/λ through the precipitate is also shown in **Figure 63c** for comparison with the elemental signal profiles. It can be seen that this profile matches very well to the form of the elemental profiles.

It is clear from the maps that the elemental distributions within the precipitate are more or less homogeneous. While there may be local variations in the atomic ratios within the precipitate, there is no evidence of a classical core-shell structure in which a precipitate of one composition forms first and is then overgrown by material of a different composition [218].

Background fitting and edge intensities in the Nb Steel

In the Nb steel, the difficulties are slightly different. Extraction of the C K-edge intensity is complicated by the fact that the C K-edge sits on the Nb $M_{4,5}$-edges, which makes the background subtraction much more difficult. The problem of the effect of carbon contamination remains but the level of carbon contamination is much lower in the best datasets acquired from this steel. This is because the datasets were recorded later in the study, at which point the contamination-control was much better. As there is no V in the steel, it is not necessary to correct for residual O. So far, no N K-edge has been reliably detected in this steel.

Figure 64a shows the results of background subtraction using the window shown in by the pale pink box in front of the Nb $M_{4,5}$-edges The sample has a total t/λ of 0.18 and the precipitate has t/λ of 0.08. As in the case of vanadium steel, the results are shown at three stages of the processing: after splicing (green); after deconvolution (red); and after removal of the matrix

contribution (black). Both before and after deconvolution, the background fit is very poor resulting in significant negative intensity at the start of the edge. It is impossible to find a background estimation window that gives a well-behaved background subtraction for such data. As with the V steel, the major issue here is that the EXELFS from the Mn and Fe $M_{2,3}$-edges. Subtraction of the matrix contribution is hugely beneficial as it removes the EXELFS from the Mn and Fe that perturb the background before the Nb-$M_{4,5}$ edge [219]. The black spectrum in **Figure 64a** shows a better background fit after the subtraction of the matrix signal.

However, the background window used is at ~180eV and the Nb $M_{4,5}$-edge onset is ~205eV. The intensity starting at 180eV and disappearing at 205eV, just before the edge threshold cannot be attributed to an edge from another element in the system. It is likely that it is a contribution from the EXELFS of lower-lying Nb N-edges, which looks like a feature, just in front of the real edge, but for the purpose of quantification shouldn't be included. The black spectrum in **Figure 64b** uses a narrow background window immediately before the $M_{4,5}$ edge to exclude most of these EXELFS oscillations . Also shown on **Figure 64b** are spectra from NbC (red) and NbN (green). These spectra are old data recorded using a VG HB5 using the same experimental conditions given above for the old VC data [218, 220]. A narrow background fitting window in front of the Nb $M_{4,5}$-edges was also used for these edges and they are scaled to have the same Nb $M_{4,5}$-edge intensity prior to the C K-edge. There is good agreement between the spectrum from the precipitate and that from the NbC standard but the intensity of the C K-edge is systematically slightly higher in the precipitate. This additional intensity is likely to be because the precipitate contains a small fraction of Ti, which will increase the C:Nb ratio over that for pure NbC. Subtracting the background under the C K-edges using a power law background is challenging in this case. However, the scaled NbN spectrum in **Figure 64b** provides the shape of the Nb $M_{4,5}$-edges under the C K-edge and can be subtracted to give the C K-edge intensity.

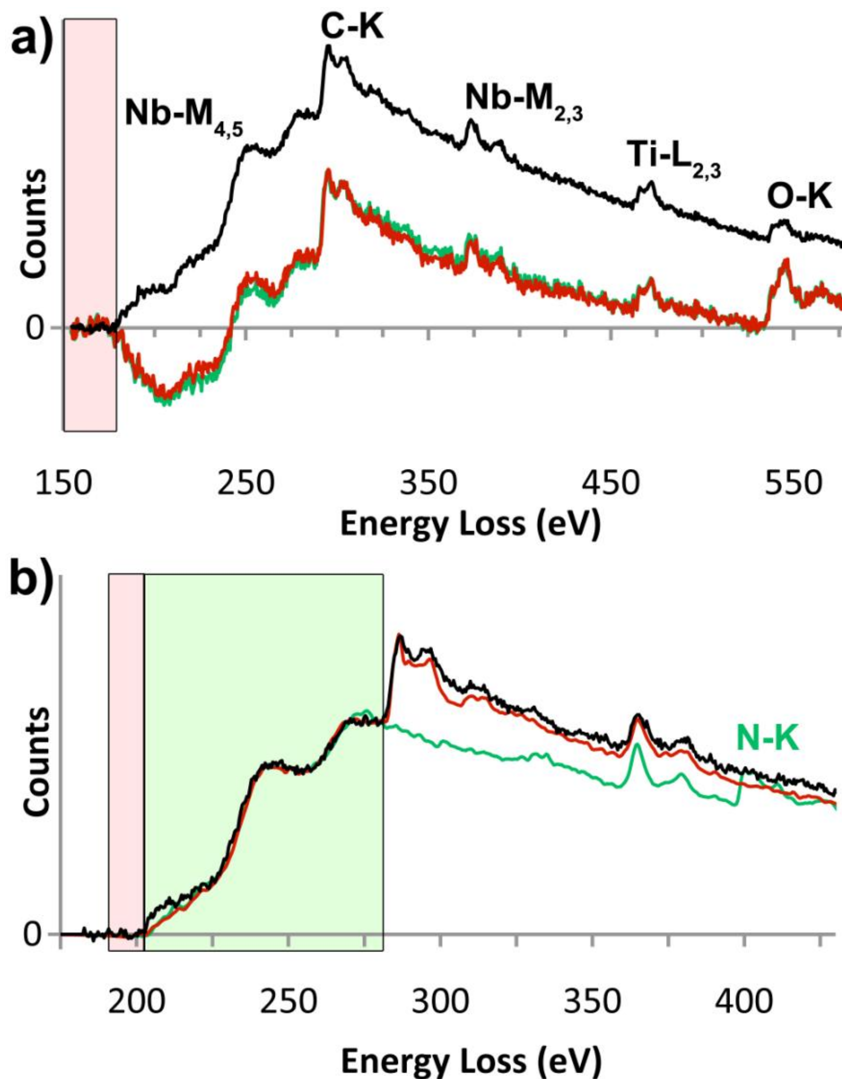

Figure 64. a) The results of background subtraction using the fitting window indicated by the pale pink box in front of the Nb-$M_{4,5}$ edge on a sample with a total t/λ of 0.18. Each is shown at three stages of the processing: after splicing (green); after deconvolution (red); and after removal of the matrix contribution (black). b) The result of background subtraction using a smaller fitting window closer to the Nb $M_{4,5}$-edge, again indicated by the pale pink box. A comparison is made of the edge shapes from the precipitate (black) with those from NbC (red) and NbN (green) standards with similar background fitting windows and scaled to have the same integrated Nb-$M_{4,5}$ intensity prior to the C-K edge. The signal integration window for the Nb maps in Figure 66 is shown by the pale green box.

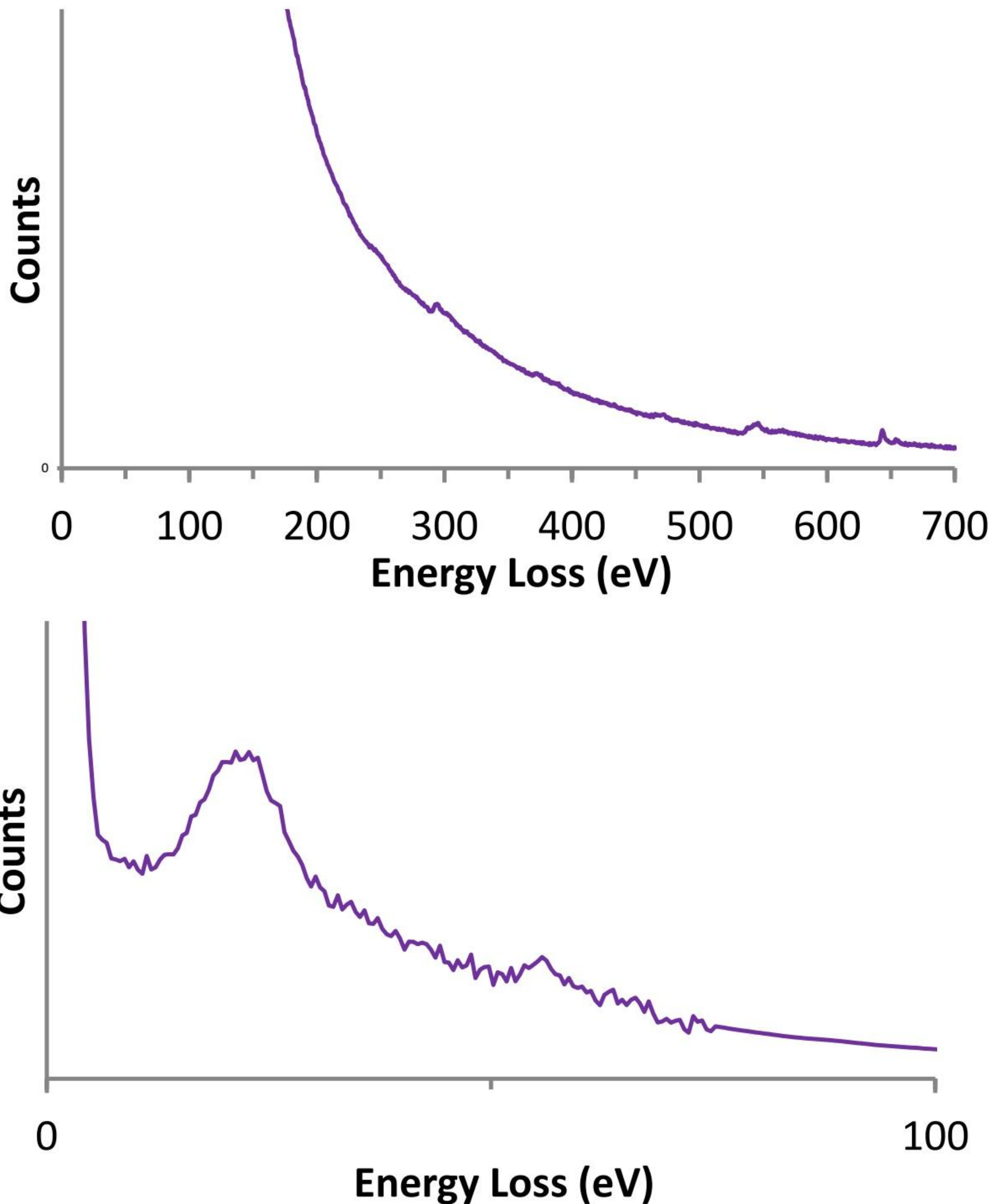

Figure 65. a) Full spliced spectrum of Nb specimen. At the left end the counts are growing rapidly, so only this part is showed, because otherwise low-intense core loss edges won't be visible. In such presented spectrum the Nb-$M_{4,5}$ edge is slightly emerging from the spectrum at 200eV loss, followed by sharp C-K edge at 284eV, there are some indications of Nb-$M_{2,3}$ edge at 360eV, and then Ti, O and Mn. b)Close up at low loss and first part of the core loss, where the splice point is.

The **Figure 65a** shows problems that occur with the Nb data. First, and the most important problem is that the Nb-$M_{4,5}$ edge sits on a low energy loss part of the core loss region, which is in the region of high intensity. It means, that the background is dominant, and fitting the background in front of it is difficult - may cause over or under subtractions. In case of this specimen, the conditions of splice were set to be as low as possible, in the very beginning of the core loss, and it is around 70eV. The splice point and surrounding background is presented in the **Figure 65b.** There is a

significant difference in the noise in low loss, which is much more intense than core loss, so the acquisition time is lower, which increases the noise. The core loss region is recorded with longer exposure times, due to the lower intensity, so the signal to noise ratio is much higher. Unfortunately, this noise step change causes problems during the Fourier-log deconvolution. However, with narrow background windows just prior to the Nb-$M_{4,5}$ edge, which do not include too much fluctuations from the splice point errors (long distance from the Nb edge gives enough space for good fit) gives a chance to produce reasonable maps, as presented in the **Figure 66.**

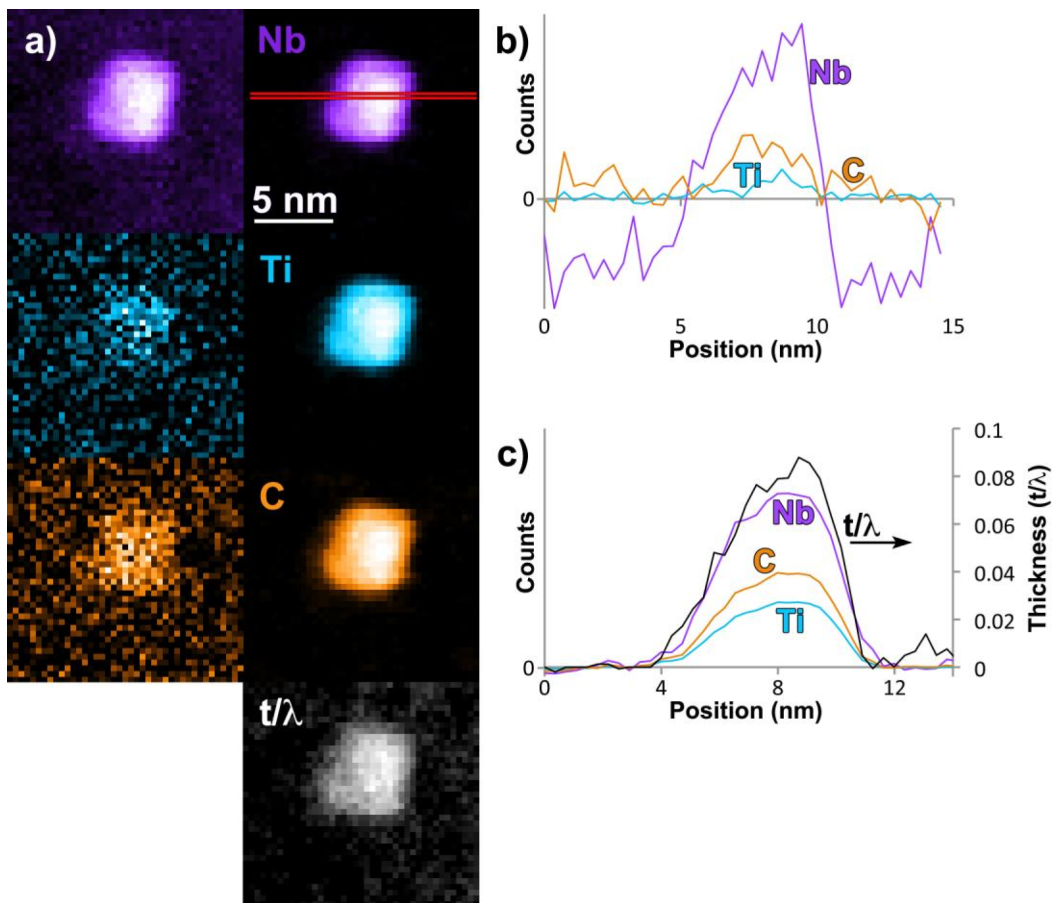

Figure 66. Maps of the edge intensities for a precipitate in the Nb steel: left column from the as-recorded data; right column from the fully processed data. Black in the maps corresponds to zero signal. b) Line profiles across the maps from the unprocessed data (the position of the line for the profiles is shown in the upper right Nb map). c) Line profiles across the maps from the fully processed data.

The significant amount of work involving development of the techniques in the case of the Nb-steel and comprehension of the occurrence of the noise is depicted in **Figure 66**. The datasets from early versions of the processing method coupled with a lack of understanding the origins of

noise and errors resulted in elemental profiles that were not only noisy and difficult to interpret, but also were impossible to analyse quantitatively, just as for V-steel. It is especially clear that early processing results were often noisy outside or on the edges of precipitates, whereas the latest results have much more robust background subtraction allowing reliable analysis of the edges of the precipitates. The results of the improved processing are shown for the Nb precipitate in **Figure 66**, where on the left graph preliminary subtraction results are presented, in comparison to the right, where the subtraction is done with more, careful steps, like discussed at the beginning of this chapter (x-ray subtraction, noise minimising, volume extraction to avoid errors, limited window width for background subtraction etc.). The right graph demonstrates that these procedures provide a powerful way to prepare datasets suitable for quantitative analysis. Specifically, there are no negative counts in the region outside the precipitate. Also the noise in the elemental profiles is much reduced giving a better chance to interpret the interface behaviour between the matrix and the precipitate. Moreover the Ti profile is similar to that for the precipitates in the V-steel, and does not suggest any core-shell structure for this steel.

Black in the maps corresponds to zero signal. As before, maps generated from the raw EELS-SI data are shown to the left and maps from the extracted precipitate spectrum image are shown to the right. The t/λ map is shown at the bottom of the right hand column. The Nb map from the unprocessed data is rather noisy and there are major problems with over-subtraction of the background outside the precipitate resulting in negative counts. This arises due to problems in the background fitting due to the EXELFS from lower lying edges as discussed above. In contrast to this, the Nb map after extraction of the precipitate spectrum image is much clearer, the precipitate is well defined and there is little problem with negative counts outside the precipitate. This suggests that the counts in the precipitate are being correctly determined and that the size and shape of the precipitate is now being accurately reproduced in the map. The Ti map from the raw data is almost unusable and there is just a faint hint of a precipitate there. This mainly occurs due to the noise in the raw data. This makes background subtraction before the Ti edge difficult and the varying background introduces a large amount of excess noise into the maps. After extraction of the precipitate spectrum image, the Ti extraction is straightforward and results in a high-quality, low-noise map with clear profiles, together with a baseline outside the precipitate which is very close to zero. This is possible, because the background in front of the Ti has different slope, and the fitting is better, despite sitting on the Nb-edge tale. The C map from the raw data is also very noisy and strongly affected by the problems of background subtraction due to the shape of the Nb $M_{4,5}$ edge. The corresponding map from digitally extracted precipitate spectrum image is much clearer, with

well-defined precipitate edges. The shapes of all the elemental profiles also match very well to the corresponding profile through the t/λ map.

In this precipitate, the elemental distributions are, if anything, more homogeneous than those in the precipitate in the V steel above. Thus, again, there is no evidence of a classical core-shell structure [221, 222].

Removal of the amorphous C and the O

If there is carbon contamination, the intensity in the C K-edge will be a mixture of contributions from the carbon in the precipitate and the amorphous carbon. However, these have very different ELNES and this can be used to estimate the two contributions [157]. A more quantitative approach is to use multiple linear least squares (MLLS) fitting of edge shapes from standards. The edge shape from amorphous carbon can be extracted from the matrix region of the deconvolved spectrum image. Ideally the edge shape for the carbon in the precipitate should be taken from spectra recorded from an isolated precipitate of the same composition, using the same experimental conditions and processed in the same way.

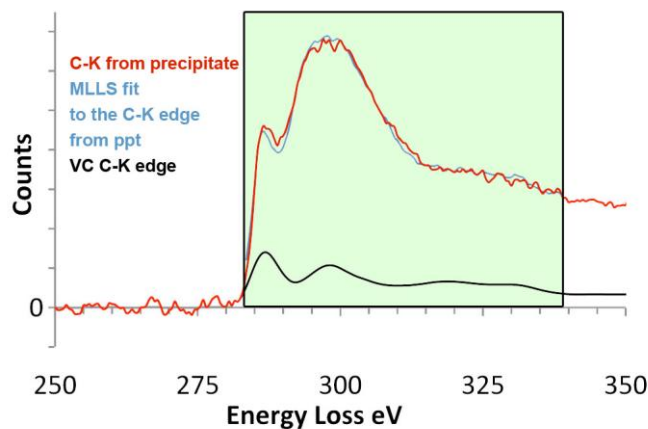

Figure 67. The background subtracted C K-edge shape from the precipitate spectrum image is shown in red(dark grey in print). It is the sum of spectra over several pixels in the centre of the precipitate. The MLLS fit to this edge is shown in blue (light grey in print) and the fitting window in pale green(pale grey in print). The contribution of the shape of the C K-edge shape from VC is shown in black, and this is the signal of interest. The difference between this and the MLLS fit is the contribution from surface amorphous carbon. (Note, this result is taken from a dataset where there was significant carbon build-up in order to illustrate the point).

Data for VC standard specimen recorded previously in a VG HB5 STEM with post-specimen lenses and a Gatan 666 PEELS spectrometer operated at 100keV was available. A probe half-angle of

11 mrad and a collection half-angle of 12.5 mrad was used in recording such data. The data processing used is described in Craven and Garvie [218] and the plural scattering has been deconvolved. The VC standard spectrum is showed in black in the **Figure 67**.

An intricate factor is that the precipitate contains both Ti and N. However, there is much more V than Ti and very much more C than N. Since the shapes of the C K-edges in VC and TiC and the shapes of the C and N K-edges in VC and VN are relatively similar [218, 220], the carbon edge shape from VC should provide a reasonable standard for the crystalline C K-edge in the precipitate.

As there is only a very small contribution from amorphous carbon in the data shown in **Figure 67**, a dataset in which there had been significant build-up of amorphous carbon is used to illustrate the procedure. The red line in **Figure 67** shows the background subtracted crystalline C K-edge summed over 5 by 6 pixels from the centre of the precipitate. The blue line shows the MLLS fit to the data using the two standards described above. The fit was carried out over the energy range shown by the pale green rectangle (pale grey in print). Note the close agreement of the fit and the standard. The contribution to the MLLS fit of the VC standard is shown in black. This is the best estimate of the crystalline C K-edge intensity from the precipitate alone. With this level of amorphous carbon build up, there will be a significant uncertainty in the intensity of the carbon K-edge from the precipitate and so every effort should be made to limit the carbon contamination when collecting the data.

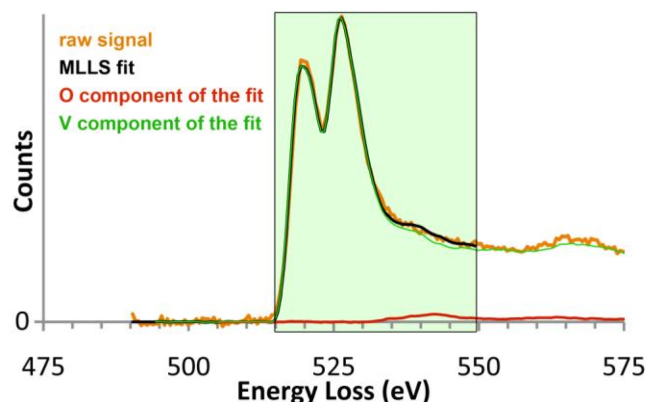

Figure 68. MLLS fitting to separate O from the V signal for a VC precipitate. The raw signal is shown in gold, the MLLS fit in black, the O component of the fit in red, and the V component in green (the MLLS fit window is in pale green). The O-K standard was selected from within the spectrum image from an area containing no precipitate, and the V-$L_{2,3}$ standard was from previous work on bulk VC [218].

In a similar way, the residual O K-edge can be separated from the V $L_{2,3}$-edges using MLLS fitting of the spectra in the spectrum image as a weighted sum of the O K-edge shape from the matrix-only regions of the spectrum image and the V $L_{2,3}$-edge shape from the VC standard above [218]. The results are shown in **Figure 68** for the V edge in **Figure 62**. The residual O signal is small since the majority of it was removed by the earlier subtraction of the matrix signal. The O signal is

taken from the region close to the specimen, almost vacuum, so it can be used for subtraction or MLLS fit.

Linearisation and final corrections of the data

Apart from removal of unwanted signals, the linearization of the precipitate data has to be done and rescaling the core loss region to be time ratio scaled instead of splice ratio factor prior to quantification. The lack of linearisation may lead to errors in partial cross-section calculations, because it base on integration window range of energy losses. It is necessary because the precipitate data has been recorded prior to linearization of the GIF QuantumER, and some non-linear dispersion of energy may occur. The linearization should be done as soon as possible, but there is no low loss features to relinearise the low loss data only, so the linearization is done after the multiple scattering is removed.

The linearization is done on basis of polynomial fit between standard specimen, which is a high manganese steel with V particles in it, and the deconvolved spectrum image of precipitate that is going to be quantified, and it is performed by script in DM (see appendix 4). Then the value for each edge is set up, and by first, second, third and fourth order polynomial fit the values are fitted to each other. The higher the polynomial order, the better the fit in the region containing the calibration points but the more rapidly regions outside this range are likely to deviate from their true energies as the extrapolated fit is unlikely to be correct.

During splice the core loss is divided by some splicing factor to match the low loss. This should correspond to a time ratio between the core loss and the low loss. However due to the errors in electronic fast shutter, the time ratio in data acquired before total realignment of GIF QuantumER varies significantly from the splice ratio. The calculations of cross-sections with and without the correction of splice ratio, and comparison of the results with differential cross-sections for C-K and N-K values from previous DigitalMicrograph versions suggest, that the correction is necessary.

The correction is done as a simple math multiplication of integrated signal edge of certain element by splice ratio and division of time ratio.

It has been demonstrated that the DualEELS data, acquired from steel specimen with fully embedded precipitates can be successfully PCA cleaned, Fourier deconvolved and divided into two signals subtracted one from another. As a consequence of this procedure, the result is a full range spectrum from one precipitate only signal, which can be presented in form of a map, or a spectrum image. The subtraction process is well developed, as the whole matrix is removed without significant under subtractions, resulting in small noise oscillating around zero in the maps, where the matrix suppose to be. With similar manner all unwanted signals, such as oxidation, or organic carbon contaminations can be separated. This procedure can be used to separate the vanadium or

niobium precipitates, however with the second ones there is still some progress to do, regarding the acquisition conditions, splice and subtraction of the matrix signal. Spectrum images in its final stage is a clean spectrum, which can be used for further quantification, what is shown in next chapter.

7. The absolute quantification - determination of mean free paths and differential cross-sections in EELS

Having extracted the precipitate spectrum image from the matrix, as demonstrated in the previous chapter, it is now necessary to work towards the quantification of such spectrum images. This chapter details the next steps required for performing the absolute quantification of DualEELS data of nanosized particles fully embedded in a physically distinct matrix. As previously stated, most similar analyses carried out so far have been limited to just the chemical distribution unsupported by any quantitative information. The previous analysis [99, 129, 222] on nanosized carbides in HSLA steels shows that there is a difficulty in obtaining a clear relation between phases and their absolute quantification [108, 167, 184, 223-225]. This papers showed that the absolute quantification with high accuracy is impossible, if the differential cross-sections are not known, and if the spectrum image is not a single scattering event spectrum. All the classic EELS data are single spectra (core loss only or low loss only) without a chance to record the ZLP under the same conditions. Only the DualEELS gives the opportunity to record the core los and low loss separately with individual time ratios.

In simple words, an absolute quantification is the representation of experimental analytical results presented as a thickness in nanometers, or as an absolute number of atoms along the beam direction. This can only be performed when the EELS partial cross-section is known with high accuracy for each absorption edge used in the analysis, and when all data can be normalised to the intensity in the zero loss peak. Therefore, there are two requirements for this work.

Firstly, it is only possible to gain the zero loss intensity for every pixel along with the core loss intensities using DualEELS acquired spectra. Despite this, the effects of plural scattering can be removed from the data using deconvolution so the intensity of the edges have a linear dependence on thickness, and this is only possible by having the low loss and core loss for every pixel from DualEELS (recorded simultaneously).

Secondly, the cross sections used in the evaluation must be accurate. Much of the quantitative work performed previously has used calculated cross-sections, either using the hydrogenic or the Hartree-Slater model for the calculation of the cross-sections [108, 167, 223, 224]. Such calculations are based on isolated atoms and contain no information on white lines, fine structure ELNES or extended fine structures EXELFS. In addition, as the energy loss range normally accessible to EELS is a few keV at most, the estimated accuracy for the cross-sections varies with

atomic number. For the light elements, the thresholds of the K-edges fall in the accessible energy loss range and the accuracy of these cross-sections are usually thought to be within a few percent [224]. At some point the K-edges become unreachable, the $L_{2,3}$ edges are used, but their uncertainty is thought to be about 15%, at least for low collection angles [224]. This uncertainty is compounded when the valence *d*-states are close to the lowest occupied state as in the transition metals, giving rise to white lines, which are not included in the model. When the $L_{2,3}$ edges become inaccessible, the $M_{4,5}$ edges are used and the uncertainty is these is even greater [224]. Again, white lines are an issue when the valence *f*-states are close to lowest unoccupied state, as in most of the lanthanides.

Such theoretical cross-sections are widely used (for example, they are implemented in Digital Micrograph). In most experiments where quantification has been performed, the value of I_o in **equation 18)** has not been available. Thus N (number of atoms per unit area) for each element cannot be obtained. However their ratios can be calculated, and hence the percentage of each element present can be calculated. If all the edges involved come from one group of edges (K, L, M), the uncertainty in the percentages should be much reduced since the value is determined by the ratio of cross-sections, and any systematic errors should cancel. This benefit does not apply if the ratio of a K and L cross-section is involved, although it's possible that the systematic error is reduced.

Some previous work has attempted to determine absolute cross-sections [106, 107, 226-228] and this has clearly demonstrated errors in calculated cross sections of 10-20% [108]. This requires both low loss and the core loss spectra from the same area. In most cases, however, absolute quantification was impractical for more than one or two probe positions, because the EELS spectrometers could only record one energy range, and had insufficient dynamic range to record both the bright zero loss peak and the weak core-loss edges in the same spectrum.

However, excellent relative quantification (i.e. of concentration ratios, not absolute elemental quantities) can be performed using single range EELS together with standards of well-known composition. For example, Bach *et al.* [229, 230] showed that it is possible to separate different Nb-oxides, both using the fine structure and using careful standards-based quantification. This standards based quantification was performed using a the *k*-factor method (chapter 35.4 of D. B. Williams and C. B. Carter [164]). The *k*-factor is a sensitivity factor characteristic for any study and standard specimen, which means it is not constant for the same specimen. Firstly the *k*-factors determined by standards were described by Goldstein in 1977[231] for EDX, and later on, Leapman discussed it for EELS [167].

$$\boldsymbol{k_{AB} = \frac{N_A}{N_B} = \frac{I(\beta,\Delta)_A\sigma_B(\beta,\Delta)}{I(\beta,\Delta)_B\sigma_A(\beta.\Delta)}} \qquad \mathbf{17)}$$

where *A,B* denote the elements, I is the edge intensity, σ is ionisation cross-section,. The theoretical k-factor calculation is rapid and can be used for all spectra data. All data required for this

expression are given, apart from the *Q* cross-sections, which are a source of significant errors (up to 20%). It is crucial to study a well-prepared TEM standard specimen of known stoichiometry. This method is recommended when a quick answer is enough. When high accuracy is needed, other methods are advised.

Whilst it was possible to determine absolute cross sections previously, as described above, the practical difficulties meant that cross sections were often calculated from experimentally determined ratios with a better known cross section (e.g. Manoubi et al. [232]), rather than by direct measurement, i.e. another *k*-factor method. Neither method is particularly applicable to EELS mapping using spectrum imaging, especially as none of these methods takes any account of thickness variations of edge intensities.

The introduction of DualEELS allows the ZLP to be used for normalisation of the signal and makes quantification possible on an absolute scale. It also allows deconvolution to remove the effects of plural scattering. Thanks to the single scattering full energy range spectrum it is possible to obtain experimental differential cross-sections from well-characterised bulk standard material. Also it is possible to quantify large datasets collected via spectrum imaging from inhomogeneous samples with few Ångström resolution acquired under similar experimental conditions to the standard data. By using the experimentally determined cross sections, each element's absolute thickness can be calculated.

7.1. Basic principles of determining a cross section from a standard

The quantification is connected with cross-section with equation

$$\mathbf{I_k = I_0 N \sigma}\,, \qquad 18)$$

where *N* is the areal concentration in atoms/nm^2 at given ionisation edge, I_0 is the number of counts of zero loss intensity, and σ is the cross-section, which is called partial cross section and is obtained from differential cross section by choosing a suitable energy range window. Before further analysis it has to be remembered that the I_k only has a sensible value if the plural scattering is removed prior to quantification (indeed, the equation assumes single scattering only [224]). Otherwise the shape of the edge will be distorted by plural scattering, will be thickness dependent, and consequently the *N* value will not be a linearly related to I_k and accurate quantification will be impossible. How the results of quantification are expressed is dependent on the application, but commonly quantification users may wish for the areal density, the effective thickness of material in nm or the number of atoms, as well as accurate and reliable relative composition measurements.

The areal density can be converted to effective thickness based on the lattice known parameters and the number of that specific atom per unit cell.

Two key issues have to be addressed in order to obtain accurate partial differential cross-sections. The first is the fact that making thin samples from bulk material can change the material and, in particular, can result in the formation of a surface layer of significantly different composition to that found in the bulk. The second is that the thickness of the sample must be determined accurately. This latter issue can be solved by using previously published formulae for the mean free path as a function of microscope parameters and the details of the specimen (e.g. from Malis *et al*. [233] and Iakoubovskii *et al*. [234]), although it was felt that checking this experimentally with a needle specimen from one of the standards was wise. The first issue actually affects both experimental determination of mean free paths and cross sections, and is tackled in this work by taking data over a range of specimen thicknesses and using a least squares fitting technique to extract the bulk behaviour in a manner similar to that used in earlier work [235]. The following sections set out the full details of how firstly the mean free paths and then the differential cross sections were calculated for the standards.

As stated above, the spectrum to be quantified has to be a full-range single-scattering spectrum, which means that the low loss spectrum must contain the ZLP. Therefore, as was done in the previous chapter on extraction of precipitate signals from a matrix, it is crucial to work with spliced and Fourier-log deconvolved spectra. However with few approximations, the routine of quantitative analysis can be simplified. The first assumption for this calculation is that the inner-shell excitation is the only excitation taken into account, which is obtained by removal of the background. It is usually found that the background far from the plasmon loss region is given by a Power Law function $J(E)=AE^{-r}$, where A and r are constants. This only applies, however, when plural scattering is negligible or removed altogether. Otherwise, the *r* constant altered by the addition of the multiple scattering in a way that depends on energy, changes the shape of the background [236]. The scattering events are independent, so the final product of the multiple scattering is just a sum of individual scattering events. The intensity of edge with certain energy loss contains the contribution from a number, *n*, of plasmons summed up as individual scattering events resulting in it being spread out to higher energy by plural scattering. The multiple event scattering adds signals from whole range of spectrum to every edge signal. Consequently the investigated area contains the information not only from the core losses of the atoms in one atomic column, but also contributions from other parts of the spectras. After the removal of the multiple scattering, and only then, the calculations of the thickness of individual elements in the precipitate can be calculate with the equation 18**)**.

Fulfilling these stated above requirements, to get the absolute quantification the determination of the total mean free path for inelastic scattering and the edge cross sections for individual elements are the two key parameters that must be determined. Therefore, the experiment with the needle-shaped specimen was conducted to get the accurate mean free path, which is described in next subchapter. It is then followed by determination of the differential cross sections complementary data for final quantification.

7.2. Geometrical estimation of thickness by needle-shaped specimen and mean free path

The thickness of each pixel in a spectrum image can be determined by a combination of log-ratio relative thickness routine in Digital Micrograph with use of an accurate mean free path for inelastic scattering, λ. The result is an intensity map of t/λ presented in mean free paths. To convert this to a representation in nm, the intensity map has to be multiplied by the mean free path for the specific material under investigation. One approach to determine the mean free path is to use a parameterisation of experimental data, for example that of Iakoubovskii *et al*. [237] in terms of sample density. This gives an improved fit to the data originally parameterised by Malis *et al.* [233] in terms of mean atomic number. The essential points emerging from these publications are that mean free path depends on total inelastic scattering. The total inelastic scattering per atom scales with the total number of electrons in the atom to scatter from, which means it should scale with Z. This approach explains the original Malis parameterisation. However Malis *et al.* [233] misses the density with which atoms are packed, which was taken into account by Iakoubovskii *et al*. [237].
So, there is then a parameterisation in terms of density, which is what Iakoubovskii did, and what was used for absolute quantification in this thesis together with the experimental check of its correctness.

Most early EELS work was done on uncorrected microscopes, so convergence angles were below 10 mrad. So spectrometers only needed to collect low angles to about 10 mrad. That makes the optics easier, and the physics of calculating the inelastic scattering easier. Modern probe-corrected STEMs use much higher angles of incidence, so the collection angle into the spectrometer is much higher. This makes everything harder for the optics designers, both for the microscope and for the spectrometer. And there is now a huge mix between the effects of a huge range of incident angles, and a huge range of scattering angles, so it is complicated with modern machines. But it's also simpler because it averages out most of the crystal orientation effects. Therefore subsequent analysis of Iakoubovskii's parameterisation by Zhang *et al.* [233, 238] showed that it performed very

well for the high convergence and collection angles used in modern aberration corrected STEM instruments in general and in particular, gave discrepancies of less than 2% with experimentally measured values for Mg.

In order to determine an absolute mean free path for one standard, and in order to check the parameterisation of Iakoubovskii [234] a needle-shaped specimen was used to allow correlation of real thickness measured in HAADF imaging with t/λ measured by EELS-SI. This check has to be done, because the explanation of equations used by [237] is based on phenomenological biases but lack of experimental results, which questions its accuracy. While an experimental check using MgO showed it was accurate to a few per cent [238], its accuracy for transition metal compounds needs to be evaluated. Using an ideal needle sample of circular cross-section and with no surface layers, this would be a straightforward procedure and the width could be assumed to be equal to the thickness. However, for a real sample where the geometrical cross section may not be perfectly circular, t/λ can be measured on the axis of the needle and the diameter of the needle can be measured at that point after tilting through 90°. The latter is equal to the thickness measured at the equivalent point in the spectrum image as t/λ. Hence, at the same time there are two values t and t/λ at the same point, giving an experimental value of λ that can be compared to that obtained from Iakoubovskii's parameterisation (or any other calculation). Moreover, this can be done for many points on the needle to eliminate systematic and random errors.

Firstly, a needle-shaped specimen of $TiC_{0.98}$ was prepared using a FIB dual beam workstation, and this is shown in **Figure 69.** The sample was then mounted in a high-tilt tomography holder and a tilt series of both HAADF images and EELS spectrum images was then taken at ~10^0 intervals from ~-80^0 to ~+80^0. t/λ maps were calculated in each case, and the thickest line along the needle axis was extracted in each case. t was determined for each image as a function of distance from the tip. Pairs of t/λ plots with position from goniometer tilt α and plots of t versus position from a tilt angle of $\alpha + 90°$ could then be correlated and plotted, and the results are shown in **Figure 70.**

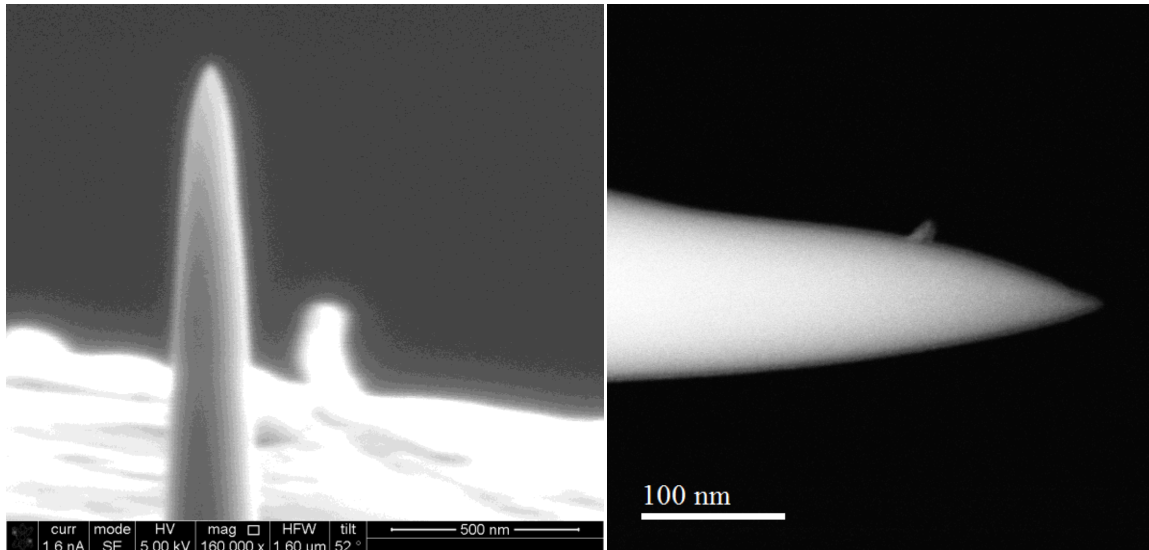

Figure 69. The needle-shaped specimen in FIB, observed with the electron source straight after preparation, and during experiment in ARM, observed with HAADF.

In practice, this analysis is not so straightforward. The needle, like any sample prepared in the FIB and subsequently exposed to atmosphere, has a surface layer that is different from the bulk material of interest. Such a needle specimen rarely has a circular cross-section. The presence of surface oxide meant that the analysis was carried out only in the middle part of the needle, because at the tip there was no bulk material present, which is the reason why there are higher t/λ values than t at this point. Fortunately, the widths measured at a particular point on the axis in a tilt series can be fitted to those of an ellipse with good accuracy and so the thickness on the axis at zero tilt can be found. Finally, the pixel size in the SI used to measure t/λ is larger than that used for the HAADF images of the tilt series, leading to some uncertainty in the origins of the measurements of axial position in the two cases.

The result of plot t/λ versus the real axial position with the geometrical t is shown in **Figure 70**. in the top part, with the standard deviation in the bottom. The straight line shows the fit to the plot resulting in the gradient described in previous paragraph.

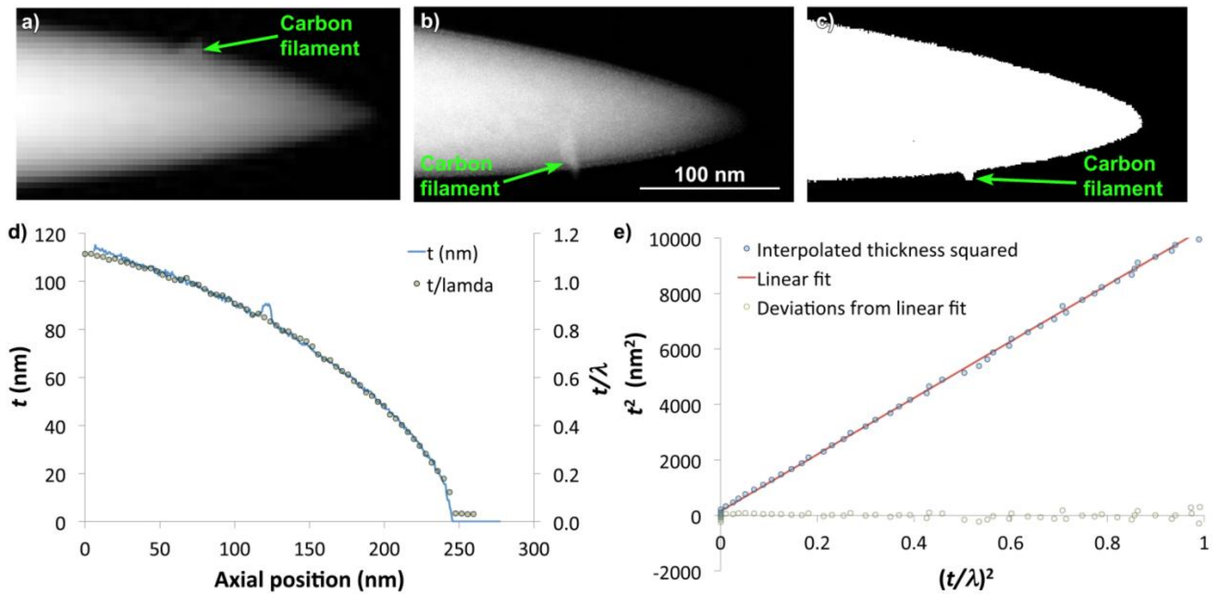

Figure 70. a) a map of t/λ from the TiC0.98 tip; b) the HAADF image after rotating 90° about the tip axis: c) the HAADF image after thresholding; d) plots of maximum values t/λ in each vertical line of the image and the corresponding values of t from the HAADF image versus axial position (i.e. the horizontal direction, from left to right); e) a plot of t^2 against $(t/\lambda)^2$ together with a linear fit and the corresponding deviations. The plot describes the t^2 against $(t/\lambda)^2$ because the λ varies approximately as the square root of the axial position.

Figure 70a shows the t/λ map taken from SI corresponding with the HAADF image presented in the **Figure 70b**. The maximum values of t/λ taken along the vertical profile of the image **Figure 70a** are plotted against axial position, and presented in the **Figure 70d**. To make it easier, the mask with the threshold is applied so that all the pixels in the vacuum was zero, which is presented in the figure **Figure 70c**. The geometrical thickness is obtained by taking the profile and summing the values in each pixel together with scaling the pixel size. Both types of thickness were plotted against axial position, and they follow each other closely in the centre section of **Figure 70d** and these points are used in the analysis. The small piece of debris, which is observed in all images is not a problem, because it does not perturb the profiles and values, in other acquisitions it is rotated, and at some point it may affect the profile.

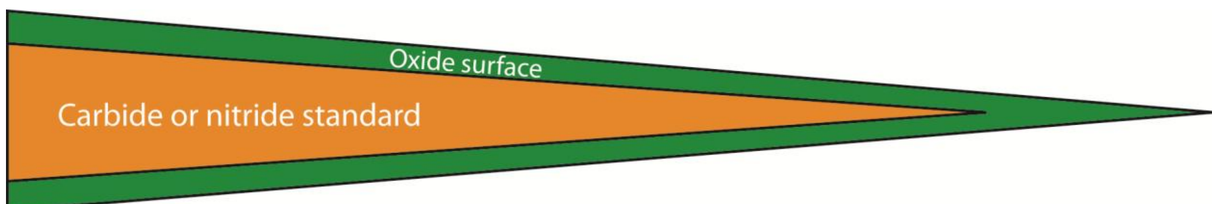

Figure 71. Specimen contribution of bulk and surface phases.

Points from the very tip, and from the thick regions (where the *t* gets higher than the t/λ) are excluded from the analysis. It might be caused by too thick specimen, wrong background

subtraction or some errors during deconvolution. As it was already proved by others, the best samples are with the thickness in the range $0.2<\lambda<0.8$ mfp's [239, 240]. Further on, these parts of the specimen are excluded in the least squared fitting while calculating the differential cross-sections, because otherwise, the fit gets wrong values.

Also, in **Figure 70e** , the mean free path is given by the square root of the gradient of the plot of t^2 versus $(t/\lambda)^2$. The square root is chosen, because the needle was not a linear profile of thickness with position, but roughly parabolic, and it was easier to work with a parabolic fit to what is presented in **Figure 70d.** The error on each of the presented values from the fits is <0.25%. Their average gives a value of λ_B for $TiC_{0.98}$ of 103nm. Comparing with the value of Iakoubovskii parametrisation calculated mean free path which is 126nm suggests that a significant difference between calculations and experiment requires some correction to the formula. The experimental value of λ_B for $TiC_{0.98}$ is extrapolated for other values for standard *MX* by assuming that $(\lambda_{MX}/\lambda_{TiC})_{\mathrm{expt}} = (\lambda_{MX}/\lambda_{TiC})_{\mathrm{Iakoubovskii}}$, which comes to about 20% less than calculated from Iakoubowskii parametrisation. **Figure 70e** also confirms the good agreement between two types of thickness. These types of plots are performed for all standard specimens, but not with the needle shapes, but for classic FIB lamella. The behaviour of the deviations allow choosing which part of the SI is used for further analysis, i.e. as a result the final estimation of the partial cross-section. The rest of the images are presented in the **Figure 73, Figure 74** and **Figure 75.**

Based on such a good agreement between the thickness obtained from HAADF and from the spectrum image, it can be assumed that the λ calculated from the Iakoubovskii parameterisation can be used for further quantifications, i.e. calculations of the λ from other standards, but a modification has to be made. Because the differences in the value of experimental value and the Iakoubovskii calculations, the real value of λ has to be reduced by 20%. If the plots of t and t/λ increased linearly with axial position, the solution would be straightforward giving by the ratio of the slopes the λ_B. However, in reality, the profiles vary approximately as the square root of the axial position. The most stable results are obtained by plotting of t^2 against $(t/\lambda)^2$ and taking the slope. Here, the values of t are interpolated onto the sampling points of t/λ using a quartic fit to a plot of t^2 versus axial position. Since such a plot is a straight line (see **Figure 70e**) and, assuming a single surface layer of constant thickness, the relationship between of t and t/λ can be expressed as a straight line of slope, *m*, and intercept, *c:*

$$(\boldsymbol{t_B} + \boldsymbol{t_s})^2 = \boldsymbol{m}\left(\frac{\boldsymbol{t}}{\boldsymbol{\lambda_B}} + \frac{\boldsymbol{t_s}}{\boldsymbol{\lambda_s}}\right)^2 + \boldsymbol{c}, \qquad 19)$$

where t_s is thickness of the surface layer, and t_B is the thickness of the bulk. Differentiating this with respect to t and re-arranging gives

$$\boldsymbol{\lambda_B^2 = m\left[1 + \left(\frac{t_s}{t_B + t_s}\right)\left(\frac{\lambda_B}{\lambda_s} - 1\right)\right].} \quad 20)$$

Both of the terms in round brackets will turn out to be much less than unity and so λ_B can be written as

$$\boldsymbol{\lambda_B = \sqrt{m}\left[1 + \frac{1}{2}\left(\frac{t_s}{t_B + t_s}\right)\left(\frac{\lambda_B}{\lambda_s} - 1\right)\right]} \quad 21)$$

To deal with this problem the specimen material has to be divided into two phases - bulk and surface. A subscript ***b*** is added to the parameters appropriate to the bulk of the standard, considered a variables. A subscript ***s*** is added to the parameters appropriate to the surface layer and all these parameters are considered as constants.

Similarly, the measured value of t/λ is composed of two contributions.

$$\frac{t}{\lambda} = \frac{t_b}{\lambda_b} + \frac{t_s}{\lambda_s} \quad 22)$$

Even after "polishing" a FIB section with low energy ions to reduce surface damage, some will always remain and, when the lamella is removed from the FIB, it is likely that some oxidation of this surface layer will occur. While the nature of the surface layer may vary with depth, it will eventually end, leaving the original bulk material. Also, due to its method of formation, it will be homogeneous across the surface of the lamella. Thus, provided that there is bulk material between the two surface layers on the lamella and the surface layer remains approximately normal to the electron beam, an increase in thickness of the lamella will result in an increase of signal from the bulk but not from the surfaces.

So, if the thickness is calculated by following the above equations, *t* does not give the correct value for the thickness of the standard but t' where

$$t' = t_b + t_s \frac{\lambda_b}{\lambda_s} \quad 23)$$

so instead of *N*, N' is obtained where

$$N' = n_b t' = n_b t_b + n_b t_s \frac{\lambda_b}{\lambda_s} \quad 24)$$

Nevertheless, the gradient I/I_0 against N' can be a straight line. Since t_s is assumed constant, $d(I/I_0)/dt_b = \sigma_b n_b$ and $d(N')/dt_b = n_b$ so that

$$d(I/I_0)/dN' = \sigma_b \quad 25)$$

Thus, the gradient of the plot of I/I_0 against N' gives the correct value of σ_b for each of the standards provided that the projected thickness of the surface layer is constant across the sample surface.

Despite careful removal of the surface contributions by cleaning the specimen, and separation of the spectrum image signals, still some small surface contribution remains, which is visible in the graphs of $I(\Delta E, \alpha, \beta)/I_0$ against N with fits, where the graphs have non-zero intercepts on the *y*-axis. All the graphs are presented in **Figure 73, Figure 74,** and **Figure 75**.

In previous research, the mean free path is calculated with use of the equation

$$\boldsymbol{\lambda = \frac{t}{\ln\left(\frac{I}{I_0}\right)}} \qquad 26)$$

which is a variation of equation 18**),** and according to Hartree-Slater equation

$$\boldsymbol{I = I_0 n\left(\frac{t}{\lambda}\right)\lambda\sigma,} \qquad 27)$$

where the n is volume density. This equation was showed by [241] to underestimate the value of total mean free path, but Malis *et al.* [233] added correlation with the atomic number of the elements giving the effective mean free path. The most recent research done by Iakoubovskii *et al.* [237] improves the formulas and allow the absolute calculations with an error down to 10%. The experiment with the needle-shaped specimen it was shown that the mean free path is overestimated by about 20%, but by a simple reduction it still can be used for quantification. So by simple mathematical manipulation, n in $\frac{atoms}{nm^3}$ can be calculated, giving direct information about the quantity of each element.

The mean free path of each single element is necessary for calculations of the N, which is number of atoms, per unit area, in other words areal density. The mfp is calculated from the formula given by Iakoubovskii equation:

$$\frac{1}{\lambda} = \frac{11\rho^{0.3}}{200FE_0}\ln\left(\frac{\alpha^2+\beta^2+2\theta_E^2+\left|\alpha^2-\beta^2\right|}{\alpha^2+\beta^2+2\theta_C^2+\left|\alpha^2-\beta^2\right|}\cdot\frac{\theta_C^2}{\theta_E^2}\right) \qquad 28)$$

which includes the convergence α and collection β semi-angles, acceleration energy of the electrons E_0 and density of the material for which the mean free path is calculated.

The values of N_M were calculated from the lattice parameter data given by Goldschmidt [242] using Vegard's Law to interpolate to the value corresponding to the composition. This also provided the density used to calculate λ_B using the Iakoubovskii parameterisation [237]. The values are not

sensitive to the exact stoichiometries. The values of the lattice parameter, *a*, N_M and λ_B used are given in **Table 4**.

Compound	*a*	N_M	ρ	λ_B (nm) calculated	λ_B (nm) corrected
$TiC_{0.98}$	0.4328	49.37	4.889	126	103
$TiN_{0.88}$	0.4239	52.51	5.249	124	101
$VC_{0.6-0.8}$	0.4156	55.73	5.636	122	99
$VN_{0.97}$	0.4131	56.74	6.079	120	98
$NbC_{0.9}$	0.4156	55.73	8.198	111	86
NbN	0.4380	47.60	8.448	110	87

Table 4: Calculated mean free paths for the standards used in this work, according to equation 28). The convergence semi-angle is 36mrad and collection semi-angle is 72mrad.

These calculations include systematic errors, based on square root of the sum of squared errors. The errors include the gradient of standard cross-section calculated from least squared fitting, error on mean free path calculations, which is limited down to 3%. The total error is given by the equation below:

$$\frac{dN}{N} = \sqrt{\frac{\delta_n}{n}} = \sqrt{(\frac{\delta\sigma}{\sigma})^2 + (\frac{\delta\lambda}{\lambda})^2 + \frac{1}{I}} \quad 29)$$

The overall calculated errors do not exceed the value of few atoms. This equation contains three parts, one which is from the gradient error $(\frac{\delta\sigma}{\sigma})^2$, one which includes the error for mean free path calculations $(\frac{\delta\lambda}{\lambda})^2$, and one which includes random errors in the real raw data $\frac{1}{I}$.

As it is presented by Iakoubovskii *et al.* [234], there is little evidence for calculations of mean free paths and cross-sections of material such as carbides or carbonitrides. The reasons are multiple, such as extraction replica – where there is no chance for quantification of carbon mean free path, or, that the detection techniques are not sufficient to acquire low signals like C or N. Also the separation of other contributions such as contaminations was not known well enough to be performed allowing quantification on this level of precision. Usually the most difficult obstacle was carbon contamination, which occurs during acquisition. The organic carbon products make it impossible to absolute and real quantification, i.e. calculate the mean free path or cross-sections. In the case presented here, the amorphous carbon or oxide layer is not a problem, because it is removed in the way described in previous chapter. It has to be removed, otherwise the mean free paths or thickness are overestimated.

7.3.Choice of the edge and background subtraction

The quantification of the chemical composition is highly dependent on the function extrapolating the background shape [224, 233, 243]. Only then the determination of the chemical composition with high accuracy is possible, because the shape of the background affects the cross-section. Usually, the background is fitted in front of the quantified core-loss edge and extrapolated through the whole range of the energy range used for the integration signal of chosen edge [225]. The fitting of the background in front of the edge is essential because the extrapolation process enhances any error in the data (for example underestimations of the cross-sections, or overestimations of the thickness). On a large scale it might be observed in the thick specimen, where multiple scattering is a large fraction of the collected signal. The processing procedure allows subtraction of the matrix and surface contributions resulting in signal without multiple scattering and matrix EXELFS, so the background fitting is much better than without this step [244]. Without these steps, the integration of the signal for quantification is impossible or very difficult and suffers from several errors and overestimations or underestimations of the real signal.

The choice of edge used for quantification is an important step. In case of our specimen, the elements that have to be quantified are: C, N, Ti, and V. C and N have only one edge in the core-loss region, which is a K-edge. For Ti and V, the most sensible edges to use were the $L_{2,3}$ edges at 464 eV and 513 eV, as the K-edges are at very high energy, and the M-edges are only just above the plasmon peak in the complex low-loss region. The integrated signal used for quantification has to be strong enough to give good signal to noise and thus, good statistics and all these edges fulfil this criterion. There are some minor complications, however, as the V-$L_{2,3}$ edge is at 513eV. Unfortunately, this is preceded by the Ti-$L_{2,3}$ edge, which is at 456eV, and followed by Ti L_1 which is at 564eV loss, and the O-K edge, which is at 530eV. So, the fitting window for background extrapolation under the V-$L_{2,3}$ edge is quite narrow (between 25 and 30eV width, where usually 50eV is used), and even then may not give a perfect fit due to the tails of the Ti edge. Moreover, the integration window must be quite narrow to avoid alterations by the O-K and Ti-L_1 edges. Therefore the calculation of V thickness as a single element benefits from removal of the O-K surface contributions, as described in previous chapter.

The electronic configuration of Ti and V is very similar; the only difference is the additional electron in the *3d* shell in V. The edge used for quantification is the $L_{2,3}$ edge, which occurs at 456eV loss. The intensity of white lines of this edge is high enough to perform quantification. There is enough range to fit a wide window for background extrapolation, but the signal window is limited by the presence of the V-$L_{2,3}$, so the maximum possible integration width is approximately 55eV.

7.4. Determination of the differential cross-sections

The calculated cross-section is used for estimation of the thickness of certain elements. With use of the same background and integration window set in DM for standards and real specimens, a signal maps represented in counts per unit area can be created. The signal of each edge is a standard integration of the signal above the edge.

The calculation of the cross-sections requires standards, which are the specimens prepared from materials of known stoichiometry. The standards were prepared using standard FIB lamella. The choice of preparation depends on the form of standard available material. Most of used standards had a solid form, so it was easy to prepare a lift-out lamella from each of them (the procedure was similar to the one used for steel lamellae described in chapter **3.2.3.2** , based on [156] and described also in [195]). The TiC, TiN and VC were provided by Sandvik Coromant as bulk materials, two with known stoichiometries – $TiC_{0.98}$ and $TiN_{0.88}$. The VC was believed based on the information provided by the manufacturer to have a composition of $VC_{0.83}$ and showed diffraction patterns in TEM consistent with the V_6C_5 phase described by [66]. The VN standard specimen was provided by Prof. Dr. Walter Lengauer of the TU Wien [245] also as a bulk material and the stoichiometry of it was $VN_{0.969}$.

The differential cross-section is extracted from the least squares fit between $I(\Delta E,\alpha,\beta)/I_0$ against N in DM. The least squares fit is a mathematical function, which takes all the points, and fits the line between them, finding the shortest path between all the points and the line, as described in the **Figure 72**. In most cases the gradient, in other words, this line has intercept other than zero value at the *y* axis. It is due to the constant surface layer, which is present in almost all specimen (apart from one TiC specimen). The assumption that it is constant allows its impact on the cross-section to be eliminated by simple reduction of the cross-section of bulk σ_b material by cross-section of the surface layer σ_s (better explained later in this section). Because of the plural scattering deconvolution, the cross sections can be subtracted one from another without affecting the slope of the least squares fitting, i.e. the cross-section value.

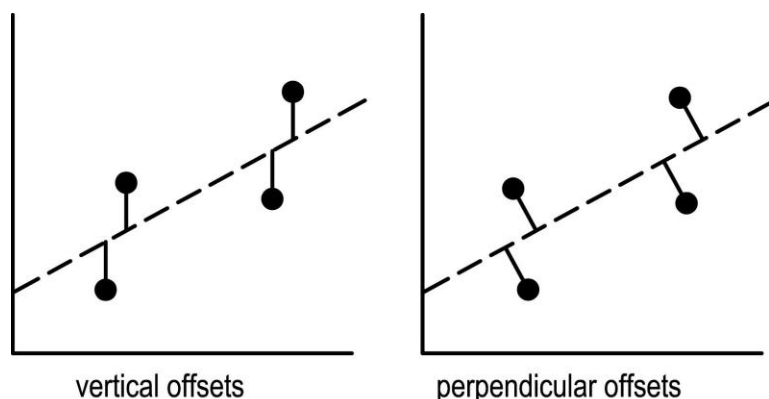

Figure 72. The scheme of the least squares fit with the vertical and perpendicular offsets. Both offsets work good, and their choice is arbitrary, with negligible effect on final results. The perpendicular are used in the DM script in this thesis. The positive intercept at the *y* axis arise from the surface contribution, and its value stands for σ_s.

The fitting is made on standard specimen TiC, TiN, VC, VN and NbC and NbN. VC and NbC are powder specimen, which can question its stoichiometry, therefore there have been several spectrum images recorded per each standard specimen, from which the best were chosen for further analysis. Apart from the VC standard, at least 3 good sets of spectrum images were used for analysis. The fit result performed in DM is a differential cross-section used for further quantification.

The absolute quantification of the precipitates is straightforward with differential cross-sections (thus integrated (partial) cross-sections. The final quantification is presented in **the chapter 8**. To avoid contamination of the lamella and needle specimens overnight baking at 100°C was performed, followed by 3-5 minutes plasma cleaning. As the latest experiments have shown, even the 3 minutes plasma cleaning significantly reduces amorphous carbon growth during STEM experiments. This is crucial in terms of producing the C maps and the estimation the metal to non-metal elements ratios within the particles. Therefore this step is included into the standard procedure of standard specimen preparation. However, despite this, there are some residue surface phases.

The problem of two, or more surface contaminations is depicted in **Figure 71**. It shows the needle shaped specimen with the thin layer of oxide on the surface and the bulk material underneath. Any difference in calculation of the mean free paths caused by wrong estimation of thickness of each phase (bulk and surface) may lead to errors in calculations of absolute thicknesses of separate elements. Each of the phases have a different mean free path, and they are λ_S and λ_B respectively, and removal of the surface contribution is extremely important. If it is impossible, the calculations have to take into account the presence of oxides, such as Fe_3O_4 with 134nm mean free path (calculated from Iakoubovskii parametrisation).

To carry out these fits a script was written in Digital Micrograph. This script generates a spreadsheet of values of the points, fit values and deviations for each energy in the spectrum as well as plots of the differential cross-section and the errors from the least squares fits as a function of energy. With the sizes of the SI sub-regions used, the values of the fit parameters match those from the routines in EXCEL. The onset of rounding errors in the least squares fit will set a limit to the maximum number of pixels that the sub-region can contain.

The fitting script (see appendix 6) takes a part of the spectrum image, creates the 3d array of values, and extracts the mean values from it. Then the *y* mean values are set up as a 3d array, so that it can be subtracted using DM script used already to the matrix subtraction. Then the results are created in the form of an spectrum image and put the coefficient and error data into 4 byte form.

The cross-section for TiN extracted from the dataset is compared to the average spectrum from it in **Figure 76**. The error on each point from the fit is ~1%. It can be seen that the O K-edge from the surface layer has now been removed. Also the fits presented in **Figure 74** top row (TiC) are well fitted, which confirms that the O-K edge is separated successfully from the bulk specimen signal.

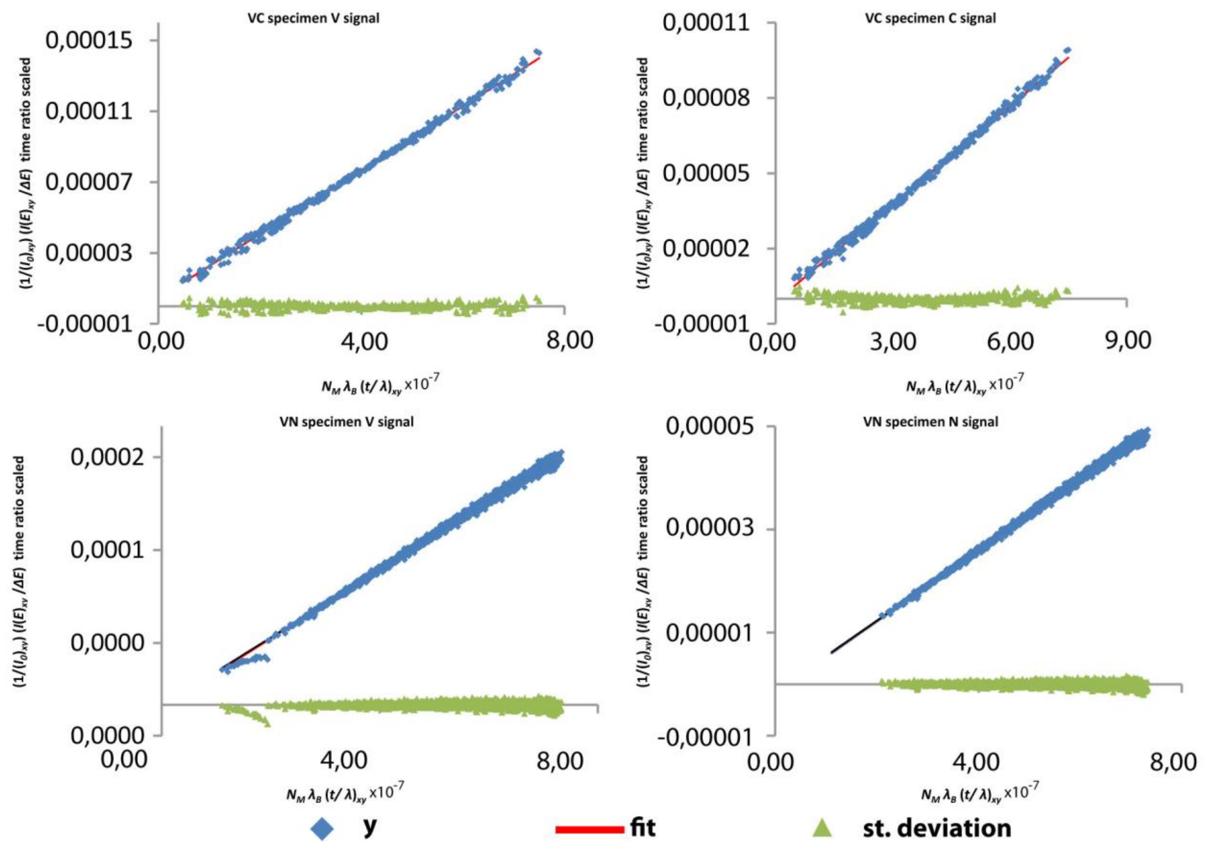

Figure 73. Plots of [$(1/(I_0)_{xy})$ $(I(E)_{xy}/\Delta E)$ (S_{xy}/T)] versus [$N_M\ \lambda_B\ (t/\lambda)_{xy}$] for for two V-standards, VC and VN of high intensity energy at the edge including white lines. The top row presents fitting two graphs from VC, the left top is fitting of V signal, the right top is C fitting. The bottom row presents graphs for VN separated on V and N fitting. All fitting are presented with the standard deviations (green).

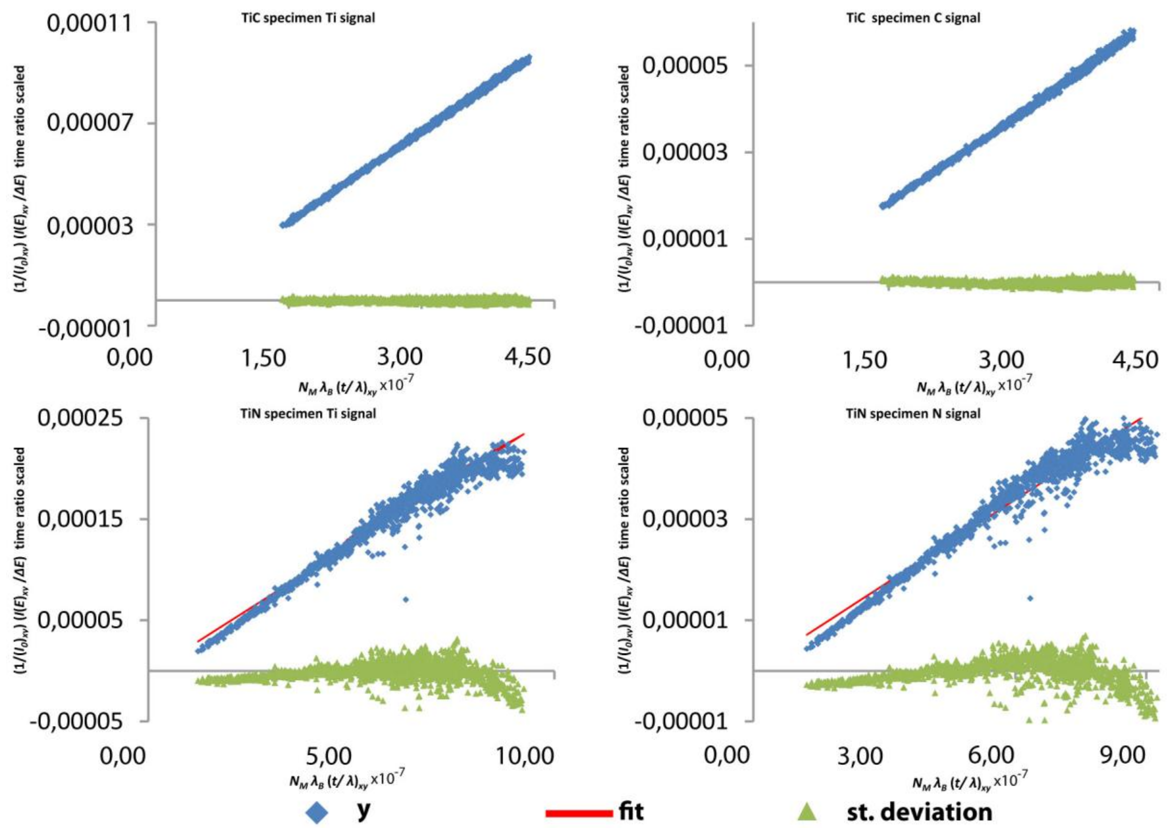

Figure 74. Plots of [(1/(I_0)$_{xy}$) ($I(E)_{xy}$ /ΔE) (S_{xy}/T)] versus [N_M λ_B (t/ λ)$_{xy}$]for for two Ti-standards, TiC and TiN of high intensity energy at the edge including white lines. The top row presents fitting two graphs from TiC, the left top is fitting of Ti signal, the right top is C fitting. The bottom row presents graphs for TiN separated on Ti and N fitting. All fitting are presented with the standard deviations (green).

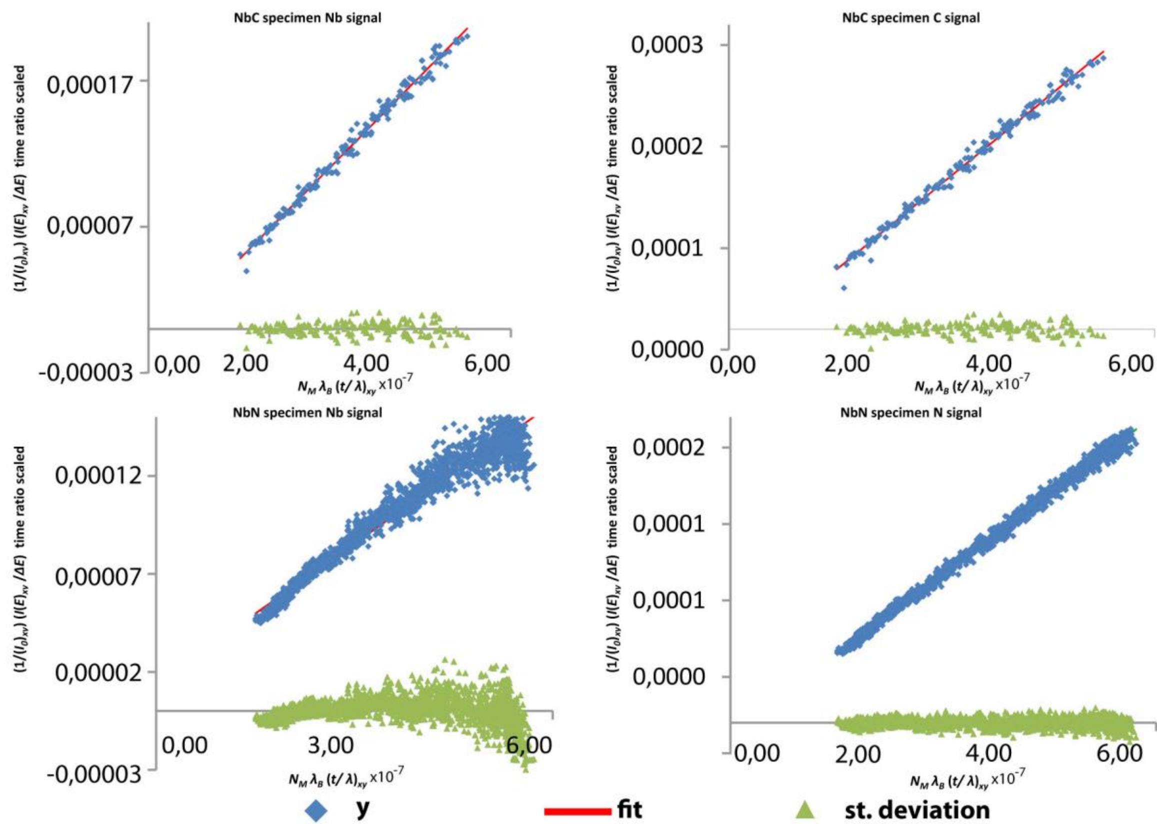

Figure 75. Plots of [(1/$(I_0)_{xy}$) ($I(E)_{xy}$ /ΔE) (S_{xy}/T)] versus [N_M λ_B ($t/\lambda)_{xy}$]for for two Nb-standards, NbC and NbN of high intensity energy at the edge including white lines. The top row presents fitting two graphs from NbC, the left top is fitting of Nb signal, the right top is C fitting. The bottom row presents graphs for NbN separated on Nb and N fitting. All fitting are presented with the standard deviations (green).

Figure 73, Figure 74, and **Figure 75** shows plots of [(1/$(I_0)_{xy}$) ($I(E)_{xy}$ /ΔE) (S_{xy}/T)] versus [N_M λ_B ($t/\lambda)_{xy}$] for VC, VN, TiC, TiN, NbC and NbN standards. These fits were done using the script in DM, where the precision can be higher than the same fits performed in EXCEL. It is clear from the deviation plots that the data are well fitted by a straight lines for V, C, N and Ti. There are few discrepancies, such as the one visible in VN for V signal, where for the thin part of the specimen the fit goes wrong. This may happen because the specimen is too thin, and the bulk material is not playing the main role now, but the surface contributions. Also it can be a reason for a small deviation for TiN, but here also the thickness of the specimen may be important. If the specimen is thicker the fit is less precise, and there are more deviations from the straight line. In general it is true provided that $0.2<t/\lambda<0.8$. It is assumed that, at lower thicknesses, surface effects are too important while, at higher thicknesses, issues arise with the Fourier-log deconvolution process. This is very much visible at Nb-standards fits, where the Fourier deconvolution suffers the most problems due to the splice point errors. Also in case of the NbC standard, there is little points in comparison to other fits, therefore it suggests that the tendency might not be real for all NbC specimen. The problem with Nb-

standards are errors with acquisition and unknown stoichiometry and purity with NbC powder specimen, because it was as standard specimen for former studies years ago. Problems related to the insufficient standards specimen, or incorrectly prepared specimens (too thick, for example) can be eliminated with future research beyond this work.

Figure 73, Figure 74, and **Figure 75** were just preliminary results demonstrate that the way of differential cross-section extraction is a good approach and can be performed for all standards V and Ti together with enough accuracy to calculate the thickness with errors down to few atoms. Also these graphs were helpful in making a choice which specimen should be used for further analysis. The ones which have the highest standard deviations are excluded. Below is described a way of revision of obtained integrated cross-section using EXCEL, with signals and maps extracted from DM. These values are later on used for comparison studies, and final quantification of precipitates. The revision is necessary, because the integrated cross-section was never obtained using DualEELS with such precision, so elimination of any potential errors is very important.

The following procedure is used to give a partial cross-section appropriate to the integration window (usually 50eV) that can be used on the same edge in the spectrum from the sample of interest and standard specimen. This relationship in equation 30**)** between intensity of integrated signal of standard and intensity of zero loss peak and number of atoms per volume is used to calculate the partial cross-section, which is in this case the gradient between given values:

$$\frac{I(\Delta E,\alpha,\beta)}{I_0} = N\sigma(\Delta E,\alpha,\beta) = nt\sigma(\Delta E,\alpha,\beta) = n\left(\frac{t}{\lambda}\right)\lambda\sigma(\Delta E,\alpha,\beta) \quad \textbf{30)}$$

where ΔE is an energy window, n is the number of atoms this type per unit volume of the standard, σ(ΔE, α, β) is the partial cross-section of the edge of interest in the energy window, I_0 is the integrated zero loss in intensity, I(ΔE, α, β) is the intensity of the background subtracted edge integrated over the energy window – a value, that can be extracted from the data.

By plotting $I(\Delta E,\alpha,\beta)/I_0$ against *N'* as it was described in previous paragraphs the differential cross-section can be determined, but this time it is presented in the form of a spectrum, which is a 3D data, instead of graphs obtained in EXCEL. It is performed in DM in a form of a script. All the pixels in the dataset can be used to give data points for this graph. The spectrum data are prepared in formalised and already discussed way [195] up to the point of removal of the multiple scattering. The gradient is derived by use of the script developed for this purpose of this research (see appendix 5) written in DigitalMicrograph. The script requires four images - deconvolved spectrum image, relative thickness t/λ, where mean free path λ is calculated from equation [237] with 20% error correction, map of a spliced factor, and map of the ZLP intensities. For the script the

whole range deconvolved spectrum can be used, or the edge signal integrated over the background. However many trials proved that using the whole spectrum instead the integrated edge signal reduces the noise in the integrated partial-cross section evaluation. Using the script after the extraction of the signal generates more noise than extraction the differential cross-section from whole range spectrum. The real partial cross-section value is the cross-section signal integrated over the background multiplied by 0.5 (number of channels per 1 eV).

Calculating partial cross-sections will allow a direct comparison with the differential cross-sections values already integrated into the DigitalMicrograph, and which are implemented in the quantification routine, and as [246] proved, they are wrong, which suggest that all quantifications done with their use are somewhat wrong. According to [246] the K-shells are almost correctly calculated, but the L-shells are almost 10% wrong. The situation is even worse for M-shells, where there is even impossible to estimate the errors.

The edge of each element to be quantified, is extracted with a fixed background fitting window and integration signal window. The same width of the windows is used for the extraction of the signal from the real data, so this is important to keep notes about the start and the width of the windows used for the extraction. Only when the windows are in exactly the same place with the same width the cross-section calculated from the standard spectrum can be used for quantification of the precipitate spectrum.

The calculated and graphically presented differential cross-sections are shown below in **Figure 76**, **Figure 77, Figure 78**. In **Figure 76** are presented shapes for TiC and TiN together with the differential cross-section taken from the DM. The TiC only and TiN only graphs are separated below in **Figure 76** b) and **Figure 76** c) respectively. In **Figure 76** b) and **Figure 76** c) it is possible to see, that the cross-sections are a little bit different from each other, but in overall they are very similar. The small variations in shape may arise from a little bit different electronic configuration of Ti and V resulting from a different content of C and N between standards. One reason for the variations is the surface damage during the FIB specimen preparation. They may arise as a consequence of stoichiometry variations across the specimen – as there are different areas where the spectra were collected. However as the first attempt, these results are very consistent and encouraging. If other materials can be prepared that way there is no objection to get cross-sections for other materials.

Figure 77 shows similar results but for the VC and VN standards. The top graph presents all results together with DM differential cross-sections. In this case also there are little variations between each standard records. But as it was described in previous paragraph it is very possible that there might be sub-stoichiometry variations on different areas on specimen or some of the damage during preparation. Also in case of VC it is much harder to synthesize a controlled stoichiometry of

the specimen than in other cases. Important thing to note is the shape of the V white lines in VC and VN. In case of the VC the first fine structure is lower, which means that the ejection energy from the L_2 edge, which in this case is electron from 2p orbital is lower in comparison to VN L_2 edge. It may suggest that the number of valence electrons in N (3) has an impact on the strength of the bonding between V and N. In comparison the C has only two valence electrons, which may suggest that the first ejection energy will be lower, due to the slightly weaker bonding. In fact, such conclusions were beyond this research, because the data collected was insufficient enough. Such research requires much better dispersion, to discuss in details the behaviour and reasons for such differences in white lines of one element.

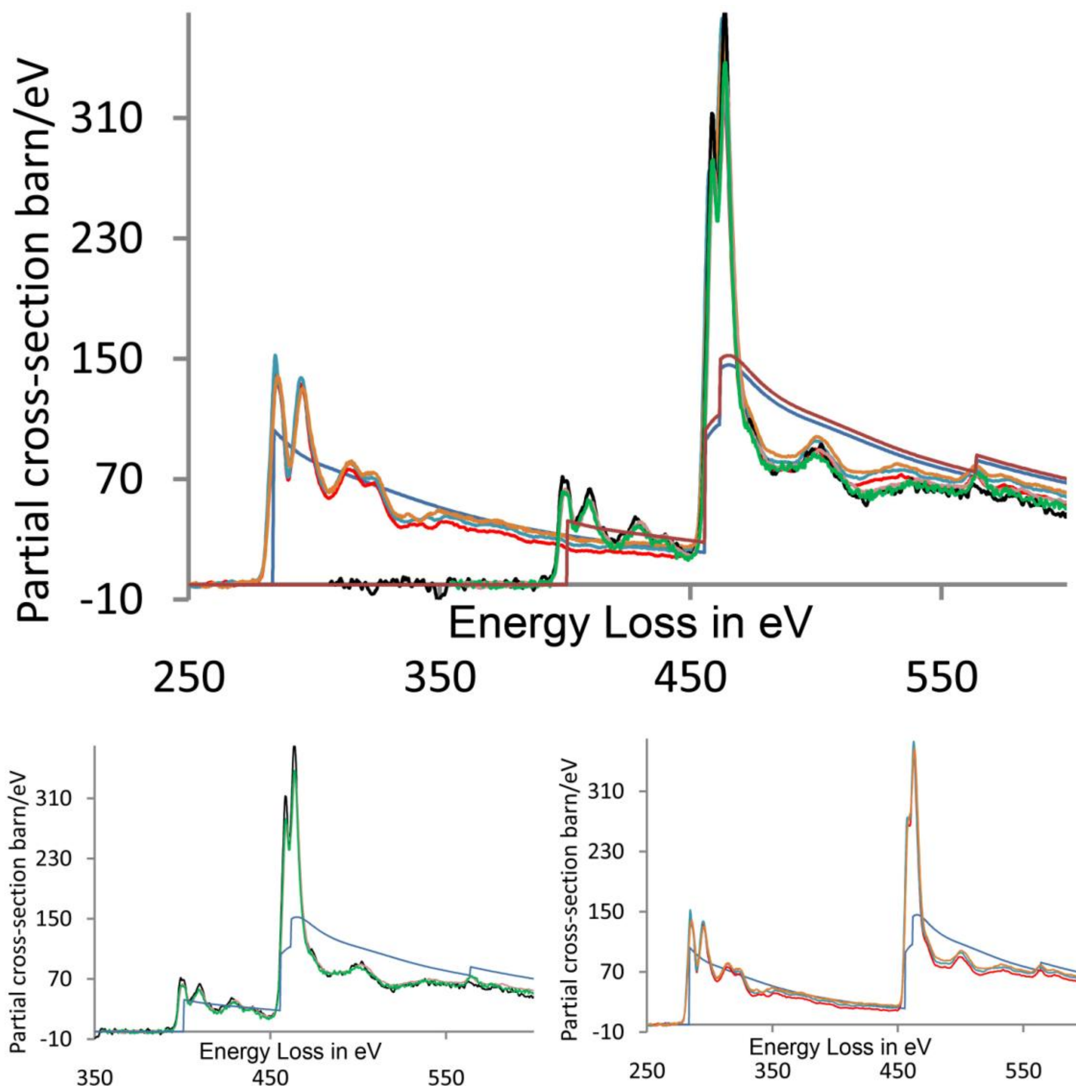

Figure 76. TiC and TiN cross-sections, a) TiC, TiN cross section overlapped with differential cross sections from DM for C, N and Ti, b)TiN cross-sections from two specimens and DM values, c) TiC cross-sections with DM differential cross-section. The light blue, orange and red are TiC standard cross-sections, the dark blue is DM TiC cross section. The black, green and dark orange is TiN cross-section followed by dark red DM cross-section for TiN.

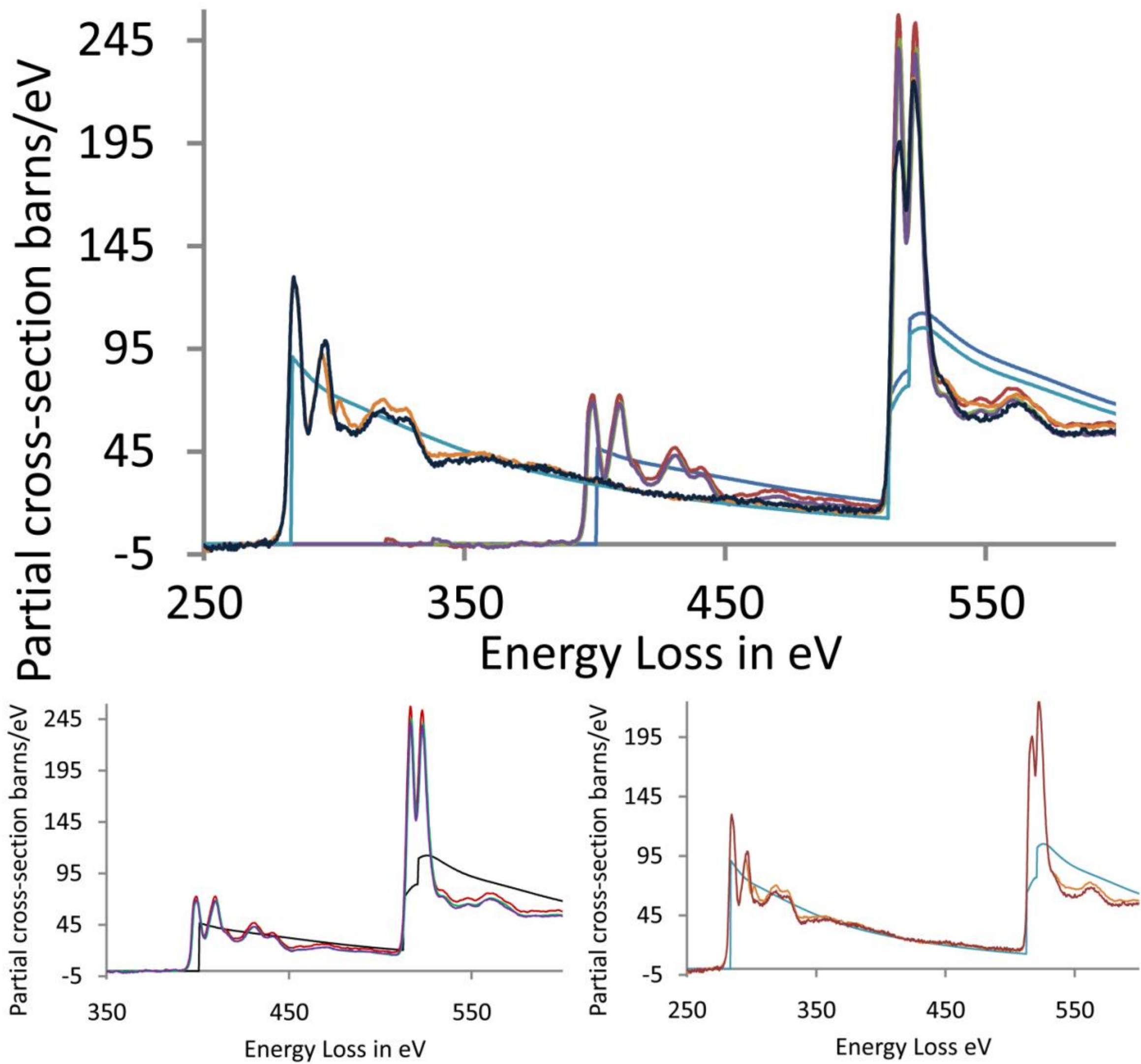

Figure 77. VC and VN cross-sections, a) VC, VN cross section overlapped with differential cross sections from DM for C, N and V, b)VN cross-sections from two specimens and DM values, c) VC cross-sections with DM differential cross-section. The black and orange is for VC standard cross-section with blue DM cross-section for VC. The dark red, violet and green are for VN cross-sections, with dark blue as DM cross-section for VN.

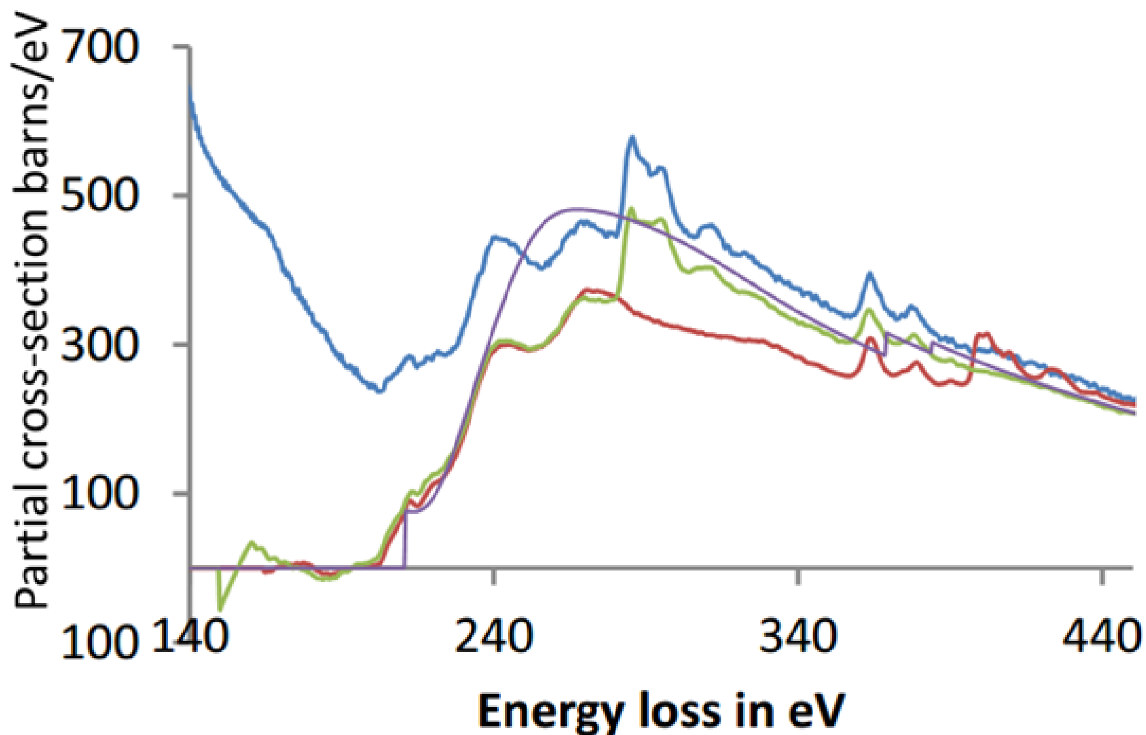

Figure 78. NbC and NbN cross-sections. Blue line shows NbC standard with the background, green is a extracted NbC differential cross-section, red is extracted NbN differential cross-section and violet one is a Nb-$M_{4,5}$ differential cross-section extracted from DM.

Figure 78 shows NbC cross-section with the background, NbN, and NbC (green and red) shows the partial cross-sections and all of them are overlapped with the DM partial cross-section (violet). The differential cross-section with the background is presented here to show what problems the evaluation of partial cross-sections are facing in the case of the Nb-standards. Close to the 150-160eV loss there is a step at the splice point, which is resulting from matrix influence (probably Fe-Mn ELNES), or errors during splicing (some data has insufficient space prior to Nb-edge due to incorrectly chosen splice point). This step generates errors during Fourier deconvolution, unable the good background fit in front of the Nb-edge, and is a source of errors in absolute quantification. The background, when it is well-fitted in front of the edge should oscillate around zero and be featureless, whereas in this case all backgrounds have some huge errors. Also, the Nb-$M_{4,5}$ edge should start at 205eV loss, whereas here some bump, occurs at 180eV loss, and it is consistent for all Nb data. The origin of it is still unknown, but further investigation may give some answers. It might be related to the differences in the oxide states of $M_{4,5,}$

The violet line, which is a DM cross-section is a hugely overestimated value of cross-section in comparison to results obtained during this PhD, which suggest that all $M_{4,5}$ edges may suffer such problems in DM.

Element	C	N	V	Ti	Nb
Integration window	**275-325 eV**	**400-450 eV**	**518-568 eV**	**460-510 eV**	**205-255 eV**
TiC 1	**4534**			**6245**	
TiC 2	**4705**			**6530**	
TiC 3	**4710**			**6570**	
TiC 4	**4626**			**6531**	
Av. ± errors	**4644 ± 41**			**6469 ±71**	
VC 1	**4451**		**5128**		
VC 2	**4423**		**4828**		
Av. ± errors	**4437±14**		**4978±150**		
VN 1		**2252**	**4998**		
VN 2		**2380**	**5062**		
VN 3		**2253**	**4826**		
Av. ± errors		**2295±43**	**4962±70**		
TiN 1		**2364**		**6632**	
TiN 2		**2432**		**6450**	
TiN 3		**2263**		**6398**	
Av. ± errors		**2353± 49**		**6493 ± 61**	
NbN 1		**2373**			**11885**
NbN 2		**2299**			**12151**
NbN 3		**2355**			**11335**
Av. ± errors		**2343± 22**			**11791± 240**
NbC 1	**5009**				**11295**
NbC 2	**4733**				**11439**
NbC 3	**5222**				**11380**
Av. ± errors	**4871±141**				**11371±41**
Hartree-Slater	**4238**	**2264**	**4206**	**5515**	**16 782**
Ratio H-S/exp	0.93	0.97	0.86	0.85	1.45

Table 5. Experimental 50 eV window cross-sections for all elements in all standards used in this work together with averages and uncertainties, together with values from Digital Micrograph calculated using the Hartree-Slater method.

In the **Table 5** the cross-sections for all prepared standards are presented. Because they were extracted from the differential cross-sections the integration window was chosen to be 50eV wide. For TiC there have been four specimen post-processed till the moment of choosing the integration window for extraction of differential cross-section. For TiN, NbC, NbN and VN there have been three specimen post-processed, and only two were post-processed from VC specimen. In case of the VC specimen. For TiC, VN and TiN it was quite straightforward to extract the differential cross-

sections. However in other cases it was not so simple. For example in case of the VC, only two datasets were good enough to apply post-processing, due to the powder specimen and not-known stoichiometry, other extracted differential cross-sections can't be use for calculations. A similar problem occurred with the NbN and NbC standards. In the case of NbC, which was also a powder specimen, but the data used for the Ph.D was limited by time and financial resources. In case of NbN data, there were problems with unknown stoichiometry of the material used for standard preparation, and similarly to NbC it required a reordering of the material and further development beyond this Ph.D. In the case of the NbC and NbN there was also an acquisition problem, because the splice point (usually around 120eV) does not leave enough background in front of the Nb-$M_{4,5}$ edge. For each individual elements there have been individual calculation of cross-section value, averaged with errors, and compared with the Hartree-Slater cross-section. The compared values were presented in the form of ratio. The errors are in the range of ±14 in case of the C calculated from VC, through ± 61 for Ti from TiN up to ± 240 for Nb. Most of the errors oscillate between 14 and 70, which is quite a good agreement between data (the cross-sections from the same element and the same specimen are compared). The comparison between cross-sections taken from DM shows that all cross-sections apart from Nb are underestimated by about 7-15%. The value of N cross-sections are the closest to each other, and their difference between experimental cross-section and DM cross-section is 3%. Also C which is usually inaccessible data in case of the VC standards, shows agreement at the level of 7%, which may suggest that the K-edge cross-sections are calculated with the lowest errors, as suggested previously. In the case of Ti and V cross-sections, which is the L-edge the level of agreement is 15%. However in case of the Nb cross-sections, the difference between experimental and DM value is 45% and it is overestimated. The disagreement between Nb values is also expected, because the M-edges give the highest errors so far. For further calculations of elemental thicknesses, the averaged values of cross-sections are used.

This chapter demonstrates highly successful methods of measuring the experimental inelastic mean free path and the differential cross-section using DualEELS technique, which can be widely used in other research materials. Both methods deal with the effects of surface layers and the method for the mean free path deals with non-ideal shape of the needle specimen. The cross-sections extracted from the experimental data have precisions of few percent, close to 2%. These values are used in a following chapter to quantify data from precipitates in steels. The calculated mean free paths and cross-sections provide an accurate method of quantifying binary, ternary and quaternary compounds of C, N, Ti , Nb and V, minimising the issues and errors associated with methods available so far. The success of these values is confirmed in next chapter showing the absolute quantification of spectrum images of single precipitates.

8. Towards absolute quantification of precipitates using experimental cross sections

In the previous two chapters the procedure for extracting the precipitate signal from the matrix was described and cross sections for the different EELS edges and the mean free paths for inelastic scattering were determined from experimental data. The purpose of this chapter is to then use these advances to perform absolute quantification of precipitates in high-Mn steels. In the case of the precipitates investigated during this research, these were assumed to be VC_x or NbC_x. In practice, as already shown in chapter 7, both V and Nb steels contained some Ti impurities and this element had to be included in the quantification. Furthermore, N was found at low levels in some precipitates, and so nitride standards had to be included too. In chapter 7 calculations with estimated errors allow the elemental thickness assessment down to a few atoms. In the analysis presented in this thesis, the few nanometer nitrogen thickness is detected (where 2nm thickness gives about 5 atoms of N, see **Figure 79** and following figures). With such detection ability it is obvious that the precipitates are really carbonitrides and the ratios between C and N can be obtained. Such level of detection, and calculations of non-metal ratios are novel in the precipitates' research field, because of FIB lamella used as a specimen, instead of common used extraction replica. The way of sample preparation is also important, because it allows estimate the metal non-metal ratios values, because the total thickness acquired by the corrected Iakoubovskii equation is a cross-check. If the summed up thickness of all elements comes up to approximately the same as the value of total thickness estimated from t/λ it means it was calculated correctly.

The results of absolute quantification are presented by elemental maps with chemical profiles and cleaned spectra together with estimated ratios between elements locally. The procedure leading to quantification consists from preparation of a standard specimen, processing the standard spectra, and evaluation of cross-sections for each element including the calculations of mfp. In case of this study, the standard specimens are made from TiC, TiN, VC, VN, NbC and NbN. The choice of these standards was conducted because of the V, Ti, Nb, C and N which were the part of the precipitates. The standards with known stoichiometry and crystallographic lattice parameter were collected under similar conditions that the one used for acquisition during precipitates spectra with DualEELS. Then data were processed according to the method proposed in chapter 6 up to the point of having a full range deconvolved spectrum. The specimen for this purpose were prepared in

two ways – FIB lamella and needle-shaped. The classic FIB lamella were used for partial-cross-section calculations based on known lattice parameters of the specimens and their thickness.

The base for the absolute quantification of the edge is extracted integrated edge signal, which is obtained by a standard background extrapolation procedure in DM. Then the information about the intensities of zero loss peak in every ZLP pixel of the deconvolved spectrum is pulled out. The intensity of the edge divided by ZLP intensity, resulting in a intensity ratio used for, which is equal to number of atoms per area multiplied by the measured cross-section, as described in equation 25). So if the intensity ratio is divided by the cross section, calculated properly from standards, it results in the *N* value which is the number of atoms per unit area. This map of *N* can be then transformed into an equivalent thickness in nm by dividing by the number of that species of atoms per unit cell volume, n.

This technique combined with the extraction procedure of the previous chapter will allow absolute quantification of such nanosized particles in other nanostructured samples, not just those studied in this thesis. Moreover, this method for absolute quantification by DualEELS is an excellent opportunity because it is one of very few techniques for the absolute quantification of chemistry at the nanoscale. The only others are EDX, provided that appropriate standards have been used, and combined with a beam current measurement, and 3DAP, provided the evaporation yield for each atom type in the sample is known. The drawback of this procedure is relative high difficulty in comparison to rather straightforward HAADF imaging, or other analytical techniques. Also, it requires deep knowledge about EELS and understanding about the characteristics of elements involved in analysis, so it might be a limitation for quick and easy supportive technique for other analytical methods.

8.1.Analytical characterisation of V steel

The specimen presented in **Figure 63** is an example of (V+Ti)(C,N) precipitate after absolute quantification. The maps represent the C, N, V and Ti in nm with the corresponding profiles taken along the horizontal line in the middle of particle, which is presented in the **Figure 79**. The total length of the precipitate is approximately 9nm in length, the elemental thickness of V is 9nm, the Ti is 5nm, which makes the total metal thickness approximately 14nm. The thickness calculated from the corrected Iakoubovskii method, called total thickness, is close to 12nm, which indicates that there is a slight underestimate of the mean free path, or partially the oxygen was not removed during calculation of the V thickness (the O-K edge is just behind the white lines of V-$L_{2,3}$ edge), or the cross-section is overestimated. On the other hand the C is 8.5nm thick and N is almost 2nm thick (given the 1:6 ratio), which gives a little bit less than 11nm total thickness. This clearly suggests that this carbonitrides is non-stoichiometric with the stoichiometry close to $(V,Ti)_{0.56}(C,N)_{0.44}$.

Moreover, as it was described in previous chapter, the Ti is not an intentional part of the alloy, it is only a contamination on a level below 70ppms. Nevertheless it takes part together with V in nucleation of the carbonitrides, because there is no obvious evidence of core-shell structure. The sensitivity of these calculations can be checked by the detect level achieved during this experiment. If the total thickness of the precipitate is ~12nm, the overlying matrix is ~37nm, and assuming that the materials were viewed along their [100] crystal directions, there would be ~106 metal sites along an atomic column in the matrix and ~20 anion sites in the precipitate, of which~3 are N which is a ~2at. % of the sample. So the sensitivity of these calculations are of 2%.

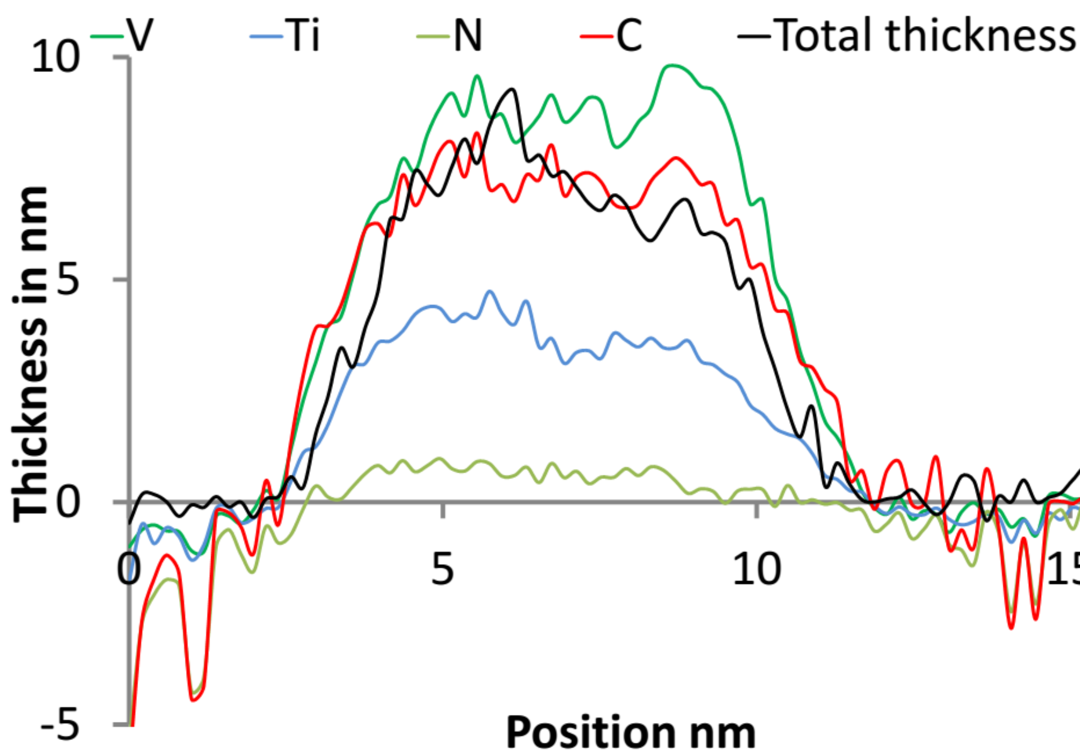

Figure 79. Chemical profiles of all elements in nanometers compared with relative thickness, also in nm. These profiles presents full quantification of VC precipitate presented in the Figure 63. Its elemental composition is V,Ti)$_{0.56}$(C,N)$_{0.44}$.

The steel specimens used for **Figure 63** and **Figure 80** were processed in the same way, and the precipitates present similarities such as sharp interfaces at each of the sides. The **Figure 80** is observed under the [011] direction, which allowed the preparation a pseudo-3D reconstruction. The maps were prepared with the improved method as on the right hand side of **Figure 63**, which resulted in clear, sharp elemental maps with minimum errors and negative counts in the matrix region. The processing allows the preparation of clean maps of metal elements - V and Ti, and low noise maps of non-metal elements - C and N. Both of the precipitates were more noticeably faceted

than that other vanadium (for example the one presented in **Figure 83**) or niobium precipitates, although it is not yet clear if the stronger faceting is a general feature of precipitates grown at the slightly higher temperature or whether this is simply an exception to the rule of most V precipitates having a fairly rounded appearance at this relatively small size. As for the other precipitates, the V, Ti and C are closely correlated and there is little sign of any local segregation. The one surprise here is that a small quantity of nitrogen could be detected, although the number of nitrogen atoms is clearly a tiny fraction of the number of carbon atoms (compare the relative height of the C-K and N-K edges in the spectrum in **Figure 61**, which is the spectrum related to the maps presented in the **Figure 63**). This suggests that although the majority of the nitrogen should have been removed from the steel in the formation of AlN, very low levels may remain in some locations and may then precipitate when carbides are formed. There was no indication, however, of any strong clustering of the N to one point, and thus no evidence of N playing a strong role in the nucleation of the carbide at this extremely low level, e.g. through the formation of TiN nuclei.

Apart from elemental maps, the thickness is mapped, so it is possible to make a comparison between the summed up metal thicknesses and total thickness from the low loss. The results of comparison is presented in the **Figure 80b**, where the black line is a total thickness, which comes to about 14nm. The blue line represents Ti thickness (4nm), dark green represents V (12nm), pale green represents N (1nm) and orange represents C (about 9nm). The summed up metal comes to about 16nm, which is a little bit more than total thickness based on calculated mean free path, which is 14nm. The reason for that might be with the wrong stoichiometry used for the elemental thickness estimations, or some unidentified errors during mean free path calculations. Also the higher metal elements sum suggests a slight underestimation of the effective partial cross sections for these EELS edges under the acquisition and processing conditions used. However this is one of the first real estimations of elemental thicknesses with cross-check done using DualEELS with such high level of detection. Also, the high spatial resolution of acquired spectra allowed to prepare a pseudo 3D-recostruction, which is done pixel by pixel in vertical Z direction in DualEELS data with a TERT function. TERT function sets a threshold above or below which all the pixles or values are excluded. The reconstruction is done by the 3D imaging software Amira (FEI) for life science imaging. The assumptions for this reconstruction are based on the well defined shape (HAADF images and EELS mapping) and symmetry orientation, therefore it can be called pseudo-tomography representation of shape and size, and assumes ideal symmetry. The reconstruction revealed a truncated octahedron shape of the precipitate with the thickness 14nm. Based on these thicknesses, the elemental composition is $(V+Ti)_{0.75}(C+N)_{0.25}$. This is a novelty to get a 3D representation of object without using tomography in TEM, which gives results in two dimensional space. Together with the

pseudo 3D-representation the gradient of elemental thickness is obtained (**Figure 81a**), which agrees with what is presented in the chemical profiles. This software also allowed a few-second movie to be prepared, presenting spinning precipitate in two directions. One of the screens is saved as an image and presented in the **Figure 81b**. There is a three dimensional space (*x*,*y*,*z*) with axis up to 18nm and violet particle in the middle. By spinning the particle around *Z* and *Y* axis the shape of truncated octahedron is confirmed.

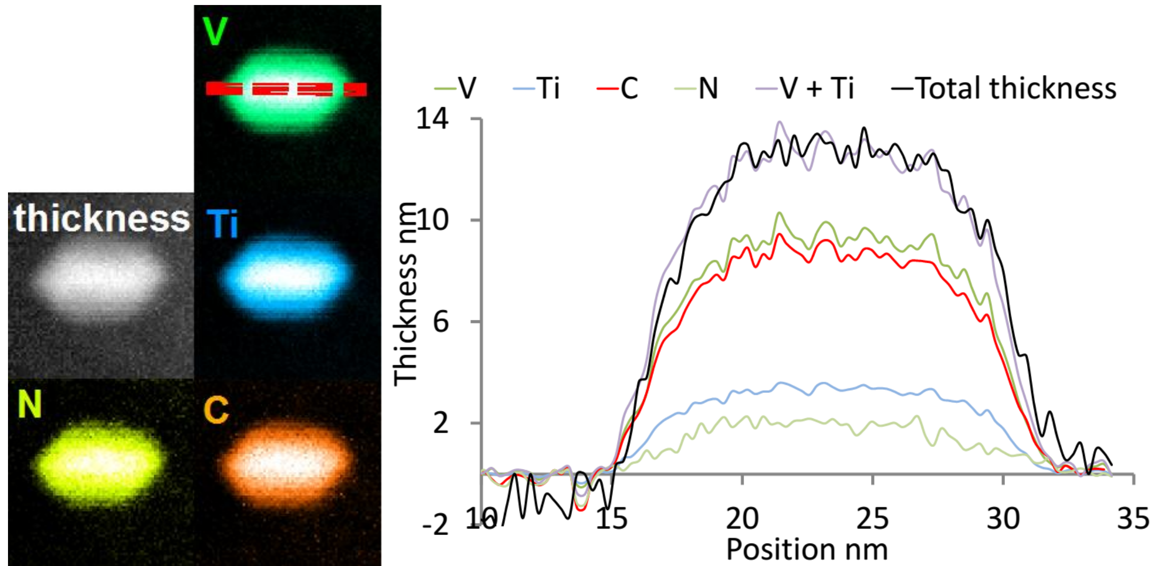

Figure 80. a) Maps of the edge intensities for a precipitate in the V steel from the fully processed data. Black in the maps corresponds to zero counts. b) Line profiles across the maps; (colours as for the maps in a), the position of the line for the profile is shown in the upper right V map). Its elemental composition is $(V+Ti)_{0.75}(C+N)_{0.25}$.

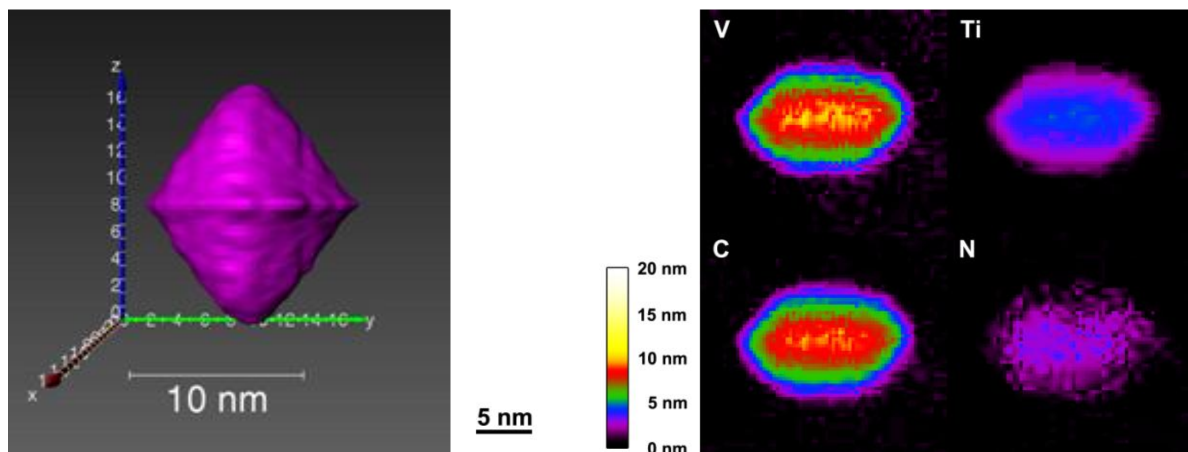

Figure 81. The pseudo 3D-representation of the vanadium precipitate with vertical profiles of all elements. The left part is a reconstructed image from Amira software, based on TERT function, the right profiles show gradient of thickness for individual elements - the black colour correspond to 0 thickness, the brighter colour, the higher thickness.

Above two precipitates were treated for 100s and 900°C, which was the most interesting isothermal treatment for the steelmakers, and for that reason most of the results were focused on

them. Some of the vanadium particles clearly contained vanadium and carbon, as expected, but almost no nitrogen was detected. This is due to the level of contamination that occurred during examination, as well as the progress that was made on technique. Because some of the studies were done at the beginning, and were never retaken, the quality of the data is not sufficient enough to remove bleedthrough, which is a major problem in N detection. Therefore the absolute quantification is not performed in this precipitates. Consistently for all precipitates observed, there is Ti homogeneously distributed throughout the precipitate, closely mirroring the V distribution. This suggests that Ti associates with V in the growth of carbides and there is no hint of Ti acting as a nucleation point for their formation.

Further additional precipitates were quantified to demonstrate the strength and analytical abilities of proposed methods in this Ph.D. The absolute quantification is presented in the form of chemical maps and profiles in nm. All profiles have similar behaviour, which is steady growth in thickness starting just from the edge of the precipitate, which is a confirmation of lack of core-shell structure in these. Usually the metal sum (V+Ti) is with a good agreement with relative thickness, which is regarded as a scientific success. All estimated compositions are based on the metal sum calculated from thicknesses. It means that both methods of quantification, which is the evaluation of mean free paths and the evaluation of cross-sections, are in somewhat agreement. It is also possible to estimate the local stoichiometries in all quantified precipitates. For example the vanadium particle presented in the **Figure 82** has a total non-metal to metal ratio almost 0.7, which suggest that one third of the precipitate is taken by non metal elements. The ratio between C and N suggest that the are four times more C atoms than N atoms. Also the V/V+Ti and Ti/V+Ti ratios shows that $\frac{1}{3}$ of the total metal is Ti, similarly to the one showed in **Figure 79.** Its estimated composition is $(V+Ti)_{0.7}(C+N)_{0.3}$.

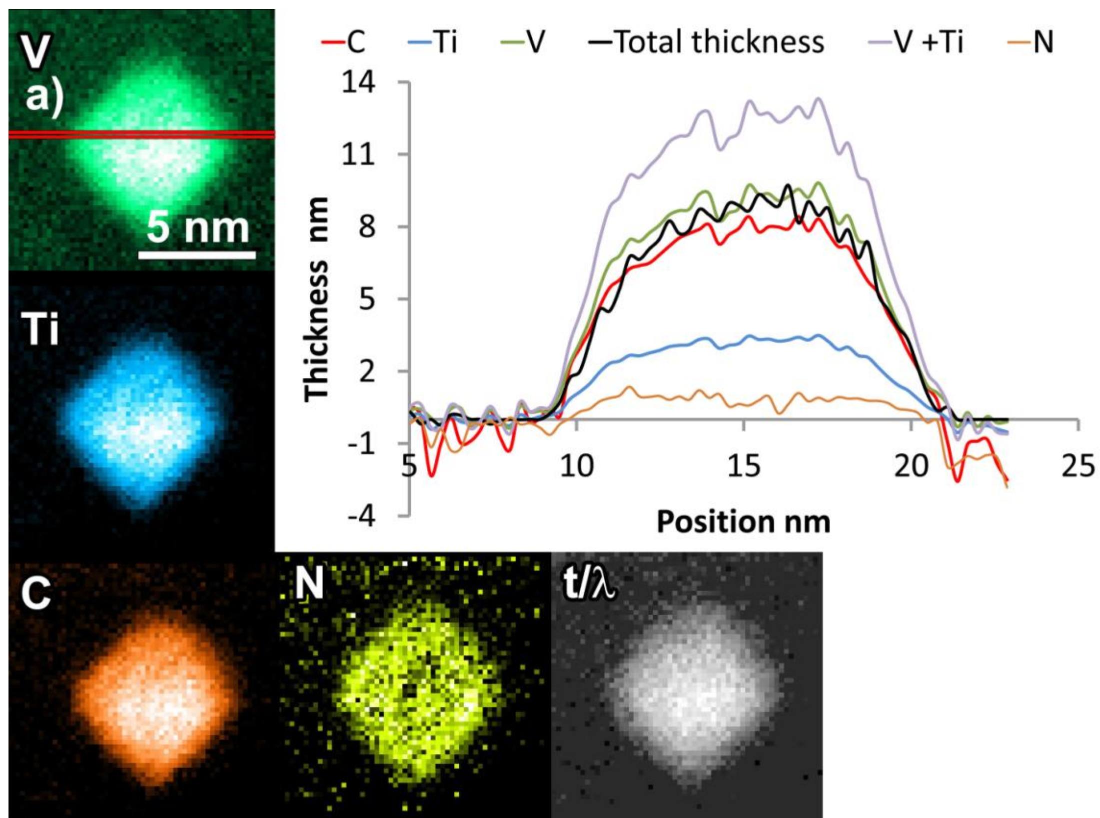

Figure 82. Maps of the edge intensities for a precipitate in the V steel from the fully processed data. Black in the maps corresponds to zero counts. Line profiles across the maps; the position of the line for the profile is shown in the upper right V map.

In **Figure 83** another fully quantified precipitate is presented. It is smaller than previously quantified precipitates therefore it was a bit more difficult to extract the matrix from the precipitate and any surface contributions. However, it was still possible to present data in form of the maps in nm supported by chemical profiles all elements. Collating these results with previous vanadium precipitates it can be said that the behaviour of all elements is the same - no core shell structure, despite the presence of Ti. However, different local stoichiometry was obtained for **Figure 83** suggest that some of the precipitates can have less non-metal elements, and the total non-metal to total metal is up to 0.86, with a stoichiometry very close to $(V+Ti)_{0.5}(C+N)_{0.5}$. But also in this case Ti atoms are $\frac{1}{3}$ of the total metal atoms, and the N atoms are no more than 6% of total atoms in this particle. Furthermore, the relative thickness is far beyond the level of total metal thickness in this precipitate. There is a high chance, because it is an early dataset from our work, that there was incomplete bleedthrough removal. This is a reason for negative counts around the precipitate region in the relative thickness profiles. Such deep fluctuation-like negative counts might be a consequence of Fourier-log deconvolution errors due to the overestimation the signal of matrix that has to be removed to gain the precipitate only signal. Usually reason for that is the surface contribution, like large portions of amorphous, organic carbon, which hinders the estimation of the accurate amount

of matrix that has to be subtracted. So in this case setting together the relative thickness and experimentally calculated cross-section thickness is impossible.

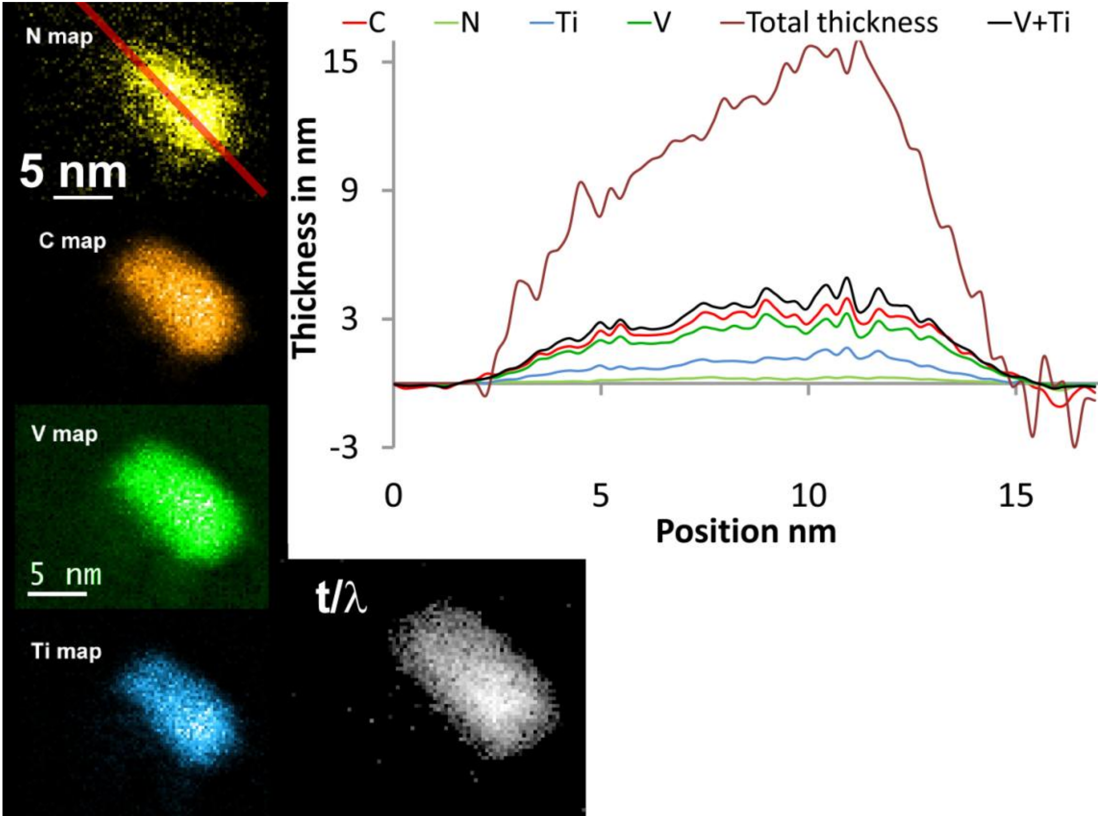

Figure 83. Maps of the edge intensities for a precipitate in the V steel from the fully processed data of steel isothermally treated for 100s in 900°C. Black in the maps corresponds to zero counts. Line profiles across the maps; the position of the line for the profile is shown in the upper right N map.

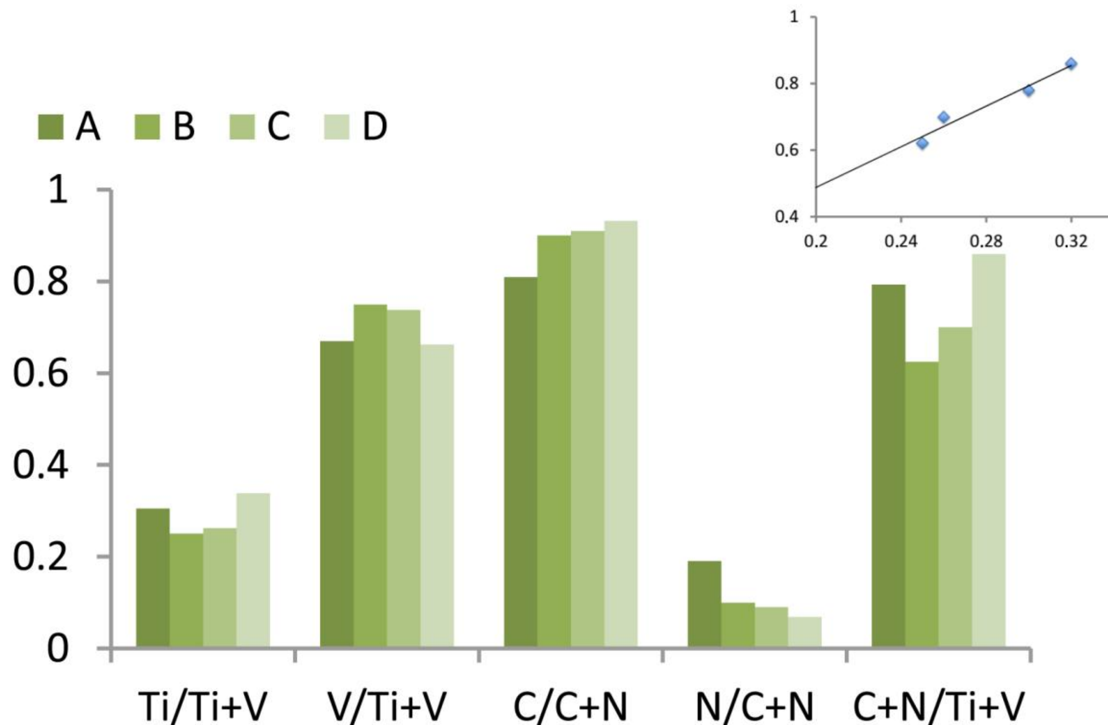

Figure 84. Comparison of ratios and stoichiometries in three fully quantified V precipitates presented in this thesis. In the small insider in the right top corner the C:M versus Ti:M is ploted.

Figure 84 shows a summary of all stoichiometries calculated from quantified precipitates. In all cases the V:M or Ti:M ratios were similar. However there are small differences in Ti content. In two precipitates (B and C) has almost similar content of the V, close to 0.8, whereas the rest (A and D) is close to 0.7, which suggest richer content of Ti. These features are followed by higher ratios non-metal thickness to metal for precipitates with more Ti in it. In the case of B, C and D precipitate the N content is similar, but in 1 the content is significantly higher. The C content is different in each precipitate, and it scatters from 0.78 to about 0.86. However consistently the C/M ratio follows the Ti/M ratio, which shows that the higher content of Ti is followed by higher content of C. It is shown in the right top corner. Such agreement is important notice, because Billingham [67, 247] showed that the VC nucleates as very off stoichiometric structure, with C down to 0.8. Also during preparation of standards during this thesis it was impossible to find out a stoichiometric standards of VC. Contrary to TiC, which usually nucleates close to stoichiometry, which also was confirmed during standard preparation, because the stoichiometry of it was 0.98. So, by mixing less stoichiometric structure with more stoichiometric structure, it would increase the content of C in mixture, which it does. Also the variation of Ti content between carbides suggests some Ti microsegregation in the cast.

In general these stoichiometries seems to behave accurately, showing that the quantification can also be used in estimations the total stoichiometries of precipitates. Based on the calculations, it

can be said that the V:Ti ratio is in the range of 0.8:02 down to 0.65:0.35 depending on the precipitate that is investigated. In the case of the precipitate presented in the **Figure 63** the V:Ti ratio is 0.65:0.35. In the case of the precipitate presented in the B the same ratio is 0.8:0.2. This may suggest that the precipitation process starts with enriched regions of Ti, because the smaller precipitate contains more Ti. The bigger one, which is almost 14nm in width has more V, however the formation process is still unclear, because although most of the thermodynamic models suggest core-shell structure, there have been none of this in analysed specimen.

8.2.Analytical characterisation of Nb steel

Figure 85 shows maps of the C, Nb and Ti content of a carbide in a niobium steel. The improved DualEELS processing allowed a very clear, almost noise-free mapping of the particle, and shows that Ti, despite being not an intentional alloying element occurs throughout the particle. Unfortunately because the C edge sits on the top of Nb edge it is difficult to remove all of the additional amorphous-C contamination which was formed during the studies. In this case some of the extensive C remains. There is also no evidence of any core-shell structure with a Ti nitride or carbide core. It is not currently possible to estimate the elemental ratios with any degree of certainty due to the lack of accurate interaction cross-sections for quantification, and work is underway to determine these from standards beyond this Ph.D. However the preliminary results show that the stoichiometry is close to $Nb_{0.9}Ti_{0.1}$ with the C to the total metal thickness ratio almost 0.6.

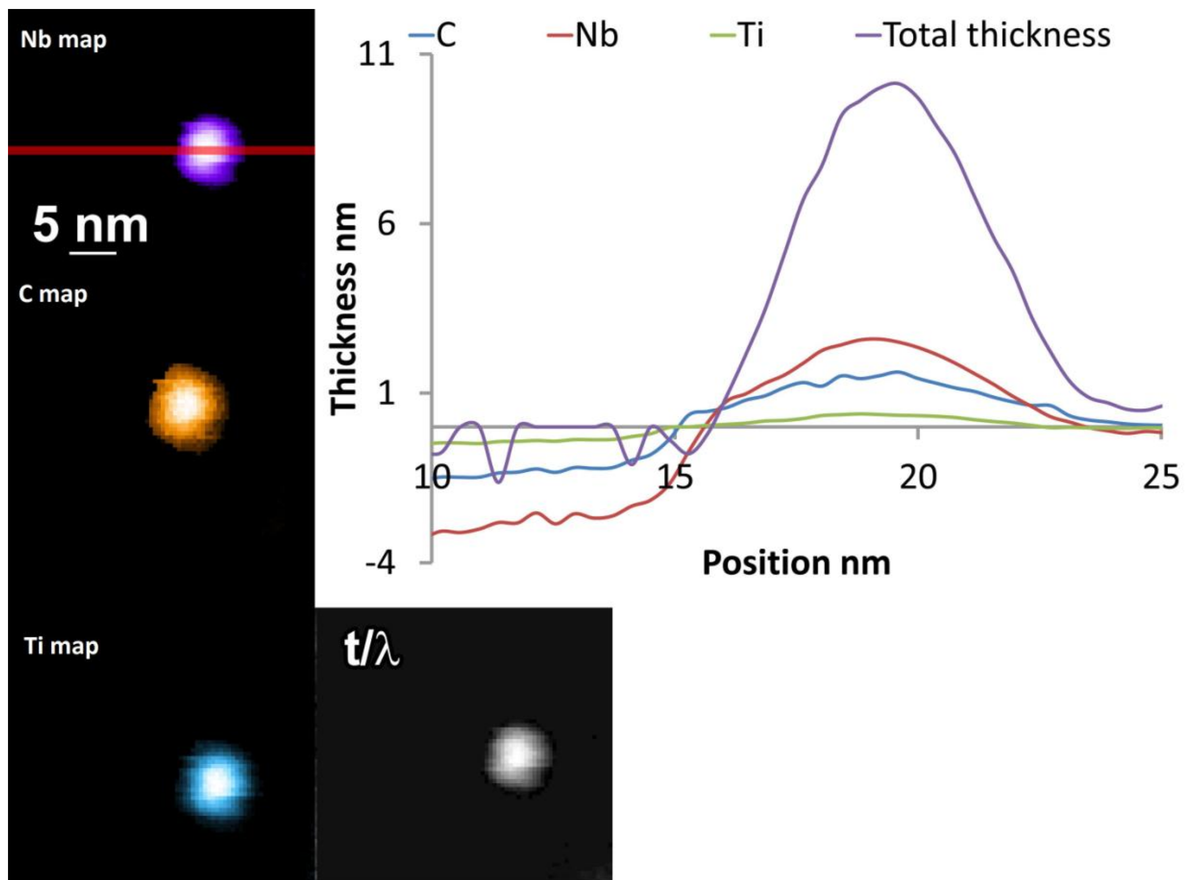

Figure 85. ***Elemental maps of the C, Nb and Ti distribution in nm, compared with relative thickness in a typical carbide in the Nb steel after heat treatment at 900°C for 100s, together with the chemical profiles taken across the red line at Nb map.***

Niobium precipitates showed similar tendencies to the vanadium carbides discussed above, as shown in **Figure 66, Figure 85**, **Figure 86** and **Figure 88**. Titanium is found in almost all particles and follows the Nb content consistently, and both correlate well with the carbon content. In the particles analysed to date, no nitrogen has been detected. In the **Figure 85** the elemental maps with the chemical profiles of Nb particle are shown. The steel was isothermally treated for 100s in 900°C. The Ti and Nb are easy to extract but the C shows always some additional signal from amorphous carbon, which is too complicated to remove with MLLS fit, due to the failure of fitting in front of the Nb edge, where the counts go negative, and the function is not AE^{-r}. The precipitate has approximately 8nm in *x* direction and probably around 10-11nm in z direction. The cross-sections for some reason failed in this time, showing highly underestimated thicknesses. But if trust the ratios between them, the Nb is again close to 0.85 and Ti to 0.15, with the C content close to 0.6. This gives the stoichiometry

As before, there is a reasonable match between the C-K edge shape and previously recorded spectra from a NbC standard, but only for the data recorded at the final stage of this studies, because only then there was sufficient enough background in front of the Nb-$M_{4,5}$ edge and before

the splice point, otherwise the background shape was unfittable. This is shown in the **Figure 86**, where orange colour represents the C shape extracted from NbC standard and violet is a shape of the C edge after subtraction of the NbN standard from specimen spectrum. The overall shape is consistent apart from the first feature, where the NbC standard is higher than the specimen spectrum shape. It may suggest that the stoichiometry of the specimen is different than standard. The spectrum was used to create maps presented in the **Figure 66**, for each of the map an integration 50eV wide window was used (windows are shown in the **Figure 64**).

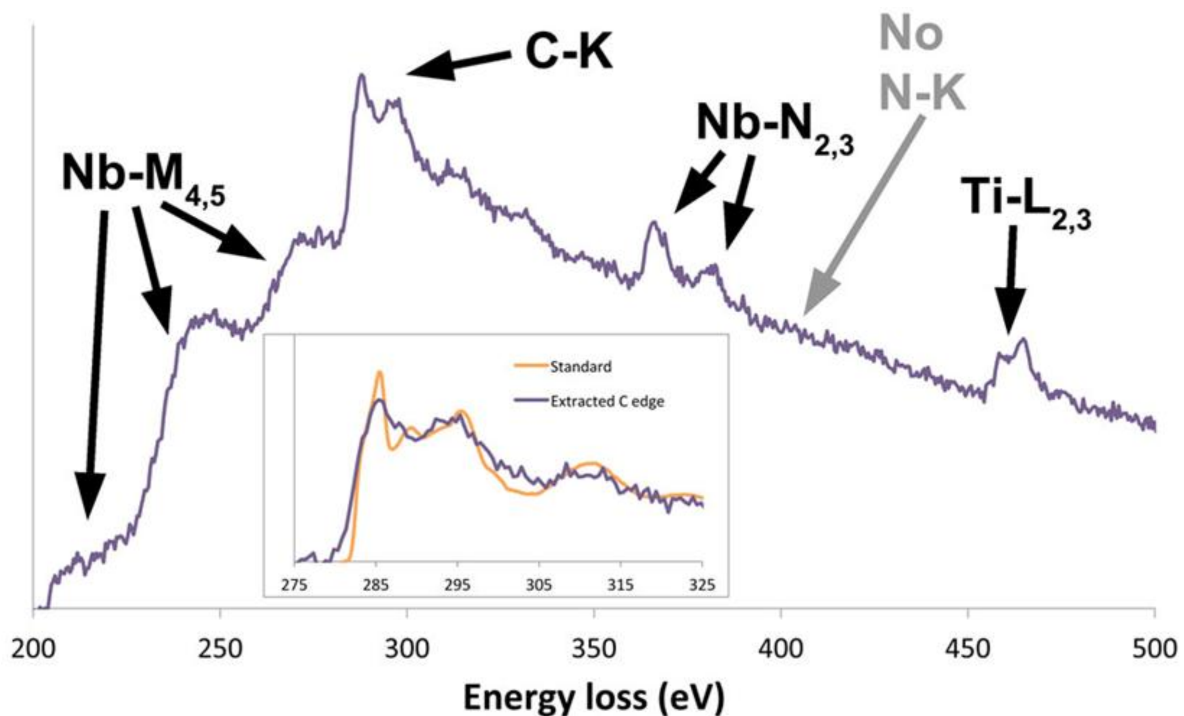

Figure 86. A background subtracted spectrum of the core loss EEL spectrum from the central region of Nb particle, compared with NbC standard. The spectrum is taken from the precipitate presented in the Figure 66.

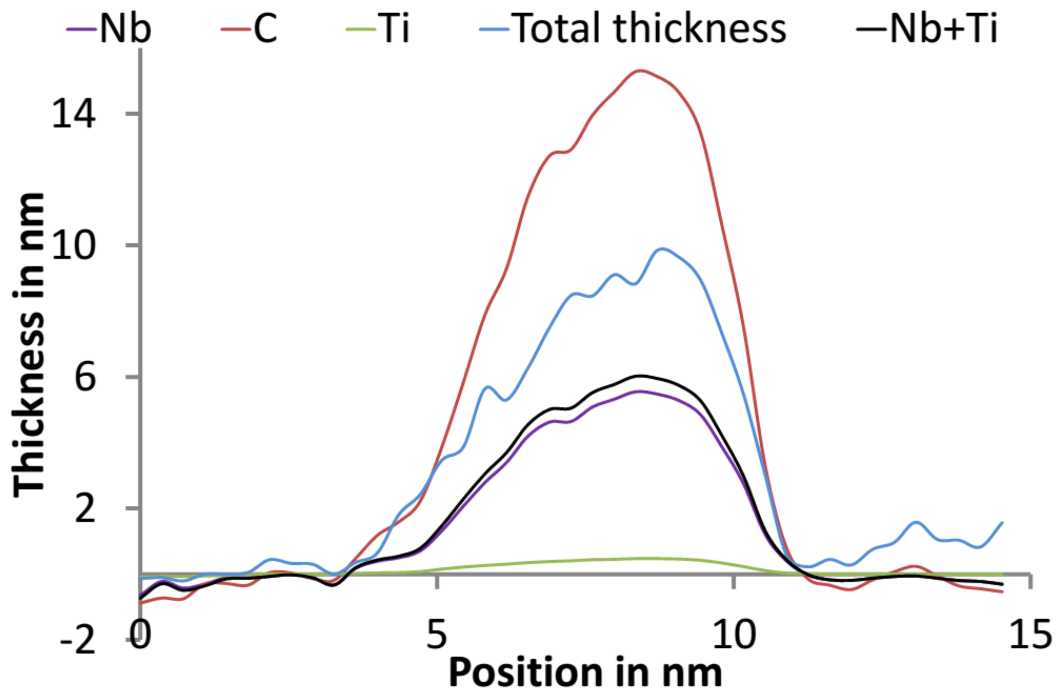

Figure 87. C, Nb and Ti chemical profiles in nm, compared with relative thickness in a typical carbide in the Nb steel after heat treatment at 900°C for 100s, the chemical profiles taken across the red line at Nb map in the Figure 66.

In **Figure 87** the chemical profiles of the fully quantified Nb precipitate (maps in **Figure 66)** are presented. Similarly to previous Nb particles, also there are some differences between relative thickness and total metal thickness. In **Figure 86** the background subtracted Nb precipitate spectrum from the same particle is presented. It can be said that the Nb edge is well-subtracted, which means that the background shape was following the power Law function quite well, allowing to form a clean map (free from artifacts in the area outside the precipitate). However in case of the Ti, there is a problem with the background subtraction, because it sits on the long edge of the strong Nb-$M_{4,5}$ edge. Therefore it might be a reason why the Ti thickness is usually so small in comparison to Nb, because it is over subtracted. The same problem is with the C-K edge, there is little space in front of this edge, because it sits directly behind three strongest fine Nb structures. The best method to extract the C-K signal is subtraction of the scaled NbN signal obtained from the standards. In the inset there is a extracted C signal from the precipitate and C signal from the NbC standard, and by direct comparison it can be seen that there is almost no other contribution than crystalline carbon shape. The edge shape fits very well from the first structures up to the extended features close to 320eV loss. Thus, such a well-subtracted signal was quantified with the cross-section value ending with a C thickness close to 25nm. Still, in comparison to relative thickness, or total metal thickness it is overestimated, but as very preliminary analysis, these errors are not so huge, and give hope for the future calculations. The calculated elemental composition in case of this precipitate is

$(Nb+Ti)_{0.3}C_{0.7}$. But it is a high probability, that this value is not true, because comparing the total thickness the C content is much lower.

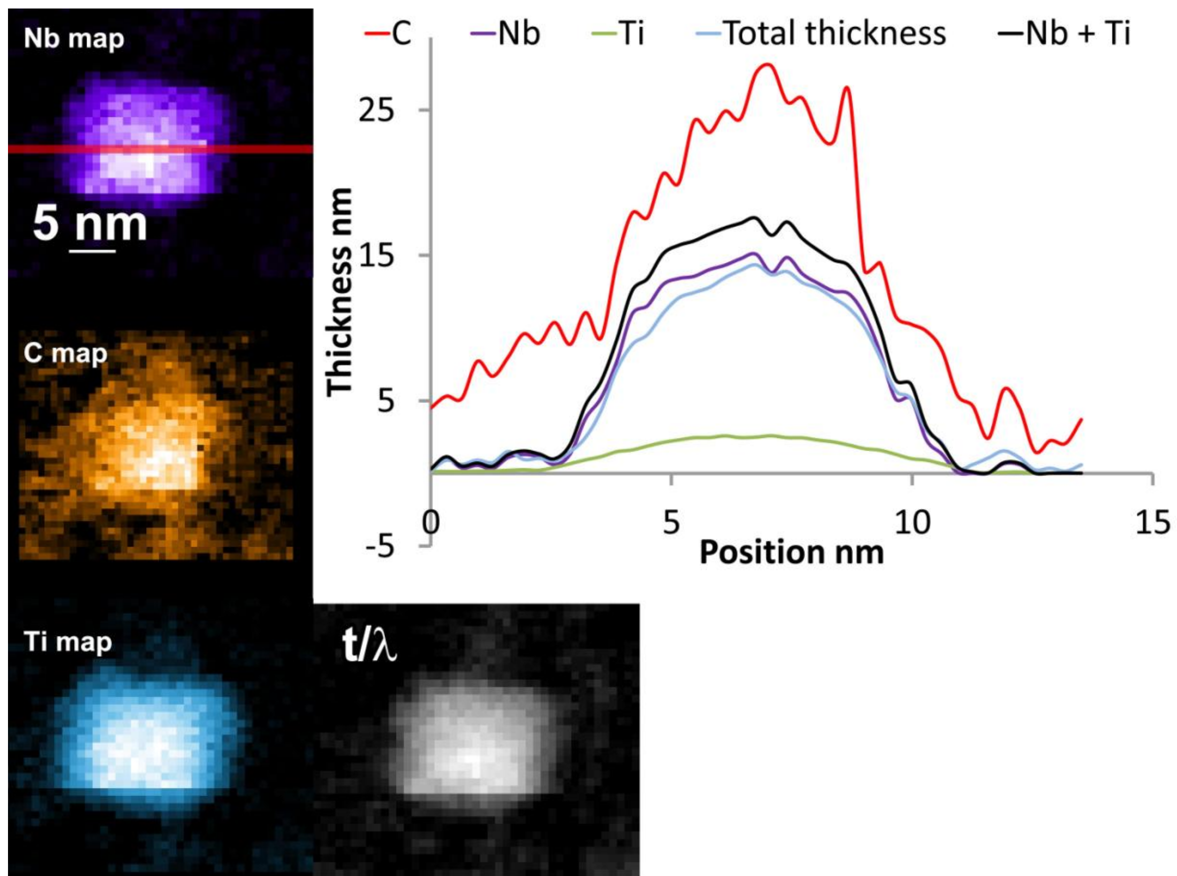

Figure 88. Elemental maps of the C, Nb and Ti distribution in nm, compared with relative thickness in a typical carbide in the Nb steel after heat treatment at 900°C for 100s, together with the chemical profiles taken across the red line at Nb map.

In **Figure 88** one of the Nb precipitates is presented. This acquisition suffered from errors arising from software reasons or some failure in magnetic shutter. Nevertheless it is possible to present the elemental thicknesses in maps supported with chemical profiles in horizontal direction and preliminary stoichiometries. The results are consistent with previous data, where the Nb precipitates contains the Ti element. Also this time, it was impossible to present any N map, so it is not sure if N was involved in precipitation. However of high importance is a extremely good agreement between relative thickness (calculated from corrected Iakoubovskii mean free path) and total metal thickness Nb+Ti (calculated from preliminary Nb cross-section). Notwithstanding is the problem with growing carbon during acquisition, which is visible in the C map, making it difficult to estimate any realistic C thickness or non-metal to metal ratio. But, with such good agreement it can be said that this precipitate is close to 16nm in thickness, and ~9nm in horizontal direction (see red line in **Figure 88**). Because of the obvious reasons the perpendicular direction is not possible to

estimate with enough accuracy to put this under discussion. Also the metal ratios show that there is 0.85 Nb and 0.15 Ti in this particular precipitate, but it is similar to the previous precipitates, which may suggest some likelihood of favourable stoichiometry, which is presented in the **Figure 89**, together with other precipitate's ratios. The carbon thickness is 27 nm, which is unfortunately, not a realistic C content, as the MLLS failed to separate the signal due to the too much contamination or failure background subtraction in front of the Nb edge. So the ratios are beyond 1, which makes any reasonable conclusions impossible. Similarly like in case of previous precipitate the stoichiometry is unrealistic, due to the too high C value, and it goes up to $(Nb+Ti)_{0.38}C_{0.62}$.

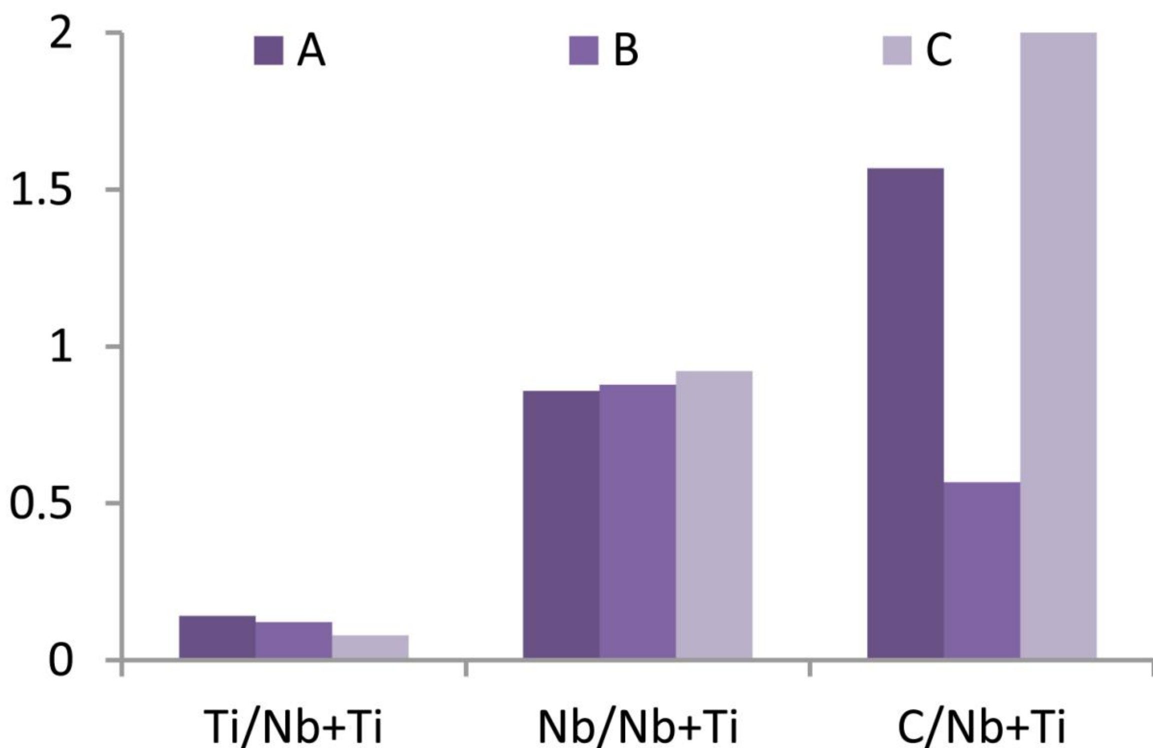

Figure 89. Juxtaposition of ratios and stoichiometries in three fully quantified Nb precipitates presented in this thesis.

Figure 89 shows a summary of all stoichiometries calculated from quantified Nb precipitates. In all cases the Nb:M or Ti:M ratios were similar. However there are small differences in Ti content starting from the precipitate A, which has the highest content of Ti (close to 0.15), by B, which is less and finishing at C precipitate which has Ti content close to 0.07 The limiting concentration of Ti seems to be replaced with Nb. Unfortunately no reasonable result can be extracted from the C presence. In case of these precipitates Ti seem like an impurity, because of little amount of it, also the lack of the core-shell structure, similarly like in case of the V precipitates.

8.3.Summary

The chemistry and microstructure of the precipitates is crucial in dispersion strengthening mechanism in the steels. The DualEELS technique has been proven to successfully analyse the data with the details down to few atoms. The proposed post-processing technique allowed to digitally extract seven datasets and fully quantified and presented in form of elemental maps and chemical profiles. Four of these are vanadium precipitates, and three are niobium. The vanadium precipitates were quantified using well-established cross-sections from standard specimens, but in case of the Nb, the cross-sections are somewhat overestimated, and the full quantification is not certain. In case of the V precipitates it was possible to quantify V, Ti, C and N. The Ti and N are directly extracted from the data, whereas the V and C are subjected to further cleaning - removal of unwanted signals such as contaminations, or oxidation products. This allows the estimation of the thickness with errors down to a few percent, which in case of nanoprecipitates is just a few atoms. In case of the Nb precipitates there is limited possibility to estimate the Nb signal due to the shape of the edge, and therefore the extraction of the C, which sits on the Nb edge was not possible in this work. The only way to get reasonable value of the C is extraction of the NbN signal from the standard, from the precipitate signal, however this process suffer more errors due to the mathematical scaling, which has to be done prior to quantification. In case of the niobium steel no N signal was detected, or separated at any point of data analysis of Nb-precipitates. Also, no aluminium was detected at any point of the analysis. All the errors in case of Nb-steel arise from problems with background fitting in front of the Nb edge. The process requires better acquisition conditions, such as controlled splice point, controlled linearisation, time ratios between low loss and core loss, which is done beyond this PhD. Despite this, some reasonably looking stoichiometries are obtained on Ti and Nb.

9. Conclusions and future work

The work presented in this thesis focused on analytical studies of nanosized Nb and V precipitates in high Mn steels containing 20% Mn and 1.5 % Al with an innovative technique called DualEELS spectrum imaging. The main points of this work were optimisation of the FIB sample preparation, the development of a post processing methodology for the raw data, measurement of the EELS differential cross-sections for each individual element in the precipitates, and initial steps towards robust absolute quantification of the precipitates using these cross sections. This chapter summarises these results and presents a short discussion of possible future work to be carried out beyond what was possible in this PhD. project together with other possibilities for uses of the techniques developed here.

The development of an optimised FIB procedure for steel sample preparation allowed the preparation of a steel specimen thin enough to be used for DualEELS from relatively small specimens, such as dilatometer samples cut in half. FIB technique is ideal for this since it is site specific and material can be extracted from any desired orientation to the strain axis in the specimen. Additionally, it has an advantage over the classic carbon extraction replica technique in that the spatial orientation of the precipitates is preserved, whereas this can be lost in replica extraction. Moreover, replica extraction can dissolve small precipitates or dissolve the outer layers of larger precipitates.

The FIB was also used for preparation of a needle-shaped specimen, which could also be used for tilt tomography experiments. The procedure was based on the preparation for APT needles [153]. This specimen was used for determination of the absolute mean free path for inelastic scattering in EELS for each of the carbide and nitride standards.

The principal novel contribution in this Ph.D. was a post-processing method for DualEELS datasets that allows the digital separation of the precipitate DualEELS signal from the matrix and other contributions. This method includes the correction of a variety of systematic effects, including problems with the spectrometer and the microscope, as well as making full use of PCA to separate the real signals from random noise contributions. The procedure has huge benefits for the quantitative analysis of the size and chemistry of the precipitates, which is much easier to perform both qualitatively and quantitatively on the extracted spectrum images. In the Nb microalloyed steel the precipitates were found to be almost pure carbides with little or no detectable N. A few percent of N could be detected and mapped in some precipitates in the V steel. Most carbides were also found to contain Ti arising from impurities in the feedstock (recycled steel) or the casting facility. In

the absence of significant N content in the steel, this Ti was evenly distributed through the precipitates and did not form any core-shell structures. In all precipitates there was found no more elements, such as Al, Fe, or Mn, which is confirmation of results obtained from modelling.

Using high quality spectrum images recording from standards VC, VN, TiC and TiN, all of well-known stoichiometry, it was possible to calculate the absolute partial cross-sections for all elements present in the precipitates in the vanadium microalloyed steel, which are: C, N, Ti and V. Because of the lack of a high quality NbC standard it was impossible to do the same thing for Nb- steel, although some standard spectra were acquired for NbN, and some preliminary data were taken for a NbC powder of unknown stoichiometry. The calculated cross-sections for V, Ti, C and N were compared with the values given in Digital Micrograph, which were calculated using the Hartree-Slater model and the results show that the values used so far might be underestimated, making the standardless quantification in Digital Micrograph wrong by a factor of at least 10%. One part of calculating the absolute cross sections is to be able to determine the absolute thickness from the low loss EELS. This was done by correcting the mean free path equation of Iakoubovskii [234, 237] using data from a needle specimen from the TiC standard.

The combination of the precipitate digital extraction with an absolute quantification of atomic areal density in each pixel of the spectrum image using the measured cross sections then allows the calculation of the precipitate thickness in terms of individual elemental contributions. For example, the addition of the quantified thickness for all metal cations in the rock-salt-structured carbide allow the calculation of a total thickness, and this can be compared with the total thickness calculated from the t/λ method [224]. It would also be possible to calculate the total equivalent thickness for the carbon and nitrogen anions, although this may fall short of the total thickness, since such carbides are often known to be substoichiometric [242].

It was possible to absolutely quantify the vanadium particle and confirm the predicted shape of truncated octahedron with use of the mean free path and calculated cross-sections. The absolute quantification of spectrum image of precipitate only in 3D with use of DualEELS is a novelty, and such level of precision (with errors down to a few atoms) is a unique in common research fields. The precipitate in **Figure 63** has dimensions 10x10x8nm, that of **Figure 80** has 16x14x8nm, and precipitate in **Figure 82** has dimensions 11x12nm, which are very good agreements. The precipitate in **Figure 83** has a dimensions 11nmx5nm, which suggest some errors in thickness estimations. Most of these stoichiometries are between $V_{0.7\text{-}0.85}Ti_{0.3\text{-}0.15}$. The total non-metal to metal ratio is close to 0.6 in most cases.

It was possible to use a preliminary partial cross-sections and quantify a few Nb particles, showing that the metal stoichiometry is in range $Nb_{0.85\text{-}0.9}Ti_{0.15\text{-}0.1}$. However there were limitations

regarding estimation of accurate carbon content measurements of these. The total thickness of particles can be presented in nanometers and for **Figure 85** the dimensions are 6x4nm, for **Figure 87** the dimensions are 8x12nm, and for **Figure 88** the dimensions are 9x15nm approximately. The total non-metal to metal ratio is close to 0.6 in most cases, but these calculations are might be wrong due to errors in partial cross-section values.

This results were important for the European project, because it confirmed thermodynamical calculations, that the precipitates will precipitate at certain temperatures, and that they will increase the Yield strength. So far experiments were done based on extraction replicas, so the results obtained from this thesis were of a significant meaning for understanding and accuracy of modelling of such precipitates.

9.1.Future plans, works, research

Improvements to the methodology

Of course, there is possible a further improvement of the quality of the signal extraction. The "bleed-through" of background signal into the low loss spectrum in the acquisition of the DualEELS datasets needs to be minimised. Since this work was carried out, a redesign of an assembly in the spectrometer detector chamber by Gatan has now significantly reduced this bleed-through. As long as care is taken in spectrometer setup (specifically to ensure that the bright, low-loss region of the core-loss spectrum is fully absorbed in the beam trap), then it should be possible to acquire DualEELS datasets with minimal bleed-through. Additionally, minimising the ratio of acquisition times between the core loss and low loss spectra reduces the stray scattering, although this needs to be balanced against having enough signal in the core loss to be visible above the noise. Thus, also reducing readout noise in a future spectrometer design would improve this.

Any non-linearity of the energy axis in the dataset causes problems with energy calibration and thus will affect the scaling factor at the splice point and the number of counts in the channel relative to those in a channel of fixed width. These issues need to be addressed to obtain accurate quantification of the data. The alignment procedures for the GIF Quantum spectrometer have already been revised since the acquisition of the data presented here, and a realignment of the Glasgow spectrometer has already resulted in much reduced non-linearity across the spectrum. Nevertheless, when working with very large energy ranges (e.g. at dispersions of 0.5 or 1 eV per channel), some non-linearity is inevitable. Thus, it will be desirable to develop a method for the measurement of the non-linearity and the subsequent re-binning and linearisation of the spectra as part of the data processing procedure. This non-linearity in the dispersion may go some way to explaining an unresolved observation i.e. that the average scaling factor between the core loss and the low loss used for the splicing process differs significantly from the ratio of the integration times

for the two regions. Further investigation of this is required before a full quantification of the data can be achieved.

Although procedures were included here to remove the effects of surface oxidation and carbon contamination, it would be better if there were no need to perform such corrections. Thus, improved sample preparation and handling to minimise surface damage, surface oxidation and contamination by volatile organics would help to ensure the best quality datasets and, consequently, the best quality extraction of the precipitate or inclusion signal from the matrix or support. This suggests that the use of optimised procedures for the use of low energy focussed ion beam milling [156] or the use of post-FIB low energy argon ion milling may be essential for achieving optimal sample quality to minimise sample damage and surface oxidation. Rigorous procedures for the minimisation of contamination such as sample storage protocols, plasma cleaning of the sample holder and sample, and vacuum baking of samples prior to microscopy, as well as the use of the "beam shower" (which is bombarding the surface of the specimen with a broad, high current electron beam) in the microscope when necessary are essential for this kind of work. Finally, the acquisition of standard spectra from particles, precipitates or inclusions free of matrix contributions may provide useful standards for MLLS fitting when separating the particle spectrum image from other contributions to the total deconvolved SI and its subsequent quantification.

It would be ideal to improve the quantification methodology beyond that presented in this thesis, whereby quantification is performed by simple background subtraction and integration. A more noise-tolerant approach is to fit the whole spectrum against the experimental cross sections using Multiple Linear Least Squares (MLLS) fitting. This has been implemented in a successor PhD project to this, and a paper on this is in preparation. It would also be desirable to implement the same routines for niobium-containing precipitates. It is noted that a high-quality niobium carbide standard was acquired after the completion of this work, and work is in progress by another Ph.D. student on doing just this.

Applications to other materials

In addition to the specific steel studied here, this method for absolute quantification of nanoscaled features, supported by optimised sample preparation process, would be widely applicable to other steels containing nanoscale precipitates, including HSLA steels, reactor pressure vessel steels (some work was performed on this in collaboration with the University of Oxford, but is reported elsewhere [248], and oxide dispersion strengthened steels. It will work well in any case where the sample consists of a matrix or other dominating feature which contains a reasonable proportion of an element that is not present in the second phase. This would also apply in many

cases of heavy metal heterogeneous catalysts on supports, nanocomposites, and helium bubbles in irradiated materials. Thus, it is expected that this method will be of widespread applicability in many nanostructured, chemically inhomogeneous systems. However, it would be more difficult to apply where the same element is present in both the matrix and the precipitate or second phase, as is the case in many aluminium alloys.

10. Bibliography

1. A. T. Vandermonde, C.L Berthollet, and G. Monge, *Mémoire sur le fer considéré dans ses différens états métalliques.* French Academy of Science, May 1786.
2. Sir H. Bessemer, *The manufacture of iron (steel) without fuel.* Cheltenham Meeting of the British Association [of iron makers], August 13, 1856.
3. Sir H. Bessemer, *On the manufacture and uses of steel with special reference to its employment for edge tools.* Paper read at Cutlers' Company of London, December 1, 1880.
4. S.G. Thomas and P.C. Gilchrist, *On the elimination of phosphorus.* Journal of the Iron and Steel Institute, 1879. **1**: p. 120-134.
5. J. Guertin, J. A. Jacobs, and C. P. Avakian, *Chromium(VI) Handbook*, ed. I.E.T.E. Group. December 28, 2004: CRC Press
6. Y. Ivanisenko, I. MacLaren, X. Sauvage, R. Z.Valiev, and H. J Fecht, *Shear-induced alpha ->gamma transformation in nanoscale Fe-C composite.* Acta Materialia, 2006. **54**(6): p. 1659-1669.
7. Y. Ivanisenko, I. MacLaren, R. Z. Valiev, and H. J. Fecht, *A new deformation mechanism in nanoscale Fe-C composite as a result of a stress-induced alpha ->gamma transformation*, in *Nanomaterials by Severe Plastic Deformation*, Z. Horita, Editor. 2006. p. 439-445.
8. Y. Ivanisenko, I. MacLaren, R. Z. Valiev, and H. J. Fecht, *The first observation of a shear-induced bcc -> fcc transformation in nanocrystalline ferrite.* Advanced Engineering Materials, 2005. **7**(11): p. 1011-1014.
9. Pavlina, E.J. and C.J. Van Tyne, *Correlation of Yield Strength and Tensile Strength with Hardness for Steels.* Journal of Materials Engineering and Performance, 2008. **17**(6): p. 888-893.
10. I. Tsukatani, S. Hashimoto, and T. Inoue, *Effects of Silicon and Manganese Addition on Mechanical Properties of High-strength Hot-rolled Sheet Steel Containing Retained Austenite.* ISIJ International, 1991. **31**(9): p. 992-1000.
11. Jitendra Patel, Christian Klinkenberg, and Klaus Hulka *Hot rolled HSLA strip steels for automotive and construction applications* January 2003.
12. J. N. Cordea and R. E. Hook, *Recrystallization behavior in deformed austenite of high strength low alloy (HSLA) steels.* Journal of Metals, 1969. **21**(3): p. A126
13. J. A. Vaccari, *HSLA steels get stronger find more uses.* Materials Engineering, 1969. **69**(4): p. 42.
14. J. A. Vaccari, *New HSLA, stainless and carbon steels improve family properties.* Materials Engineering, 1969. **70**(7): p. 26.
15. R. L. Hickey and E. V. Bravenec, *An HSLA steel for heavy sections.* Metal Progress, 1969. **96**(2): p. 75.
16. J. A. Vaccari, *New generation HSLA steels are stronger and more formable.* Materials Engineering, 1974. **79**(2): p. 24-28.
17. H. L. Gao, Y. H. Dong, and R. W. Hendricks, *Microstructure transformation and brittlement of a ultra-low carbon QT steel during double welding thermal cycle.* Acta Metallurgica Sinica, 2001. **37**(1): p. 34-38.
18. M. F. Stevens and I. M. Bernstein, *Microstructural effects on hydrogen embrittlement of a ti-containing HSLA steel.* Journal of Metals, 1983. **35**(8): p. A47-A47.
19. M. F. Stevens and I. M. Bernstein, *The role of aging reactions in the hydrogen embrittlement susceptibility of an HSLA steel.* Metallurgical Transactions a-Physical Metallurgy and Materials Science, 1985. **16**(10): p. 1879-1886.

20. Federation, E.U.R. *European Road Statistics 2010*. European Union Road Federation [www.erf.be] 2010; Available from: www.erf.be.
21. O. Bouaziz, S. Allain, C. P. Scott, P. Cugy, and D. Barbier, *High manganese austenitic twinning induced plasticity steels: A review of the microstructure properties relationships.* Current Opinion in Solid State and Materials Science, 2011. **15**(4): p. 141-168.
22. G. R. Ebrahimi, H. Arabshahi, and M. Javdani, *Hot deformation behavior of Nb-V microalloyed steel.* Journal of Materials Engineering Research, 2010. **2**(5): p. 92-96.
23. H. K. D. H. Bhadeshia and Sir R. Honeycombe, *4 - The Effects of Alloying Elements on Iron-Carbon Alloys*, in *Steels (Third Edition)*. 2006, Butterworth-Heinemann: Oxford. p. 71-93.
24. Zhi-ping Xiong, Xue-ping Ren, Wei-ping Bao, Shu-xia Li, and Hai-tao Qu, *Dynamic mechanical properties of the Fe–30Mn–3Si–4Al TWIP steel after different heat treatments.* Materials Science and Engineering: A, 2011. **530**: p. 426-431.
25. H. K. D. H. Bhadeshia and Sir R. Honeycombe, *2 - The Strengthening of Iron and its Alloys*, in *Steels (Third Edition)*. 2006, Butterworth-Heinemann: Oxford. p. 17-38.
26. D. R. Gaskell, *CHAPTER 5 - METALLURGICAL THERMODYNAMICS A2 - CAHN, Robert W*, in *Physical Metallurgy (Fourth, Revised and Enhanced Edition)*, P. Haasen†, Editor. 1996, North-Holland: Oxford. p. 413-469.
27. H. Gleiter, *CHAPTER 9 - MICROSTRUCTURE A2 - CAHN, Robert W*, in *Physical Metallurgy (Fourth, Revised and Enhanced Edition)*, P. Haasen†, Editor. 1996, North-Holland: Oxford. p. 843-942.
28. G. Krauss, *Steels : processing, structure, and performance*. 2005, Materials Park, Ohio: ASM International.
29. T. B. Massalski, *CHAPTER 3 - STRUCTURE AND STABILITY OF ALLOYS* A2 - CAHN, Robert W*, in *Physical Metallurgy (Fourth, Revised and Enhanced Edition)*, P. Haasen†, Editor. 1996, North-Holland: Oxford. p. 135-204.
30. J. L. Bocquet, G. Brebec, and Y. Limoge, *CHAPTER 7 - DIFFUSION IN METALS AND ALLOYS A2 - CAHN, Robert W*, in *Physical Metallurgy (Fourth, Revised and Enhanced Edition)*, P. Haasen†, Editor. 1996, North-Holland: Oxford. p. 535-668.
31. J. P. Hirth, *CHAPTER 20 - DISLOCATIONS A2 - CAHN, Robert W*, in *Physical Metallurgy (Fourth, Revised and Enhanced Edition)*, P. Haasen†, Editor. 1996, North-Holland: Oxford. p. 1831-1875.
32. O. Dmitrieva, D. Ponge, G. Inden, J. Millán, P. Choi, J. Sietsma, and D. Raabe, *Chemical gradients across phase boundaries between martensite and austenite in steel studied by atom probe tomography and simulation.* Acta Materialia, 2011. **59**(1): p. 364-374.
33. W. Hume-Rothery and B. R. Coles, *Atomic theory for students of metallurgy*. 1988, London.
34. J. P. Bailon and J. M. Dorlot, *Thermal treatment effects on Hall-Petch relation for armco iron.* Acta Metallurgica, 1971. **19**(2): p. 71.
35. O. Dmitrieva, P. Choi, S. S. Gerstl, D. Ponge, and D. Raabe, *Pulsed-laser atom probe studies of a precipitation hardened maraging TRIP steel.* Ultramicroscopy, 2011. **111**(6): p. 623-7.
36. Y. N. Dastur and W. C Leslie, *Mechanism of Work Hardening in Hadfield Manganese Steel.* Metallurgical Transactions A, 1981. **12A**: p. 749-759.
37. P. H. Adler, G. B. Olson, and W. S. Owen, *Strain Hardening of Hadfield Manganese Steel.* Metallurgical and Materials Transactions A. **17**(10): p. 1725-1737.
38. H. M. Otte, *The formation of stacking faults in austenite and its relation to martensite.* Acta Metallurgica, 1957. **5**(11): p. 614-627.
39. J. S. T. Vanaswegen, D. H. Warrington, and Sir R. Honeycombe, *Precipitation on stacking faults in Cr-Ni austenitic steels.* Acta Metallurgica, 1964. **12**(1): p. 1.
40. L. Rémy, *Maclage et transformation martensitique CFC-HC induite par déformation plastique dans les alliages austénitiques à basse énergie de défaut d'empilement des systèmes Co-Ni-Cr-Mo et Fe-Mn-Cr-C*, in *Paris* 1977, Université Paris-Sud: Université Paris-Sud.

41. T. W. Kim, J. K. Han, R. W. Chang, and Y. G. Kim, *Austenitic high manganese steel having superior formability, strength and weldability, and manufacturing process therefor*. 1993, Google Patents.
42. A. S. Argon, *CHAPTER 21 - MECHANICAL PROPERTIES OF SINGLE-PHASE CRYSTALLINE MEDIA: DEFORMATION AT LOW TEMPERATURES A2 - CAHN, Robert W*, in *Physical Metallurgy (Fourth, Revised and Enhanced Edition)*, P. Haasen†, Editor. 1996, North-Holland: Oxford. p. 1877-1955.
43. A. S. Argon, *CHAPTER 22 - MECHANICAL PROPERTIES OF SINGLE-PHASE CRYSTALLINE MEDIA: DEFORMATION IN THE PRESENCE OF DIFFUSION A2 - CAHN, Robert W*, in *Physical Metallurgy (Fourth, Revised and Enhanced Edition)*, P. Haasen†, Editor. 1996, North-Holland: Oxford. p. 1957-2007.
44. H. W. Pollack, *Materials Science and Metallurgy (4th Edition).* 1988: p. 554.
45. T. Gebhardt, D. Music, M. Ekholm, I. A. Abrikosov, J. von Appen, R. Dronskowski, D. Wagner, J. Mayer, and J. M. Schneider, *Influence of chemical composition and magnetic effects on the elastic properties of fcc Fe–Mn alloys.* Acta Materialia, 2011. **59**(4): p. 1493-1501.
46. D. Barbier, N. Gey, S. Allain, N. Bozzolo, and M. Humbert, *Analysis of the tensile behavior of a TWIP steel based on the texture and microstructure evolutions.* Materials Science and Engineering: A, 2009. **500**(1-2): p. 196-206.
47. E. Jimenez-Melero, N. H. van Dijk, L. Zhao, J. Sietsma, S. E. Offerman, J. P. Wright, and S. van der Zwaag, *Characterization of individual retained austenite grains and their stability in low-alloyed TRIP steels.* Acta Materialia, 2007. **55**(20): p. 6713-6723.
48. B. Dutta and E. J. Palmiere, *Effect of prestrain and deformation temperature on the recrystallization behavior of steels microalloyed with niobium.* Metallurgical and Materials Transactions a-Physical Metallurgy and Materials Science, 2003. **34A**(6): p. 1237-1247.
49. A. S. Hamada, L. P. Karjalainen, and M. C. Somani, *The influence of aluminum on hot deformation behavior and tensile properties of high-Mn TWIP steels.* Materials Science and Engineering: A, 2007. **467**(1-2): p. 114-124.
50. M. Gomez and S. F. Medina, *Role of microalloying elements in the microstructure of hot rolled steels.* International Journal of Materials Research, 2011. **102**(10): p. 1197-1207.
51. S. Allain, O. Bouaziz, and J. P. Chateau, *Thermally activated dislocation dynamics in austenitic FeMnC steels at low homologous temperature.* Scripta Materialia, 2010. **62**(7): p. 500-503.
52. S. Allain, O. Bouaziz, T. Lebedkina, and M. Lebyodkin, *Relationship between relaxation mechanisms and strain aging in an austenitic FeMnC steel.* Scripta Materialia, 2011. **64**(8): p. 741-744.
53. S. Allain, J. P. Chateau, O. Bouaziz, S. Migot, and N. Guelton, *Correlations between the calculated stacking fault energy and the plasticity mechanisms in Fe–Mn–C alloys.* Materials Science and Engineering: A, 2004. **387-389**: p. 158-162.
54. S. Allain, J. P. Chateau, D. Dahmoun, and O. Bouaziz, *Modeling of mechanical twinning in a high manganese content austenitic steel.* Materials Science and Engineering: A, 2004. **387-389**: p. 272-276.
55. O. Grassel, L. Kruger, G. Frommeyer, and L.W. Meyer, *High Strength Fe-Mn-(Al, Si) TRIP/TWIP steels developement - properties - application.* International Journal of Plasticity, 2000. **16**: p. 1391-1409.
56. H. K. D. H. Bhadeshia and Sir R. Honeycombe, *10 - Thermomechanical Treatment of Steels*, in *Steels (Third Edition)*. 2006, Butterworth-Heinemann: Oxford. p. 209-234.
57. X. Liang, J. R. McDermid, O. Bouaziz, X. Wang, J. D. Embury, and H.S. Zurob, *Microstructural evolution and strain hardening of Fe–24Mn and Fe–30Mn alloys during tensile deformation.* Acta Materialia, 2009. **57**(13): p. 3978-3988.
58. O. Bouaziz, C. P. Scott, and G. Petitgand, *Nanostructured steel with high work-hardening by the exploitation of the thermal stability of mechanically induced twins.* Scripta Materialia, 2009. **60**(8): p. 714-716.

59. A. Dumay, J. P. Chateau, S. Allain, S. Migot, and O. Bouaziz, *Influence of addition elements on the stacking-fault energy and mechanical properties of an austenitic Fe–Mn–C steel.* Materials Science and Engineering: A, 2008. **483-484**: p. 184-187.
60. H. K. D. H. Bhadeshia and R. W. K. Honeycombe, *Steels Microstructure and Properties Third edition*. 2006.
61. A. Kneissl, *Precipitates in HSLA steels.* Zeitschrift Fur Metallkunde, 1990. **81**(9): p. 646-653.
62. H. J. Eckstein and A. Franke, *Niobium microalloying of HSLA-steel.* Neue Hutte, 1990. **35**(8): p. 281-285.
63. M. Militzer, W. J. Poole, and W. P. Sun, *Precipitation hardening of HSLA steels.* Steel Research, 1998. **69**(7): p. 279-285.
64. W. S. Williams, *Physics of transition-metal carbides.* Materials Science and Engineering a-Structural Materials Properties Microstructure and Processing, 1988. **105**: p. 1-10.
65. P. Duwez and F. Odell, *Phase relationships in the binary systems of nitrides and carbides of zirconium, columbium, titanium, and vanadium.* Journal of the Electrochemical Society, 1950. **97**(10): p. 299-304.
66. J. Billingham, P. S. Bell, and M. H. Lewis, *A superlattice with monoclinic symmetry based on the compound V6C5.* Philosophical Magazine, 1972. **25**(3): p. 661-671.
67. Billingham, J., P.S. Bell, and M.H. Lewis, *Vacancy short-range order in substoichiometric transition metal carbides and nitrides with the NaCl structure. I. Electron diffraction studies of short-range ordered compounds.* Acta Crystallographica Section A, 1972. **28**(6): p. 602-606.
68. E.K. Storms and R. J. McNeal, *Vanadium-vanadium carbide system.* Journal of Physical Chemistry, 1962. **66**(8): p. 1401
69. W. Dawihl and Rix. Rix, *On the lattice parameters of carbides and nitrides of titanium and vanadium.* Zeitschrift Fur Anorganische Und Allgemeine Chemie, 1940. **244**(2): p. 191-197.
70. K. Farrell and E.H. Lee, *Characterization of precipitates in a Fe-10Cr-6Mo-0.5Nb ferritic steel.* Scripta Metallurgica, 1983. **17**: p. 791-796.
71. H.K.D.H. Bhadeshia, S. Kundu, and H. Abreu, *Microstructure and Texture in Steels, Chapter 2. Mathematics of Crystallographic Texture in Martensitic and Related Transformations.* 2009.
72. D. G. Pettifor, *CHAPTER 2 - ELECTRON THEORY OF METALS A2 - CAHN, Robert W*, in *Physical Metallurgy (Fourth, Revised and Enhanced Edition)*, P. Haasen†, Editor. 1996, North-Holland: Oxford. p. 47-133.
73. H. J. Kestenbach and J. Gallego, *On dispersion hardening of microalloyed hot strip steels by carbonitride precipitation in austenite.* Scripta Materialia, 2000(44): p. 791–796.
74. A. Deschamps, F. Danoix, F. De Geuser, T. Epicier, H. Leitner, and M. Perez, *Low temperature precipitation kinetics of niobium nitride platelets in Fe.* Materials Letters, 2011. **65**(14): p. 2265-2268.
75. J. Akre, F. Danoix, H. Leitner, and P. Auger, *The morphology of secondary-hardening carbides in a martensitic steel at the peak hardness by 3DFIM.* Ultramicroscopy, 2009. **109**(5): p. 518-523.
76. H. Leitner, K. Stiller, H. O. Andren, and F. Danoix, *Conventional and tomographic atom probe investigations of secondary-hardening carbides.* Surface and Interface Analysis, 2004. **36**(5-6): p. 540-545.
77. F. Danoix, R. Danoix, J. Akre, A. Grellier, and D. Delagnes, *Atom probe tomography investigation of assisted precipitation of secondary hardening carbides in a medium carbon martensitic steels.* Journal of Microscopy, 2011. **244**(3): p. 305-310.
78. F. Danoix, E. Bémont, P. Maugis, and D. Blavette, *Atom Probe Tomography I. Early Stages of Precipitation of NbC and NbN in Ferritic Steels.* Advanced Engineering Materials, 2006. **8**(12): p. 1202-1205.
79. J. A. Wilson, A. J. Craven, Y. Li, and T. N. Baker, *Dispersion strengthening in vanadium microalloyed steels processed by simulated thin slab casting and direct charging Part 2 –*

Chemical characterisation of dispersion strengthening precipitates. Materials Science and Technology, 2007. **23**(5): p. 519-527.

80. D. V. Wilson, *Effects of plastic deformation on carbide precipitation in steel.* Acta Metallurgica, 1957. **5**(6): p. 293-302.
81. W. C. Leslie, R. M. Fisher, and N. Sen, *Morphology and crystal structure of carbides precipitated from solid solution in alpha iron.* Acta Metallurgica, 1959. **7**(9): p. 632-644.
82. S. K. Ray, S. Mishra, and O. N. Mohanty, *TEM study of carbide precipitation in a phosphorus-bearing low-carbon steel.* Scripta Metallurgica, 1982. **16**(1): p. 43-47.
83. Y. C. Hirsch and B. A. Parker, *Fine carbonitride precipitates in high strength low alloy steels.* Micron (1969), 1980. **11**(3–4): p. 317-319.
84. J. D. L'Ecuyer, G. L'Espérance, M. G. Akben, and B. Bacroix, *Precipitation behavior of a HSLA steel containing molybdenum, aluminum and trace amounts of titanium.* Acta Metallurgica, 1987. **35**(5): p. 1149-1158.
85. A. Güth, L. Kaun, A. Köthe, D. Müller, and J. Richter, *Investigation of the influence of the reheating temperature on size and composition of precipitates in microalloyed HSLA steels by analytical electron microscopy.* Scripta Metallurgica, 1987. **21**(2): p. 163-168.
86. H. S. Ubhi and T. N. Baker, *The influence of manganese and silicon on the precipitation of vanadium carbide in steel.* Materials Science and Engineering: A, 1989. **111**: p. 189-199.
87. Hillier, J. and R.F. Baker, *Microanalysis by Means of Electrons.* Journal of Applied Physics, 1944. **15**(9): p. 663-675.
88. Jeanguillaume, C., *Spectrum-image: the next step in EELS digital acquisition and processing.* Ultramicroscopy, 1989. **28**: p. 252-257.
89. A. Bourret and C. Colliex, *Combined HREM and STEM microanalysis on decorated dislocation cores.* Ultramicroscopy, 1982. **9**(3): p. 183-189.
90. C. Colliex and P. Trebbia, *Performance and applications of electron energy loss spectroscopy in stem.* Ultramicroscopy, 1982. **9**(3): p. 259-266.
91. C. Colliex, V. E. Cosslett, R. D. Leapman, and P. Trebbia, *Contribution of electron energy loss spectroscopy to the development of analytical electron microscopy.* Ultramicroscopy, 1976. **1**(3–4): p. 301-315.
92. A. L. Bleloch, A. Howie, R. H. Milne, and M. G. Walls, *Elastic and inelastic scattering effects in reflection electron microscopy.* Ultramicroscopy, 1989. **29**(1–4): p. 175-182.
93. A. L. Bleloch, A. Howie, and R. H. Milne, *High resolution secondary electron imaging and spectroscopy.* Ultramicroscopy, 1989. **31**(1): p. 99-110.
94. R. F. Egerton, *Quantitative analysis of electron-energy-loss spectra.* Ultramicroscopy, 1989. **28**(1): p. 215-225.
95. R. F. Egerton, P. A. Crozier, and P. Rice, *Electron energy-loss spectroscopy and chemical change.* Ultramicroscopy, 1987. **23**(3): p. 305-312.
96. C. J. Rossouw, R. F. Egerton, and M. J. Whelan, *Applications of energy analysis in a transmission electron microscope.* Vacuum, 1976. **26**(10–11): p. 427-432.
97. A. J. Craven and T. W. Buggy, *Design considerations and performance of an analytical stem.* Ultramicroscopy, 1981. **7**(1): p. 27-37.
98. L. A. J. Garvie, A. J. Craven, and R. Brydson, *Use of electron-energy loss near-edge fine structure in the study of minerals.* American Mineralogist, 1994. **79**(5-6): p. 411-425.
99. A. J. Craven and M. M. Cluckie, *Analysis of small vanadium carbide precipitates using electron energy loss spectroscopy* Ultramicroscopy, 1988. **28**: p. 330-334.
100. F. Hofer, P. Warbichler, H. Kronberger, and J. Zweck, *Mapping the chemistry in nanostructured materials by energy-filtering transmission electron microscopy (EFTEM).* Spectrochimica Acta Part A, 2001. **57**: p. 2061-2069.
101. F. Hofer, P. Warbichler, and W. Grogger, *Imaging of nanometer-sized precipitates in solids by electron spectroscopic imaging.* Ultramicroscopy, 1995. **59**(1): p. 15-31.

102. C. Allison, W. S. Williams, and M. P. Hoffman, *Quantitative electron energy loss spectroscopy of vanadium carbide.* Ultramicroscopy, 1984. **13**(3): p. 253-263.
103. J. H. Scofield, *Hartree-Slater subshell photoionization cross-sections at 1254 and 1487 eV.* Journal of Electron Spectroscopy and Related Phenomena, 1976. **8**(2): p. 129-137.
104. L. E. Thomas, *Light-element analysis with electrons and x-rays in a high-resolution STEM.* Ultramicroscopy, 1985. **18**(1): p. 173-184.
105. F. Hofer and P. Golob, *Quantification of electron energy-loss spectra with k and l shell ionization cross-sections.* Micron and Microscopica Acta, 1988. **19**(2): p. 73-86.
106. F. Hofer, P. Golob, and A. Brunegger, *EELS quantification of the elements Sr to W by means of M45 edges.* Ultramicroscopy, 1988. **25**(1): p. 81-84.
107. F. Hofer, *EELS quantification of M edges by using oxidic standards.* Ultramicroscopy, 1987. **21**(1): p. 63-68.
108. R. F. Egerton, *Oscillator-strength parameterization of inner-shell cross sections.* Ultramicroscopy, 1993. **50**(1): p. 13-28.
109. S. P. Duckworth, Z. X. Guo, and T. N. Baker, *Microanalysis A microanalytical study of the apparent iron content of vanadium carbide precipitates in HSLA steel.* Materials Characterization, 1990. **25**(1): p. 17-36.
110. T. N. Baker, *Processes, microstructure and properties of vanadium microalloyed steels.* Materials Science and Technology, 2009. **25**(9): p. 1083-1107.
111. F. Hofer, P. Warbichler, B. Buchmayr, and S. Kleber, *On the detection of MX-precipitates in microalloyed steels using energy-filtering TEM.* Journal of Microscopy, 1996. **184**(3): p. 163-174.
112. F. Hofer and P. Warbichler, *Improved imaging of secondary phases in solids by energy-filtering TEM.* Ultramicroscopy, 1996. **63**: p. 21-25.
113. G. Kothleitner and F. Hofer, *Optimization of the Signal to Noise Ratio in EFTEM Elemental Maps with Regard to Different Ionization Edge Types.* Micron, 1998. **29**(5): p. 349-357.
114. E. Courtois, T. Epicier, and C. Scott, *EELS study of niobium carbo-nitride nano-precipitates in ferrite.* Micron, 2006. **37**(5): p. 492-502.
115. C. P. Scott, D. Chaleix, P. Barges, and V. Rebischung, *Quantitative analysis of complex carbo-nitride precipitates in steels.* Scripta Materialia, 2002. **47**(12): p. 845-849.
116. E. W. Müiller and G. B. Walter, *Field Emission Microscopy A2*, in *Physical Methods in Chemical Analysis*. 1956, Academic Press. p. 135-182.
117. E. W. Müller, *Pseudospirals, imperfect structures and crystal habit produced by field evaporation of metal crystals.* Acta Metallurgica, 1958. **6**(10): p. 620-630.
118. E. W. Müller, *Field Ionization and Field Ion Microscopy*, in *Advances in Electronics and Electron Physics*, L. Marton and M. Claire, Editors. 1960, Academic Press. p. 83-179.
119. D. G. Brandon, *The structure of field-evaporated surfaces.* Surface Science, 1965. **3**(1): p. 1-18.
120. N. Nir and D. G. Brandon, *A preliminary field-ion microscope study of grain-boundary junctions in tungsten.* Metallography, 1975. **8**(5): p. 375-390.
121. B. Deconihout, A. Bostel, P. Bas, S. Chambreland, L. Letellier, F. Danoix, and D. Blavette, *Investigation of some selected metallurgical problems with the tomographic atom probe.* Applied Surface Science, 1994. **76**: p. 145-154.
122. J. A. Panitz, *Imaging atom-probe mass spectroscopy.* Progress in Surface Science, 1978. **8**(6): p. 219-262.
123. M. K. Miller, P. A. Beaven, R. J. Lewis, and G. D. W. Smith, *Atom probe microanalytical studies of some commercially important steels.* Surface Science, 1978. **70**(1): p. 470-484.
124. Stiller, K., M. Hättestrand, and F. Danoix, *Precipitation in 9Ni–12Cr–2Cu maraging steels.* Acta Materialia, 1998. **46**(17): p. 6063-6073.
125. Danoix, F. and P. Auger, *Atom Probe Studies of the Fe–Cr System and Stainless Steels Aged at Intermediate Temperature: A Review.* Materials Characterization, 2000. **44**(1–2): p. 177-201.

126. W. Lefebvre, S. Morin-Grognet, and F. Danoix, *Role of Niobium in the nanocrystallization of a Fe73.5Si13.5B9Nb3Cu alloy.* Journal of Magnetism and Magnetic Materials, 2006. **301**(2): p. 343-351.
127. A. Menand, B. Deconihout, E. Cadel, and D. Blavette, *Atom-probe investigations of fine-scale features in intermetallics.* Micron, 2001. **32**(8): p. 721-729.
128. M. Thuvander, J. Weidow, J. Angseryd, L. K. L. Falk, F. Liu, M. Sonestedt, K. Stiller, and H. O. Andrén, *Quantitative atom probe analysis of carbides.* Ultramicroscopy, 2011. **111**(6): p. 604-608.
129. A. J. Craven, M. MacKenzie, A. Cerezo, T. Godfrey, and P. H. Clifton, *Spectrum imaging and three-dimensional atom probe studies of fine particles in a vanadium micro-alloyed steel.* Materials Science and Technology, 2008. **24**(6): p. 641-650.
130. M. Nöhrer, S. Zamberger, S. Primig, and H. Leitner, *Atom probe study of vanadium interphase precipitates and randomly distributed vanadium precipitates in ferrite.* Micron, 2013. **54–55**: p. 57-64.
131. Larson, D.J., D.T. Foord, A.K. Petford-Long, H. Liew, M.G. Blamire, A. Cerezo, and G.D.W. Smith, *Field-ion specimen preparation using focused ion-beam milling.* Ultramicroscopy, 1999. **79**(1): p. 287-293.
132. Thuillier, O., F. Danoix, M. Gouné, and D. Blavette, *Atom probe tomography of the austenite–ferrite interphase boundary composition in a model alloy Fe–C–Mn.* Scripta Materialia, 2006. **55**(11): p. 1071-1074.
133. J. Scott, P. J. Thomas, M. MacKenzie, S. McFadzean, J. Wilbrink, A. J. Craven, and W. A. P. Nicholson, *Near-simultaneous dual energy range EELS spectrum imaging.* Ultramicroscopy, 2008. **108**(12): p. 1586-1594.
134. A. V. Khvan and B. Hallstedt, *Thermodynamic description of the Fe-Mn-Nb-C system.* Calphad-Computer Coupling of Phase Diagrams and Thermochemistry, 2012. **39**: p. 62-69.
135. W. Huang, *An assessment of the Fe-Mn system.* Calphad, 1989. **13**(3): p. 243-252.
136. W. Huang, *Thermodynamic Properties of the Fe-Mn-V-C System.* METALLURGICAL TRANSACTIONS A, 1990. **22A**: p. 1991 -- 1911.
137. W. Huang, *A thermodynamic evaluation of the Fe-V-C System*
138. G. Paul, e.a., *Precipitation in High manganese steels.* Technical Report No:1 Issued on: 30/03/2011, 2011.
139. R. F. de Morais, A. Reguly, and L. H. de Almeida, *Transmission Electron Microscopy Characterization of a Nb Microalloyed Steel for Carburizing at High Temperatures.* Journal of Materials Engineering and Performance, 2006. **15**(4): p. 494-498.
140. W.M. Rainforth, C.M. Sellars, M.P. Black, I. Prabst, R.L. Higginson, E.J. Palmiere, P. Warbichler, and F. Hofer, *Precipitation of NbC in a model austenitic steel.* Acta Materialia, 2002. **50**: p. 735-747.
141. E. J. Palmiere, C. I. Garcia, and A. J. DeArdo, *The influence of niobium supersaturation in austenite on the static recrystallization behavior of low carbon microalloyed steels.* Metallurgical and Materials Transactions A, 1996. **27**(4): p. 951-960.
142. O. Kwon and A.J. DeArdo, *Interactions between recrystallization and precipitation in hot-deformed microalloyed steels.* Acta Metallurgica Materialia, 1991. **39**(4): p. 529-538.
143. K. A. Elfawakhry, M.F. Mekkawy, M.L. Mishreky, and M.M. Eissa, *Characterisation of precipitates in vanadium and titanium microalloyed steels.* ISJJ International, 1991. **31**(9): p. 1020-1025.
144. A. Fukami, *Evaporated carbon film for use in extraction replica technique* Journal of Electron Microscopy, 1956. **4**: p. 31-35.
145. J. Ngyelim, O. T. Woo, and G. J. C. Carpenter, *A replica technique for extracting precipitates from zirconium alloys for transmission electron-microscopy analysis* Journal of Electron Microscopy Technique, 1990. **15**(4): p. 400-405.

146. I. G. Palmer and G.C. Smith, *A disc technique for combined thin-foil and carbon-extraction replica electron microscopy.* Journal of the Institute of Metals, 1965. **93**: p. 326.
147. L. Cave, T. Al, D. Loomer, S. Cogswell, and L. Weaver, *A STEM/EELS method for mapping iron valence ratios in oxide minerals.* Micron, 2006. **37**(4): p. 301-9.
148. M. J. Kim and R. W. Carpenter, *TEM specimen heating during ion-beam thinning - microstructural instability.* Ultramicroscopy, 1987. **21**(4): p. 327-334.
149. D. Bahnck and R. Hull, *Reduced amorphization of ion-milled silicon cross-section transmission electron-microscope samples by dynamic annealing during milling*. Specimen Preparation for Transmission Electron Microscopy of Materials - Iii, ed. R. Anderson, B. Tracy, and J. Bravman. Vol. 254. 1992. 249-256.
150. D. Bahnck and R. Hull, *Experimental-measurement of transmission electron-microscope specimen temperature during ion milling*. Specimen Preparation for Transmission Electron Microscopy of Materials Ii, ed. R. Anderson. Vol. 199. 1990. 253-261.
151. L. A. Giannuzzi, B. W. Kempshall, C. A. Urbanik, B. I. Prenitzer, J. L. Drown, T. Shofner, S. R. Brown, R. B. Irwin, F. A. Stevie, and A. Aesf, *TEM analysis of galvanized steel using the FIB lift-out specimen preparation technique*. 9th Continuous Steel Strip Plating Symposium, Proceedings. 1999. 163-166.
152. D. Kiener, C. Motz, M. Rester, M. Jenko, and G. Dehm, *FIB damage of Cu and possible consequences for miniaturized mechanical tests.* Materials Science and Engineering: A, 2007. **459**(1-2): p. 262-272.
153. M. K. Miller, K. F. Russell, K. Thompson, R. Alvis, and D. J. Larson, *Review of atom probe FIB-Based specimen preparation methods.* Microscopy and Microanalysis, 2007. **13**(6): p. 428-436.
154. D. R. P. Singh, N. Chawla, and Y. L. Shen, *Focused Ion Beam (FIB) tomography of nanoindentation damage in nanoscale metal/ceramic multilayers.* Materials Characterization, 2010. **61**(4): p. 481-488.
155. J. Yu, J. Liu, J. Zhang, and J. Wu, *TEM investigation of FIB induced damages in preparation of metal material TEM specimens by FIB.* Materials Letters, 2006. **60**(2): p. 206-209.
156. M. Schaffer, B. Schaffer, and Q. Ramasse, *Sample preparation for atomic-resolution STEM at low voltages by FIB.* Ultramicroscopy, 2012. **114**: p. 62-71.
157. J. A. Wilson and A. J. Craven, *Improving the analysis of small precipitates in HSLA steels using a plasma cleaner and ELNES.* Ultramicroscopy, 2003. **94**: p. 197-207.
158. L. A. Giannuzzi, *Introduction to Focused Ion Beams Instrumentation, Theory, Techniques and Practice*. 1 ed. 2005, New York: Springer US. 379.
159. L. A. Giannuzzi and F. A. Stevie, *A review of focused ion beam milling techniques for TEM specimen preparation.* Micron, 1999. **30**(3): p. 197-204.
160. T. L. Shofner, J. L. Drown, S. R. Brown, B. B. Rossie, M. A. Decker, Y. S. Obeng, F. A. Stevie, and A. S. M. Asm, *Planar TEM analysis of nanoindented samples using the focused ion beam lift-out technique*. Istfa 2000: Proceedings of the 26th International Symposium for Testing and Failure Analysis. October 01, 2000 Seattle US ASM International. 459-461.
161. M. Milani, F. P Pucillo, M. Ballerini, M. Camatini, M. Gualtieri, and S. Martino, *First evidence of type debris characterization at the nanoscale by focused ion beam.* Materials Characterization, 2004. **52**(4-5): p. 283-288.
162. D. Mathys, *University of Basel: Die Entwicklung der Elektronenmikroskopie vom Bild über die Analyse zum Nanolabor.* Zentrum für Mikroskopie: p. p. 8.
163. L. Lambert and T. Mulvey, *Ernst Ruska (1906–1988), Designer Extraordinaire of the Electron Microscope: A Memoir*, in *Advances in Imaging and Electron Physics*, W.H. Peter, Editor. 1996, Elsevier. p. 2-62.
164. D. B. Williams and C. B. Carter, *Transmission Electron Microscopy*. 2009, New York: Springer.
165. A. V. Crewe, J. Wall, and J. Langmore, *Visibility of single atoms.* Science, 1970. **168**(3937): p. 1338-40.

166. J. Wall, J. Langmore, M. Isaacson, and A. V. Crewe, *Scanning transmission electron microscopy at high resolution.* Proc Natl Acad Sci U S A, 1974. **71**(1): p. 1-5.
167. R. D. Leapman, P. Rez, and D. F. Mayers, *K-shell, l-shell and m-shell generalized oscillator-strengths and ionization cross-sections for fast electron collisions.* Journal of Chemical Physics, 1980. **72**(2): p. 1232-1243.
168. M. Isaacson, *The microanalysis of light elements using transmitted energy loss electrons.* Ultramicroscopy, 1975. **1**(1): p. 33-52.
169. A. V. Crewe, *High Resolution Scanning Microscopy of Biological Specimens.* Philosophical Transactions of the Royal Society of London. Series B, Biological Sciences, 1971. **261**(837): p. 61-70.
170. A. Howie, *Image Contrast And Localized Signal Selection Techniques.* Journal of Microscopy, 1979. **117**(1): p. 11-23.
171. S .J. Pennycook and D.E. Jesson, *High-resolution Z-contrast imaging of crystals* Ultramicroscopy, 1991. **37**: p. 14-37.
172. O. Scherzer, *Over some errors of electrons lenses.* Zeitschrift Fur Physik, 1936. **101**(5): p. 593-603.
173. O. Scherzer, *The weak electrical single lens lowest spherical aberration.* Zeitschrift Fur Physik, 1936. **101**(1): p. 23-26.
174. O. L Krivanek, N. Dellby, and A. R. Lupini, *Towards sub-Å electron beams.* Ultramicroscopy, 1999. **78**(1): p. 1-11.
175. R. Brydson, *Aberration-corrected analytical transmission electron microscopy*. 2011, Chichester, West Sussex, U.K.: RMS-Wiley. xv, 280 p.
176. O. Scherzer, *Sphärische und chromatische Korrektur von Elektronen-Linsen.* OPTIK 2, 1947: p. 114 - 132.
177. J. Zach and M. Haider, *Aberration correction in a low voltage SEM by a multipole corrector.* Nuclear Instruments and Methods in Physics Research Section A: Accelerators, Spectrometers, Detectors and Associated Equipment, 1995. **363**(1): p. 316-325.
178. J. Zach and M. Haider, *Correction of spherical and chromatic aberrations in a LVSEM.* Proc. 13th Int. Congr. Electron Microscopy, Paris, France, 1994. **1**: p. 199-200.
179. M. Haider, G. Braunshausen, and E. Schwan, *Correction of the spherical aberration of a 200 kV TEM by means of a hexapole-corrector.* Optik, 1995. **99**(4): p. 167-179.
180. M. Haider, S. Uhlemann, E. Schwan, H. Rose, B. Kabius, and K. Urban, *Electron microscopy image enhanced.* Nature, 1998. **392**: p. 768-769.
181. O. L Krivanek, N. Dellby, A. J. Spence, R. A. Camps, and L. M. Brown. *Aberration correction in the STEM*. in *Institute of Physics Conference Series*. 1997. Bristol [England]; Boston: Adam Hilger, Ltd., c1985-.
182. Haider, M., S. Uhlemann, and J. Zach, *Upper limits for the residual aberrations of a high-resolution aberration-corrected STEM.* Ultramicroscopy, 2000. **81**(3): p. 163-175.
183. K. Y. Xie, T. Zheng, J. M. Cairney, H. Kaul, J. G. Williams, F. J. Barbaro, C. R. Killmore, and S. P. Ringer, *Strengthening from Nb-rich clusters in a Nb-microalloyed steel.* Scripta Materialia, 2012. **66**(9): p. 710-713.
184. R. F. Egerton, *Physical Principles of Electron Microscopy An Introduction to TEM, SEM, and AEM*. Springer. 2005, New York: Springer.
185. R. Brydson and Royal Microscopical Society (Great Britain), *Electron energy loss spectroscopy*. Microscopy handbooks. 2001, Oxford: Bios in association with the Royal Microscopical Society. xii, 137 p.
186. Hall, C.R. and P.B. Hirsch, *Effect of thermal diffuse scattering on propagation of high energy electrons through crystals.* Proceedings of the Royal Society of London. Series A. Mathematical and Physical Sciences, 1965. **286**(1405): p. 158-177.
187. Rutherford, E., *The scattering of α and β particles by matter and the structure of the atom.* Philosophical Magazine, 1911. **92**(4): p. 379-398.

188. Gubbens, A., M. Barfels, C. Trevor, R. Twesten, P. Mooney, P. Thomas, N. Menon, B. Kraus, C. Mao, and B. McGinn, *The GIF Quantum, a next generation post-column imaging energy filter.* Ultramicroscopy, 2010. **110**(8): p. 962-970.
189. Jeanguillaume, C. and C. Colliex, *Spectrum-image: The next step in EELS digital acquisition and processing.* Ultramicroscopy, 1989. **28**(1): p. 252-257.
190. A. Gubbens, M. Barfels, C. Trevor, R. Twesten, P. Mooney, P. Thomas, N. Menon, B. Kraus, C. Mao, and B. McGinn, *The GIF Quantum, a next generation post-column imaging energy filter.* Ultramicroscopy, 2010. **110**(8): p. 962-970.
191. Craven, A.J., J.A. Wilson, and W.A.P. Nicholson, *A fast beam switch for controlling the intensity in electron energy loss spectrometry.* Ultramicroscopy, 2002. **92**(3): p. 165-180.
192. Craven, A.J., M. MacKenzie, and S. McFadzean. *Dual energy range EELS spectrum imaging using a fast beam switch*. in *EMC 2008 14th European Microscopy Congress 1–5 September 2008, Aachen, Germany*. 2008. Berlin, Heidelberg: Springer Berlin Heidelberg.
193. D. W. Johnson and J. C. H. Spence, *Determination of the single-scattering probability distribution from plural-scattering data.* Journal of Physics D: Applied Physics, 1974. **7**(6): p. 771.
194. R. F. Egerton, *Electron Energy-Loss Spectroscopy in the Electron Microscope*. 2011, New York: Springer. 491.
195. J. Bobynko, I. MacLaren, and A. J. Craven, *Spectrum imaging of complex nanostructures using DualEELS: I. digital extraction replicas.* Ultramicroscopy, 2015. **149**: p. 9-20.
196. R. F. Egerton, *Physical Principles of Electron Microscopy An Introduction to TEM, SEM, and AEM*. 2005.
197. T. Epicier, *Transmission Electron Microscopy and Nano-Precipitation.* Advanced Engineering Materials, 2006. **8**(12): p. 1197-1201.
198. Anderson, R., *Practical Aspects of FIB Tem Specimen Preparation*. 2005.
199. Langford, R.M. and A.K. Petford-Long, *Preparation of transmission electron microscopy cross-section specimens using focused ion beam milling.* Journal of Vacuum Science & Technology A: Vacuum, Surfaces, and Films, 2001. **19**(5): p. 2186-2193.
200. Langford, R.M., *Focused ion beams techniques for nanomaterials characterization.* Microsc Res Tech, 2006. **69**(7): p. 538-549.
201. Reiner, J.C., P.M. Nellen, and U. Sennhauser, *Gallium artefacts on FIB-milled silicon samples*. Vol. 44. 2004. 1583-1588.
202. Schaffer, M., B. Schaffer, Q. Ramasse, M. Falke, D. Abou-Ras, S. Schmidt, R. Caballero, and K. Marquardt, *Optimized FIB Sample Preparation for Atomic Resolution Analytical STEM at Low kV - A Key Requirement for Successful Application.* Microscopy and Microanalysis, 2017. **17**(S2): p. 630-631.
203. Wang, L., B. Schaffer, A.J. Craven, I. MacLaren, S. Miao, and I.M. Reaney, *Atomic Scale Structural and Chemical Quantification of Non-Stoichiometric Defects in Ti and Bi Doped BiFeO3*. Vol. 17. 2011. 1896-1897.
204. A. Fischione Instruments, I., *NanoMill TEM speciment preparation system.* 2013.
205. E. V. Pereloma, I. B. Timokhina, M. KMiller, and P. D. Hodgson, *Three-dimensional atom probe analysis of solute distribution in thermomechanically processed TRIP steels.* Acta Materialia, 2007. **55**(8): p. 2587-2598.
206. S. Rubanov and P. R. Munroe, *The effect of the gold sputter-coated films in minimising damage in FIB-produced TEM specimens.* Materials Letters, 2003. **57**(15): p. 2238-2241.
207. MacKenzie, M., A.J. Craven, and C.L. Collins, *Nanoanalysis of very fine VN precipitates in steel.* Scripta Materialia, 2006. **54**(1): p. 1-5.
208. R. C. Pond, *Review of the principal contrast effects observed at interphase boundaries using transmission electron microscopy.* Journal of Microscopy, 1984. **135**(3): p. 213-240.
209. Dudarev, S.L. and M.I. Ryazanov, *Multiple scattering theory for fast electrons in single crystals and Kikuchi patterns.* Acta Crystallographica Section A, 1988. **44**(1): p. 51-61.

210. D. Djurovic, B. Hallstedt, J. von Appen, and R. Dronskowski, *Thermodynamic assessment of the Fe–Mn–C system.* Calphad, 2011. **35**(4): p. 479-491.
211. D. Ramakrishna and S. P. Gupta, *Coarsening kinetics of grain boundary VC in a HSLA steel.* Scripta Metallurgica, 1986. **20**(3): p. 355-360.
212. Storms, E.K. and N.H. Krikorian, *The Variation of Lattice Parameter with Carbon Content of Niobium Carbide.* The Journal of Physical Chemistry, 1959. **63**(10): p. 1747-1749.
213. Egerton, R.F., *A revised expression for signal/noise ratio in EELS.* Ultramicroscopy, 1982. **9**(4): p. 387-390.
214. M. Bosman, M. Watanabe, D. T. L. Alexander, and V. J. Keast, *Mapping chemical and bonding information using multivariate analysis of electron energy-loss spectrum images.* Ultramicroscopy, 2006. **106**(11-12): p. 1024-1032.
215. G. Lucas, P. Burdet, M. Cantoni, and C. Hebert, *Multivariate statistical analysis as a tool for the segmentation of 3D spectral data.* Micron, 2013. **52-53**: p. 49-56.
216. S. Lichtert and J. Verbeeck, *Statistical consequences of applying a PCA noise filter on EELS spectrum images.* Ultramicroscopy, 2013. **125**: p. 35-42.
217. Sparrow, T.G., B.G. Williams, C.N.R. Rao, and J.M. Thomas, *L3/L2 white-line intensity ratios in the electron energy-loss spectra of 3d transition-metal oxides.* Chemical Physics Letters, 1984. **108**(6): p. 547-550.
218. A. J. Craven and L. A. J. Garvie, *Electron Energy Loss Near Edge Structure (ELNES) on the Carbon K-Edge in Transition Metal Carbides with the Rock Salt Structure.* Microscopy Microanalysis Microstructures, 1995. **6**(1): p. 89-98.
219. D. E. Gai, V. I. Grebennikov, O. R. Bakieva, D. V. Surnin, and A. N. Deev, *Spectroscopy of Extended Electron Energy Loss Fine Structures for Quantitative Analysis of the Local Atomic Structure in Ultrathin Oxide Films on the Surface of 3d-Metals.* Journal of Structural Chemistry, 2008. **49**: p. S174-S189.
220. A. J. Craven, *The electron energy-loss near-edge structure (ELNES) on the N K-edges from the transition metal mononitrides with the rock-salt structure and its comparison with that on the C K-edges from the corresponding transition metal monocarbides.* Journal of Microscopy, 1995. **180**(3): p. 250-262.
221. A. J. Craven, K. He, L. A. J. Garvie, and T. N. Baker, *Complex heterogeneous precipitation in titanium–niobium microalloyed Al-killed HSLA steels—I. (Ti,Nb)(C,N) particles.* Acta Materialia, 2000. **48**(15): p. 3857-3868.
222. B. G. Mendis and A. J. Craven, *Characterising the surface and interior chemistry of core-shell nanoparticles using scanning transmission electron microscopy.* Ultramicroscopy, 2011. **111**(3): p. 212-26.
223. R. F. Egerton, *Values of K-shell partial cross-section for electron energy-loss spectrometry.* Journal of Microscopy, 1981. **123**(3): p. 333-337.
224. R. F. Egerton, *Electron Energy-Loss Spectroscopy in the Electron Microscope*. 2011.
225. R. F. Egerton, *Improvement of the hydrogenic model to give more accurate values of K-shell ionization cross sections.* Ultramicroscopy, 1996. **63**(1): p. 11-13.
226. F. Hofer and P. Wilhelm, *EELS microanalysis of the elements Ca to Cu using M23 edges.* Ultramicroscopy, 1993. **49**(1): p. 189-197.
227. F. Hofer, G. Kothleitner, and P. Rez, *Ionization cross-sections for the L23-edges of the elements Sr to Mo for quantitative EELS analysis.* Ultramicroscopy, 1996. **63**(3): p. 239-245.
228. P.A. Crozier†, *Measurement of inelastic electron scattering cross-sections by electron energy-loss spectroscopy.* Philosophical Magazine Part B, 1990. **61**(3): p. 311-336.
229. D. Bach, R. Schneider, and D. Gerthsen, *EELS of Niobium and Stoichiometric Niobium-Oxide Phases-Part II: Quantification.* Microscopy and Microanalysis, 2009. **15**(6): p. 524-538.
230. D. Bach, R. Schneider, D. Gerthsen, J. Verbeeck, and W. Sigle, *EELS of Niobium and Stoichiometric Niobium-Oxide Phases-Part I: Plasmon and Near-Edges Fine Structure.* Microscopy and Microanalysis, 2009. **15**(6): p. 505-523.

231. Goldstein JI, Costley JL, Lorimer GW, and Reed SJB, *Quantitative X-ray Analysis in the Electron Microscope Scanning Electr. Microsc. : Proc. Workshop Anal. Electron Microsc* C. IIT Research Institute, IL, USA Editor. 1977: IIT Research Institute, Chicago, IL, USA p. 315.
232. T. Manoubi, C. Colliex, and P. Rez, *Quantitative electron energy loss spectroscopy on M45 edges in rare earth oxides.* Journal of Electron Spectroscopy and Related Phenomena, 1990. **50**(1): p. 1-18.
233. T. Malis, S. C. Cheng, and R. F. Egerton, *EELS log-ratio technique for specimen-thickness measurement in the TEM.* Journal of Electron Microscopy Technique, 1988. **8**(2): p. 193-200.
234. K. Iakoubovskii, K. Mitsuishi, Y. Nakayama, and K. Furuya, *Mean free path of inelastic electron scattering in elemental solids and oxides using transmission electron microscopy: Atomic number dependent oscillatory behavior.* Physical Review B, 2008. **77**(10): p. 7.
235. B. G. Mendis, M. MacKenzie, and A. J. Craven, *A new analytical method for characterising the bonding environment at rough interfaces in high-k gate stacks using electron energy loss spectroscopy.* Ultramicroscopy, 2010. **110**(2): p. 105-117.
236. C. R. Swyt and R. D. Leapman, *Plural scattering in electron-energy loss spectroscopy (EELS) microanalysis.* Scanning Electron Microscopy, 1982: p. 73-82.
237. K. Iakoubovskii, K. Mitsuishi, Y. Nakayama, and K. Furuya, *Thickness measurements with electron energy loss spectroscopy.* Microsc Res Tech, 2008. **71**(8): p. 626-31.
238. H.-R. Zhang, R. F. Egerton, and M. Malac, *Local thickness measurement through scattering contrast and electron energy-loss spectroscopy.* Micron, 2012. **43**(1): p. 8-15.
239. R. F. Egerton, *Factors affecting the accuracy of elemental analysis by transmission EELS.* Microscopy Microanalysis Microstructures, 1991. **2**(2-3): p. 203-213.
240. N. J. Zaluzec, *Influence of specimen thickness in quantitative electron energy loss spectroscopy*. 38th Annual Proceedings: Electron Microscopy Society of America. . 1980, United States: Electron Microscopy Society of America.
241. F. Lenz, *Zur Streuung mittelschneller Elektronen in kleinste Winkel*, in *Zeitschrift für Naturforschung A*. 1954. p. 185.
242. Goldschmidt, H.J., *Occurrence of the beta-manganese structure in transition metal alloys and some observations on chi-phase equilibria.* Metallurgia, 1957. **56**: p. 17-26.
243. R. F. Egerton and M. Malac, *EELS in the TEM.* Journal of Electron Spectroscopy and Related Phenomena, 2005. **143**(2-3): p. 43-50.
244. R.F. Egerton and S.C. Cheng, *Measurement energy-loss of local thickness by electron spectroscopy.* Ultramicroscopy, 1987. **21**(231-244).
245. W. Lengauer and P. Ettmayer, *Physical and mechanical-properties of cubic delta-VN1-x.* Journal of the Less-Common Metals, 1985. **109**(2): p. 351-359.
246. F. Hofer, *Determination of inner-shell cross-sections for EELS quantification.* Microscopy Microanalysis Microstructures, 1991. **2**(2-3): p. 215-230.
247. Billingham, J., P.S. Bell, and M.H. Lewis, *A superlattice with monoclinic symmetry based on the compound V6C5.* Philosophical Magazine, 1972. **25**(3): p. 661-671.
248. Lim, J.J.H., S. Lozano-Perez, M.G. Burke, P.D. Styman, I. Maclaren, K. Wilford, and C.R.M. Grovenor, *The Evolution of Precipitates in High Cu and High Ni RPV Welds under Long-term Thermal Ageing.* Microscopy and Microanalysis, 2015. **21**(S3): p. 1009-1010.

APPENDIX 1

This script creates a 3D spectrum with the normalized background shape to the appropriate size per pixel in a new spectrum image, and then subtracted from the original low loss spectrum and leave a new version of the low loss without any bleedthrough.

```
/* Create "3D spectrum" */
// This script takes a 1D spectrum and a 3D block as input and
// creates a 3D block which contains the 1D spectrum in each x/y
position
image spec, block
gettwoimageswithprompt("Select 1D Spectrum and 3D
block","Select",spec,block)
number sx,sy,sz
block.getsize(sx,sy)
sz = spec.imagegetdimensionsize(0)
image out:=realimage("",4,sx,sy,sz)
out:=block.imageclone()
out*=0
out=spec[iplane,0]
out.showimage()
out.imagesetdimensionscale(2,spec.imagegetdimensionscale(0))
out.imagesetdimensionorigin(2,spec.imagegetdimensionorigin(0))
out.imagesetdimensionunitstring(2,spec.imagegetdimensionunitstring(0
))
// multiply 3D by image
// Takes a 3D block and a 2D image and scales all spectra in the 3D
block by the according pixel-value //of the 2D image
image img, block
gettwoimageswithprompt("Select 2D Image and 3D
block","Select",img,block)
image out:=block.imageclone()
out*=img[icol,irow]
out.setname(block.getname()+" mult")
out.showimage()

// subtract two 3D data sets
// Takes a 3D block and subtracts a second 3D block of the same
dimensions
image img, block
```

```
gettwoimageswithprompt("Select 3D block and the one to subtract","Select",img,block)
image out:=img.imageclone()
out=img-block
out.setname(img.getname()+" minus")
out.showimage()
```

APPENDIX 2

This script applies smoothing procedure, by taking the LL spectrum, extracts the fitted power law for the energy window used for tail up to the splice point.

```
// Assumes that there is a suitably corrected low loss SI
// Assumes that a background SI has been derived from it using AE-r fit
// Assumes that the fit channels are known
// The left fit channel is the first channel for replacement
// The last channel for replacement is decided by the user
// but is noramlly the last channel of the spectrum
//Declarations
image LLSI, LLSIBkg, LLSISmooth
number sx,sy,sz,left, right
// Prompt for the low loss and core loss SIs
gettwoimageswithprompt("Select low loss SI and then background","Select",LLSI,LLSIBkg)
// showimage(LLSI)
// showimage(LLSIBkg)
//Get the image size
LLSI.get3dsize(sx,sy,sz)
// Get the ROI boundaries for the replacement.
// The left hand channel for the replacement is the start channel of the background window
// The right hand channel for the repacement should go beyond the splice point.
// Default is the last channel of the spectrum.
GetNumber("Enter the first CHANNEL used for the background window:",180,Left)
GetNumber("Enter the last CHANNEL for repacement - default end of spectrum:",sz,Right)
//result ("Boundaries are "+Left+" "+Right+ "\n")
//Set up the corrected low loss spectra to start as the low loss spectra
LLSISmooth:=LLSI.imageclone()
```

```
//Load the low loss section from channel 0 to channel (VSM+R4L)
using "slice3"
//Load the scaled core loss section from channel (VSM+R4L) to SZ
using slice 3"
// Axes of input data set axes specified as
// 0 = x-axis, 1 = y-axis , 2 = z-axis
// slice 3 extracts the data from the input data set
// The axes of the output dataset are in the order x,y,z
// slice3 has arguments
// startx, starty, startz, x-axis, number-x, step-x,
// y-axis, number-y, step-y, z-axis, number-z, step-z)
// Here original x is going to new x, y to y and z to z
//i.e. arguments 4,7 and 10 are 0,1 and 2 respectively.
//  The dataset can be rotated by changing the order
//but then sx,sy and sz have to be chosen approriately
LLSISmooth[0,0,Left,sx,sy,Right]=   LLSIBkg.slice3(0,0,0,   0,sx,1,
1,sy,1, 2,(Right-Left),1)
//Change name
LLSISmooth.setname(LLSI.getname()+" Smooth")
//ShowImage(LLSISmooth)
ShowImage(LLSISmooth)
```

APPENDIX 3

The splice ratio is extracted from the data by applying this script.

```
image src := GetFrontImage();
number xSize, ySize, zSize;
Get3DSize(src, xSize, ySize, zSize);
TagGroup tgs = src.ImageGetTagGroup();
TagGroup processingTags;
if(tgs.TagGroupGetTagAsList("Processing", processingTags))
{
	number nTags = processingTags.TagGroupCountTags();
	TagGroup splice_tags;
	if(processingTags.TagGroupGetIndexedTagAsTagGroup(nTags  -  1,
splice_tags))
	{
		Image  out  :=  RealImage("splice  factor  map",  4,  xSize,
ySize);

if(splice_tags.TagGroupGetTagAsArray("Parameters:Scaling", out))
			ShowImage(out);
		else
			OKDialog("Could not find splice tags!")
	}
}
```

APPENDIX 4

Thih script performs the linearization, which is done on basis of polynomial fit between standard specimen, which is a high manganese steel with particles in it, and the deconvolved spectrum image of precipitate that is going to be quantified.

```
//SI SPECTRUM ENERGY LINEARISATION SCRIPT
//NB A FEW CHANNELS AT EITHER END OF THE LINEARISED SPECTRUM WILL BE UNRELIABLE
//This script is to correct minor non-linearity in the energy scale.
//It assumes that the intensity in one channel of the non-linear data never requires
//redistributing into more than three channels of the linearised data.
//It assumes that the LINEAR energies can be fitted by a polynomial of up to
//fourth order in the NON-LINEAR energies.
//The energy zero must be accurately calibrated before the polynomial fit.
//The fit should normally force the constant to be ZERO
//This fit must be done prior to running the script and the coefficients entered
//into the script when requested.
Image SI, SILinear
Number sx,sy,sz,ScaleX, OriginX, ScaleY, OriginY, ScaleZ,OriginZ,OriginChannel,type,EnergyNonLinear, EnergyLinear
String  SpectrumName, UnitsX,UnitsY,UnitsZ
//Read in the spectrum
GetOneImageWithPrompt("Enter the non-linear SI","Spectrum Image",SI)
//Get the file name
SpectrumName=GetName(SI)
//Result(SpectrumName+"\n")
//Get the data size of the spectrum
SI.get3dsize(sx,sy,sz)
//Result(sx+" "+sy+" "+sz+"\n")
//Get the calibration of the spectrum
```

```
//NB UNLIKE "IMAGE DISPLAY/CALIBRATION", this gives the origin in
CALIBRATED UNITS
//and not in CHANNELS
OriginX=ImageGetDimensionOrigin( SI,0)
ScaleX=ImageGetDimensionScale( SI,0)
UnitsX=imagegetdimensionunitstring(SI,0)
OriginY=ImageGetDimensionOrigin( SI,1)
ScaleY=ImageGetDimensionScale( SI,1)
UnitsY=imagegetdimensionunitstring(SI,1)
OriginZ=ImageGetDimensionOrigin( SI,2)
ScaleZ=ImageGetDimensionScale( SI,2)
UnitsZ=imagegetdimensionunitstring(SI,2)
OriginChannel=-OriginZ/scaleZ
//Result(scale+" "+origin+" "+originchannel+" "+"\n")
//Get the polynomial fit coefficents
Number a4,a3,a2,a1,a0
GetNumber("Enter the cofficient of E^4",-4.53620509927506E-10,a4)
GetNumber("Enter the cofficient of E^3",8.47038004907199E-07,a3)
GetNumber("Enter the cofficient of E^2",-4.68788583037412E-04,a2)
GetNumber("Enter the cofficient of E^1",1.06645480082660E+00,a1)
GetNumber("Enter the constant",0,a0)
//Result(a4+" "+a3+" "+a2+" "+a1+" "+a0+" "+"\n")
//*************************************************************
***
//SET UP THE DATA STRUCTURE FOR THE TRANSFER FACTORS
//*************************************************************
*****
//Define the number of columns in the data structure.
//1st column is non-linear energy
//2nd column is linear energy
//3rd column is real true energy channel centre
//4th column is the bottom limit of the real channels over-lapping
with the
// experimental channel in the spectrum in terms of the real channel
//5th column is the integer below this
//6thcolumn is the channel width
```

```
//7th column is the transfer factor of the intensity in the
experimental channel
// to the bottom channel
//8th column is the tranfer factor to the channel above the bottom
one
//9th column is the transfer factor to the channel two above
Number Size
size=9
//Define the data structure to match the spectrum length
Image TransferFactors:= realImage("TransferFactors",4,size,sz)
//Zero the data structure
TransferFactors=0
//Set the display type to spreadsheet for FitResults
//To convert the display type of an image use
//SetDisplayType(img,type)
//img is the image of interest
//n is the display type required
//By trial and error
// type=1 raster
// type=2  surface plot
// type=3  error - not sure
// type=4  Line plot
// type=5  Spreadsheet
// type=6  error not sure
// type=7 spreadsheet
type=5
setdisplaytype(TransferFactors,type)
//******************************************************************
*********
//CALCULATE THE TRANSFER FACTORS FOR THE INTENSITY IN EACH CHANNEL
//******************************************************************
*********
//Initialise counter
Number I
I=0
While (I<sz)
      {
```

```
	//Put non-linear energy in 1st column
	EnergyNonLinear=OriginZ+I*ScaleZ
	TransferFactors[I,0,I+1,1]=EnergyNonLinear
	//Put true energy in 2nd column  BEWARE x^4 notation gives big
errors.  Use x*x*x*x
	TransferFactors[I,1,I+1,2]=TransferFactors[I,1,I+1,2]+a4*Energy
NonLinear*EnergyNonLinear*EnergyNonLinear*EnergyNonLinear
	TransferFactors[I,1,I+1,2]=TransferFactors[I,1,I+1,2]+a3*Energy
NonLinear*EnergyNonLinear*EnergyNonLinear
	TransferFactors[I,1,I+1,2]=TransferFactors[I,1,I+1,2]+a2*Energy
NonLinear*EnergyNonLinear
	TransferFactors[I,1,I+1,2]=TransferFactors[I,1,I+1,2]+a1*Energy
NonLinear
	TransferFactors[I,1,I+1,2]=TransferFactors[I,1,I+1,2]+a0
	//Put channel number of true energy in column 3
	TransferFactors[I,2,I+1,3]=(TransferFactors[I,1,I+1,2]-
OriginZ)/ScaleZ
	I=I+1
	}
//*******************************************************************
************
//Now we take the average of the true channel and the one below so
start at row 1.   In column 4, //the value in row zero is already
zero
I=1
While (I<sz)
	{
	//Calculate lower boundary of the true energy channel and put
it in column 4.
	number Dummy
	Dummy=  (sum(TransferFactors[I,2,I+1,3])+sum(TransferFactors[I-
1,2,I,3]))/2
	TransferFactors[I,3,I+1,4]=dummy
	//set to integer below
	dummy =nearest(dummy-0.5)
	// If channel number of the lower bound is negative, set to
zero
```

```
      If (Dummy<0)
            TransferFactors[I,4,I+1,5]=0
      Else
            TransferFactors[I,4,I+1,5]=dummy
      // Set channel references that refer outside the size of the
spectrum to zero.
      // Make it greater than(sz-3) so that when 2 channels are added
later it's still
      // doesn't go outside the dataset
If (Dummy>sz-3)
            TransferFactors[I,4,I+1,5]=0
      I=I+1
      }
//*******************************************************************
***************
//To calculate channel width, which is next channel minus current
channel, we need to re-start the loop and stop at (sz-1)
// Reset I to 1
I=1
While(I<sz-1)
      {
      //Calculate the width of the experimnetal channel and put in
column 6
      TransferFactors[I,5,I+1,6]=sum(TransferFactors[I+1,3,I+2,4])-
sum(TransferFactors[I,3,I+1,4])
      //calculate fraction of experimental intensity in this channel
goes into the lower chanel of the linear spectrum; put in column 7
      //Set the values correponding to negative real channels or
channels beyond the end of the spectrum to zero
      If(sum(TransferFactors[I,4,I+1,5])==0)
            TransferFactors[I,6,I+1,7]=0
      Else

      TransferFactors[I,6,I+1,7]=(sum(TransferFactors[I,4,I+1,5])+1-
sum(TransferFactors[I,3,I+1,4]))/sum(TransferFactors[I,5,I+1,6])
      //Check for transfer factor greater than 1.  If so set to 1
      IF(   sum(TransferFactors[I,6,I+1,7])>1)
```

```
            TransferFactors[I,6,I+1,7]=1
      //calculate fraction that goes into the upper channel.  Note
the jump in column is deliberate
      If((sum(-TransferFactors[I,4,I+1,5])-
2+sum(TransferFactors[I+1,3,I+2,4]))>0)
            TransferFactors[I,8,I+1,9]=(sum(-
TransferFactors[I,4,I+1,5])-
2+sum(TransferFactors[I+1,3,I+2,4]))/sum(TransferFactors[I,5,I+1,6])
      Else
            TransferFactors[I,8,I+1,9]=0
      //Set the values correponding to negative real channels or
channels beyond the end of the spectrum to zero
      If(sum(TransferFactors[I,4,I+1,5])==0)
            TransferFactors[I,8,I+1,9]=0
      //Set the mid channel fraction to 1 minus the upper plus lower
      TransferFactors[I,7,I+1,8]=1-TransferFactors[I,8,I+1,9]-
TransferFactors[I,6,I+1,7]
      //Set the values corresponding to negative real channels or
channels beyond the end of the spectrum to zero
      If(sum(TransferFactors[I,4,I+1,5])==0)
            TransferFactors[I,7,I+1,8]=0
      I=I+1
      }
ShowImage(TransferFactors)
//Set File Name
SetName(TransferFactors,"Tranafer Factors for "+SpectrumName)
//*******************************************************************
***************//LINEARISING THE ENERGY SCALE OF THE SPECTRUM
//*******************************************************************
***************
//First Step is to get the lower channel signal
//Extract the lower channel transfer factors
Image Factor1 := RealImage("Factor1",4,1,sz)
Factor1=TransferFactors[6,irow]
//Create clone of the SI
Image Factor1SI=SI.imageclone()
```

```
//Use this to create a 3D dataset with the factor at all spatial
pixels
Factor1SI*=0
Factor1SI=Factor1[0,iplane]
//Multiply the SI by the transfer factors to get one contribution to
the final linearised spectrum
Image SILinear1=SI*Factor1SI
//ShowImage(SILinear1)
//showImage(Factor1SI)
//Showimage(factor1)
//*****************************************************************
***************
//Now do the mid-channel transfer
//*****************************************************************
***************
//Extract the mid channel transfer factors
Image Factor2 := RealImage("Factor2",4,1,sz)
Factor2=TransferFactors[7,irow]
//Create clone of the SI
Image Factor2SI=SI.imageclone()
//Use this to create a 3D dataset with the factor at all spatial
pixels
Factor2SI*=0
Factor2SI=Factor2[0,iplane]
//showImage(Factor2SI)
//Multiply the SI by the transfer factors to get one contribution to
the final linearised spectrum
Image SILinear2=SI*Factor2SI
//ShowImage(SILinear2)
//*****************************************************************
***************
//Now do the upper channel transfer
//*****************************************************************
***************
//Extract the upper channel transfer factors
Image Factor3 := RealImage("Factor3",4,1,sz)
Factor3=TransferFactors[8,irow]
```

```
//Create clone of the SI
Image Factor3SI=SI.imageclone()
//Use this to create a 3D dataset with the factor at all spatial
pixels
Factor3SI*=0
Factor3SI=Factor3[0,iplane]
//showImage(Factor3SI)
//Multiply the SI by the transfer factors to get one contribution to
the final linearised spectrum
Image SILinear3=SI*Factor3SI
//ShowImage(SILinear3)
//*****************************************************************
***************
//NOW FORM THE COMPLETE LINEARISED SI, CALIBRATE IT, TITLE AND TAG
IT
//*****************************************************************
***************
//Set up the final Linear SI
SILinear=SI.ImageClone()
SILinear=0
Image Temp1 := RealImage("Temp1",4,sx,sy,1)
Image Temp2 := RealImage("Temp1",4,sx,sy,1)
Image Temp3 := RealImage("Temp1",4,sx,sy,1)
//Set up a loop
I=0
While (I<sz-1)
      {
      Number Z
      Z=sum(TransferFactors[4,I])
      Temp1=SILinear1.slice3(0,0,I,0,sx,1,1,sy,1,2,1,1)
      SILinear[icol,irow,Z]+=Temp1
      Temp2=SILinear2.slice3(0,0,I,0,sx,1,1,sy,1,2,1,1)
      SILinear[icol,irow,Z+1]+=Temp2
      Temp3=SILinear3.slice3(0,0,I,0,sx,1,1,sy,1,2,1,1)
      SILinear[icol,irow,Z+2]+=Temp3
      //Result(I+"\n")
      I=I+1
```

```
      }
//Convert to EELS SI
ShowImage(SILinear)
ChooseMenuItem("Spectrum","Convert Data To", "EELS")
//*****************************
//Set Tags to record polynomial coefficients and original file name
//*******************************
SILinear.SetNumberNote("Polynomial  Fit  Parameters:Fit  Coefficient
E^4  ", a4)
SILinear.SetNumberNote("Polynomial  Fit  Parameters:Fit  Coefficient
E^3  ", a3)
SILinear.SetNumberNote("Polynomial  Fit  Parameters:Fit  Coefficient
E^2  ", a2)
SILinear.SetNumberNote("Polynomial Fit Parameters:Fit Coefficient E
", a1)
SILinear.SetNumberNote("Polynomial  Fit  Parameters:Fit  Coefficient
Const", a0)
SILinear.SetStringNote("Polynomial Fit Parameters:Parent File Name",
SpectrumName)
//
//Set File Name
SetName(SILinear,SpectrumName+" LINEARISED")
//Calibrate the SI
SILinear.imagesetdimensionscale(0,ScaleX)
SILinear.imagesetdimensionorigin(0,OriginX)
SILinear.imagesetdimensionunitstring(0,UnitsX)
SILinear.imagesetdimensionscale(1,ScaleY)
SILinear.imagesetdimensionorigin(1,OriginY)
SILinear.imagesetdimensionunitstring(1,UnitsY)
SILinear.imagesetdimensionscale(2,ScaleZ)
SILinear.imagesetdimensionorigin(2,OriginZ)
SILinear.imagesetdimensionunitstring(2,UnitsZ)
```

APPENDIX 5

This script takes an image and presents a gradient between signal and normalized ZLP signal, and presented in BARNS/eV.

```
//SCRIPT TO EXTRACT THE DIFFERENTIAL CROSS-SECTION OF AN EDGE FROM A
SPECTRUM IMAGE
// CONTAINING A BACKGROUND SUBTRACTED EDGE
//Tags added to output spectrum to give processing conditions
//The gradient is differential cross-section is in BARNS/eV.
//The vertical axis and intercept is the signal per eV normalised by
Io
//The horizontal scale is atoms/barn
//**********************   INPUT THE DATA   *******************
Image EdgeSI,TLamda,Io,SpliceRatio,EdgeSI2,TLamda2,Io2,SpliceRatio2
number TimeHigh, TimeLow
GetFourImagesWithPrompt("Enter  Edge  SI,t/lamda  map,Io  map,Splice
ratio map","Enter Data",EdgeSI,TLamda,Io, SpliceRatio)
//Put the file names in strings to put in the tags below
string EdgeSIname, TLamdaName, IoName,SpliceRatioName
EdgeSIName=GetName(EdgeSI)
TLamdaName=GetName(TLamda)
IoName=GetName(Io)
SpliceRatioName=GetName(SpliceRatio)
//Result(EdgeSIName+"\n")
//Result(TLamdaName+"\n")
//Result(IoName+"\n")
//Result(SpliceRatioName+"\n")
//Put the input images into duplicates
EdgeSI2=EdgeSI.imageclone()
TLamda2=TLamda.imageclone()
Io2=Io.imageclone()
SpliceRatio2=SpliceRatio.imageclone()
//Get the acquisition times
GetNumber("Enter the High Loss Acquistion Time",49700,TimeHigh)
GetNumber("Enter the Low Loss Acquistion Time",298.2,TimeLow)
// Get image sizes and test for compatiblity
```

```
Number sxEdge, syEdge, szEdge, sxTL, syTL, sxIo, syIo, sxSplice,
sySplice
EdgeSI2.get3dsize(sxEdge,syEdge,szEdge)
TLamda2.get2dsize(sxTL,syTL)
Io2.get2dsize(sxIo,syIo)
SpliceRatio2.get2dsize(sxSplice,sySplice)
//Result(sxEdge+" "+ syEdge+" "+  szEdge+" "+  sxTL+" "+  syTL+" "+
sxIo+" "+  syIo+" "+  sxSplice+" "+  sySplice+" \n")
If (sxTL != SxEdge) OKCancelDialog("Dimensions of t/lamda map wrong
CANCEL")
If (sxIo != SxEdge) OKCancelDialog("Dimensions of Io map wrong
CANCEL")
If (sxSplice != SxEdge) OKCancelDialog("Dimensions of Splice Map map
wrong CANCEL")
If (syTL != SyEdge) OKCancelDialog("Dimensions of t/lamda map wrong
CANCEL")
If (syIo != SyEdge) OKCancelDialog("Dimensions of Io map wrong
CANCEL")
If (sySplice != SyEdge) OKCancelDialog("Dimensions of Splice map
wrong CANCEL")
If (TimeHigh/TimeLow<1) OKCancelDialog("Ratio of Core and Low Loss
Acquisition Time <1.  Expect >1.")
//********************  OPTION TO CHANGE SPLICE RATIO TO TIME RATIO
**********************
// Ask for choice
number choice
choice = 0
getnumber("To change from Splice Ratio to Time Ratio enter
1",0,choice)
//result(choice+" \n")
//set string for tags if splice ratio is used
string RatioChoice
RatioChoice = "Splice"
// Change Io if "Choice" is 1
If (Choice==1)  Io2 = Io2/SpliceRatio*TimeHigh/TimeLow
//showimage(Io2)
//Change string for tags if time ratio is used
```

```
If (Choice==1)  RatioChoice = "Time"
//Normalise the EdgeSI by dividing by Io
Image IoverIo
IoverIo=EdgeSI.imageclone()
IoverIo /=Io2[icol,irow]
//Convert to IoverIoPerEV
number dE
dE=EdgeSI.imagegetdimensionscale(2)
//Result(dE+" \n")
IoverIo=IoverIo/dE
//ShowImage(IoverIo)
//*****************************************************************
//Enter Lamda (nm) and Number of atoms per nanometre cubed
//*****************************************************************
Number Lamda, AtomsPerVol,BarnConversion
getnumber("Inelastic Lamda (nm)",122,Lamda)
getnumber("Atoms per cubic nm",52.47,AtomsPerVol)
TLamda2=TLamda2*Lamda*AtomsPerVol
// Convert to Barns^-1 by dividing by 10^10
BarnConversion=10000000000.
TLamda2=TLamda2/BarnConversion
//ShowImage(TLamda2)
//*** DO THE LEAST SQUARES FITTING
number N,M //running variables for loops in least square fit
number sx,sy,sz  // data size for least square fit
number meanx,bytes,meany,type //numbers for least squares fit
//set the array sizes to match the data
sx=sxEdge
sy=syEdge
sz=szEdge
//Set the number of bytes to be used for the calculation
Getnumber ("Enter the number of bytes",8,bytes)
//Put the variables into variables used in the routine below
//First get the x-arrays
image xArray2D := RealImage("x-array",bytes,sx,sy,sz)
image xArray3D := RealImage("x-array3D",bytes,sx,sy,sz)
// take T/lamada as the x-array
```

```
xarray2D += Tlamda2[icol,irow]
//Copy xArray2D into each slice of xArray3D
xarray3D +=xarray2D[icol,irow]
//Showimage(xarray3D)

//Then get the yarray
image yArray3DplusNoise := RealImage("y-array with
noise",bytes,sx,sy,sz)
//Set the yArray to be the signal intensity per eV normalised by Io
yArray3DplusNoise += IoverIo[icol,irow,iplane]
//ShowImage(yArray3DplusNoise)
//The equations for the least squares fit are taken from
//Least Squares Fitting -- from Wolfram MathWorld on the web
//calculate the mean of the x-array2D
meanx=average(xarray2D)
//result(meanx+"\n")
//Calculate the xArray3D minus the mean
image xMinusMeanxArray3D := RealImage("X minus meanX
3D",bytes,sx,sy,sz)
xMinusMeanxarray3D=xarray3D-meanx
//ShowImage(xMinusMeanxarray3D)
//Calculate the mean of each slice of the y-array 3d and put in a 3D
array
image yMeanArray3D := RealImage("yMeanArray3D",bytes,sx,sy,sz)
image yMinusMeany3D := RealImage("Y minus meanY 3D",bytes,sx,sy,sz)
N=0
While(N<sz)
	{
	// The axes of the output dataset are in the order x,y,z
	// slice3 has arguments
	// startx, starty, startz, x-axis, number-x, step-x,
	//y-axis, number-y, step-y, z-axis, number-z, step-z)
	yMeanArray3D.slice3(0,0,N,0,sx,1,1,sy,1,2,1,1)=yArray3DplusNois
e.slice3(0,0,N,0,sx,1,1,sy,1,2,1,1).average()
	N=N+1
	}
//ShowImage(yMeanArray3D)
```

```
// subtract the mean y from the y array
yMinusMeany3D=yArray3DplusNoise-yMeanArray3D
//ShowImage(yMeanArray3D)
//ShowImage(yMinusMeany3D)

//Form the the arrays (x-mean)^2 (y-meany)^2 and (x-meanx)*(y-meany)
image xxProduct := RealImage("xx product",bytes,sx,sy,sz)
image yyProduct := RealImage("yy product",bytes,sx,sy,sz)
image xyProduct := RealImage("xy product",bytes,sx,sy,sz)
xxproduct=xMinusMeanxarray3D*xMinusMeanxarray3D
yyproduct=yMinusMeany3D*yMinusMeany3D
xyproduct=xMinusMeanxarray3D*yMinusMeany3D
//ShowImage(xxProduct)
//ShowImage(yyProduct)
//ShowImage(xyProduct)
//Form the sums SSxx, SSyy SSxy and put them into "FitResults" in
cols 1,2,3 of row 1 (as used in a spreadsheet)
// DM would have it as 0,1,2, in row 0
number sxresults, syresults
sxresults=4
syresults=3
image            FitResults            :=            RealImage("Fit
Results",bytes,sxresults,syresults,sz)
FitResults[0,0,iplane] += xxProduct
FitResults[1,0,iplane] += yyProduct
FitResults[2,0,iplane] += xyProduct
//Evlaute the fit results plane by plane
N=0
While (N<sz)
      {
      //Form s and put it into  row 1 column 4
      FitResults[3,0,N]=sqrt((FitResults[1,0,N]-
FitResults[2,0,N]*FitResults[2,0,N]/FitResults[0,0,N])/(sx*sy-2))
      //Put xmean and ymean into row 2 cols 1,2 of FitResults
      FitResults[0,1,N]=Meanx
      FitResults[1,1,N]=yMeanArray3D[0,0,N]
```

```
	//Calculate, gradient, gradient error, interecept, intercept
error
	//Put in row 3 columns1,2,3,4 of fit results
	FitResults[0,2,N]=	FitResults[2,0,N]/FitResults[0,0,N]
	FitResults[1,2,N]=  FitResults[3,0,N]/sqrt(FitResults[0,0,N])
	FitResults[2,2,N]=	FitResults[1,1,N]-
FitResults[0,2,N]*FitResults[0,1,N]
	FitResults[3,2,N]=
FitResults[3,0,N]*sqrt((1/sx/sy)+(FitResults[0,1,N]*FitResults[0,1,N
]/FitResults[0,0,N]))
	N=N+1
	}
//Set the display type to spreadsheet for FitResults
//To convert the display type of an image use
//SetDisplayType(img,type)
//img is the image of interest
//n is the display type required
//By trial and error
// type=1 raster
// type=2  surface plot
// type=3  error - not sure
// type=4  Line plot
// type=5  Spreadsheet
// type=6  error not sure
// type=7 spreadsheet
type=5
setdisplaytype(FitResults,type)
ShowImage(FitResults)
//*******************************************************************
********
// Put the data into 4 byte form so that it can be recognised
//as a Spectrum Image and Convert to EELS
//*******************************************************************
********
//results currently in nm squared not Barns
//*******************************************************************
********
```

```
//Put the coefficient and error data into 4 byte form
number sxResults4byte, syResult4byte, BytesResults4Byte
BytesResults4Byte=4
sxResults4byte=4
syResult4byte=1
image FitResults4byte := RealImage("Fit results 4 byte",BytesResults4Byte,sxResults4byte,syResult4byte,sz)
FitResults4byte=FitResults[icol,2,iplane]
//Calibrate energy scale
FitResults4byte.imagesetdimensionscale(2,EdgeSI.imagegetdimensionscale(2))
FitResults4byte.imagesetdimensionorigin(2,EdgeSI.imagegetdimensionorigin(2))
FitResults4byte.imagesetdimensionunitstring(2,EdgeSI.imagegetdimensionunitstring(2))
ShowImage(FitResults4Byte)
//Change to EELS data.
//"FitResults$Byte is now the front image.
//Change to EELS using the menu command.
ChooseMenuItem("Spectrum","Convert Data To", "EELS")
//Set the display type to spreadsheet for FitResults4Byte
//To convert the display type of an image use
//SetDisplayType(img,type)
//img is the image of interest
//n is the display type required
//By trial and error
// type=1 raster
// type=2  surface plot
// type=3  error - not sure
// type=4  Line plot
// type=5  Spreadsheet
// type=6  error not sure
// type=7 spreadsheet
type=1
setdisplaytype(FitResults4Byte,type)
//Add tags to FitResults$Byte under dSigma/dE conditions
//High loss time in arb units
```

```
FitResults4Byte.SetNumberNote("dSigma/dE conditions:High Loss Aquisition Time", TimeHigh)
//Low loss time in arb units
FitResults4Byte.SetNumberNote("dSigma/dE conditions:Low Loss Aquisition Time", TimeLow)
//Splice or Time Ratio
FitResults4Byte.SetStringNote("dSigma/dE conditions:Time or Splice Ratio", RatioChoice)
//In elastic mean free path
FitResults4Byte.SetNumberNote("dSigma/dE conditions:Mean Free Path (nm)", Lamda)
//Atoms/vol
FitResults4Byte.SetNumberNote("dSigma/dE conditions:Atoms per cubic nm", AtomsPerVol)
//Bytes for processing
FitResults4Byte.SetNumberNote("dSigma/dE conditions:Bytes for fitting process", Bytes)
//EdgeSI file name
FitResults4Byte.SetStringNote("dSigma/dE conditions:EdgeSI file name", EdgeSIName)
//TLamda file name
FitResults4Byte.SetStringNote("dSigma/dE conditions:T/Lamda Map file name", TLamdaName)
//Io file name
FitResults4Byte.SetStringNote("dSigma/dE conditions:Io Map file name", IoName)
//EdgeSI file name
FitResults4Byte.SetStringNote("dSigma/dE conditions:Splice Ratio Map file name", SpliceRatioName)
//*******************************************************************
//put the results in a form suitable for transfer to EXCEL for plotting
//*******************************************************************
//the results in a given plane are in columns of length sx*sy.
//The first column contains the x-values
```

```
//The second column contains the y values
//The third column contains the fity values
//The fourth column contained the deviaitons
image EXCELResults := RealImage("EXCEL Results",bytes,4,sx*sy,sz)
//Define TEMP images to do the transfers.
//To do this assign the relevant section of the array to the TEMP
function
//by using ":="
number sxTemp
sxTemp=1
Image TEMPx := RealImage("",bytes,sxTemp,sy,sz)
Image TEMPy := RealImage("",bytes,sxTemp,sy,sz)
Image TEMPfit := RealImage("",bytes,sxTemp,sy,sz)
Image TEMPdev := RealImage("",bytes,sxTemp,sy,sz)
//initialise loop parameters
N=0
M=0
//Create a loop over the x-direction
//NB icol addresses X   irow addresses Y
While (N<sx)
      {
      //Select the current position down the array
      TEMPx:=EXCELResults.slice3(0,M,0,  0,1,1,  1,sy,1,  2,sz,1)
      // Transfer the current column in
      TEMPx=Xarray3D[N,irow,iplane]
      //Select the current position down the array
      TEMPy:=EXCELResults.slice3(1,M,0,  0,1,1,  1,sy,1,  2,sz,1)
      //Transfer the current column in
      TEMPy=yArray3DplusNoise[N,irow,iplane]
      //Select the current position down the array
      TEMPfit:=EXCELResults.slice3(2,M,0,  0,1,1,  1,sy,1,  2,sz,1)
      // Transfer the current column in
      TEMPfit=Xarray3D[N,irow,iplane]
      // multiply by the gradiesnt
      TEMPfit *=FitResults[0,2,iplane]
      //add the intercept
      TEMPfit +=FitResults[2,2,iplane]
```

```
      //Select the current position down the array
      TEMPdev:=EXCELResults.slice3(3,M,0,  0,1,1,  1,sy,1,  2,sz,1)
      // Subtract the fit from the y data
      TEMPdev=TEMPy-TEMPfit
      N=N+1
      M=M+sy
      }
//Set the display type to spreadsheet for EXCELresults
//To convert the display type of an image use
//SetDisplayType(img,type)
//img is the image of interest
//n is the display type required
//By trial and error
// type=1 raster
// type=2  surface plot
// type=3  error - not sure
// type=4  Line plot
// type=5  Spreadsheet
// type=6  error not sure
// type=7 spreadsheet
type=5
setdisplaytype(EXCELresults,type)
ShowImage(EXCELresults)
```

APPENDIX 6

This script takes a part of the SI, creates the 3d array of values, extracts the mean values from it. Then the y mean values are set up as a 3d array and the subtraction means from 3d array is straightforward using the subtract two 3D array. Then the results are created in form of an spectrum image and put the coefficient and error data into 4 byte form.

```
//Building a test least squares fitting script for SI data
//The equations for the least squares fit are taken from
//Least Squares Fitting -- from Wolfram MathWorld on the web
number N,M, sx,sy,sz,meanx,bytes,meany,type
//input the size of the test data
Getnumber("Enter number of x pixels",5,sx)
Getnumber("Enter number of y pixels",5,sy)
Getnumber("Enter number of z pixels",5,sz)
Getnumber ("Enter the number of bytes",4,bytes)
//make a 2D array that increases in integer steps
image xArray2D := RealImage("x-array",bytes,sx,sy,sz)
xArray2D = irow+(icol*iheight)
ShowImage(xArray2D)
//make a 3D array that increases in integer steps
image xArray3D := RealImage("x-array3D",bytes,sx,sy,sz)
//set loop variable
N=0
While (N<sz)
{
xArray3D[icol,irow,N] = xArray2D
N=N+1
}
ShowImage(xArray3D)
//make a 3D array where the x-y plane is a linear function of the
values
//in the x-array
//with each slice having different slope and intercept
//with them being equal to the plane index plus 1
image yArray3D := RealImage("y-array",bytes,sx,sy,sz)
```

```
yarray3D = (iplane+1)*xArray3D+(iplane+1)
ShowImage(yArray3D)
//add random noise to the y array.  the "-0.5" is to make the mean of
//the noise zero
image yArray3DplusNoise := RealImage("y-array with noise",bytes,sx,sy,sz)
yArray3DplusNoise = yArray3D + Random()-0.5
ShowImage(yArray3DplusNoise)
//calculate the mean of the x-array2D
meanx=average(xarray2D)
//result(meanx+"\n")
//Calculate the xArray3D minus the mean
image xMinusMeanxArray3D := RealImage("X minus meanX 3D",bytes,sx,sy,sz)
xMinusMeanxarray3D=xarray3D-meanx
ShowImage(xMinusMeanxarray3D)
//Calculate the mean of each slice of the y-array 3d and put in a 3D array
image yMeanArray3D := RealImage("yMeanArray3D",bytes,sx,sy,sz)
image yMinusMeany3D := RealImage("Y minus meanY 3D",bytes,sx,sy,sz)
N=0
While(N<sz)
	{
	// The axes of the output dataset are in the order x,y,z
	// slice3 has arguments
	// startx, starty, startz, x-axis, number-x, step-x,
	//y-axis, number-y, step-y, z-axis, number-z, step-z)
yMeanArray3D.slice3(0,0,N,0,sx,1,1,sy,1,2,1,1)=yArray3DplusNoise.slice3(0,0,N,0,sx,1,1,sy,1,2,1,1).average()
	N=N+1
	}
ShowImage(yMeanArray3D)
// subtract the mean y from the y array
yMinusMeany3D=yArray3DplusNoise-yMeanArray3D
ShowImage(yMeanArray3D)
ShowImage(yMinusMeany3D)
```

```
//Form the the arrays (x-mean)^2 (y-meany)^2 and (x-meanx)*(y-meany)
image xxProduct := RealImage("xx product",bytes,sx,sy,sz)
image yyProduct := RealImage("yy product",bytes,sx,sy,sz)
image xyProduct := RealImage("xy product",bytes,sx,sy,sz)
xxproduct=xMinusMeanxarray3D*xMinusMeanxarray3D
yyproduct=yMinusMeany3D*yMinusMeany3D
xyproduct=xMinusMeanxarray3D*yMinusMeany3D
ShowImage(xxProduct)
ShowImage(yyProduct)
ShowImage(xyProduct)
//Form the sums SSxx, SSyy SSxy and put them into "FitResults" in
cols
//1,2,3 of row 1 (as used in a spreadsheet)
// DM would have it as 0,1,2, in row 0
number sxresults, syresults
sxresults=4
syresults=3
image FitResults := RealImage("Fit
Results",bytes,sxresults,syresults,sz)
FitResults[0,0,iplane] += xxProduct
FitResults[1,0,iplane] += yyProduct
FitResults[2,0,iplane] += xyProduct
//Evaluate the fit results plane by plane
N=0
While (N<sz)
     {
     //Form s and put it into  row 1 column 4
FitResults[3,0,N]=sqrt((FitResults[1,0,N]-
FitResults[2,0,N]*FitResults[2,0,N]/FitResults[0,0,N])/(sx*sy-2))
     //Put xmean and ymean into row 2 cols 1,2 of FitResults
     FitResults[0,1,N]=Meanx
     FitResults[1,1,N]=yMeanArray3D[0,0,N]
     //Calculate, gradient, gradient error, interecept, intercept
error
     //Put in row 3 columns1,2,3,4 of fit results
     FitResults[0,2,N]=    FitResults[2,0,N]/FitResults[0,0,N]
     FitResults[1,2,N]=  FitResults[3,0,N]/sqrt(FitResults[0,0,N])
```

```
     FitResults[2,2,N]=                          FitResults[1,1,N]-
FitResults[0,2,N]*FitResults[0,1,N]
     FitResults[3,2,N]=
FitResults[3,0,N]*sqrt((1/sx/sy)+(FitResults[0,1,N]*FitResults[0,1,N
]/FitResults[0,0,N]))
     N=N+1
     }
//Set the display type to spreadsheet for FitResults
//To convert the display type of an image use
//SetDisplayType(img,type)
//img is the image of interest
//n is the display type required
//By trial and error
// type=1 raster
// type=2  surface plot
// type=3  error - not sure
// type=4  Line plot
// type=5  Spreadsheet
// type=6  error not sure
// type=7 spreadsheet
type=5
setdisplaytype(FitResults,type)
ShowImage(FitResults)
//Put the coeeficient and error data into 4 byte form
number sxResults4byte, syResult4byte, BytesResults4Byte
BytesResults4Byte=4
sxResults4byte=4
syResult4byte=1
image      FitResults4byte      :=      RealImage("Fit      results
4byte",BytesResults4Byte,sxResults4byte,syResult4byte,sz)
FitResults4byte=FitResults[icol,2,iplane]
ShowImage(FitResults4Byte)
//Change to EELS data.
//"FitResults$Byte is now the front image.
//Change to EELS using the menu command.
ChooseMenuItem("Spectrum","Convert Data To", "EELS")
```

```
//Set the display type to spreadsheet for FitResults4Byte
//To convert the display type of an image use
//SetDisplayType(img,type)
//img is the image of interest
//n is the display type required
//By trial and error
// type=1 raster
// type=2  surface plot
// type=3  error - not sure
// type=4  Line plot
// type=5  Spreadsheet
// type=6  error not sure
// type=7 spreadsheet
type=1
setdisplaytype(FitResults4Byte,type)
//put the results in a form suitable for transfer to EXCEL for
plotting
//the results in a given plane are in columns of length sx*sy.
//The first column contains the x-values
//The second column contains the y values
//The third column contains the fity values
//The fourth column contained the deviaitons
image EXCELResults := RealImage("EXCEL Results",bytes,4,sx*sy,sz)
//Define TEMP images to do the transfers.
//To do this assign the relevant section of the array to the TEMP
function
//by using ":="
number sxTemp
sxTemp=1
Image TEMPx := RealImage("",bytes,sxTemp,sy,sz)
Image TEMPy := RealImage("",bytes,sxTemp,sy,sz)
Image TEMPfit := RealImage("",bytes,sxTemp,sy,sz)
Image TEMPdev := RealImage("",bytes,sxTemp,sy,sz)
//initialise loop parameters
N=0
M=0
//Create a loop over the x-direction
```

```
//NB icol addresses X   irow addresses Y
While (N<sx)
     {
     //Select the current position down the array
     TEMPx:=EXCELResults.slice3(0,M,0,  0,1,1,  1,sy,1,  2,sz,1)
     // Transfer the current column in
     TEMPx=Xarray3D[N,irow,iplane]
     //Select the current position down the array
     TEMPy:=EXCELResults.slice3(1,M,0,  0,1,1,  1,sy,1,  2,sz,1)
     //Transfer the current column in
     TEMPy=yArray3DplusNoise[N,irow,iplane]
     //Select the current position down the array
     TEMPfit:=EXCELResults.slice3(2,M,0,  0,1,1,  1,sy,1,  2,sz,1)
     // Transfer the current column in
     TEMPfit=Xarray3D[N,irow,iplane]
     // multiply by the gradiesnt
     TEMPfit *=FitResults[0,2,iplane]
     //add the intercept
     TEMPfit +=FitResults[2,2,iplane]
     //Select the current position down the array
     TEMPdev:=EXCELResults.slice3(3,M,0,  0,1,1,  1,sy,1,  2,sz,1)
     // Subtract the fit from the y data
     TEMPdev=TEMPy-TEMPfit
     N=N+1
     M=M+sy
     }
//Set the display type to spreadsheet for EXCELresults
//To convert the display type of an image use
//SetDisplayType(img,type)
//img is the image of interest
//n is the display type required
//By trial and error
// type=1 raster
// type=2  surface plot
// type=3  error - not sure
// type=4  Line plot
// type=5  Spreadsheet
```

```
// type=6  error not sure
// type=7 spreadsheet
type=5
setdisplaytype(EXCELresults,type)
ShowImage(EXCELresults)
```

Table of figures

Figure 1. Crystal structures of iron. (*a*) Body-centred cubic (BCC) α-iron. (*b*) Face-centred cubic (FCC) γ-iron. 6

Figure 2. Fe-Fe_3C phase diagram with areas of existence each of system phases. 7

Figure 3. A graph showing the Ultimate Tensile Strength in the function of elongation, together with the years, when the studies of each materials have started [22]. In the left bottom corner the steel properties are the lowest, and knowledge about them is the oldest. IN the right top corner the properties of the steel are the highest (both elongation and UTS). In the top left corner the newest steels are summarised, which are characterised by the highest UTS but short elongation. Republished with permission of O. Bouaziz, S. Allain, C. P. Scott, P. Cugy, and D. Barbier, from *High manganese austenitic twinning induced plasticity steels: A review of the microstructure properties relationships.* Current Opinion in Solid State and Materials Science, 2011. 15(4): p. 141-168, permission conveyed through Copyright Clearance Center, Inc. 10

Figure 4. The graph of tensile test of high manganese steels with different Mn and C content. The graphs of 12%wt Mn and 17%wt Mn show the oscillations of the lines resulting from TRIP effect occurring in these steels. Republished with permission of O. Bouaziz, S. Allain, C. P. Scott, P. Cugy, and D. Barbier, from *High manganese austenitic twinning induced plasticity steels: A review of the microstructure properties relationships.* Current Opinion in Solid State and Materials Science, 2011. 15(4): p. 141-168, permission conveyed through Copyright Clearance Center, Inc. 18

Figure 5. Technological scheme of precipitation treatment during production of steels used in the project [138], the temperature of the two hits and the isothermal holding was varied for different samples and was either 850°C, 900°C or 950°C. 30

Figure 6. Interactions and possible effects during sputtering of a solid surface by an Ar^+ ion. The surface of specimen (blue dots) is bombarded by argon ions (red plus dot) and cause displacement of atoms randomized and showed by arrows with the final effect (red dot); sputtering with sputtered atom (white dot); and electron release due to the excitation process (green dot with minus), which then can interact with argon ions. 32

Figure 7.The scheme of Focused Ion Beam process [161]. The grey ball of Ga^+ bombards the surface causing emission of electrons, ions and neutral particles, as a result of knock-on damage. The gas assisted injector (for example Pt deposition) is inserted on the right, the ion detector is on the left. 35

Figure 8. Scheme of columns in DualBeam. The SEM column is in the zone axis, the focused ion beam source is on the 52° off axis. The backscattered electrons are shown, as they occur as an effect of the surface interactions. The block face is the place, where the lift-out take place. 36
Figure 9. The scheme of the position of GIS needle in the column in relation with the electron and ion beams and the specimen surface. 37
Figure 10. The cross-section cut out from the bulk material, a) with the ion beam from the top, b) at 52° with the electron beam. The figure shows the same moment of the operation - the lamella attached (GIS Pt deposited rectangle visible on the contact between Omniprobe and specimen)to the Omniprobe, just after the specimen was cut away of the bulk. 38
Figure 11. Specimen attached to the Omniprobe grid a) before b) after separation of the micro manipulator, c) the Omniprobe holder with specimen on the left B holder seen with 400x magnification with electron source, d) specimen after thinning from both sides, with the visible platinum and other sample contrast. Photos were acquired during standard specimen preparation session. 39
Figure 12. The schematic microscope rays. The source is in the top named electron gun. Then the rays are passing through C1 and C2 lens, forming a beam which illuminates the specimen, which is at the same height as the objective lens. The objective aperture is just below the specimen, and below are magnifying lens - intermediate and projector. The end of the electron rays path is a viewing screen. 41
Figure 13. A schematic diagram of a thermionic gun source with 1) cathode, 2) Wehnelt cup, 3) anode. 45
Figure 14. Schematic diagram of a field emission gun [164]. The electrons are emitted due to the high electric potential $V_{1,}$ which provides extraction voltage to pull the electrons out of the tip. The fine cross-over is formed by two anodes reacting as electrostatic lens. The second anode accelerates the electrons to 100, 200 or more KV. Republished with permission of D. B. Williams and C. B. Carter , from *Transmission Electron Microscopy*. 2009, New York: Springer; permission conveyed through Copyright Clearance Center, Inc. 46
Figure 15. Scheme of the cross-section of magnetic lens. Two separated pole pieces are visible, with bore and gap. The polepieces are cooled with water, and filled with copper coils. The magnetic field deflect the electrons with the strength directly proportionally to the off-axis position of the electrons [164]. Republished with permission of D. B. Williams and C. B. Carter , from *Transmission Electron Microscopy*. 2009, New York: Springer; permission conveyed through Copyright Clearance Center, Inc. 48

Figure 16. Scheme of the rays in microscope suffering from spherical aberration. a point object is imaged as a disk with radius $r_s \approx C_s \alpha^3$ due to spherical aberration that causes the off-axis rays are not focused at the same point F. 54
Figure 17. Scheme of the rays in microscope suffering from coma, which means that electrons travelling through outer parts of the lens are focused in different point that the ones travelling closer to the axis. The result is off-axis object point image in the form of a comet-shape disc. 55
Figure 18. Simulation of Ronchigram with aberrations and uncorrected Cs[175]. In the figure the beam rays are scattered through the amorphous sample, and presented in the position on Ronchigram. The outer rings presents the infinite magnification, the inner 'flat' circle represents the shadow image of specimen. The ronchigram was simulated with a defocus of 500nm and for a spherical aberration of 3.1mm. Republished with permission of [Rightsholder's name], from [Work's title, author, volume, edition number and year of copyright]; permission conveyed through Copyright Clearance Center, Inc. 56
Figure 19. The scheme of sextupole correcting the Cs in the electron beam travelling through the electron column [175]. The multipole of 6th order with an impression of the correspodning field line. The resulting forces on an electron beam travelling down the optic axis have effect as impart a triangular distortion to the beam. Republished with permission of [Rightsholder's name], from [Work's title, author, volume, edition number and year of copyright]; permission conveyed through Copyright Clearance Center, Inc. 57
Figure 20. The different types of electron interactions with specimen in TEM [164]. Republished with permission of D. B. Williams and C. B. Carter , from *Transmission Electron Microscopy*. 2009, New York: Springer; permission conveyed through Copyright Clearance Center, Inc. 58
Figure 21.The two basic operations of TEM imaging system showing a)diffraction pattern on the viewing screen, b)classic imaging . In each case the intermediate lens selects either the back focal plane or the image plane of the objective lens as its object. Republished with permission of D. B. Williams and C. B. Carter , from *Transmission Electron Microscopy*. 2009, New York: Springer; permission conveyed through Copyright Clearance Center, Inc. {D. B. Williams, 2009 #333} 60
Figure 22. The scattering of the rays on the crystallographic planes together with the Bragg angle. . 61
Figure 23. Two diffraction patterns obtained from V-steel. a) shows the DP taken on 111 zone axis, with the indexing of austenite (yellow) and probably precipitates (green) b) shows the DP taken on 110 zone axis with indexing of austenite (red), and green and violet being the patterns from Fe_3O_4 which is an oxide formed on the surface, dominating the whole signal from precipitates. The distances r_1, r_2, and r_3 which are used for indexing are presented on both; red arrows for precipitate, blue arrows for austenite. 62

Figure 24. STEM BF, ADF and HAADF detectors and their annular ranges. The conventional ADF and BF detectors are shown as well as the HAADF detector set-up for Z- contrast imaging, together with the range of electron scattering angles for each detector. 65
Figure 25. The ionization process. An inner (K) shell electron is ejected from the atom by a high energy electron. When the hole in the K shell is filled by an electron from the L shell, characteristic X-ray emission occurs. The beam electron loses energy but continues on through the specimen. [164] Republished with permission of [Rightsholder's name], from [Work's title, author, volume, edition number and year of copyright]; permission conveyed through Copyright Clearance Center, Inc. 66
Figure 26. Schematic layout of GIF Quantum showing the location of key components [189]. Republished with permission of [Rightsholder's name], from [Work's title, author, volume, edition number and year of copyright]; permission conveyed through Copyright Clearance Center, Inc. 68
Figure 27. Schematic spectrum of the electron energy loss. Contains the ZLP, two plasmon peaks, and spliced core loss. The splice point is around 170eV loss (visible step change at that region in blue graph). This spectrum is from the vanadium precipitate, where C-K edge is visible at 280eV, Ti L-edge is visible at 450eV, Vanadium L-edge visible at 513eV followed by oxygen K-edge is slightly visible (525eV loss),and manganese edge (640eV loss). The spectrum shows the splice problem, which is described in chapter 7. 69
Figure 28. *A* schematic diagram of spectrum imaging technique, which can be used for quantitative analysis. 72
Figure 29. Figure 23: Simplified setup of the electron-optical path for energy-filtered imaging using a post-column energy filter (GIF). 76
Figure 30. Three window method, shows the part of the spectrum with the edge. Three window method uses two pre-edge windows of chosen energy width, and one post- edge window, which width is chosen to include the edge intensity.. 77
Figure 31. Modeling results in SRIM PRO Ga^+ ions interacting with the surface at 90° with different ion energy.. 87
Figure 32. Dark Field TEM Images of V steel a) without deposition of protection layer of Au, b) with protection layer of Au. In first case the artifacts such as curtaining are visible; in second case despite a lot of contrast in different grains no such thing is visible. 92
Figure 33. A grain boundary between two grains in the base steel (without microalloying elements), showing no precipitates even in such places. 94
Figure 34. A DF image of vanadium steel with only a few precipitates visible(pointed out by white arrows). The red arrows points out the FIB artifacts like curtaining and second type contrast arising from surface oxidation, which are undesirable features. 95

Figure 35. The DF image of a vanadium steel with additional second contrast occurring during tilting the beam. Also the artifacts like curtaining from the FIB are visible (pointed by the red arrows). There is one clear precipitate (pointed by white arrow), but the rest possible ones are hidden beneath the second type contrast. Some of the dislocations are also visible, due to the dislocation contrast. 96
Figure 36. A dark field image of a vanadium steel sample deformed for 100s in 900°C. Despite a lot of contrast, which reveals such things like grain boundaries, dislocations, parallel fringes, and surface oxide just a few precipitates are nearly visible. 97
Figure 37. BF TEM image of the microstructure of the Nb microalloyed steel after thermomechanical treatment at 900°C for 100s. A classic thermomechanical structure in the stage of dynamic recovery is visible - the stair like pattern of relaxed dislocations. Most of them are in the oriented line, whereas the grains stay free from dislocations. 98
Figure 38. DF TEM image of the same area shown in Figure 37. A high density of subgrain boundaries are visible as a result of dynamic recovery during warm deformation, with a precipitates shining brightly (pointed out by white arrows), which are different than the ones highlighted in Figure 37. 98
Figure 39. A classic dark field image of Nb steel isothermally treated for 100s at 900°C with plenty of precipitates highlighted at the same time with subtle contrast overall, especially to the top right, probably from surface oxide. 99
Figure 40. Precipitates in Nb steels heat treated at 900°C: a) Untypical area after 1s, with several small precipitates and one rather large one (most areas were free of precipitates); b) typical area in the 40s sample with numerous precipitates; c) typical area in the 100s sample with many precipitates..................... 100
Figure 41. DF image of Nb steel isothermally treated for 40s in 900°. The grain boundary visible in the middle, and precipitates are highlighted in both grains suggesting the grains have the same crystallographic orientation. Some residue second type contrast is showing up in the right top corner. 100
Figure 42. a) A [110] selected area diffraction pattern from a vanadium steel sample. Three groups of spots are indicated with coloured outlines: austenite in white, and two others in pink and green. Green is purely from Fe_3O_4, whereas pink may be a combination of Fe_3O_4 and vanadium carbide. . 102
Figure 43. Zone axis diffraction patterns from Nb steels heat-treated for different times at 900°C showing weak spots originating from different sources. Pale blue refers to the austenite matrix; yellow refers to spots which could relate to NbC in cube-on-cube orientation relationship; red and orange refers to spots that relate to Fe_3O_4, but not in the cube-on-cube orientation relationship. e) Schematic diagram of the indexing a [110] diffraction pattern from cube-on-cube Fe-Mn, Fe_3O_4 and

NbC, where green is Fe_3O_4, blue is austenite and red is NbC (for Fe_3O_4 large circles represent strong spots, and small circles represent weak spots). 103
Figure 44. EFTEM imaging of a V steel held at 900°C for 100s: a) the chemical map of Ti, b) the chemical map of V, c) the chemical map of C, and d) a combined three colour map of the three chosen elements. The precipitates are highlighted by the white arrows on the Ti, V elemental maps, and general map. They are not visible in the C map. 106
Figure 45. EFTEM image taken before ARM session prior investigation is to find desirable area for spectrum imaging. This is a V steel isothermally treated for 100s in 900°C, which in a very thin region has clear precipitate of a size of 20nm (see white arrow) 107
Figure 46. EFTEM three window method of Nb $N_{2,3}$ edge imaging of three precipitates. The specimen was isothermally held for 40s at 900°C. Two pre- edge windows starts at 26eV and 31 eV loss, and the post-edge window starts at 46eV. The last image presents the subtracted edge signal. The images presents three precipitates which nucleated on dislocation (see white arrow), which have approx. 15nm.. 107
Figure 47. Nb-steel specimen imagined with DF and EFTEM isothermally held for 40s at 900°C. a) Precipitates nucleated on dislocations or grain boundary recorded with the DF imaging technique; b) precipitates observed by DF with different imaging conditions than a); c) EFTEM imaging using energy loss $N_{2,3}$-edge at 34eV, matching the Nb edge. The images presents three precipitates which nucleated on a dislocation or grain boundary (see white arrow), which have approx. 15nm. 108
Figure 48. EFTEM mapping with the Nb $N_{2,3}$ edge down to 4nm sized precipitates in a steel isothermally held for 40s at 900°C. Three precipitates are recorded (see white arrrows). Two of them have the size of about 8nm and one is half that size. The top one has elongated shape, whereas the two below seem to be round. 109
Figure 49. Mapping and imaging of C and Nb in precipitates using EFTEM in sample isothermally held for 40s at 900°C: a) jump ratio image at the C-K edge; b) jump ratio image at the Nb-$M_{4,5}$ edge; c) elemental map at the Nb $N_{2,3}$ edge (a slightly different area); d) dark field imaging of a the precipitates seen in c). 109
Figure 50. LEFT: The survey image for spectrum imaging from V steel isothermally treated for 100s in 900°C. Two areas highlighted – area of spectrum imaging data, and of spatial drift. a) The HAADF image without noise correction image taken with Gatan detector on ARM before the spectrum image is taken, b) The HAADF image without noise correction image taken with Gatan detector on ARM after the spectrum image is acquired. There is a significant improvement in the quality of the image with the noise cancellation on. Unfortunately in the region of spectrum image and spatial drift there is a huge amorphous carbon contamination due to the thigh current in ARM (brighter circles). 110

Figure 51. Elemental maps obtained by post-processing of a spectrum image from the V-steel held at 900°C for 100s using standard procedures within Digital Micrograph: a) vanadium; b) iron; c) titanium; d) oxygen; e) manganese; f) multicoloured map with iron in orange, vanadium in green and titanium in blue. 112
Figure 52. Chemical composition profiles across the precipitate of Figure 51. A) horizontal profile, b) vertical profile. Blue indicates vanadium, green – titanium, red - iron, and violet - manganese. 113
Figure 53. Atomic resolution HAADF image of a precipitate in a V steel held at 900°C for 100s. The light grey region represents the matrix, the darker shade of circle represents the vanadium precipitate of size about 14nm. 114
Figure 54. HAADF STEM image of a carbide in the Nb steel viewed along [011]. The darker spots represents the matrix, whereas the lighter spots represents the Nb precipitate of size approx. 8nm. The precipitate is on cube-on-cube orientation with the matrix. Also the Moiré fringes can be seen across the precipitate suggesting the lattice parameter mismatch between matrix and precipitate. 114
Figure 55. The HAADF image of NbC particle surrounded by the matrix. The image was acquired with a Jeol ADF detector at 8cm camera length. The red spots represents the matrix, whereas the violet spots represents the Nb precipitate of size approx. 11nm. The precipitate is on cube-on-cube orientation with the matrix. Also the Moiré fringes can be seen across the precipitate suggesting the lattice parameter mismatch between matrix and precipitate. 115
Figure 56. Schematic diagrams of the ideal (a) and real (b) samples with the contributing material left after removal of the matrix in the ideal (c) and real (d) cases. All the Fe_3O_4 and amorphous carbon are shown on one surface for clarity. 119
Figure 57. Schematic graph of individual post-processing steps for removal of the matrix, and unwanted signals resulting in precipitate only signal. 121
Figure 58. The effect on the low loss spectrum of the bleed-through between the core-loss and low-loss regions (green), together with the corrected low-loss spectrum (black). 125
Figure 59. Example of splice factors map for vanadium steel specimen obtained from post-processed data up to the splice. Extraction of the splice factor was with use of script (see appendix 3). 126
Figure 60. Comparison of splicing the low loss and core loss regions of the spectra without and with prior smoothing of the end of the low loss spectrum using a power law fit. Details can be found in the text. The raw low loss data is shown in blue, the smoothed low-loss in red, the spliced high-loss to the raw low loss in thin black, and the spliced high loss to the smoothed low-loss in thick black. 127

Figure 61. The effects of matrix subtraction on the summed spectrum from 5 x 6 pixels in the centre of a (V,Ti)C precipitate. The deconvolved spectrum without removal of the signal from steel matrix is shown in red. The spectrum after removal of the matrix contribution, i.e. the (V,Ti) precipitate only, is shown in black. The low loss region is shown inset. 130
Figure 62. Edge intensities extracted at three points in the processing: after splicing (green); after deconvolution (red); and after removal of the matrix contribution (black). a) the C K-edge; b) the N K-edge ; c) the Ti $L_{2,3}$-edge; d) V $L_{2,3}$-edge ; e) the V L_1-edge and the Mn $L_{2,3}$-edge; f) the Fe $L_{2,3}$- edge. The background-fitting window is shown as a pink box on each plot. The signal integration windows used for the maps in figure 9 are shown as boxes above the edges in pale green. 132
Figure 63. a) Maps of the edge intensities for a precipitate in the V steel: left column from the as-recorded data; right column from the fully processed data. Black in the maps corresponds to zero counts. b) Line profiles across the maps from the unprocessed data (colours as for the maps in a), the position of the line for the profile is shown in the upper right V map). c) Line profiles across the maps from the fully processed data; the elemental signals are plotted against the left hand *y* axis and the thickness plot (black) is plotted against the right hand *y* axis. 135
Figure 64. a) The results of background subtraction using the fitting window indicated by the pale pink box in front of the Nb-$M_{4,5}$ edge on a sample with a total t/λ of 0.18. Each is shown at three stages of the processing: after splicing (green); after deconvolution (red); and after removal of the matrix contribution (black). b) The result of background subtraction using a smaller fitting window closer to the Nb $M_{4,5}$-edge, again indicated by the pale pink box. A comparison is made of the edge shapes from the precipitate (black) with those from NbC (red) and NbN (green) standards with similar background fitting windows and scaled to have the same integrated Nb-$M_{4,5}$ intensity prior to the C-K edge. The signal integration window for the Nb maps in Figure 66 is shown by the pale green box. 138
Figure 65. a) Full spliced spectrum of Nb specimen. At the left end the counts are growing rapidly, so only this part is showed, because otherwise low-intense core loss edges won't be visible. In such presented spectrum the Nb-$M_{4,5}$ edge is slightly emerging from the spectrum at 200eV loss, followed by sharp C-K edge at 284eV, there are some indications of Nb-$M_{2,3}$ edge at 360eV, and then Ti, O and Mn. b)Close up at low loss and first part of the core loss, where the splice point is. 139
Figure 66. Maps of the edge intensities for a precipitate in the Nb steel: left column from the as-recorded data; right column from the fully processed data. Black in the maps corresponds to zero signal. b) Line profiles across the maps from the unprocessed data (the position of the line for the profiles is shown in the upper right Nb map). c) Line profiles across the maps from the fully processed data. 140

Figure 67. The background subtracted C K-edge shape from the precipitate spectrum image is shown in red(dark grey in print). It is the sum of spectra over several pixels in the centre of the precipitate. The MLLS fit to this edge is shown in blue (light grey in print) and the fitting window in pale green(pale grey in print). The contribution of the shape of the C K-edge shape from VC is shown in black, and this is the signal of interest. The difference between this and the MLLS fit is the contribution from surface amorphous carbon. (Note, this result is taken from a dataset where there was significant carbon build-up in order to illustrate the point). 142
Figure 68. MLLS fitting to separate O from the V signal for a VC precipitate. The raw signal is shown in gold, the MLLS fit in black, the O component of the fit in red, and the V component in green (the MLLS fit window is in pale green). The O-K standard was selected from within the spectrum image from an area containing no precipitate, and the V-$L_{2,3}$ standard was from previous work on bulk VC [219]. 143
Figure 69. The needle-shaped specimen in FIB, observed with the electron source straight after preparation, and during experiment in ARM, observed with HAADF. 152
Figure 70. a) a map of t/λ from the TiC0.98 tip; b) the HAADF image after rotating 90° about the tip axis: c) the HAADF image after thresholding; d) plots of maximum values t/λ in each vertical line of the image and the corresponding values of t from the HAADF image versus axial position (i.e. the horizontal direction, from left to right); e) a plot of t^2 against $(t/ \lambda)^2$ together with a linear fit and the corresponding deviations. The plot describes the t^2 against $(t/ \lambda)^2$ because the λ varies approximately as the square root of the axial position. 153
Figure 71. Specimen contribution of bulk and surface phases. 153
Figure 72. The scheme of the least squares fit with the vertical and perpendicular offsets. Both offsets work good, and their choice is arbitrary, with negligible effect on final results. The perpendicular are used in the DM script in this thesis. The positive intercept at the *y* axis arise from the surface contribution, and its value stands for σ_s. 160
Figure 73. Plots of $[(1/(I_0)_{xy}) (I(E)_{xy} /\Delta E) (S_{xy}/T)]$ versus $[N_M \lambda_B (t/ \lambda)_{xy}]$ for for two V-standards, VC and VN of high intensity energy at the edge including white lines. The top row presents fitting two graphs from VC, the left top is fitting of V signal, the right top is C fitting. The bottom row presents graphs for VN separated on V and N fitting. All fitting are presented with the standard deviations (green). 162
Figure 74. Plots of $[(1/(I_0)_{xy}) (I(E)_{xy} /\Delta E) (S_{xy}/T)]$ versus $[N_M \lambda_B (t/ \lambda)_{xy}]$for for two Ti-standards, TiC and TiN of high intensity energy at the edge including white lines. The top row presents fitting two graphs from TiC, the left top is fitting of Ti signal, the right top is C fitting. The bottom row presents graphs

for TiN separated on Ti and N fitting. All fitting are presented with the standard deviations (green). 163
Figure 75. Plots of $[(1/(I_0)_{xy})\ (I(E)_{xy}/\Delta E)\ (S_{xy}/T)]$ versus $[N_M\ \lambda_B\ (t/\ \lambda)_{xy}]$for for two Nb-standards, NbC and NbN of high intensity energy at the edge including white lines. The top row presents fitting two graphs from NbC, the left top is fitting of Nb signal, the right top is C fitting. The bottom row presents graphs for NbN separated on Nb and N fitting. All fitting are presented with the standard deviations (green). 164
Figure 76. TiC and TiN cross-sections, a) TiC, TiN cross section overlapped with differential cross sections from DM for C, N and Ti, b)TiN cross-sections from two specimens and DM values, c) TiC cross-sections with DM differential cross-section. The light blue, orange and red are TiC standard cross-sections, the dark blue is DM TiC cross section. The black, green and dark orange is TiN cross-section followed by dark red DM cross-section for TiN. 167
Figure 77. VC and VN cross-sections, a) VC, VN cross section overlapped with differential cross sections from DM for C, N and V, b)VN cross-sections from two specimens and DM values, c) VC cross-sections with DM differential cross-section. The black and orange is for VC standard cross-section with blue DM cross-section for VC. The dark red, violet and green are for VN cross-sections, with dark blue as DM cross-section for VN. 168
Figure 78. NbC and NbN cross-sections. Blue line shows NbC standard with the background, green is a extracted NbC differential cross-section, red is extracted NbN differential cross-section and violet one is a Nb-$M_{4,5}$ differential cross-section extracted from DM........ 169
Figure 79. Chemical profiles of all elements in nanometers compared with relative thickness, also in nm. These profiles presents full quantification of VC precipitate presented in the Figure 63. Its elemental composition is $V,Ti)_{0.56}(C,N)_{0.44}$. 174
Figure 80. a) Maps of the edge intensities for a precipitate in the V steel from the fully processed data. Black in the maps corresponds to zero counts. b) Line profiles across the maps; (colours as for the maps in a), the position of the line for the profile is shown in the upper right V map). Its elemental composition is $(V+Ti)_{0.75}(C+N)_{0.25}$. 176
Figure 81. The pseudo 3D-representation of the vanadium precipitate with vertical profiles of all elements. The left part is a reconstructed image from Amira software, based on TERT function, the right profiles show gradient of thickness for individual elements - the black colour correspond to 0 thickness, the brighter colour, the higher thickness. 176
Figure 82. Maps of the edge intensities for a precipitate in the V steel from the fully processed data. Black in the maps corresponds to zero counts. Line profiles across the maps; the position of the line for the profile is shown in the upper right V map. 178

Figure 83. Maps of the edge intensities for a precipitate in the V steel from the fully processed data of steel isothermally treated for 100s in 900°C. Black in the maps corresponds to zero counts. Line profiles across the maps; the position of the line for the profile is shown in the upper right N map. 179
Figure 84. Comparison of ratios and stoichiometries in three fully quantified V precipitates presented in this thesis. In the small insider in the right top corner the C:M versus Ti:M is ploted. 180
Figure 85. *Elemental maps of the C, Nb and Ti distribution in nm, compared with relative thickness in a typical carbide in the Nb steel after heat treatment at 900°C for 100s, together with the chemical profiles taken across the red line at Nb map.* 182
Figure 86. A background subtracted spectrum of the core loss EEL spectrum from the central region of Nb particle, compared with NbC standard. The spectrum is taken from the precipitate presented in the Figure 66. 183
Figure 87. C, Nb and Ti chemical profiles in nm, compared with relative thickness in a typical carbide in the Nb steel after heat treatment at 900°C for 100s, the chemical profiles taken across the red line at Nb map in the Figure 66. 184
Figure 88. Elemental maps of the C, Nb and Ti distribution in nm, compared with relative thickness in a typical carbide in the Nb steel after heat treatment at 900°C for 100s, together with the chemical profiles taken across the red line at Nb map. 185
Figure 89. Juxtaposition of ratios and stoichiometries in three fully quantified Nb precipitates presented in this thesis. 186